Search for Dark Matter in the Milky Way Halo with the High Energy Stereoscopic System

D I S S E R T A T I O N

zur Erlangung des akademischen Grades

Dr. rer. nat.
im Fach Physik

eingereicht an der
Mathematisch-Naturwissenschaftlichen Fakutät I
Humboldt-Universität zu Berlin

von
Gerrit Christian Spengler

Präsident der Humboldt-Universität zu Berlin:
Prof. Dr. Jan-Hendrik Olbertz

Dekan der Mathematisch-Naturwissenschaftlichen Fakutät I:
Prof. Stefan Hecht, PhD

Gutachter:
1. Prof. Dr. Thomas Lohse
2. Dr. Gernot Maier
3. Prof. Dr. Christopher van Eldik

eingereicht am: 15.8.2013
Tag der mündlichen Prüfung: 28.1.2014

Abstract

An indirect search for the presence of dark matter particles in the halo of the Milky Way with data that were recorded with the High Energy Stereoscopic System (H.E.S.S.) is discussed in this work. For this, the prediction is used that besides other known particles also photons can be created in the decay or mutual annihilation of dark matter particles. For dark matter particles with TeV masses, this process can produce diffuse photon fluxes with TeV energies that can be detected with imaging Cherenkov telescopes like the H.E.S.S. array. The spatial proximity of the halo of the Milky Way leads to the expectation of the presence of larger high energy photon fluxes on the earth from the Milky Way halo than for other astrophysical objects that are investigated in this context like for example dwarf galaxies. However, the extension of the Milky Way halo is challenging for the observation with small field of view Cherenkov telescopes. In particular the need for a subtraction of background events that are mostly generated by cosmic ray events, which Cherenkov telescopes cannot always distinguish from high energy photon events, requires the application of special observation methods for the halo of the Milky Way. Three different methods (driftscan, On/Off and rotated pixel) to observe the Milky Way halo with Cherenkov telescopes are compared in this thesis. Data that were recorded with the H.E.S.S. telescopes in all considered observation modes are analyzed for this purpose. Of special importance in this context is the investigation and control of systematic effects that influence the subtraction of background events. One result of the consideration of the different systematic effects is that the observation of the Milky Way halo in the so called driftscan mode is not recommended. The sensitivity of all three investigated methods to search for the presence of dark matter in the Milky Way halo is compared. One result is that the sensitivity of the so called On/Off method is in general better than for the other considered methods. However, the sensitivity to search for the presence of dark matter in the Milky Way halo with Cherenkov telescopes depends strongly on the unknown distribution of dark matter in the Milky Way. For the most frequently assumed dark matter distributions, the sensitivity of all three investigated methods for the presence of dark matter in the Milky Way halo is at a comparable level. Upper limits on the velocity averaged annihilation cross section $\langle \sigma v \rangle$ are derived from the recorded H.E.S.S. data in the framework of models for the distribution of dark matter in the Milky Way and the creation of photons in the dark matter annihilation. Depending on the observation method and the exposure, values of $\langle \sigma v \rangle$ that are larger than $3 \cdot 10^{-25}$ cm^3/s for dark matter particles with mass 1.8 TeV can be excluded at 95% confidence level. Currently discussed models predict a value for $\langle \sigma v \rangle$ that are about one order of magnitude smaller than the best exclusion limit that is derived in this work.
Additionally, the possibility to search for the presence of dark matter with the planned CTA observatory which will be about one order of magnitude more sensitive than H.E.S.S. is investigated. The possibility that the increased sensitivity of CTA to high energy photon fluxes does not lead to a substantial improvement in sensitivity to search for the presence of dark matter particles in the Milky Way halo is discussed. An analysis strategy that can be used to search for a diffuse high energy photon flux at TeV energies from the galactic plane with Cherenkov telescopes is developed in this context based on data that were recorded with the H.E.S.S. array. Besides other processes, the presence of diffuse TeV energy emission

from the galactic plane is expected because neutral pions that decay into photons are created among other particles in hadronic reactions of galactic cosmic rays with the interstellar medium. This effect can potentially be used in future to measure the energy spectrum of cosmic rays in the energy range between some 100 GeV to some 10 TeV far away from the vicinity of the earth.
Eventually, a new method for the subtraction of background events that does not rely on the precise knowledge of the location and shape of an expected signal region in an observed field of view is developed. First results of this so called harmonic background subtraction that are derived from the analysis of data that were recorded with the H.E.S.S. telescopes are discussed.

Zusammenfassung

In dieser Arbeit wird mit Hilfe von Daten, die mit dem High Energy Stereocopic System (H.E.S.S.) in Namibia aufgenommen wurden, indirekt nach dunkler Materie im Halo der Milchstraße gesucht. Dazu wird die Vorhersage ausgenutzt, dass die Teilchen der dunklen Materie zerfallen oder sich gegenseitig vernichten können wobei neben anderen bekannten elementaren Teilchen auch Photonen entstehen. Für Teilchen der dunklen Materie mit Massen im TeV Bereich, wie sie in gegenwärtig diskutierten Erweiterungen des Standardmodells der Elementarteilchenphysik vorhergesagt werden, könnten so Flüsse von Photonen mit TeV Energien erzeugt werden, die mit abbildenden Cherenkov Teleskopen wie H.E.S.S. nachgewiesen werden können. Der Halo der Milchstraße ist räumlich näher als andere bisher in diesem Zusammenhang intensiv studierte Objekte wie z.B. Zwerg-Galaxien, weshalb ein vergleichsweise großer Photofluß durch den Zerfall oder die gegenseitige Annihilation von Teilchen der dunklen Materie im Halo der Milchstraße auf der Erde erwartet wird. Andererseits stellt die Ausdehung des Halos der Milchstraße eine besondere Herausfordung für die Beobachtung mit Cherenkov-Teleskopen dar. Die Notwendigkeit einer Subtraktion von Untergrundereignissen, die hauptsächlich durch kosmische Strahlung ausgelöst werden aber für Cherenkov Teleskope nicht immer von Ereignissen, die durch hochenergetische Photonen ausgelöst werden, unterschieden werden können, erfordert im vorliegenden Fall die Anwendung besonderer Methoden. Drei verschiedene Strategien für die Beobachtung des Halos der Milchstraße werden in der vorliegenden Arbeit verglichen. Dazu werden Daten, die mit den H.E.S.S. Teleskopen mit allen drei Strategien aufgenommen wurden, analysiert. Besondere Bedeutung kommt dabei der Untersuchung und Kontrolle von systematischen Fehlern, die bei der Subtraktion von Untergrundereignissen auftreten, bei. Ein Ergebnis der Betrachtung der verschiedenen systematischen Effekte ist, dass die Beobachtung des galaktischen Halos im sogenannten Driftscan Modus nicht empfohlen werden kann. Weiter wird die Sensitivität der drei Methoden für die Suche nach Teilchen der dunklen Materie im galaktischen Halo verglichen. Ein Ergebnis ist, dass die Sensitivität der sogenannten On/Off-Beobachtungsstrategie verglichen mit der Sensitivität der anderen untersuchten Methoden am höchsten ist. Jedoch ist die Sensitivität der verschiedenen Methoden stark von der unbekannten Verteilung der dunklen Materie in der Milchstraße abhängig. Für die zur Zeit am häufigsten benutzten Modelle für die Verteilung der dunklen Materie in der Milchstraße ist die Sensitivität von allen Methoden vergleichbar. Aus den Daten, die mit den H.E.S.S.-Teleskopen aufgenommen wurden und deren Analyse in dieser Arbeit beschrieben wird, werden im Rahmen von Modellen für die Verteilung der dunklen Materie in der Milchstraße und die Erzeugung von hochenergetischen Photonen in der Vernichtung von Teilchen der dunklen Materie, obere Schranken auf den geschwindigkeits-gemittelten Vernichtungswechselwirkungsquerschnitt $\langle \sigma v \rangle$ abgeleitet. Abhängig von der Beobachtungsmethode und der Größe des vorliegenden Datensatzes werden Werte von $\langle \sigma v \rangle$, die größer sind als $3 \cdot 10^{-25}\,\mathrm{cm}^3/\mathrm{s}$, für Teilchen der dunklen Materie mit einer Masse von 1.8 TeV bei einem Konfidenzniveau von 95% ausgeschossen. Gegenwärtig diskutierte Modelle sagen einen Wert für $\langle \sigma v \rangle$ vorher, der etwa eine Größenordnung kleiner ist als die beste in dieser Arbeit abgeleitete Auschlußgrenze.
Weiterhin werden in der vorliegenden Arbeit die Möglichkeiten einer Suche nach Teilchen der dunklen Materie im Halo der Milchstraße mit dem geplanten Cherenkov Teleskop System CTA, das etwa eine Größenordnung sensitiver sein wird als

als H.E.S.S., untersucht. Dabei wird die Möglichkeit diskutiert, dass die erhöhte Sensitivität von CTA für die Detektion hochenergetischer Photonen nicht zu einer erhöhten Sensitivität für die Suche nach dunkler Materie in der Milchstraße führt. In diesem Zusammenhang wird an Hand von Daten, die mit den H.E.S.S. Teleskopen aufgenommen wurden, eine Analysemethode entwickelt, die in Zukunft genutzt werden kann, um nach diffuser Emission von Photonen im TeV Bereich von der galaktischen Ebene zu suchen. Unter anderem wird eine solche diffuse Emission von der galaktischen Ebene erwartet, weil in hadronischen Reaktionen der kosmischen Strahlung mit dem interstellaren Medium neben anderen Teilchen auch neutrale Pionen erzeugt werden, welche in Photonen zerfallen. Unter Ausnutzung dieses Effektes kann mit Hilfe von Cherenkov-Daten in Zukunft möglicherweise indirekt das Energiepektrum der galaktischen kosmischen Strahlung im Energiebereich von einigen 100 GeV bis zu einigen 10 TeV weit entfernt von der Erde gemessen und mit dem lokalen Spektrum verglichen werden.
Abschließend wird eine neue Methode der Untergrundsubtraktion entwickelt, die unabhängig von der genauen Kenntnis der Form und Position der erwarteten Signalregion in einem beobachteten Gesichtsfeld angwendet werden kann. Erste Ergebnisse dieser sogenannten harmonischen Untergrundsubtraktion werden an Hand der Untersuchung von Daten, die mit den H.E.S.S. Teleskopen aufgenommen wurden, diskutiert.

Contents

1 Introduction

This chapter gives an introduction into the work described in the subsequent chapters. An introduction into astroparticle and γ-ray astrophysics is given from a general perspective. Although the focus of this thesis is the search for particle dark matter self annihilation in the dark matter halo of the Milky Way, many methods and results that belong traditionally to the wider field of γ-ray astrophysics are used and therefore introduced in the first section. The properties of our own galaxy, the Milky Way, are discussed in the subsequent section and lead naturally to the introduction of 'dark matter' which is the topic of the third section. A general introduction to 'dark matter' from an astrophysical as well as a particle physics point of view is given there. The final section connects the different sections of this chapter and outlines the thesis.

1.1 Astroparticle and γ-ray Astrophysics

1.1.1 Cosmic Rays

Viktor Hess and Carl David Anderson were awarded the 1936 Nobel prize in physics for the discovery of Cosmic Rays[1] (CRs) and the experimental verification of the existence of the positron predicted by P.A.M. Dirac in 1928 (Dirac [1928]). Viktor Hess deployed an electrometer in an air balloon to observe that the intensity of ionisating radiation increases with height above the earth surface (Hess [1912]). This result was found independently in other experiments and was in conflict with the hypothesis that natural radioactivity in the earth is the source of the observed ionizing radiation. In contrast, the measurements pointed towards the existence of previously unexpected exotic sources of high energy radiation in outer space. After establishing that there is a source of ionizing radiation outside the earth in the 1920s, the measurements of the composition and the question of the nature of the ionizing radiation received much attention in the 1930s. Carl D. Anderson discovered the positron in a Wilson cloud chamber installed in a strong magnetic field while trying to measure the mass and charge of CRs by means of their deflection in a magnetic field (Anderson [1932]). Subsequently also the muon (initially named mesotron) was detected in 1937 with a platinum shielded cloud chamber by C.D. Anderson and S. Neddermeyer (Neddermeyer and Anderson [1937]) and it became clear that the investigation of CRs is a prime source of information on particles and firmly established the field of particle physics. Around the time of the discovery of the muon, two essentially equivalent models of how secondary particles can be produced in so called air showers by primary CRs were published (Carlson and Oppenheimer [1937], Bhabha

[1] The expression Cosmic Rays was coined by R. A. Millikan who interpreted them as high energy photons (Millikan [1925]).

and Heitler [1937]). These suggested that the detected CRs are secondary products of the primary CRs interacting in the earth atmosphere. The models of air showers predicted that the extension of air showers increases with energy and enabled Pierre Auger to measure CR events with energies of $\sim 10^{15}$ eV in the late 1930s (Auger et al. [1939]) by deploying Geiger counters in coincidence circuits. The order of magnitude of the inferred primary cosmic ray energy was highly surprising as it was 'actually impossible to imagine a single process able to give a particle such an energy' (Auger et al. [1939]). The nature and origin of CRs became even more mysterious and the newly discovered particles as well as their energy spectra attracted the work of many physicists by the end 1930s. Investigations of the influence of the earth magnetic field on CRs showed ∼1941 that the majority of CRs are protons. The intensive investigation of CRs triggered the isolation of problems and formation of new branches of physics. Astroparticle physics evolved to be more concerned with the question of the origin and nature of primary CRs. Particle physics in contrast developed from the investigation of the reaction products and constitution of CRs. However, still there is a considerable overlap of particle and astroparticle physics. The search for dark matter certainly defines one of the overlapping regions as will be discussed in the course of this thesis.
The origin of CRs is by now still not found, however, important steps for answering this puzzling question have been achieved. The establishment that there is a non-vanishing magnetic field in the inter stellar medium of the Milky Way in the early 1950s destroyed the initial hope of detecting the sources of CRs by measuring their arrival direction as CRs are deflected by the galactic magnetic field and thus their arrival direction is nearly isotropic[2] after many deflections, except for low energy CRs ($E \lesssim 1$ GeV) shielded by the solar and earth magnetic field and possibly for ultra high energies $E \gg 100$ GeV. The energy spectra of primary cosmic rays follow in general a power law $d\Phi(E)/dE \sim E^{-\Gamma}$. This energy dependence is a major hint in favor of modeling the acceleration of CRs by the Fermi theory of CR acceleration (Fermi [1949]) and derived models (see Hillas [2005] for a review). Those models naturally lead to power law spectra where the spectral index reflects the physical properties of the acceleration and propagation conditions.
The primary CR proton energy spectrum with $E \gtrsim 30$ GeV, i.e. the particle flux Φ differential in energy above the solar wind influence, up to ~ 100 TeV, i.e. below the so called 'knee', is described by

$$\frac{d\Phi(E)}{dE} = (1.8 \pm 0.1)\frac{\text{protons}}{\text{m}^2\,\text{s}\,\text{sr}\,\text{GeV}} \cdot 10^4\,(E/\text{GeV})^{-2.7\pm0.1}. \tag{1.1}$$

[2] Anisotropies in the ~ 100 GeV to the ~ 10 TeV energy range are at the level of $\sim 0.3\,\%$ for the dipole amplitude (see IceCube Col. [2010] and references therein).

Compatible within the given errors[3] on the spectral index is the energy dependence of the primary cosmic ray helium flux, however, primary protons constitute $\sim 80\%$ and primary helium $\sim 15\%$ (Eidelman et al. [2004]) of the cosmic ray flux. The residual flux is from heavier elements as well as electrons[4]. Electrons follow a steeper spectrum than hadronic CRs reflecting their fast energy loss mainly due to synchrotron radiation in the galactic magnetic fields and inverse Compton scattering on low energy radiation fields. The CR electron spectrum in the energy range $\sim 10\,\mathrm{GeV} - 40\,\mathrm{TeV}$ is well described by a broken power law

$$\frac{d\Phi}{dE} = (1.4 \pm 0.1)\frac{\text{electrons}}{\mathrm{m^2\ s\ sr\ TeV}} \cdot 10^{-4} \left(\frac{E}{E_b}\right)^{-\Gamma_1} \left(1 + \left(\frac{E}{E_b}\right)^{1/\alpha}\right)^{-(\Gamma_2-\Gamma_1)\alpha}.$$

Here $\alpha \sim 0.3$, $\Gamma_1 = 3.0 \pm 0.1_{\mathrm{stat}} \pm 0.3_{\mathrm{sys}}$, $\Gamma_2 = 4.1 \pm 0.3_{\mathrm{stat}} \pm 0.3_{\mathrm{sys}}$. A spectral break, i.e. a rapid transition of the spectral index from Γ_1 to Γ_2 occurs in the measured electron spectrum at the energy $E_b = (0.9 \pm 0.1)$ TeV. For more information on the electron cosmic ray spectrum measurement see H.E.S.S. Col. [2008] and H.E.S.S. Col. [2009].
The stated precision of the flux normalizations and spectral indices agrees in order of magnitude for the proton and electron spectrum. The more complicated structure of the electron spectrum regarding the spectral break hints towards a more complicated production mechanism and propagation history for CR electrons compared to CR protons. No convergence in modeling the CR electron spectrum has yet been reached but convincing results can be obtained by assuming that the CR electron spectrum up to energies of ~ 1 TeV is produced in an ensemble of nearby pulsar wind nebulae where the cooling time of the electrons due to inverse Compton scattering and synchrotron radiation limits the diffusion length of CR electrons to a few hundred parsec (Grasso et al. [2009]) from their source. For electrons with an energy above ~ 1 TeV, the secondary production of electrons and positrons in decays of charged pions produced in interactions of hadronic CRs with ambient gas can lead to the harder spectrum (see Grasso et al. [2009] for this but also for alternative interpretations).
The study of the spectrum and the composition are main sources of direct information about the origin and nature of cosmic rays. At the highest energies, also the anisotropy in the primary CR arrival direction could help to identify their astrophysical sources. However, in the $\sim$TeV scale the CR arrival directions are as stated above very uniformly distributed and indirect methods to study the CR origin have to be deployed. Particles traveling without deflection from astrophysical particle accelerators can back-trace the acceleration mechanism and origin of CRs. The detection of neutrinos or γ-rays produced

[3] The errors do not represent the best achieved precision of individual experiments sensitive to different energy ranges. However, within the given errors many different experiments operating with independent techniques and different circumstances can be well described. Individual experiments reach a factor ~ 10 better precision and recently also report spectral breaks in the energy range $\sim 1\,\mathrm{GeV} - 1\,\mathrm{TeV}$ (PAMELA Col. [2011]) and significant differences in the spectral index of the helium and proton CR spectra in the quoted energy range. Those effects are, however, not significant within the error on the spectral index given above.

[4] Electrons are in this special case understood as electrons and positrons. The positron fraction in the primary CR flux is $\sim 10\,\%$ at 100 GeV (PAMELA Col. [2009], Fermi Col. [2012], AMS-II Col. [2013]).

f.i. in charged or neutral pion decays, which can in turn be produced in interactions of hadronic CRs with interstellar gas, is an important technique to yield information on the origin of CR. Recently, the detection of γ-rays with energies around the kinematic cut off for neutral pion production in proton matter interactions towards two supernovae remnants with the Fermi satellite gave the first 'direct evidence that cosmic-ray protons are accelerated in SNRs' (Ackermann et al. [2013]).

1.1.2 γ-ray Astrophysics and Instrumentation

Photons with energy $E \gtrsim 1$ MeV are called γ-rays[5]. The γ-ray energy window thus marks the highest currently accessible photon energy range with energies higher than for X-rays. As described above, the direction of astrophysical γ-rays points towards their production source and their energy spectrum contains information on the physical conditions and mechanisms at the acceleration site. Astronomy with γ-rays is therefore a central method to derive information on the most energetic processes at astrophysical sites and of special importance for the study of the origins and mechanisms of cosmic ray acceleration. Additionally, γ-ray observations led to important conclusions on fundamental physics. High precision tests of Lorentz invariance (see f.i. H.E.S.S. Col. [2011]) and the search for particle dark matter at the TeV mass scale described in this thesis and in previous works are two applications that attracted much attention in the past decade.
This section briefly sketches the different technical realizations of astrophysical γ-ray detectors. Depending on their design energy window, the deployed instrumentation varies significantly and this overview might help to recognize the advantages and disadvantages of the individual methods as concerns the prospects for indirect dark matter searches towards the Milky Way center region investigated in this thesis.

Imaging Atmospheric Cherenkov Telescopes

Imaging atmospheric Cherenkov telescopes (IACTs) are earth based telescopes sensitive to the optical and near UV Cherenkov light emitted by relativistic charged secondary particles created in the electromagnetic shower that is induced when a γ-ray interacts with atmospheric air molecules. Details on the physical foundations of the underlying processes can be found in the sections below. Current representative experiments are the Major Atmospheric Gamma Ray Imaging Cherenkov (MAGIC) telescope, the Very Energetic Radiation Imaging Telescope Array (VERITAS) and the High Energy Stereoscopic System (H.E.S.S.) located in La Palma on the Canary Islands, in Arizona (USA) and in the Khomas Highland (Namibia), respectively. All mentioned IACTs have a very similar design and are built considerably above sea level (1300 m for VERITAS, 2200 m for MAGIC and 1800 m for H.E.S.S). As will be explained later, high altitudes are together with sites that are free of artificial optical light very favorable for IACTs, especially in respect to their energy threshold. Additionally, the sites are selected to

[5] Villard discovered γ-rays in 1900 while investigating decays of radium. Ernst Rutherford coined the modern name 'γ-ray' in 1903.

minimize the occurrence of clouds and rain in order to maximize the possible observation time. Observations with IACTs are typically performed during dark time, i.e. when the moon as well as the sun are below the horizon and the meteorological conditions are sufficiently good. The H.E.S.S. experiment accumulates typically about 1000 hours of observation time on different targets per year.
The H.E.S.S. experiment has together with the VERITAS and MAGIC observatories made its design energy window (100 GeV - 100 TeV) accessible to astronomers studying sites in the universe where particles can be accelerated to extreme energies in order to produce γ-ray particles in the Very High Energy (VHE) range. Currently, the number of detected astrophysical VHE sources exceeds 100 (see http://tevcat.uchicago.edu/ for an up to date catalog). Prior to 1990 there was with the Crab Nebula only one known VHE γ-ray source detected by the Whipple telescope after about 30 years of operation and optimization (Weekes et al. [1989]). The Whipple telescope has been constructed at the site where currently the VERITAS telescope is in operation and was itself the result of a decade devoted to technical optimization from the beginning 1960s until finally commissioned in 1968. The first interest in funding for an IACT were in turn triggered by the first successful proof of principle of this technique with two photomultiplier tubes each of which was placed in the focal plane of a small mirror and shielded by a garbage-can. The two garbage-can shielded mirrors with photomultiplier detector were operated in coincidence mode and showed triggering events, probably due to Cherenkov light from cosmic ray induced particle showers (Galbraith and Jelley [1953]). The eventual detection of the Crab Nebula by the Whipple telescope made clear that the imaging atmospheric Cherenkov technique offers a window to an up to then astronomically unexplored energy range. A number of new experiments were planned and the experimental technique was optimized subsequently in the 1990s f.i. with experiments like HEGRA (constructed at the site where now the MAGIC is operating), CAT in the French Pyrenees and CANGAROO as well as Mark 6 in Australia. Those experiments increased the number of γ-ray sources to about ten at the end of the 1990s. The most influential technical result of this phase was the stereoscopic approach, i.e. the operation of multiple telescopes at the same time with an optimized trigger system. All current generation IACT experiments are stereoscopic systems, offering the possibility to suppress cosmic ray (CR) background events to a considerable degree at a multi-telescope trigger level. High energy cosmic rays are the dominant source of background for IACTs as they trigger air showers with relativistic charged secondary particles that emit Cherenkov radiation in a way similar to primary γ-rays. A more detailed discussion of the cosmic ray background will be given below. However, the use of advanced trigger and data analysis methods makes it possible to suppress the vast majority of the hadronic background particles (protons, helium and heavier elements). The electron background and a small remaining hadronic background has to be handled separately using a background subtraction algorithm that uses in general that CRs in the relevant energy range are entering the earth atmosphere isotropically in contrast to γ-rays. Background suppression and subtraction methods will be discussed later in detail.
Typical design parameters of IACTs are effective detection areas $\mathcal{O}(10^4\,\mathrm{m}^2) \sim (100\,\mathrm{m})^2$ which are basically determined by the radius in which Cherenkov photons emitted in

$\approx$ 10 km height above sea level with a typical Cherenkov angle of 0.8° hit the observation level. The detection area can be increased by distributing IACTs over a much bigger spatial range than current generation instruments do. This increases besides the overall sensitivity to γ-rays also the maximum energy to which IACTs are sensitive as this parameter is limited by the particle flux which decreases with increasing energy. The energy threshold in contrast is determined by the minimum number of detectable Cherenkov photons. Increasing the size of the telescope mirrors, i.e. the telescope aperture, to image more Cherenkov photons decreases the energy threshold. Observations at high altitude and low pointing zenith angle far away from the horizon lead also to lower energy thresholds as the atmospheric absorption (especially in the ultraviolet band) is lower then. Typical energy thresholds are in the range of some 10 GeV to some 100 GeV. The field of view of current generation IACTs is f.i. limited by the quality of the imaging of Cherenkov light incident off the optical telescope axis. Typically, the width of the point spread function for current generation IACTs is $\lesssim 0.1°$, optimized to the intrinsic width of a γ-ray particle shower. Depending on the F-ratio[6], the optical aberration is increasing for light incident off the optical axis. Large F-ratios are preferred for the minimization of aberration but lead to either large focal length or small apertures (see f.i. Bernlöhr et al. [2003]). The focal length is limited by mechanical considerations of the telescope construction. Small apertures are on the other hand limiting the light collection area and therefore the IACT energy threshold. A compromise that is realized in all current generation IACTs is an F-ratio of $\sim f/1$ and an aperture of $\gtrsim 10$ m which leads to an off-axis aberration determined optical point spread function whose width reaches $\sim 0.1°$ at a radial distance to the camera center of $\sim 2°$. The field of view of current generation IACTs is therefore $\sim \int_0^{2^\circ} d\theta \int_0^{2\pi} d\phi \sin(\theta) = 2\pi(1 - \cos(2°)) \sim 3.8 \cdot 10^{-3} \cdot \mathrm{sr}$. However, different mechanical designs of IACTs allow in principle to increase the field of view at the expense of other limitations (see f.i. Actis et al. [2011]).

Extensive Air Shower Arrays and Satellite γ-ray Detectors

Apart from IACTs there are other techniques to detect γ-rays. The most successful ones are Extensive Air Shower (EAS) arrays and satellite detectors.
EAS arrays are charged particle detectors (wire chambers, scintillation counters or similar) that are spread over a large area $\mathcal{O}(10^6\ \mathrm{m}^2)$ on earth in high altitude to detect the charged particles of a γ-ray induced air shower directly instead of the Cherenkov light tentatively emitted from the air shower and detected by IACTs. Being essentially not an optical instrument like an IACT but a charged particle detector, an EAS can operate also during daytime which is increasing significantly (factor ~ 6) the duty cycle compared to IACTs. The field of view of EAS arrays is not limited by the imaging optics of the instrument as for IACTs and therefore typically much larger, making EAS instruments interesting for the study of transient high energy sources. EAS array energy thresholds to γ-rays are, however, much higher when compared to IACTs, typically $\mathcal{O}(1\,\mathrm{TeV})$. CR background can be rejected to some degree by not triggering on events that are accompanied by significant muon fluxes that are expected to be produced by CRs. A modern

[6]The F-ratio is the ratio of the focal length and the telescope aperture.

	H.E.S.S.	Fermi	CTA	HAWC
Energy resolution	15%	10-20%	15%	50%
Angular resolution	0.1°	1.0°	0.1°	0.5°
Energy range	0.3-50 TeV	0.1-100 GeV	0.1-70 TeV	1-100 TeV
Sensitivity (TeV/cm^{2}s)	$3\,10^{-12}$@100h	$3\,10^{-12}$@10yr	10^{-13}@100h	$3\,10^{-13}$@5yr
Field of view	$3.7\,10^{-3}$sr	2.5sr	$3.7\,10^{-3}$sr	2sr
Obs. time per year	1000h	365d	1000h	365d

Table 1.1: Comparison of typical technical parameters of different γ-ray experiments. The table should give an impression of typical parameters, the exact parameters depend in part strongly on energy and other parameters. The sensitivity stated is referring to a 5σ detection of the given differential point source photon flux E^2dN/dE within the stated livetime. Data taken from H.E.S.S. Col. [2006] (H.E.S.S.), Funk and Hinton [2012] (Fermi and CTA) and Deyoung et al. [2010] (HAWC).

EAS array that is going to start data taking soon is the HAWC (High Altitude Water Cherenkov detector) which is the successor of the Milagro detector (see Deyoung et al. [2010]). Given the design parameters, it is obvious that EAS arrays are currently well suited for γ-ray measurements at the highest explored energies in the multiple 10 TeV regime where IACTs loose sensitivity due to there limited collection area and duty cycle. The low energy γ-ray regime (MeV-GeV) regime cannot yet be studied with earth based instruments. Instead, satellite experiments with much smaller collection areas ($\sim 3\,\mathrm{m}^2$) are used. Due to the small collection area and the γ-ray fluxes which become steeply smaller with energy, the maximum energy to which satellite γ-ray detectors are sensitive is limited to typically $\sim 100\,\mathrm{GeV}$. The most important current instrument is the Fermi γ-ray Space Telescope (see Atwood et al. [2009]) being the technical refinement of the Energetic Gamma Ray Energy Telescope (EGRET, see Kanbach et al. [1989]). The Fermi detector is essentially a compactified and robust high energy particle detector that is tuned for operation in space. A pair conversion foil creates an electron positron pair from an incoming γ-ray in the Fermi detector. The path of the created electron positron pair is measured with a silicon tracking system and points towards the direction of the original γ-ray. The γ-ray energy is measured in a subsequent electromagnetic calorimeter. A plastic scintillator at the telescope entry operated in anti-coincidence mode with the other detector parts is enabling the instrument to have an almost perfect suppression of background CRs as they trigger the scintillator due to their electric charge. The usage of the calorimetric energy measurement limits the energy threshold to some 10 MeV. Angular and energy resolution of Fermi are comparable to IACTs at the highest accessible energies but considerably worse at low energies. The large field of view and high duty cycle are additional advantages of satellite γ-ray detectors.
Table 1.1 gives a quantitative comparison of current γ-ray detector design specifications.

1.2 The Milky Way

1.2.1 History, Morphology and Rotation Curve

The observation of the sky during the night at a site without significant civilization light reveals the presence of a band where the density of stars is higher than elsewhere. The band is more obvious in the northern hemisphere summer (or southern hemisphere winter). All stars visible on the sky with the naked eye form a structure, the Milky Way. The Milky Way is obviously to a good approximation a flat disc as indicated by the band of stars. The density of stars is increasing towards a region located in the Sagittarius constellation which is best visible in the northern/southern hemisphere summer/winter during night time. The question of the structure of the Milky Way and its relation to outer space has long been investigated with varying methods but initially the observational data had little relation to the theoretical modeling. The observation of 'deep sky objects' that are not visible with the naked eye but with telescopes of initially moderate size revealed the presence of diffuse nebulae whose nature was initially unclear. For example, the first resolved photograph of the Andromeda nebula (now known to be the nearest spiral galaxy) was taken in 1887 by Isaac Roberts in Sussex, England. It showed spirally structured light emission and a bright central region. However, the distance and therefore the size of the nebulae could not be estimated reliably and so the nebulae could for instance be solar system type structures inside the galaxies or very bright and large objects outside the galaxy. The usage of Cepheid variables[7] to measure the distance to star nebulae by Edwin Hubble in the 1920s showed that the distance scale to the faint star nebula structures and the individually resolved stars in the Milky Way is of a different order of magnitude. This suggested that stars typically cluster in structures called galaxies and finished a long debate ('the Great Debate', see Longair [2007]) on the size and structure of the universe (see Hubble [1936]). The typical distance scale within a galaxy is kpc which compares to Mpc as the typical distance scale between galaxies. The detailed study of galaxies with large optical telescopes in the 1920s revealed that the majority of galaxies can be distinguished into either a spiral or an elliptical type. Stars within the elliptical galaxy type are distributed with decreasing density from the galaxy center in an ellipsoid volume. Spiral galaxies show on the other hand typically star distributions that are roughly symmetric to one axis with a central bulge and flat spiral arms extending far away from their origin in the center of the galaxy.
The flatness of the band of high star density visible in the night sky gives a strong hint for our own galaxy to be of a spiral type as the distribution of stars in an elliptical galaxy is supposed to be more diffuse when viewed from inside the galaxy. Further studies of the Milky Way matter distribution are, however, complicated by the galactic obscuration due to dust that absorbs large fractions of the electromagnetic spectrum used in astronomy. Especially the study of the matter distribution and the possible direct resolution

[7] Cepheid variables are a special class of stars with periodic luminosity. The period of the luminosity function exhibits a direct relation to the maximal intrinsic luminosity. Measuring the apparent luminosity and the intrinsic luminosity by using the luminosity-period relation for Cepheid leads to a reliable distance measurement (see Hubble [1936] and Longair [2007]).

of the spiral structure with optical telescopes turns out to be very difficult due to dust absorption.
The intent to resolve the Milky Way spiral structure led to the employment of radio astronomy to study the distribution of neutral atomic hydrogen (HI) within the Milky Way. The change of the relative spin directions of the electron and the proton in the hydrogen atom leads to the famous 21 cm hyperfine transition that is detectable with radio telescopes and not absorbed by dust as is f.i. optical light. In practice, the 21 cm emission line is Doppler shifted due to the motion of the HI regions around the galactic center. Thus, in principle, the amount of HI with a given velocity corresponding to a redshift can be measured via the intensity of the red-shifted 21 cm emission along a line of sight. It is, however, very difficult to convert the measured information on the velocity of an HI region to a unique origin of the emission in space. To resolve this difficulty many approaches were followed, one of them is the investigation of the 'rotation curve' of the Milky Way. The rotation curve is the velocity of objects around the galactic center as a function of distance to the galactic center. Assuming that the velocity of objects within the galactic disc depends only on the distance to the galactic center it is of course possible to translate a measured velocity of an HI emission region into a distance to the galactic center and thus construct an HI map of the Milky Way which should show directly the conjectured spiral structure. In practice it is, however, very difficult to really deduce the spiral structure with this method for several reasons (see Kalberla and Kerp [2009]).
A different problem that is in the focus of this thesis emerged, however, with the investigation of the Milky Way rotation curve: The velocity of objects around the galactic center is measured to be compatible with 230 km/s within $\sim$ 15% regardless of the distance to the galactic center up to at least $\sim$ 20 kpc. More precisely (see f.i. Weber and de Boer [2010]), the rotation curve of the Milky Way is for technical reasons (non-circular motion) only imprecisely known for distances $\lesssim$ 3 kpc. At a distance of $\sim$ 3 kpc the velocity is $\sim$ 230 km/s. Up to distances of $\sim$ 6 kpc, the velocity increases to a value of $\sim$ 250 km/s to decrease again to $\sim$ 220 km/s at a distance of 8 kpc. The velocity curve for distances $\lesssim$ 8 kpc is typically measured via the tangential velocity method (see Longair [2007]) applied to the 21 cm HI emission. For larger distances, this method is inapplicable due to a velocity distance ambiguity (see Longair [2007]). Instead, the radio emission of rotational transitions of CO molecules that become exited in collisions with molecular hydrogen is measured. Molecular hydrogen regions in the Milky Way are known to be associated to star forming regions and thus the distance to the CO emission region is inferred indirectly via the photometric investigation of associated stars. In practise, this is of course error prone and thus the precision of the Milky Way rotation curve measurement within $\sim$ 8 kpc and $\sim$ 20 kpc is worse compared to distances between $\sim$ 3 kpc and $\sim$ 8 kpc. No clear structure is therefore visible in the rotation curve between $\sim$ 8 kpc and $\sim$ 20 kpc but the velocity is compatible with $\sim$ 240 km/s within 10%. For even larger distances to the galactic center it becomes increasingly difficult to measure the rotation curve but the few data points that exist up to $\sim$ 80 kpc are compatible with $\sim$ 220 km/s within 15% (Gnedin et al. [2010]).
The problem with this rotation curve concerns the mismatch of the distribution and

gravitational potential of the visible mass in the Milky Way. The amount of stellar mass in the Milky Way that is known to be ~ 10 times larger then the total mass in (cold) gas of which the majority is in form of atomic and molecular hydrogen. Additionally, the luminosity profile of the Milky Way can be empirically described by a double exponential

$$\rho_{\text{stellar}}(R, z) = \rho_0 \exp(-R/h_R) \exp(-|z|/h_z) \tag{1.2}$$

in cylindrical coordinates where the symmetry (z) axis goes through the galactic plane and the galactic center and R is the distance to the galactic center parallel to the plane. The scaling height of the Milky Way h_z is between ~ 300 pc ('thin disc') and ~ 1 kpc for the 'thick disc'. The thin disc is populated by old metal poor stars contrary to the thin disc which consists of young metal rich and bright stars which constitute more than 95% of the total star population in the Milky Way (see Weber and de Boer [2010] and references therein for details). The radial scaling radius h_R of the Milky Way is between ~ 2 and ~ 3 kpc (Weber and de Boer [2010]) and so more than 99% of the stellar mass of the Milky Way is enclosed in a sphere with radius between 10 and 15 kpc. The rotational velocity of an object moving around the galactic center at a distance R is in Newtonian mechanics given by $v(R) \sim \sqrt{M(r < R)/R}$ where $M(r < R)$ is the total mass enclosed in a sphere with radius R around the galactic center. Assuming that most of the mass of the Milky Way is in stellar form (which is plausible as (cold) gas gives only a minor contribution), the rotation curve should thus fall according to $1/\sqrt{R}$ at least for radii larger than 10 to 15 kpc depending on the radial scaling radius of the Milky Way. Thus the transition of the rotation curve to $1/\sqrt{R}$ is supposed to be in the region between 10 and 20 kpc where the rotation curve is measured with still convincing accuracy to be compatible with a flat curve which challenges the prediction of a $1/\sqrt{R}$ velocity curve for a Milky Way where most of the mass is in form of stars. As a result, it must be considered as a hint in support of the hypothesis that there is much more mass in the Milky Way than in form of stars and (cold) gas that the measured rotation curve is compatible with a flat curve even for large distances (15 to 100 kpc) to the galactic center.

An additional hint in support of this conclusion comes from a different astrophysical observation connected to the scaling height in eq. 1.2. Jan Oort was among the first to measure the number of stars perpendicular to the galactic disc in the neighborhood of the solar system as a function of their distance perpendicular to the galactic disc (Oort [1932]). With this elegant method it is possible to derive the local gravitational potential in the solar neighborhood which in turn is proportional to the local mass density in the solar neighborhood. The method is very similar to the measurement of the air pressure as a function of the height above the earth surface with which the value of the local gravitational constant on earth can be inferred f.i. by modeling the air pressure with the barometric formula. In case of the local gravitational constant this method is of course needlessly imprecise and complicated but for the measurement of the total mass density in the solar neighborhood this is still one of the most reliable approaches today. The value for the total mass density in the solar neighborhood can be compared to the local stellar and gas mass density which are known from independent measurements.

The result is that a missing mass density of $\sim 0.3\,\mathrm{GeV/cm^3}$ is found which is commonly called the local dark matter density[8].
The overall picture resulting from the investigation of the rotation curve and the measurement of the local mass density in the solar neighborhood is thus that the dynamics of the Milky Way can probably not be explained by the assumption that most matter in the Milky Way is in form of stars. In numbers, the total mass of the Milky Way is estimated to be $\sim 10^{12}$ solar masses (see Weber and de Boer [2010] for a compilation of different kinematical measurements). The total amount of luminous matter is estimated to be $\lesssim 8 \cdot 10^{10}$ solar masses based on parametrizations of the visible matter distribution in the Milky Way (see also Weber and de Boer [2010]). This suggests that more than 90% of the total matter in the Milky Way is not visible, i.e. dark matter.
In case of the Milky Way, however, a recent study (Gupta and Mathur [2012]) must be mentioned that claims the existence of a huge reservoir of hot ionized gas which is extended to distances of more than > 100 kpc to the galactic center and has a total mass comparable or larger to the total mass of the stellar galactic disc. No clear statement on the density distribution of this claimed hot gas is made yet but it is obvious that a closer investigation of this observation needs to be undertaken to rule out that the missing mass in the Milky Way is in fact only a reservoir of hot gas surrounding the Milky Way up to large radii. Apart from the hints based on the dynamical observations of the Milky Way there are many other arguments in favor of the existence of a large amount of matter in the universe that does not couple to the electromagnetic sector of the particle physics standard model. An overview over those arguments and possible explanations is given later in this chapter.

1.2.2 High Energy Astrophysics in the Milky Way

As mentioned earlier in this chapter, the Crab Nebula was eventually detected by the Whipple Cherenkov telescope in 1989 (Weekes et al. [1989]). This was the first ever detected source of VHE γ-rays in outer space. Photons of lower energies from the direction of the Crab Nebula were detected much earlier, starting with records of observations of a suddenly appearing bright spot on the sky that was visible (probably even during daylight) with the naked eye in 1054. Today this sudden appearance of a 'guest star' is known to be the result of the violent end of the life of a massive star whose core collapsed to a rapidly rotating ~ 30 km diameter neutron star (see Longair [2011]). The magnetic field flux of the progenitor star is conserved in the core collapse and thus the magnetic field is increased by a huge factor. The rotational axis of a neutron star is typically misaligned with the magnetic field axis and the rotating magnetic dipoles become sources of intensive radiation that can be detected by a fixed observer as pulsed emission. Still

[8] Recently there has been one measurement that claimed that the local dark matter density is compatible with zero based on a very similar method (Bidin et al. [2012]). It is, however, now generally accepted that the cited measurement made one wrong assumption on the dependence of the radial rotational velocity around the galactic center as a function of the distance to the galactic disc (see Bovy and Tremaine [2012]). If this assumption is corrected the measurement results in a local dark matter density of $(0.3 \pm 0.1)\,\mathrm{GeV/cm^3}$ which is within errors compatible with the standard value for the local dark matter density of 0.3 to 0.7 $\mathrm{GeV/cm^3}$ (see Weber and de Boer [2010])

discussed is the exact location of the source of the pulsed emission for which different models exist. In case of the neutron star in the center of the Crab Nebula, i.e. the Crab pulsar, pulsed emission detected every 33 ms on earth with different telescopes that observe towards the Crab Nebula over a wide frequency band from radio to γ-rays. Recently even pulsed γ-rays up to $\sim$ 400 GeV (VERITAS Col. [2011]) have been detected from the Crab pulsar which is very challenging for theoretical models of the generation of pulsed emission because the assumed spatial origin of the pulsed emission is typically thought to be in regions of very intensive photon fields where γ-rays of several 100 GeV are expected to undergo an electron-positron pair conversion. Apart from the pulsed emission, the region in the vicinity of the Crab pulsar, i.e. the Crab Nebula, is since the Whipple detection known to be a source of (un-pulsed) γ-rays. By now (January 2013)[9] 23 similar pulsar wind nebulae (PWNe) are found to emit VHE γ-rays ($E > 100$ GeV). All but one of the detected PWNe are within the galaxy, mostly in the vicinity of the galactic plane. The one extragalactic PWN detected with Cherenkov telescopes is found in the large Magellanic cloud (H.E.S.S. Col. [2012]). In total 105 VHE γ-ray sources are detected, 84 of them are classified within the known types of VHE γ-ray emitters and 21 sources are yet unidentified. Out of the 84 identified sources, 47 are within the Milky Way.
The second most abundant galactic source type after PWNe are remnants of supernova explosions (SNRs) which consist of the expanding material ejected in a supernova. In contrast to PWNe, which are powered by the loss of rotational power ('spin down') of a pulsar, SNRs are powered by an initial supernova. In total 17 SNRs are currently detected with VHE γ-rays. All other seven detected and classified galactic VHE γ-ray sources are either star forming regions (3) or binary systems (4).
Each source class that is found to emit VHE γ-rays is interesting to be studied for different reasons, an overview is given in Hinton and Hofmann [2009]. The work discussed in this thesis is not focused on the investigation of a specific source or source class. Instead, sources of spatially very extended VHE γ-ray emission are searched for. Among the 21 not yet classified sources one is of special interest in this context. Figure 1.1 shows a region in the vicinity of the Milky Way center where VHE γ-rays have been detected. The emission is spatially correlated with molecular gas regions which are shown as white contours in fig. 1.1. The correlation between molecular gas and VHE γ-ray emission is an evidence for a hadronic production mechanism, i.e. the VHE emission is supposed to be produced by the interaction of hadrons (f.i. protons) with molecular gas which mostly produces pions of which about one third is neutral and decays into two γ-rays. An alternative explanation for the production of VHE γ-rays is that electrons scatter low energy photon fields (star light, cosmic microwave background or even synchrotron photons emitted by the electrons themself) in an inverse Compton process. This is, however, less preferred because the intensity of the γ-ray emission should be increasing with increasing low energy photon density which is not correlated with the molecular gas density in an inverse Compton scenario. Thus it seems likely that the 'diffuse γ-ray

[9] See the 'default catalog' of TeV astronomy at http://tevcat.uchicago.edu which lists all published VHE γ-ray sources. This catalog is referred to whenever a source is called 'detected' in this section.

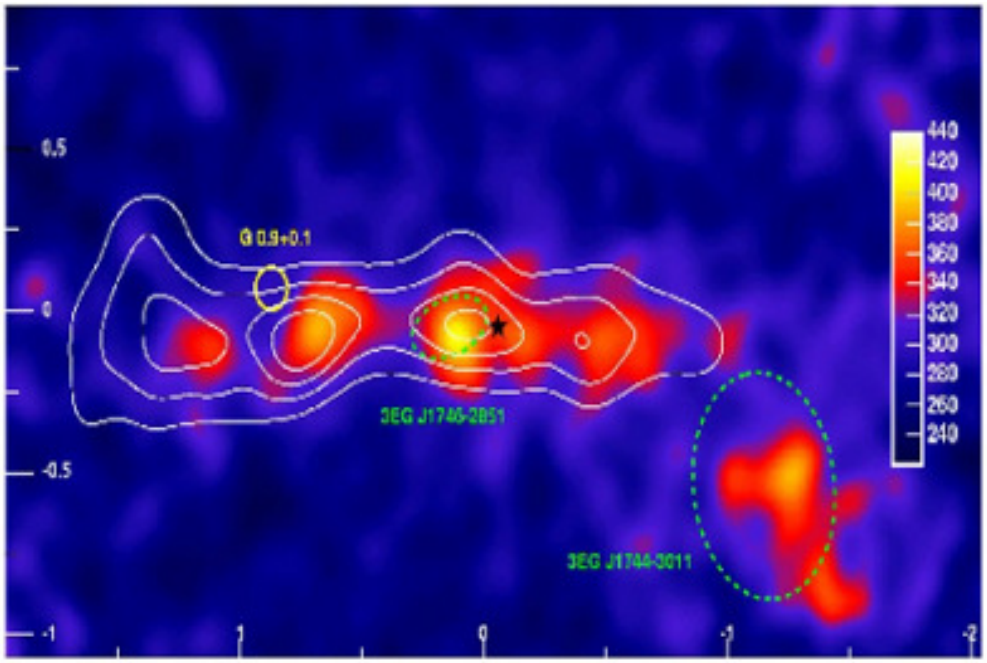

Figure 1.1: Diffuse emission in the vicinity of the galactic center region as detected with H.E.S.S. (H.E.S.S. Col. [2005b]). Shown is a γ-ray excess map (color scale). White contours indicating the density of molecular hydrogen gas as traced by CS emission. A correlation between the observed γ-ray excess and the molecular gas density is inferred which hints towards a hadronic origin of the emission.

emission' in the vicinity of the galactic center ridge mapped in fig. 1.1 is powered by a population of very energetic protons. It is not yet clear where this population of protons gains its energy. What seems clear is that no individual source in the galactic center region nor the ensemble of sources is likely to be the accelerator of the proton population (Wommer et al. [2008]).
On the other hand, there is also the hadronic component of the cosmic radiation that constantly hits the earth atmosphere with a GeV to TeV energy spectrum given in eq. 1.1. It is generally assumed that hadronic cosmic rays in the GeV to TeV energy range are produced within the Milky Way in multiple isolated sources (possibly SNRs) because the magnetic field of the Milky Way confines them within the galaxy. Additionally, cosmic rays are supposed to be moving in random directions without preference for any special direction far away from their origin as supported by the nearly isotropic cosmic ray flux on earth. This can be well explained by stochastic scattering of cosmic rays on turbulent galactic magnetic fields (see f.i. Fatuzzo et al. [2010]) and described by the energy dependent diffusion of cosmic rays within the Milky Way. A simple model (Fatuzzo et al. [2010]) with an energy dependent diffusion constant ($D \sim E^{\delta}$) predicts that the cosmic ray spectrum far away from their origin (i.e. with a distance much larger than the diffusion length) is given by $\Phi(E) \sim E^{-(\alpha+1.5\delta)}$ when particles are injected with an energy spectrum $\sim E^{-\alpha}$. The spectral slope of the flux spectrum far away from the cosmic ray sources does not depend on the location and it is thus assumed that the spectral slope of cosmic rays is the same as the slope of the cosmic ray spectrum measured on earth everywhere within the Milky Way on large scales. It is thus not surprising on a first glimpse that the vicinity of the galactic center, where the density of molecular gas is among the highest in the galactic disc, VHE γ-rays are produced in hadronic interactions. However, the measured spectral index of the diffuse emission in the galactic center ridge (-2.3) is incompatible with the spectral index of hadronic TeV cosmic rays measured on earth (-2.7) and thus the large scale cosmic ray population within the Milky Way can be ruled out as the source of this γ-ray emission.
Although the γ-ray emission detected in the galactic center ridge is unlikely to be produced by the same population of CRs that hit the earth atmosphere it is very likely that VHE γ-rays are produced by interactions of this CR population with gas in the Milky Way disc. This effect, the 'galactic diffuse emission', has yet not been detected at TeV energies with Cherenkov telescopes but its detection 'would be extremely valuable' as highlighted in the 2008 white paper for the future of ground-based TeV γ-ray astronomy of the American Physical Society (Buckley et al. [2008]). Later in this thesis, this topic will be investigated, primarily because this effect is a possible foreground for the detection of particle dark matter self annihilation in the Milky Way with Cherenkov telescopes as will become clear later.

1.3 Dark Matter

1.3.1 Observational Evidence

The mass of the solar system is to a very good approximation given by the mass of the sun. Assuming for the moment that all stars have the same mass as the sun, one is tempted to estimate the mass of distant galaxies by counting the number of stars and multiply the result with the solar mass. The result of this method is the so called luminous mass and the starting point of the ~ 80 year old history of dark matter: The luminous mass of galaxies and cluster of galaxies has very little to do with the total mass of those structures. In other words, galaxies and clusters of galaxies must be more than an accumulation of many solar systems.

Large amounts of missing luminous matter were first inferred in clusters of galaxies. Fritz Zwicky concluded 1933[10] that the Coma galaxy cluster must be by orders of magnitude more massive than expected based on the luminosity of the galaxy (Zwicky [1933]). Smith repeated Zwicky's analysis (Smith [1936]) for the Virgo galaxy cluster with a similar conclusion.

The nearest known spiral galaxy, the Andromeda nebula or M31, was studied by Babcock in 1940 (Babcock [1939]). The rotation curve of this galaxy, that is the velocity v of the individual stars around the center of the galaxy plotted against the distance r to the center, showed no evidence to follow the law $v(r) \sim 1/\sqrt{r}$ which is the prediction of Newtonian dynamics. Instead, the rotation curve was found to be increasing between $\sim 0.5\,\mathrm{kpc}$ and ~ 6 kpc which marks the endpoint of the optical rotation curve measured by Babcock. The rotation curve of the Andromeda nebula can thus not be modeled by Newtonian dynamics if the distribution of mass in M31 follows its optical luminosity.

[10] Zwickys argument can be summarized as follows: The velocities of $N = 7$ or 8 galaxies within the Coma cluster were measured with the Mt. Wilson 100-inch (~ 2.5 m) reflector telescope using the Doppler shift of optical emission and absorption. Actually just one emission line was investigated. The line was assumed to stem from 'nebulium' which is an element established by its emission line as early as 1864 in the optical spectra of 'nebulae', i.e. galaxies. Nebulium was never found to be existent in a laboratory experiment but remained a hot topic of discussion for more than sixty years after its first detection until it was finally shown to be the emission due to transitions between metastable states of oxygen and nitrogen (see Pais [1986] for more information). The mean velocity of the galaxy sample was $\bar{v} = 1/N \sum v_i \sim 7000\,\mathrm{km/s}$ with velocity dispersion, i.e. RMS, $\sigma = \sqrt{1/(N-1)\sum (v_i - \bar{v})^2} \sim 1000\,\mathrm{km/s}$. Thus the kinetic energy of the cluster with total mass M becomes $T = 1/2 \cdot 3M\sigma^2$, where the factor of 3 expresses that the velocity dispersion is only measured along the line of sight, i.e. in one out of three spatial dimensions. The total potential energy of the cluster with mass M_S within the radius $R_S \sim 10^{22}$m (apparent optical radius) is $U = GM^2/R_S$ where $G = 7\,10^{-11}\mathrm{m}^3/(\mathrm{kg\,s}^2)$ is the gravitational constant. Kinetic and potential energy are linked by the virial theorem, $U = 2T$, when the cluster is in thermal equilibrium within the radius R_S. The mass of the cluster according to the virial theorem is then $M = 3\sigma^2/GR_S \sim 10^{15}$ solar masses. On the other hand, the cluster contains according to Zwicky ~ 800 visible galaxies. The luminosity of an average galaxy in the Coma cluster was measured and translated via a luminosity to mass factor (~ 500, see Zwicky [1937]) to the average mass of $\sim 10^9$ solar masses. Thus the mass to luminosity ratio is ~ 1000. Note that this estimation of mass with the virial mass relies on a sample of 7 or 8 galaxies (in one case the association of the observed galaxy with the Coma cluster was unclear) out of 800. The lack of conclusive statistics is typical for the early observations of missing luminous mass.

Instead, the ratio of mass to luminosity must become bigger with increasing distance from the center of M31 to explain the velocity curve with Newtonian dynamics.
By $\sim$ 1960 there were thus few observations of which a representative but incomplete selection is mentioned above that concluded that the visible mass cannot explain the dynamics of galaxy clusters and individual galaxies. However, given the limited knowledge on objects in galaxies and the error-prone experimental methods together with the lack of large sample studies of the dynamics of galaxies and clusters of galaxies the results were typically not taken as being conclusive. The invention of CCD cameras being much more sensitive and easier to use than the traditional photographic plates[11] and the advent of radio astronomy enabled the much more detailed and systematic study of galaxies. The rotation curves of spiral galaxies could be studied to many times the apparent optical size of galaxies using the radio emission of rotating gas. Vera Rubin et al. studied the rotation curves of spiral galaxies up to large distances from their centers using radio telescope data in the 1970s and concluded that not one of the inferred galaxy rotation curve does in any way follow a $\sim 1/\sqrt{r}$ law (Rubin et al. [1978]). Instead, the spiral galaxy rotation curves typically increase for low distances to the center of the galaxy and become rather constant farther away. Two large sample studies of galaxies showed clearly that the mass $M(r < R)$ within a given radius R around a galaxy center is increasing linearly with R in obvious contrast to the decrease in luminosity with R (Ostriker et al. [1974], Einasto et al. [1974]). This result points towards a typical mass density $\rho(r) \sim 1/r^2$ in the outer ($r \gtrsim 10$ kpc) regions of galaxies.
The empirical evidence that the luminous matter in certain astrophysical systems cannot account in a Newtonian way for their dynamics was convincing by $\sim$1980. Since then additional measurements gave further evidence for this hypothesis on cosmological, galaxy cluster and individual galaxy scale deriving compatible conclusions with independent methods. The most important methods to infer the presence of dark matter are briefly summarized below.

Gravitational Lensing

Fritz Zwicky put forward the idea that the light from distant galaxies might be deflected by closer galaxies in the line of sight and thus a lensing effect might result (Zwicky [1937][12]). The serendipitous observation of two displaced images of apparently the same astrophysical object with the 2.1 m optical Kitt telescope in Hawaii marked the first evidence for the lensing of light by a massive galaxy (Walsh et al. [1979]). This strong gravitational lensing by a massive galaxy or a galaxy cluster stands in contrast to the

[11] The sensitivity of optical detectors can be quantified with the quantum efficiency, that is the probability that a photon hitting the detector is detected. CCD cameras have a quantum efficiency of up to $\sim$ 80% which compares to the quantum efficieny of photographic paper of $\mathcal{O}(1\%)$ (Longair [2007]).

[12] Zwicky's publication appeared ten months after a publication by Einstein (Einstein [1936]) where gravitational lensing effects have been investigated with the conclusion that 'of course, there is no hope of observing this phenomenon directly'. Zwicky did not comment on Einsteins calculations nor on the even earlier qualitative prediction of gravitational lensing in Chwolson [1924], probably because Zwicky considered the lensing of a whole galaxy in contrast to Einstein and Chwolson who only considered stars.

weak gravitational lensing by less massive galaxies or concentrations of dark matter. Weak gravitational lensing is not visible by the obvious multiplication of images (Einstein rings or similar) but the small elongation of the images of many distant light sources. The statistical analysis of a sufficient number of observed elongated images can lead to the inference of the distribution of luminous and non-luminous mass between the light source and the observer. Weak gravitational lensing is by now a main method to detect concentrations of non-luminous matter in space, typically on distance scales of ∼Mpc and more.

Temperature Anisotropies in the CMB

In 1965 Arno Penzias and Robert Wilson from the Bell Labs in New Jersey published the radio antenna measurement of a 'remaining unaccounted-for antenna temperature' of (3.5 ± 1.0) K (Penzias and Wilson [1965]). They were not able to assign this temperature to any known instrumental or physical effect and published the result without interpretation. It soon became clear that this $\sim 3.5\sigma$ effect was one of the greatest discoveries in physics of the 20th century which justified the 1978 Nobel prize to be awarded to Penzias and Wilson. What was serendipitously measured with the Bell Labs instrument was, by measurements at varying frequencies, shown to be thermal black body emission whose origin can be understood in a Big Bang model for cosmology. Within this model it is assumed that the universe cools down by spatial expansion starting from an initial singularity. At some point in time, the universe becomes cold enough to make the recombination of electrons and protons to hydrogen possible which in turn means that the mean free path of photons becomes suddenly large. In other words, photons, which are tightly coupled to the electron-proton plasma at higher temperatures, can decouple at the time of recombination and the universe becomes optically transparent. The photons which decoupled at the time of recombination were further red-shifted ($z \sim 1000$) as the universe continued to expand and so the thermal spectrum of the decoupling photons corresponds now to a black body spectrum with a low temperature measured by Penzias and Wilson, the cosmic microwave background (CMB).
Another Nobel prize connected to the investigation of the cosmic microwave background was awarded to John Mather and George Smoot in 2006 as coordinators of the COBE (Cosmic Background Explorer) experiment. The COBE collaboration eventually detected anisotropies in the CMB at the level of $\sim 10\,\mu$K on angular scales between $\sim 10^\circ$ and $\sim 90^\circ$ in 1992. This means that the universe did not have a completely uniform temperature at the time of re-combination but there were tiny temperature variations from one region to the other being displaced by $\sim 10^\circ$ to $\sim 90^\circ$. These 'large scale anisotropies' are important to gain information on the cosmological parameters that determine the general metric of the early universe, i.e. the total energy and dark energy content. This is discussed for instance in Longair [2007]. An impression of the impact of the large scale or small multipole ($l \leq 30$) anisotropy power spectrum is indicated in fig. 1.2 in the upper two plots. The total and dark energy density have a strong impact on the small multipole power spectrum. The two lower plots in fig 1.2 show that the intermediate multipole ($100 < l < 1000$) or angular scale ($\sim 0.1^\circ$ to $\sim 1^\circ$)

is heavily influenced by the total matter, i.e. dark and baryonic matter together, and the dark matter content of the early universe. The measurement of the intermediate multipole power spectrum was performed by different earth or balloon based (sensitive to small angular scale anisotropies) and satellite detectors (most notably the WMAP experiment which recently released its result based on 9 year data taking (Hinshaw et al. [2013]) and the Planck satellite (Planck Col. [2013])). From the physics point of view, the main difference between the large angular scale anisotropies detected with COBE and the intermediate angular scale anisotropies is that large angular scales ($> 1^\circ$ as seen today) were not in causal contact at the time of recombination due to the finite speed of light. Actually, the large isotropy of the CMB at large angular scales is surprising in this context and is also a problem of its own ('horizon problem') that can be solved in so called 'inflationary big bang' models, see Longair [2011]. However, the causal connection at intermediate angular scales is a condition for the appearance of 'acoustic oscillations' which are essentially sound waves (i.e. matter density perturbations) in the early universe, shortly before the re-combination epoch. The acoustic oscillations are the result of the proton-electron plasma which on the one side is compressed by an in-fall into gravitational holes generated to a large fraction by dark matter. On the other hand the heat of the compressing proton-electron plasma generates a force that drives the plasma out of the gravitational hole thereby relieving the pressure on the plasma. The result are density or acoustic oscillations in the electron-proton plasma to which the photons are strongly coupled. The gravitational potential of an initial over density of dark matter is always increasing due to the ongoing accretion of dark matter that does not oscillate because there is (by the definition of dark matter) no force that compensates the in-fall like the heat pressure for baryonic matter. The two lower plots in fig. 1.2 show the influence of the baryonic and total (baryonic plus dark) matter density on the acoustic oscillations seen for multipoles $100 < l < 1000$. Increasing the baryonic matter density increases the amplitude of the odd acoustic oscillation peaks and suppresses the even peaks. The influence of an increase of the dark matter density is a general suppression of all acoustic oscillation amplitudes.
The measurement of the temperature anisotropy spectrum with sufficient precision makes it possible to find unique solutions to the cosmological input parameters. Especially the dark matter density at the recombination time can be determined to be $\sim 20\%$ of the total energy density in the universe which compares to $\sim 5\%$ of usual baryonic matter density (see Hinshaw et al. [2013] and Planck Col. [2013] for details and more precise numbers). The remaining energy needed to fit the observational data is called 'dark energy' of which very little is currently known. More information on the physics of the temperature anisotropies can be found in Longair [1998] and references therein. The important point is that the observed acoustic oscillation peaks can only hardly be explained without the existence of dark matter, i.e. particles that do not couple to a photon radiation field, especially if the baryonic matter content used to fit the acoustic peak data is fixed to a value inferred from other measurements.

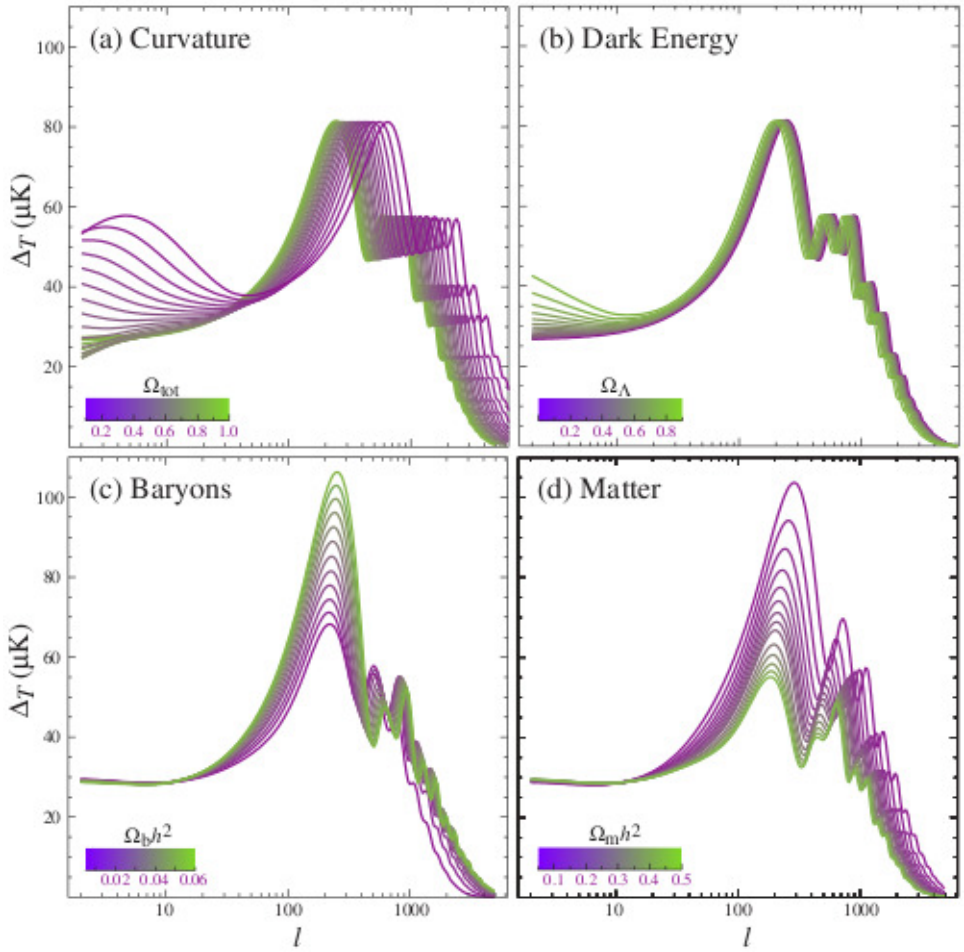

Figure 1.2: Dependence of the CMB power spectrum model on four of the input parameters within a ΛCDM description. The investigated parameters are $\Omega_{\mathrm{tot}}h^2$ (total energy density), $\Omega_\Lambda h^2$ (dark energy density), $\Omega_{\mathrm{b}}h^2$ (baryon density) and $\Omega_{\mathrm{m}}h^2$ (total matter density, i.e. the sum of the baryon and dark matter density) where every density is given in units of the critical density of the universe. The plot is taken from Hu and Dodelson [2002]. The precise experimental determination of multiple peaks in CMB anisotropy measurements lifts the correlation between the parameters and every parameter can be determined. A key result of this measurement is that the overall dark matter density in the universe must be $\sim 20\%$ of the total energy density.

1.3.2 Solutions to the Dark Matter Problem

Different solutions to the problem that a large fraction of matter is apparently not luminous, i.e. dark, have been discussed, with increased intensity since ∼1980 and an overview of models without claim of completeness is given below. The treatment of the material is covering only the most central aspects to familiarize the reader with different viewpoints. A more detailed discussion of models that are of special importance in the framework of this thesis is given in chapter 3.

Massive Compact Halo Objects

Massive Compact Halo Objects (MACHOs) are unassociated astrophysical objects of usual baryonic matter moving uniformly through space while emitting no or little electromagnetic radiation. In practice, MACHOS can be f.i. white, red or brown dwarfs or even black holes and should indeed make a 'dark' contribution to the total mass of galaxies or galaxy clusters. Searches for MACHO populations have been conducted in the Milky Way, its satellite galaxies as well as the Magellanic clouds and the Andromeda nebula. The method employed is to monitor the variability of a very large sample of stars far behind the MACHO search region and search for changes in the light flux of the stars by the gravitational lensing of MACHOs in the line of sight (gravitational microlensing). For instance the 'MACHO survey' observed 12 million stars in the large Magellanic cloud for ∼ 6 years and found $\mathcal{O}(15)$ microlensing events which was compared to a background coming f.i. from supernovae in galaxies behind the large Magellanic cloud (Alcock et al. [2000]). The study rules out that all of the Milky Way dark matter is made to 100% of MACHOs at 95% confidence level. However, a certain fraction of $\mathcal{O}(20\%)$ of the non luminous matter in the Milky Way is according to the MACHO survey likely to be composed of MACHOs. Similar conclusions were drawn by other MACHO search experiments for the Milky Way and the other mentioned galaxies. This does apparently not solve the problem of dark matter.

Modified Newtonian Dynamics

The incompatibility of the first measured large samples of spiral galaxy rotation curves with the Newtonian[13] $v(r) = \sqrt{GM(\leq r)/r}$ prediction motivated the dark matter interpretation but also the investigation of a possible failure of Newtonian dynamics. Milgrom observed (Milgrom [1983a]) that an acceleration (a) dependent modification of the Newtonian inverse square law of gravity for a test mass m to

$$\vec{F}(\vec{r}) = -\frac{\vec{r}}{r}\,\frac{GmM}{r^2\mu(a/a_0)} \text{ where } \mu(\frac{a}{a_0}) = \begin{cases} 1 & \text{if } a \gg a_0 \\ a/a_0 & \text{if } a \ll a_0 \end{cases}$$

[13] In this section $M(\leq r)$ is the mass enclosed in a sphere of radius r, $G \sim 6.7 \cdot 10^{-11}\mathrm{m}^3\mathrm{kg}^{-1}\mathrm{s}^{-2}$ is the gravitational constant and a spiral galaxy is approximated to have a spherically symmetric mass distribution.

leads together with $\vec{F} = m\vec{a}$ and the centripetal force $\vec{F} = -m(\vec{r}/r)v^2/r$ to the prediction

$$v(r) = \sqrt[4]{MGa_0} = \text{const} \tag{1.3}$$

far enough from the center of the galaxy, i.e. where the acceleration a is much smaller than the MOND parameter a_0. The comparison with measured rotation curves gives universally compatible results for $a_0 \sim 10^{-10}\,\mathrm{m/s^2}$. This Modified Newtonian Dynamics (MOND) model is thus an explanation for two a priori independent observations for spiral galaxies:

- The rotation curve of the spiral galaxy can be described by the universal MOND parameter a_0 and the total baryonic mass of the spiral galaxy. In practice, the baryonic mass of a spiral galaxy is estimated from its luminosity using typical spiral galaxy stellar mass to luminosity ratios. A surprisingly large number of observed spiral galaxy rotation curves can be described by the MOND parameter $a_0 \sim 10^{-10}\,\mathrm{m/s^2}$ and reasonable mass to luminosity values (see Begeman et al. [1991]).

- The intrinsic spiral galaxy luminosity, i.e. the galaxy's luminosity observed on earth corrected for the distance from the earth to the galaxy by the inverse square law, is proportional to the 4th power of the hydrogen velocity in the outer region of the galaxy ($L_I \sim v^4$). This relationship was first observed empirically and is known as Tully-Fisher relation for spiral galaxy's. By measuring the velocity v of hydrogen in the outer region of a spiral galaxy and the galaxies apparent luminosity L_A on earth, the distance r of a spiral galaxy to the earth can thus be estimated to be $v^4 \sim L_I/r^2 = L_A$. The most interesting point here is that the proportional constant for the Tully-Fisher relation predicted by the MOND model when the mass of a galaxy is used to trace its luminosity follows naturally from eq. 1.3 to be $1/(Ga_0)$ (see Milgrom [1983b]). This is in good agreement with the measured proportional constant if the MOND parameter $a_0 \sim 10^{-10}\mathrm{m/s^2}$, as derived from spiral galaxy rotational velocities, is used.

Apparently, the MOND model has great success in the description of spiral galaxy data. However, the observational evidence for the existence of dark matter also comes from gravitational lensing and cosmological data. The simple MOND model is, as being manifestly non-relativistic, not applicable to the investigation of those problems. A relativistic generalization of MOND, that is not in conflict with current observational data has not been found yet.
Another evidence that disfavors un-tuned MOND models is derived from the recent observation of colliding galaxies with X-ray satellites and the modeling of the gravitational potential in the colliding region with weak gravitational lensing. The X-ray intensity traces the thermal emission of the colliding gas, i.e. the luminous matter. The gravitational potential on the other hand traces the total mass. An example is seen in fig. 1.3 (left), showing the bullet cluster (Clowe et al. [2006]). The X-ray image is created from data recorded with the Chandra telescope. Overlaid are the gravitational potential contours as obtained from the weak gravitational analysis of multiple optical observations

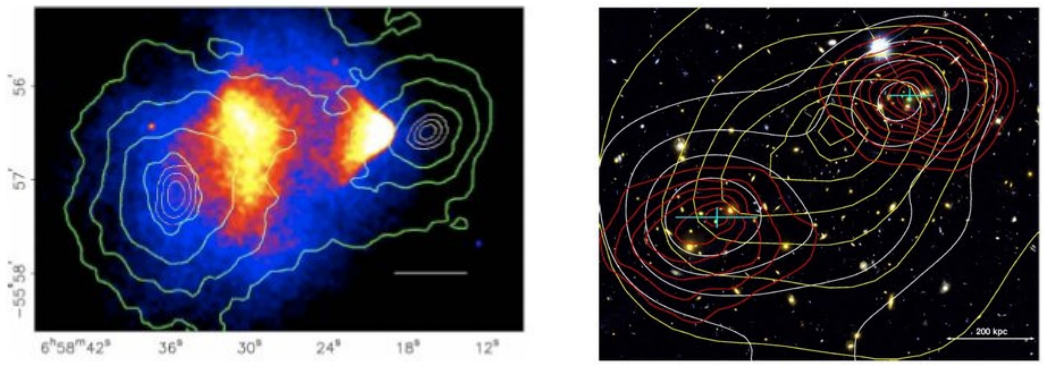

Figure 1.3: Left: The bullet cluster. The hot gas as seen in X-ray (red) observations and overlaid the gravitational potential of two recently collided galaxy clusters show a significant offset. The coordinate axes show RaDec coordinates and the white bar indicates 200 kpc at the distance of the cluster. The figure is taken from Clowe et al. [2006]. Right: The merging cluster MACS J0025.4-1222 with the gravitational potential in red and the X-ray brightness overlaid in yellow contours. The figure is taken from Bradač et al. [2008].

of background galaxies. A similar observation is shown in fig. 1.3 (right). Two galaxy clusters have been merged to one indicated by the X-ray (Chandra) brightness of the hot gas in yellow contours. The merged gas of the two cluster shows a clear spatial offset from the gravitational potential as obtained from weak and strong gravitation lensing analysis of Hubble space telescope and Keck data. It appears as if the mass concentrations of the two galaxy clusters are moving without being influenced by the collision in contrast to the material of the galaxies as traced with X-ray satellites (Bradač et al. [2008]). An interpretation of the offset between the mass and X-ray brightness in the discussed merging galaxy clusters is not yet possible in the MOND framework without fine-tuning which involves a neutrino mass of ~ 2 eV (Brownstein and Moffat [2007]). The neutrino mass scenario will be tested in the near future with the KATRIN (Karlsruhe Tritium Neutrino) experiment which measures the tail of the electron spectrum in Tritium β-decays with very high precision and is sensitive to electron neutrino masses above ~ 0.3 eV (Pascoli et al. [2003]) and thus lowering the current best upper limit on the electron neutrino mass of 2.05 eV (Eidelman et al. [2004]) by nearly one order of magnitude. The observed offset between the total and luminous mass in colliding galaxy clusters is strongly supporting the interpretation that the interacting baryonic matter in form of gas is not the main constituent of the galaxy clusters. Instead, the gravitational centers of the colliding galaxy clusters move apparently without experiencing significant collisions. This is expected from a weakly interacting particle dark matter candidate but not from baryonic matter.

Particle Dark Matter

Ordinary baryonic matter can very probably not account for all but a small part of the missing matter in galaxies and galaxy clusters. The MOND interpretation appears currently disfavored by observational data, although a definite conclusion is not yet possible. It is, however, possible to investigate the particle dark matter solution to the missing mass problem that claims the existence of one or more particle(s) not coupled to the electromagnetic sector of the standard model of particle physics. There is a diversity of extensions of the standard model of particle physics that predict the existence of particles that do not couple to photons, i.e. do not possess an electric charge. This section summarizes key properties that a viable particle dark matter candidate must have and gives example candidates.
Key properties of particle dark matter are obviously a vanishing electric charge and the stability on cosmological timescales. Standard model neutrinos obey these criteria but are, although having the advantage to be definitely existing, unlikely to be a viable particle dark matter candidate. The first argument that strongly disfavors (standard model) neutrinos as particle dark matter candidate is connected to the neutrino mass.

- The neutrino mass is known to be non-zero but small. A vanishing neutrino mass is outruled by experiments that observe neutrino oscillations which are sensitive to the squared mass difference between neutrino flavors. The current value for the squared mass difference between the electron and muon neutrino mass is $\sim 10^{-5}\,\mathrm{eV}^2$ and $\sim 10^{-3}\,\mathrm{eV}^2$ for the squared difference between the electron and the tau neutrino. Thus, the mass difference between neutrinos of different flavor is small. Additionally, the mass of the electron neutrino can be constrained to be $\lesssim 2$ eV (Eidelman et al. [2004]) from the endpoint of the tritium β-decay electron spectrum. Given that the electron neutrino mass is constrained to be $\lesssim 2$ eV and the mass differences between different neutrino flavors are much smaller than 1 eV, the sum of all neutrino flavor masses can be constraint to be < 6 eV. For the total density of matter in form of standard model neutrinos this means $\Omega_\nu h^2 = \sum_i g_i m_{\nu(i)}/(93\,\mathrm{eV})$ (see Gondolo [2003]). In the last equation, it holds $g_i = 1$ for Majorana neutrinos[14] and $g_i = 2$ for Dirac neutrinos which leads to $\Omega_\nu h^2 \lesssim 7\%$ and $\Omega_\nu h^2 \lesssim 14\%$ for Majorana and Dirac neutrinos respectivly. On the other hand, the total density of dark matter in the universe is $\Omega_{\mathrm{DM}} h^2 \sim 11\%$ (Hinshaw et al. [2013]) which already disfavours the hyptohesis that Majorana neutrinos can constitute all of the dark matter.

- CMB anisotropy measurements set an even stronger limit on the total neutrino mass, i.e. the sum of the masses of the three neutrino flavors, in the universe. Current WMAP data constrains the same sum of all three neutrino flavor masses to be < 0.4 eV (Hinshaw et al. [2013]) which is one order of magnitude more constraining than the limit derived from laboratory experiments. Planck satellite

[14] Note that the distinction between Majorana and Dirac neutrinos is often not made at this point (see f.i. Bertone et al. [2005]). In fact, the currently available laboratory data is not sufficient to rule out at least Dirac neutrinos as dark matter candidates when only mass arguments are considered.

data constrains the same quantity to be < 0.66 eV at 95% C.L. (Planck Col. [2013]). In turn, this constraint can also be translated into an upper limit on the neutrino mass which is almost one order of magnitude more constraining than the results from current laboratory neutrino experiments (Bertone et al. [2005]) and thus conclusively rule out that neutrinos constitute the missing matter.

The discussion of the neutrino as prototype for a dark matter candidate already hints towards more general criteria that a viable particle dark matter candidate must have. Assuming that a particle dark matter candidate is thermal, i.e. was in thermal equilibrium with the photon field at some very early stage in the universe development, it must have the right relic density today. This means that at some point in time (depending on the dark matter mass) the particle must have been thermally decoupled from the other particles. The interactions of the dark matter candidate from that time on led in general to a decrease (for instance via annihilation or decay) of the dark matter density. If a dark matter particle is unstable, its lifetime must be much larger than the age of the universe, i.e. $\tau \gg 10^{17}$ s. Additionally, the annihilation of two dark matter particles becomes less probable with increasing time because the probability that two dark matter particles meet is getting reduced by means of the ongoing expansion of the universe. At some point in time, the overall number of dark matter particles in the universe becomes thus nearly constant, dark matter is said to 'freeze out'. The number of dark matter particles is the smaller the larger the annihilation cross section of two dark matter particles is, i.e. the more dark matter particles annihilated before the thermal freeze out. The dark matter content of the universe has been inferred, f.i. with the fit of the CMB temperature anisotropy acoustic peaks, to be $\Omega_{\mathrm{DM}}h^2 \sim 0.1$ in units of the critical density of the universe (see Longair [2011]) where $h \sim 0.71$ is the Hubble parameter normalization (see Eidelman et al. [2004]). On the other hand, an estimation of the relic density of annihilating particle dark matter as a function of the velocity averaged annihilation cross section $\langle \sigma v \rangle$ is possible under reasonable assumptions (see Bertone et al. [2005] and Jungmann et al. [1996] for details) and gives

$$\Omega_{\mathrm{DM}}h^2 \sim \frac{3 \cdot 10^{-27}\,\mathrm{cm^3 s^{-1}}}{\langle \sigma v \rangle}\,. \tag{1.4}$$

At the time of the freeze out, dark matter is already non-relativistic. A dimensional analysis of a typical non-relativistic annihilation cross section gives (see Jungmann et al. [1996])

$$\langle \sigma v \rangle_{\mathrm{v}\to 0} = k\frac{\alpha^2}{M^2}$$

where $k \sim 1\,\mathrm{eV\,cm^3/s}$ is a fudge factor, α is a coupling constant and M is the mass scale of a particle that mediates the annihilation. The famous 'WIMP miracle' expresses that interestingly a typical weak coupling scale $\alpha \sim 10^{-2}$ and a typical weak mass scale $M \sim 100$ GeV result in a non-relativistic velocity averaged annihilation cross section that guarantees the right order of magnitude for the relic dark matter density $\Omega_{\mathrm{DM}}h^2 \sim \mathcal{O}(0.1)$. This is an order of magnitude argument to motivate a search for

WIMPs (Weakly Interacting Massive Particles) as dark matter candidates. The argument is, however, not sufficient. Nevertheless, a hint is given to possibly expect the physics of dark matter realized on the weak scale, by a yet undiscovered mechanism.
An argument that disfavors standard model neutrinos based on a relic density argument is given above. There is another argument against standard model neutrinos as a viable dark matter candidate that is not concerned with the relic abundance but with structure formation in the early universe. In general, particle dark matter candidates are classified as being 'cold', 'warm' or 'hot'. Standard model neutrinos would move with nearly the speed of light which qualifies them as hot dark matter which has been shown to erase all seeds of structure in the early universe (see f.i. Bertone et al. [2005]). A thermal relic dark matter candidate is very unlikely to be hot due to this effect. In contrast warm (i.e. keV mass scale) and cold (i.e. GeV to TeV mass scale) dark matter can form seeds for the observed structure of the universe. Computer simulations predict that warm dark matter should produce less structure than cold dark matter. Structures in this sense are for instance satellites of large galaxies for which indeed the observation points towards warm dark matter being more compatible with the observed amount of satellite galaxies than cold dark matter. However, the computer simulations used to draw this conclusion are imperfect and a conclusive point of view is not yet possible (see f.i. Bertone et al. [2005]). A typical warm dark matter particle candidate that is currently being intensively debated is a 'sterile neutrino'. Sterile neutrinos are keV mass scale extensions of the standard model neutrino sector with suppressed or vanishing coupling to Z bosons. The in comparison to the standard model neutrino modified couplings to the Z boson make the existence of warm, i.e. keV scale, neutrinos possible despite of the LEP limit ($\gtrsim$ 45 GeV) on the masses of neutrinos beyond the three standard model generations. Searches for keV mass sterile neutrinos are currently conducted, yet without positive result (see Boyarsky et al. [2009]).
Standard model or sterile neutrinos with mass larger than $\sim$ 45 GeV, i.e. cold neutrinos above the LEP bound, are not in general excluded by experiments (Dolgov [2002]).
The constraint on $\langle \sigma v \rangle$ for a viable dark matter candidate applies only to particle dark matter that has been in thermal equilibrium at some point in the development of the universe. However, thermal production and freeze out is not the only known way to produce a significant amount of particle dark matter in the development of the universe. Another possibility is that a phase transition in the early universe coming along with a spontaneous symmetry breaking generates a massive dark particle. A famous example candidate of this type is the 'axion' as pseudo-Goldstone boson resulting in the spontaneous breaking of an additional global U(1) symmetry of the standard model (see f.i. Peccei [1996]). The additional U(1) symmetry was considered by Peccei and Quinn to explain the observational exclusion of a large neutron electric dipole moment. This observation can only be explained within the standard model if the QCD sector is, in contrast to the natural standard model prediction, not or only very little violating the CP symmetry. Axions can have the right abundance in the universe to be a viable (cold) dark matter candidate if the scale of the Peccei-Quinn symmetry breaking is very high or equally if the mass of the axions is very small (10^{-6} eV $< m < 10^{-3}$ eV, Peccei [1996]). In contrast to the argument in favor to search for thermal relic dark matter

particles on the weak scale given above this smallness of the axion mass can be seen as a circular argument as an un-naturally small CP violation in the QCD sector is explained by an additional (without further justification) un-naturally small mass particle (see also Mack [2011]). Nevertheless, serious experimental efforts are directed to a search for low mass axions via a theory predicting resonant coupling of axions to photons (Primakoff effect, see Peccei [1996] and references therein) with laboratory based experiments (see f.i. Ehret et al. [2007]) and the detailed investigation of distant astrophysical objects with very high magnetic fields (Sanchez-Conde et al. [2010]).

1.4 Astroparticle Physics, the Milky Way and Dark Matter: Thesis Outline

This introduction started with a quick discussion of TeV scale CR physics, especially the CR proton and electron spectra as observed on and in the vicinity of the earth. The question of the origin and energy source of those particles has been presented as one of the driving forces of astroparticle physics research. Astronomy with γ-rays was introduced as a possible way for the investigation of this question and different detector principles sensitive to different energy regimes were quickly characterized and compared. The detection and investigation of different γ-ray sources within the Milky Way is a very interesting and active field of research. However, low energy γ-ray instruments such as the Fermi observatory not only detect isolated γ-ray sources within the Milky Way but also a large scale 'diffuse γ-ray emission' that is enhanced towards parts of the Milky Way disc. For the Fermi observatory, this diffuse emission is primarily a foreground for the detection of isolated sources. This foreground is by now not detected with TeV γ-rays to which Cherenkov telescopes are sensitive. Cherenkov telescopes have thus yet no foreground for the detection of γ-ray sources but must deal with a large background due to TeV cosmic rays whose energy deposit in the earth atmosphere leads to detector signatures that are in part hardly distinguishable from the signature of a γ-ray. The physical source of the diffuse γ-ray foreground in case of the Fermi observatory and the CR background in case of ground based γ-ray observatories is, however, very similar. In both cases CRs are the energy source - once (Fermi) in form of the interaction with galactic gas or radiation fields and once (ground based observatories) directly via the energy deposit in the earth atmosphere (Cherenkov telescopes) or the detector (Extensive Air Shower Arrays).
It will be pointed out later in this thesis that the detection of a large scale diffuse TeV γ-ray emission in the Milky Way is in fact technically difficult with established Cherenkov telescope data analysis methods. New and modified analysis methods will therefore be discussed.
Additionally, arguments that stem from very different observational results and support the existence of dark matter particles were discussed in the present chapter. Especially in the Milky Way, the dynamical properties of the material within the Milky Way hint towards the presence of dark matter in the Milky Way.
WIMP dark matter has been introduced as one plausible class of the yet undetected dark

matter. Given a sufficient WIMP density in the Milky Way, the annihilation of WIMPs is under some assumptions expected to produce a diffuse γ-ray flux from the whole Milky Way galaxy. The development and comparison of methods to search for such an extended and weak diffuse γ-ray flux caused by annihilating dark matter particles in the Milky Way with Cherenkov telescopes is the main topic of this thesis. To conduct such a search, it is necessary to develop a detailed understanding of systematic effects that come with the usage of Cherenkov telescopes as γ-ray detectors. A technical introduction to the properties of the H.E.S.S. array is given in the next chapter to prepare a discussion of systematic effects. Additionally, a search for γ-rays produced by annihilating dark matter must distinguish putative signal γ-rays due to dark matter annihilations from a possible large scale TeV diffuse γ-ray emission in the Milky Way and from γ-rays generated in ordinary small scale astrophysical γ-ray sources. A general knowledge of the properties of the Milky Way as well as typical astrophysical γ-ray sources as discussed in the present chapter is thus necessary.

2 The High Energy Stereoscopic System

The High Energy Stereoscopic System (H.E.S.S.) is an array of Imaging Atmospheric Cherenkov Telescopes (IACTs) operated since 2003 in the Khomas Highland in Namibia, about 100 km south-west of the Namibian capital Windhoek. This chapter provides a detailed discussion of the technical design and operation of the telescope array as well as a description of the standard data pipeline used in this thesis for the analysis of VHE γ-ray data out of recorded H.E.S.S. data. The chapter starts with a discussion of the physical foundations of the detection of γ-rays with Cherenkov telescopes. Of special importance are the Cherenkov effect as well as the development of γ-ray and cosmic ray shower in the atmosphere. The H.E.S.S. instrument itself is discussed in the subsequent section that covers the hardware setup of the array as well as the description of available atmospheric monitoring devices. The calibration of recorded data and the investigation of the data quality is described afterwards. Monte Carlo simulations of the instrumental response to γ-rays are important to prepare the final section which covers the data analysis chain that is used later in the thesis. Of special importance in the last section are the background suppression and event reconstruction methods as well as the description of the background subtraction.

2.1 Physical Foundations

2.1.1 Cherenkov Light

The 1958 Nobel prize in physics was awarded to P. A. Cherenkov, I. M. Franck and I. Y. Tamm for the discovery and interpretation of the Cherenkov effect which is the name for the emission of electromagnetic radiation by an electric charge moving faster than the speed of light in a medium.
Following Ginzburg [1996], the assumption of a charge with energy E_0 and velocity v leads by conservation of energy and momentum to the possibility of the emission of a photon with energy $\hbar\omega$ under the angle[1]

$$\cos\theta = \frac{c}{nv}\left(1 + \frac{\hbar\omega}{2E_0}(n^2 - 1)\right)$$

[1] The formula given here for the Cherenkov angle is derived in a purely kinematical argumentation but is in all practical cases equivalent to the usual formula $\cos(\theta) = c/(nv)$ (see f.i. Jackson [1998]). The correction stems from the recoil of the charged particle after the photon emission and is always small for optical and UV emission because no charged particle with mass m exist that is sufficiently small to have $\hbar\omega \sim 1\,\mathrm{eV} = \gamma mc^2$ with boost factor γ.

relative to the moving direction of the charged particle. Here, n is the index of refraction in a given medium and c is the vacuum speed of light. No real emission angle is possible when $v < c/n$ and $n \geq 1$, i.e. usually when the charge is moving slower than the speed of light in the medium. However, if $v > c/n$ (and $n > 1$) the emission of a real photon with frequency ω is possible under the Cherenkov angle given above. No physical preference for any frequency ω fulfilling the condition $v > c/n(\omega)$ exists and thus the number of photons emitted per frequency interval is constant, i.e. $dN/d\omega = \text{const}$. In terms of wavelength intervals this means with $d\omega \sim 1/\lambda^2 \, d\lambda$ for the number of Cherenkov photons emitted per wavelength interval

$$\frac{dN}{d\lambda} = \frac{k}{\lambda^2}$$

which is also called 'Franck-Tamm' formula. The proportional constant is $k = 2\pi\alpha Z^2 \sin^2(\theta) L$ where α is the fine structure constant, L is the path length where the charged particle emits Cherenkov photons and Z is the mean number of electrons in the medium (see Eidelman et al. [2004]). The constant can be justified in a lengthy calculation (see Jackson [1998]) but is essentially the electromagnetic coupling ($Z^2\alpha$) and a factor ($\sin^2(\theta)$) that suppresses Cherenkov photon emission for $v < c/n$. The emission of Cherenkov radiation outside of a small band in the optical and near UV is usually suppressed because then $n(\omega) \sim 1$.

2.1.2 Particle Shower

Electron, Positron and γ-ray Induced Air Showers

Electrons, positrons and γ-rays behave very similar in the earth atmosphere at high energies. In all cases, electromagnetic cascades are generated by alternating electron-positron creation and bremsstrahlungs radiation of hard photons.
Consider first a primary γ-ray entering the earth atmosphere. The pair creation process is the dominant energy loss mechanism for the considered energy range ($E > 100$ GeV in the laboratory frame or $\sim \sqrt{2 m_N E} > 10$ GeV in the center of mass frame where $m_N \sim 1$ GeV is the mass scale of an air molecule). On average, the γ-ray will therefore interact with the nucleus of an air molecule via the pair creation process after traveling one radiation length ($X_P \sim 37$ g/cm^2 in air, Eidelman et al. [2004]). This leads typically to a first interaction in a height of ~ 28 km above sea level (asl) for a γ-ray entering the earth atmosphere at zenith. The result of the pair creation process is in practice always an electron-positron pair as the generation of all other possible particles is phase space suppressed. Electrons and positrons are deflected in the electric field of air molecule nuclei and emit typically hard photons via bremsstrahlung. The emission of soft bremsstrahlung is in practice suppressed because the high energy electron or positron would have to pass an air nuclei at distances much larger than the molecular size scale where the nuclei charge is screened by the electrons (see f.i. Heitler [1954]). The alternating cascade of pair creation with subsequent hard bremsstrahlung generates a cascade of ultra relativistic charged particles and stops when the particles reach the critical energy of ~ 81 MeV after ~ 10 cascade steps in a typical atmospheric height

of $\sim$ 10 km asl. The production of particles in the bremsstrahlungs and pair creation cascade is always strongly forward directed in the laboratory frame due to the boost from the center of mass frame. However, the multiple Coulomb as well as Compton scattering lead to a finite lateral extension of a γ-ray air shower which is described by the Moliere theory. The typical radius of a 1 TeV γ-ray shower is $R_M \sim 20$ m in air (see Hillas [1996]). The outlined model of a γ-ray shower has first been described in Heitler [1954]. In practice, γ-ray showers are simulated with Monte Carlo software that is described later but does in principle implement the described effects.
If a primary electron or positron enters the earth atmosphere in contrast to a primary γ-ray the shower development is in general the same as described above but the first interaction is of course not a pair creation but a bremsstrahlungs process. The mean free path length for pair creation at high energies is slightly larger than the radiation length for bremsstrahlung (factor 9/7) which can be used to some extend to separate electron or positron air showers from γ-ray air showers based on the reconstruction of the first interaction height in the atmosphere (see H.E.S.S. Col. [2008]). In practice, electron and positron initiated shower constitute an irreducible background for the detection of γ-ray initiated showers.

Hadronic Air Showers

The majority of cosmogenic particles hitting the earth atmosphere with GeV and higher energies are hadronic particles, i.e. protons and heavier nuclei. A proton or heavier nucleus entering the earth atmosphere is in general strongly interacting with nuclei of air molecules. The nuclear interaction length in air is $\sim 90\,\mathrm{g/cm^2}$ (Eidelman et al. [2004]), i.e. a factor of ~ 3 larger than the radiation length for an incoming γ-ray. The strong interaction leads to secondary particles. Phase space considerations show that the lightest strongly interacting particles are preferred to be produced as secondary particles, i.e. the dominant component of hadronic air shower are pions followed by kaons. To a good approximation, every nuclear interaction results in $\sim 2/3$ of the energy to be deposited into charged and $\sim 1/3$ into neutral pions on average. However, statistical fluctuations can be large. The produced secondary particles are typically unstable and can either decay or undergo another strong interaction with air nuclei, depending on the nuclear interaction length and the decay time. Of primary interest is the decay of neutral pions for which the decay time is very short ($\sim 10^{-17}$ s, $c\tau \sim 25$ nm see Eidelman et al. [2004]). In contrast, charged pions have a much larger decay time ($\tau \sim 10^{-8}$ s, $c\tau \sim 7.8$ m see Eidelman et al. [2004]) for the dominant decay into muons and neutrinos. Charged pions with sufficiently large Lorentz boost factor are thus likely to interact again strongly and thus transfer again $\sim 1/3$ of their energy into neutral pions. A large fraction ($\sim 90\%$, see Engel et al. [2011]) of the energy of a primary hadron entering the earth atmosphere is thus deposited in electromagnetic subshowers.
Given the complexity of hadronic interactions, it appears very difficult to gain a quantitative understanding of the shower process in a simple model. Major differences between hadronic air and γ-ray showers are that

- the statistical fluctuations of a hadronic air shower are much larger than for a γ-ray shower. This leads to an in general less uniform and symmetric shower development (see also Longair [2011]).

- The transverse size of a hadronic air shower is typically larger than for a γ-ray shower of similar energy. The increased transverse size of a hadronic vs. a γ-ray shower is primarily connected to the few hard hadronic interactions with large transverse momentum in the final states that stand out of the larger number of soft interactions with low energy and high multiplicity final states (see also Engel et al. [2011]).

- The longitudinal size of a hadronic shower is also typically larger than for a γ-ray shower of similar energy. This is a result of the nuclear interaction length in air to be larger than the radiation length in air.

In practice, the instrumental response of a Cherenkov array to cosmic ray showers can be simulated with Monte Carlo methods (Bernlöhr [2008]). Alternatively it can be obtained by observing regions in the sky that do not contain γ-ray sources resulting in only cosmic rays (mostly protons, iron and to a small fraction electrons and positrons) triggering the array.

2.1.3 Imaging of Particle Showers

The Cherenkov light emitted towards the spherical mirror of a H.E.S.S. I telescope by charged particles moving faster than the speed of light in the atmosphere is imaged onto the telescope camera if the emission is seen in the telescope field of view. Cherenkov light emitted within a telescope field of view at the same zenith ($\tilde{\theta}$) and azimuth ($\tilde{\phi}$) angle relative to the telescope pointing is in good approximation imaged on the same point of the telescope camera by the spherical telescope mirror. To develop a qualitative understanding of the image of particle shower in a H.E.S.S. camera consider first the simple case of a particle propagating straight and without energy loss through the atmosphere while emitting Cherenkov light[2]. Typically, the emitted Cherenkov photons do not hit the $\mathcal{O}(10\,\mathrm{m})$ radius H.E.S.S. mirror for geometric reasons or are not imaged to the telescope camera due to the limited field of view (see fig. 2.1 left side). Emission that is imaged by the mirrors onto the camera is in general possible in up to two atmospheric regions differing for geometric reasons in height above the observation level (see fig. 2.1). The Cherenkov emission angle depends on the atmospheric level because the index of refraction changes with height above the observation level. The range of the Cherenkov emission angle within one of the two possible regions in the atmosphere where Cherenkov photons are emitted that are imaged on a camera is typically $\leq 0.2^\circ$ which is comparable to the FoV of a single PMT (see Spengler [2009] for details). The H.E.S.S. camera image of the Cherenkov emission of a particle propagating without energy loss straight through the atmosphere is thus given by up to two clustered PMTs with Cherenkov photon signal

[2] This is in fact a model for the Cherenkov emission of heavy magnetic monopoles. See Spengler [2009] for details of the model and the imaging process.

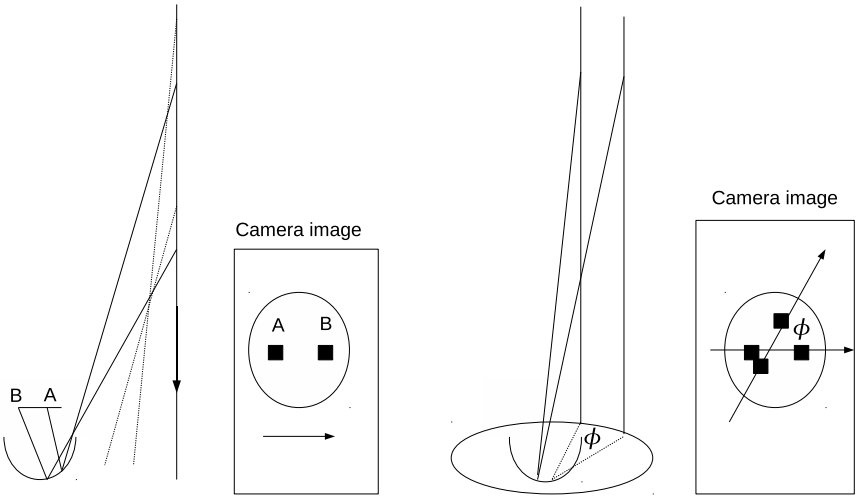

Figure 2.1: Left: Cherenkov photons emitted by a single charged particle moving straight through the atmosphere are imaged onto the camera when hitting the mirror within the field of view. Emission under different zenith angles translates to different imaging points on the radial camera axis. Right: Two Cherenkov photon emitting charged particles moving straight through the atmosphere at the same distance to a IACT but with a difference in azimuth angle. The azimuth angle between the two propagating particles translates into a width of the camera image in contrast to the radial length of the image due to the emission under different Cherenkov angles.

where each cluster has $\mathcal{O}(1)$ PMT. A line connecting the two PMT clusters triggered due to Cherenkov light intersects with the path of the Cherenkov light emitting particle in the plane of the camera. Thus, the direction of a Cherenkov emitting particle can be inferred from the connecting line between two triggered PMT clusters.
Figure 2.1 shows on the right side two Cherenkov light emitting particles propagating in the atmosphere without energy loss. The two particles propagate parallel and at the same distance to a telescope but with different azimuth angles relative to the telescope pointing. The azimuth angle difference between the two propagation directions translates into an angle between the two connecting lines between the PMT clusters triggered by the Cherenkov emission of each particle.
The simple model for the imaging of Cherenkov photons emitted by a charged particle moving on a straight line through the atmosphere can be generalized to the more complicated imaging of the Cherenkov photons emitted in a particle shower. In this case, the Cherenkov photons that are emitted at different Cherenkov angles but from particles seen at the same azimuth angle relative to the pointing axis are imaged on different points on the radial axis of the camera. The emission under different Cherenkov angles can occur due to varying particle energy or atmospheric emission height and the imaging on the radial camera axis leads to the finite length of an image in a camera. Thus, the image length of a particle shower in a Cherenkov camera reflects the longitudinal development of the shower. The lateral extension of a particle shower translates in turn into the width of a camera image (see also fig. 2.2).
As outlined above, the transverse size ($R_\gamma \sim 20$ m for a 1 TeV primary) of γ-ray showers is dominantly due to the multiple scattering of the shower particles. In contrast, the transverse size ($R_\mathrm{H} \sim 70$ m for a 1 TeV proton primary, see Hillas [1996]) of hadronic air showers is dominantly due to the transverse momentum of the neutral pions produced in hadronic interactions and typically larger than the transverse size of γ-ray showers. This difference translates into an angular width difference of the camera image for hadronic and γ-ray initiated particle showers. Hadronic air showers seen at a distance of $D \sim 10$ km have a typical image angular width of $w \sim 2R_\mathrm{H}/D \sim 0.8^\circ$ which compares to the typical angular width corresponding to a γ-ray shower of $w \sim 2R_\gamma/D \sim 0.2^\circ$. The width is used later as a very powerful tool for the separation of γ-ray events from the background due to hadronic events.

2.1.4 Night Sky Background

The photon intensity due to Cherenkov light emitting particle showers is very small compared to other photon sources even during the nights without moon- and sunlight in afield sites. In a typical γ-ray shower, $\mathcal{O}(100\,\mathrm{Photons}/(\mathrm{m}^2\,\mathrm{TeV}))$ reach altitudes of ~ 2 km asl in a radius of ~ 100 m around the primary particle (see f.i. Hillas [1996]). Thus, a 1 TeV γ-ray primary produces $\mathcal{O}(10^4)$ Cherenkov photons that are hitting a telescope mirror[3] of $\sim 100\,\mathrm{m}^2$. With an average photon detection efficiency of $\sim 10\%$ this leads

[3]This example calculation refers to the telescope mirrors of the H.E.S.S. phase one telescopes.

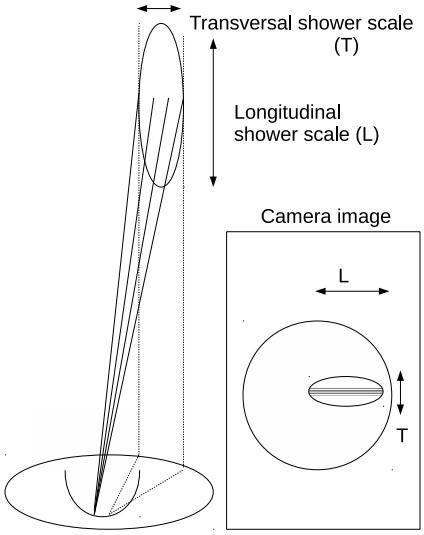

Figure 2.2: Shower images in IACT cameras with sufficient number of PMTs are elliptically shaped. The transverse development of an air shower translates into the width of an image in a Cherenkov camera. The longitudinal shower development is in turn characterized by the radial length of the shower image.

to a typical image amplitude in one H.E.S.S. camera of 1000 pe (photo electrons[4]) for a 1 TeV γ-ray shower and a dynamic range of $\sim$ 100 pe to $\sim$ 50000 pe for the typical energy range of H.E.S.S. ($\sim$ 100 GeV to $\sim$ 50 TeV). The residual light in a dark night without moon- or sunlight is called night sky background (NSB). Important sources of NSB are (see Preu et al. [2002] and Mellinger [2009] for more information):

- Chemical processes in the upper atmosphere leading to air-glow which is f.i. the optical emission of photons due to the recombination of ionized or dissociated air molecules. Ionization and dissociation of air molecules can be caused by ionizing radiation of cosmic rays or their secondary interaction products. The intensity of air-glow seen by an observer on the earth surface increases in general with the zenith angle of the viewing direction as the atmospheric depth increases with zenith.

- Resolved and unresolved starlight are obvious and unavoidable sources of NSB.

- Starlight scattered by cosmic dust clouds contribute to the NSB.

[4]The exact definition of the intensity unit photo electrons is given below. For the moment it is sufficient to compare the relative intensities of typical Cherenkov showers with the residual night sky light intensities.

- Light pollution due to light from cities. Sites for observations with Cherenkov telescopes are in general selected to be as free as possible from artificial light pollution. However, f.i. at the H.E.S.S. site in Namibia the cities Windhoek and Rehoboth are visible as faint diffuse light sources at the horizon during the night.

A typical effect of NSB is that the region towards the galactic center appears even with the naked eye much brighter than typical regions off the galactic plane. NSB leads to a typical rate of $\mathcal{O}(10^8$ pe/s) in one H.E.S.S. PMT (Preu et al. [2002], H.E.S.S. Col. [2004]) which has to be compared to the mentioned signal of typically (depending f.i. on the shower distance) $\sim$ 1000 pe in one complete H.E.S.S. camera for a 1 TeV γ-ray shower. The NSB signal defines a signal baseline that can be removed in the calibration when constantly monitoring the PMT signal in the absence of Cherenkov light (see the discussion of the H.E.S.S. data calibration below). However, in order to detect a Cherenkov signal, the Poisson fluctuations of the NSB in a given exposure time T given by typically $\sqrt{(10^8 \cdot T/\mathrm{s})}$ pe has to be much smaller than the Cherenkov signal of interest. A particle shower triggers $\sim 10 - 100$ PMTs leading to a typical signal of $\mathcal{O}(10\,\mathrm{pe})$ per PMT for a 1 TeV shower detected in a time window of $\sim$ 10 ns. In a 10 ns exposure time window, the fluctuation of the NSB photo electron signal is $\sim$ 1 pe and thus a reliable detection of Cherenkov light is possible when using very fast photon detectors. Additionally, NSB photons do not preferentially lead to photon signals within a readout window in spatially connected regions of an IACT camera as does the Cherenkov light from particle showers. This property can be used for the trigger configuration of IACTs and for the data processing to suppress NSB effects on the particle shower reconstruction as is detailed below.

2.1.5 Particle Showers in the Earth Atmosphere and Magnetic Field

The development of particle showers as discussed above takes for IACT measurements place in the earth atmosphere and under the influence of the earth magnetic field. The IACT response to a γ-ray shower becomes thus dependent on the pointing zenith- and azimuth angle[5] of the telescope system as well as on time. The dependence on the pointing zenith angle and on time is caused mainly by atmospheric layering and time dependent atmospheric changes. The dependence on the pointing azimuth angle on the other hand is introduced via the earth magnetic field and atmospheric changes in time. The earth magnetic field leads to an azimuth dependence of the width of particle showers because the more the shower particles move parallel to the earth magnetic field lines, the less deflected they are. The deflection is into opposite directions for positive and negative electric charges. Electrons and positrons of a γ-ray shower are thus spatially separated by large magnetic fields perpendicular to their momentum direction and the γ-ray shower transverse extension scale becomes larger. As a consequence, the average intensity per pixel detected in an IACT is reduced and possibly lowered below the

[5] In this thesis a zenith angle of 0° corresponds to a vertical pointing of the telescopes towards the sky. A zenith angle of 90° corresponds to a horizontal pointing respectively. An azimuth angle of 0°/90°/180° corresponds to a pointing towards the north/east/south.

trigger threshold. The result is that the energy threshold of an IACT for γ-ray showers increases with increasing perpendicular magnetic field line components. For γ-ray primaries selected based on image shape parameters (see below) out of the dominant hadronic background, the increase in angular width seen in an IACT camera can lead to a decrease in effective detection area. The influence of the geo-magnetic field has been studied for H.E.S.S. by comparing Monte Carlo simulations of particle showers at different azimuth angles (Bernloehr [2005]) and is taken into account in the calculation of the effective areas.
The sensitivity of IACTs to detect and reconstruct particle showers depends on the zenith angle θ of the IACT pointing as the vertical path from the observation level to the space out of the earth atmosphere increases with the zenith angle according to $\sim 1/\cos(\theta)$. The Cherenkov light emitted by charged particles in a shower is therefore with increasing zenith angle increasingly absorbed and Rayleigh scattered on air molecules as well as Mie scattered on aerosols leading to a reduced density of Cherenkov photons on the observation level. The effect leads to an increasing energy threshold with increasing zenith angle. On the other hand, the area illuminated by Cherenkov light on the observation level becomes increasingly elliptical with zenith angle leading to increasing effective areas ($\sim 1/\cos^3(\theta)$, see Spengler [2009]) for particles above energy threshold. The zenith angle dependence of the energy threshold and effective area as obtained from Monte Carlo simulations is taken into account in the analysis of H.E.S.S. data.
Apart from the zenith and azimuth pointing angle dependence, the energy threshold and effective area are also time dependent due to changes in the earth atmosphere that are not reflected in the average atmospheric model for the H.E.S.S. site employed for Monte Carlo simulations. This effect is investigated in detail for the dataset studied in this thesis to search for particle dark matter annihilation in the Milky Way halo.

2.2 The H.E.S.S. Instrument

2.2.1 H.E.S.S. Phase I

Figure 2.3 (left) shows a photograph of the H.E.S.S. phase I four telescope array as it was operating from January 2004 to mid 2012. Four almost identical IACTs are located in a square with 120 m side-length. The mirror of one IACT has 15 m focal length and $\sim 100\,\mathrm{m}^2$ total collection area consisting out of 382 small mirrors arranged spherically with a camera in the focal plane. More precisely, the telescopes are built in a 'Davis-Cotton design' to reduce the spherical aberration (see Davis and Cotton [1957]). Each camera dish and the mirrors are mounted in a zenith- and azimuth angle movable frame. Azimuth- and zenith angle are adjustable within $0^\circ - 360^\circ$ and $0^\circ - 90^\circ$ respectively with a mechanical precision of $\sim 0.02^\circ$ or $\sim 60''$ (Gillessen [2003])[6]. The maximum speed of the telescope azimuth and zenith drive system is $\sim 100^\circ$/min. The mirrors have a high reflectivity $\mathcal{O}(80\%)$ (wavelength dependent) that is, however, degrading in time due

[6] Note that offline pointing corrections can improve the pointing precision to around $3''$ or 0.001° (see Gillessen [2003]).

to aging effects. The reduction of the mirror reflectivity is constantly monitored and corrected for (see the discussion of the muon correction below). More information on the mechanics and optics of the H.E.S.S. IACTs can be found in Bernlöhr et al. [2003]. The camera consists of 960 photomultiplier tubes (PMTs) arranged in a plane and packed in electronic modules (drawers) consisting of 16 PMTs each. Every PMT is equipped with a Winston cone that increases the field of view of a single PMT to a diameter of 0.16° leading to a total camera field of view of $5^\circ \sim 0.16^\circ\sqrt{960}$ in diameter. The PMTs are sensitive to light between ~ 300 nm to ~ 600 nm with a typical quantum efficiency[7] of $\mathcal{O}(25\%)$ in the most sensitive wavelength band between ~ 320 nm to 420 nm (Bernlöhr [2008]). Cherenkov light emitted in the atmosphere is imaged onto the camera by the IACT mirrors and detected by PMTs using a short integration time of 16 ns to suppress night sky background (NSB). PMTs focused directly on bright stars are switched off during data taking. Photons detected by a PMT lead to a current which is amplified within the PMT and measured across a resistor as a voltage with a sampling frequency of 1GHz[8] corresponding to a time resolution of 1 ns. The voltage signal is amplified in two channels (high and low gain) and stored in a ring buffer[9]. If a camera is triggering, the sampling stops and the content of 16 ring buffer cells (corresponding to the 16 ns integration window) is summed up. The resulting event signal is converted from voltage to analog digital counts (ADC) using a fixed conversion factor of 1.22 mV/ADC.
The H.E.S.S. phase I array makes use of a two level trigger system to increase the sensitivity to γ-ray showers. The first level trigger is a single telescope trigger for which the IACT camera is divided into ~ 40 partly overlapping sectors. If more than 4 pixels

[7] The quantum efficiency is the fraction of incoming photons that contribute to a measured signal. Taking together the mirror reflectivity and the quantum efficiency, it follows that $\sim 20\%$ of the ~ 320 nm to ~ 420 nm photons falling on a H.E.S.S. mirror contribute to a signal. This estimation neglects the collection efficiency inside a PMT and the shadowing factor of the camera and dish support structure but gives a good order of magnitude estimation. In practice, the atmospheric absorption has to be taken into account when translating the number of Cherenkov photons emitted in ~ 10 km height to the number of Cherenkov photons hitting a telescope mirror in ~ 2 km height. Averaged over the ~ 300 nm to ~ 600 nm band typically $\sim 60\%$ (Bernlohr [2000]) of the emitted photons arrive at the H.E.S.S. observation level leading to a total Cherenkov light collection efficiency of $\sim 10\%$.

[8] The high sampling frequency needed to suppress NSB while being sensitive to γ-ray showers is the reason for choosing PMTs as photo sensitive elements of the camera. Currently there is no other technique that allows a stable operation with billion pictures per second. Geiger-Avalanche silicon photo diodes can in general operate at the same speed and have the advantage of a higher quantum efficiency. The development of novel photo detectors is a vital area and progress is to be expected within the next years.

[9] The ring buffer is an Analog Ring Sampler (ARS) developed initially for the ANTARES collaboration (see ANTARES Col. [2010] for details of the electronics). Each ARS is responsible for buffering the ADC values of 4 PMTs. The 16 ns integration window typically used by H.E.S.S. fills $4 \cdot 16 = 54$ buffer cells. The ring buffer needs, however, to be bigger as ADC values read out within the coincidence window of the multi telescope trigger have to be available. The design size for the ARS is 128 cells making it possible to have a $(128 - 54)$ ns $= 74$ ns coincidence window for the multi telescope trigger which is sufficient. A frequently occurring problem during the H.E.S.S. data taking is the obvious non-operation of four PMTs in a column. This is due to a problem with the corresponding ARS. See H.E.S.S. Col. [2004] and Balzer [2010] for more information.

within a sector have a signal of more than 4.7 pe[10], a camera trigger occurs. The camera trigger leads to the suppression of random camera trigger events due to NSB which have in contrast to air shower events no preference for triggering spatially close pixels and typically trigger with low intensity ($\sim$ 1 pe). As the buffering of the ADC values is stopped when a camera event is triggered, a telescope is not operating for the time of the read out of the ring buffer data and the central trigger decision. This leads to a telescope dead time of $\mathcal{O}(400\,\mu\text{s})$ (see also appendix A) during which the corresponding telescope cannot process events. A typical single telescope trigger rate for a H.E.S.S. I telescope is $\mathcal{O}(1\,\text{kHz})$.
The second trigger level of the H.E.S.S. phase I array requires at least two triggering telescopes within a coincidence window of $\sim$ 80 ns. This value has been empirically optimized to suppress random multi-telescope triggers while being sensitive to Cherenkov showers (Funk et al. [2004]). If both trigger requirements are fulfilled, an event, i.e. the ADC values of each of the 960 PMTs of each operating telescope is read out and stored for further offline processing on data tapes that are brought to a European data processing center at regular intervals. The second trigger level is significantly reducing background events due to muons produced in hadronic air showers. Typical H.E.S.S. one array trigger rates are $\mathcal{O}(200\,\text{Hz})$ showing that the second level trigger leads to a factor of ~ 5 in background suppression. More information on the trigger system of the H.E.S.S. array can be found in Funk et al. [2004].
Practical data taking with the H.E.S.S. array is conducted by typically two H.E.S.S. collaboration members that stay for one shift lasting $\sim$ 1 moon cycle starting at full moon. The array is controlled from a control building at the H.E.S.S. site. Data are taken only when the moon as well as the sun are below the horizon and the meteorological conditions are satisfactory. If no data is taken, the telescope cameras are parked in a shelter to avoid unnecessary exposure to rain etc. and the telescope mirrors point below the horizon to avoid the imaging of sunlight that can lead to dangerous situations. Around one hour prior to data taking, the cameras are heated up to avoid drifts in the camera electronics due to varying temperatures and standardized data acquisition tests are performed. In case that not all telescopes are operational, data is taken with a reduced number of telescopes. This has to be accounted for in the data analysis.
H.E.S.S. data on objects of astrophysical interest are usually taken in observation runs pointing such that the object of interest is within the 5° camera FoV for typically $\sim$ 30 min. During the observation, the earth movement is automatically compensated by source tracking, i.e. the object of interest is kept at constant position in the camera FoV while the zenith and azimuth telescope pointing angle change.

[10] At this stage a preliminary conversion from ADC to pe with 80 ADC/pe in the high gain channel (sensitive to low pixel intensities) is applied. If an event is finally read out, the ADC values are stored and converted into photo electrons during the offline calibration with an increased precision. The offline calibration is discussed later in this text.

Figure 2.3: Left: The four H.E.S.S. phase I telescopes together with the H.E.S.S. control building behind the emergency on-site power generator building in the Khomas Highland, Namibia. Right: The H.E.S.S. phase 2 array with the large fifth telescope in the center of the H.E.S.S. 1 array.

2.2.2 H.E.S.S. Phase II

The extension of the four telescope H.E.S.S. phase I array in 2012 and 2013 by a large fifth telescope built in the center of the phase I array is called H.E.S.S. phase II. The large telescope is sensitive to γ-ray showers with a primary energy of some 10 GeV compared to the energy threshold of the phase I array of around 100 GeV. The lower energy threshold is reached by the larger mirror ($\sim 600\,\mathrm{m}^2$ compared to $\sim 100\,\mathrm{m}^2$ for one H.E.S.S phase I telescope). The mirror of the large telescope is not spherical as for the smaller telescopes because spherical mirrors introduce time dispersions between photons reaching the camera in the focal plane from different points on the mirror. Instead, hexagonally shaped spherical mirror facets are mounted on a nearly parabolic mirror support structure to approximate a parabolic mirror. Apart from the mirror shape, the large H.E.S.S. II telescope is constructed very similar to the smaller H.E.S.S. I telescopes. No data from the H.E.S.S. II array are analyzed in this thesis.

2.2.3 Atmospheric Monitoring

The H.E.S.S. array consists not only of the Cherenkov telescopes but also a number of secondary instruments belong to the setup. Infrared radiometers (described in Chadwick et al. [2000]) measure the sky temperature[11] in the field of view of the camera while observations are performed. The used radiometers are installed in all four H.E.S.S. I telescopes and point towards the same direction as the telescopes do. The field of view of the radiometers is 2.9° (Aye et al. [2003]), i.e. comparable to the H.E.S.S. I field of view. The precision of the temperature measurement is ±0.2° (Aye et al. [2003]). The temperature measured with a radiometer of a given telescope is not calibrated

[11] More precisely the intensity of the far infrared radiation in the 8 μm to 14 μm band is measured and translated into the temperature of a black body emitting the same amount of radiation in the considered band.

on an absolute scale, i.e. only temperature differences are typically meaningful. The radiometer devices enable the monitoring of atmospheric changes. For instance, clouds in the field of view of a camera are visible by an increase in the radiometer temperature[12]. The radiometer temperature depends, for instance, also on the pointing zenith angle (increasing temperature with increasing zenith angle) as the amount of water vapor, carbon dioxide and ozone in the line of sight increases with zenith angle (see Chadwick et al. [2000] and Sloan et al. [1955] for details). The atmospheric monitoring with the help of the telescope radiometers will be used later in this thesis.

2.3 Data Calibration

Instrumental and environmental changes lead to the necessity to calibrate observation runs. Calibration runs are taken for this purpose on a regular basis. This section sketches the calibration procedure. More detailed information can be found in H.E.S.S. Col. [2004].
The ADC values of all PMTs recorded in a H.E.S.S. event need to be calibrated and compared to simulated events to extract the relevant information for γ-rays. The general formula used for the conversion of the measured ADC values of a given PMT to calibrated intensity data in photo electrons (pe) is

$$\frac{I_i}{\mathrm{pe}} = \frac{(\mathrm{ADC_i} - \mathrm{Pedestal_i})}{\gamma_i}\mathrm{FF}$$

where

- $\mathrm{ADC_i}$ are the ADC values measured in the channel i which can be the low or high gain channel. The low gain channel is used for intensive signals (range 15 to 1600 pe), the high gain channel is used for signals up to 200 pe.

- γ_i is the electronic amplification of the channel i. The high gain factor is measured every $\sim$ 2 days in special calibration runs where every PMT is illuminated at $\sim$ 1 pe (single photo electron runs). For this purpose, an LED pulser mounted in the camera hut is used to illuminate the camera while the camera is in the parking shelter. The LED pulser is operating at a frequency (70 Hz) that is also used to trigger the camera read out for this calibration run-type such that the signal measured in single photo electron runs is caused by the LED. The ADC value distribution resulting from the single photo electron runs is fitted to a model (see H.E.S.S. Col. [2004]) that depends on the electronic amplification in the high gain channel. The corresponding low gain factor cannot be obtained from the fitting of the single photo electron illumination signal (see Balzer [2010]). Instead it is calculated in normal observation runs from the high gain amplification factor by considering the signal in the range where both channels lead to linear

[12] The reason for this is that clouds (i.e. water molecules) absorb and re-emit the infrared radiation that is emitted from the earth surface more efficiently than the rest of the atmosphere.

signal amplification ($\sim$ 10 pe to $\sim$ 200 pe). Thus, the low gain factor can be calibrated on the high gain factor. Nominally the high gain amplification factor γ_{HG} is ~ 80 ADC/pe and the high gain to low gain ratio is ~ 14.

- $\mathrm{Pedestal_i}$ is the pedestal value of the PMT. The pedestal value is caused by electronic noise and NSB photons and has to be subtracted from the measured ADC value to find a signal of interest. The pedestal values are strongly temperature dependent and change on the timescale of minutes. Therefore, the pedestal has to be estimated multiple times for each PMT during the calibration of an observation run. Typical Cherenkov showers in a H.E.S.S. camera trigger only 10 to 100 out of 960 PMTs while all other PMTs measure only a pedestal signal. In order to measure the pedestal for each PMT in a given event, only PMTs are considered whose signals are below a 6 pe[13] threshold and which additionally do not have neighboring PMTs with a signal above 3 pe. In this way, PMTs whose signal is significantly affected by Cherenkov light are effectively excluded from the pedestal estimation in an event. Using the average value obtained for each PMT after analyzing $\sim$ 2 minutes of data (at typical data rates of 200 Hz) is appropriate to reflect the time dependence of the pedestal value and at the same time to collect sufficient statistics for a meaningful pedestal calculation.

- FF are flat-fielding coefficients that correct for differences in the light intensity measured by different PMTs at uniform illumination. Such differences can originate in several PMT inhomogeneities, f.i. with respect to their quantum efficiency. Flat-fielding coefficients are measured for every PMT of a telescope every $\sim$ 2 days. For this purpose, special flat fielding runs are taken where the camera is illuminated directly, i.e. without mirror imaging, and uniformly by an LED flasher mounted at the telescope dish. The flat fielding flasher intensity is stable at the 5% level but adjustable to lead to PMT signals in the $\sim$ 10 pe to $\sim$ 200 pe range. A flat-fielding run is analyzed by using electronic amplification gains and pedestal values obtained in the same way as for usual observation runs. The ratio of the mean signal of an individual PMT and the mean signal in a camera illuminated with a uniform light intensity is the flat fielding coefficient of the PMT. If there were no inhomogeneities between the PMTs of a camera, the flat-field fielding coefficient of each PMT would be by definition unity. Typically, flat-fielding coefficients deviate by $\sim 10\%$ from unity.

2.4 Data Quality

As stated above, data with the H.E.S.S. array are only recorded if the meteorological conditions during the dark time are apparently stable. Additionally to that, data is tested for standard quality indicators before further processing. On a camera by camera level, tests on the number of operating PMTs are performed. On a telescope by telescope basis

[13] For the selection of pedestal estimation pixel, the nominal PMT calibration of the high gain with amplification factor 80 ADC/pe and a nominal pedestal high gain value 11750 ADC counts is used.

the individual telescope trigger rate and the participation fraction of each telescope in the array trigger and the array trigger rate itself is monitored. The pointing precision of the tracking system is tested by comparing the appearance of large currents in individual camera PMTs with the position of bright stars on the sky. Data that appears suspicious with respect to the mentioned parameters is not further processed.

2.5 Monte Carlo Simulation

As outlined above, the qualitative image shape of air showers initiated by different primary particles in a H.E.S.S. camera can be described through general physics considerations. For a realistic account of the different instrumental effects (f.i. zenith and azimuth angle of pointing, different telescope array configurations, electronics, etc.) or for a detailed reconstruction of the energy and direction of primary γ-ray particles it is, however, necessary to perform Monte Carlo simulations of the imaging and detection of Cherenkov light emitted in air showers. The instrumental response of H.E.S.S. to γ-ray induced air showers is obtained in multiple steps. The simulation of γ-ray showers and the propagation of Cherenkov photons in an atmosphere that is appropriate for the H.E.S.S. site in Namibia is done with CORSIKA (Heck et al. [1998]) which uses the EGS4 code system (Hirayama et al. [2005]) for the implementation of the different electromagnetic particle interactions. Showers initiated by γ-rays are simulated for a sufficient range of telescope zenith and azimuth angle pointing positions to account for the pointing dependence due to the atmosphere and the earth magnetic field. Also a covering range of offsets of the γ-ray direction from the camera center is simulated for every telescope pointing to reflect the dependence of the γ-ray acceptance on the offset from the camera center. A realistic simulation of the H.E.S.S. array in different configurations regarding the number of operating telescopes is performed with the software package simhessarray Bernlöhr [2008]. The simhessarray package processes the CORSIKA output and takes f.i. the two level H.E.S.S. trigger, the imaging of the H.E.S.S. composite mirror and realistic quantum efficiencies for the camera PMTs into account. The output of this simulation can be processed in the same data analysis chain that is also used for real H.E.S.S. data. In the following, quantities used in the analysis presented later that are derived from the simulation of γ-ray showers and the H.E.S.S. instrumental response to them are listed.

- Effective areas A_{Eff} are calculated as a function of
  - the telescope array pointing in zenith θ, azimuth ϕ,
  - the offset ψ of the γ-ray direction from the camera pointing position,
  - the γ-ray energy E
  - and the number and spatial arrangement of operating telescopes (telc) in the array as well as their mirror reflectivity (optc).

  In practice, a sufficiently large number of γ-ray events $N(\theta, \phi, \psi, E, \mathrm{telc}, \mathrm{optc})$ is simulated and the effective area $A_{\mathrm{Eff}}(\theta, \phi, \psi, E, \mathrm{telc}, \mathrm{optc})$ is inferred from the number of events that pass a given set of event selection criteria (cuts). The effective

area depends thus explicitly on a given analysis chain, especially on the background suppression cut configuration. The analysis chain used in this thesis is described below.

- Energy look-up tables are obtained from Monte Carlo simulations of γ-ray showers by archiving the total intensity detected in a camera and the reconstructed direction of the primary γ-ray as well as the simulated γ-ray energy in look-up tables. Look-up tables are generated for a covering range of
  - telescope configurations, i.e. the number and spatial arrangement of operating telescopes (telc), as well as their mirror reflectivities (optc),
  - pointing positions in zenith and azimuth,
  - offsets of the γ-event from the array pointing position
  - and primary γ-ray energies.

  For a given H.E.S.S. data event, the energy of the event can then be reconstructed under the assumption that the event originates from a γ-ray by consulting the right look-up table. The energy reconstruction on an event by event basis is accompanied with a statistical error that is typically $\sim (15-20)\%$ (H.E.S.S. Col. [2006]) in the analyis chain discussed below. The statistical error originates from the statistical nature of the development of a γ-ray shower with respect to the number of Cherenkov emitting particles at a given atmospheric depth. Additionally to the statistical error due to shower fluctuations, there is also a systematic error in the energy reconstruction due to differences in the atmospheric light absorption between the atmosphere model used for the γ-ray shower simulation and the actual atmospheric parameters at the time of data taking. The systematic error is estimated to be 10% for H.E.S.S. on the basis of the comparision of different atmospheric models (Bernlohr [2000]). The statistical error on the energy reconstruction for a given event due to shower fluctuations and the systematic error due to atmospheric uncertainties are independent and can for an order of magnitude estimation be added in quadrature to give a total uncertainty in the energy reconstruction of $\sim 20\%$.
  For energies on the lower edge of the instrumental sensitivity there is in addition to the statistical and systematical uncertainty of the energy reconstruction also an energy bias. The energy bias results from the tendency of preferentially detecting low energy γ-ray showers that emit more Cherenkov photons than an average γ-ray shower of given primary energy. The energy bias is controlled by the usage of energy threshold values discussed in the next item.

- Energy threshold values depend again on the telescope array zenith and azimuth angle pointing, the offset of the γ-ray direction from a camera center and on the telescope array configuration as well as the mirror reflectivity and the data analysis chain. Two different energy thresholds will be used in the analysis presented later. The trigger energy threshold is in general the minimal energy that a primary γ-ray must have in order to be detected. If an unbiased energy reconstruction for

the event is necessary, the minimal energy reconstruction threshold defined as the primary γ-ray energy needed to allow an energy reconstruction with less than 10% energy bias is used.

2.6 Data Analysis Chain

After calibration and data quality checks, an event that is to be processed is the collection of all signal values measured in pe for every operating PMT. In the subsequent data analysis, a PMT is usually called a pixel. Despite the CR suppression due to the first and second level trigger, not the γ-rays that are of interest but CRs trigger the writing of events dominantly. This makes it desirable to discriminate between CR and γ-ray events to filter the γ-ray events. Additionally, the signal in the majority of the pixels in a given event is not due to Cherenkov light but due to fluctuations of NSB light around the pedestal which has to be filtered out during the data analysis. Finally, the energy and the direction of a primary γ-ray is to be reconstructed. This section sketches the data analysis chain, i.e. the background suppression for the filtering of γ-rays out of the dominant CR background and the event reconstruction as used in the later described analysis of H.E.S.S. data.

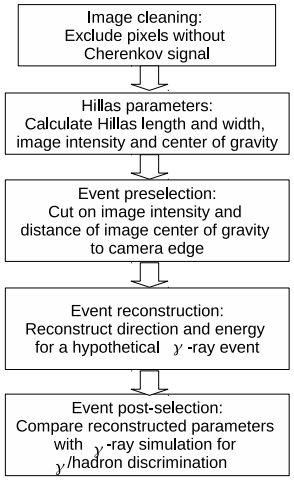

Figure 2.4: Data analysis flow

2.6.1 Image Cleaning

As outlined above, a typical CR event triggers only ~ 100 pixels by Cherenkov light. All other pixels are read out if the H.E.S.S. array receives a trigger signal but their signal is dominated by random fluctuations around the electronic pedestal value due to electronic noise and NSB photons, leading typically not to high intensities after calibration.
Pixels whose signal is only due to pedestal fluctuations are preferably to be removed in a first step of the data processing for all further analysis. This is achieved by the so called image cleaning. Only camera pixels whose calibrated signal value exceeds a threshold t_1 and which have at least one neighboring pixel whose signal exceeds a threshold $t_2 < t_1$ are considered in the analysis for Cherenkov light. In this way, clusters of pixels whose signal exceeds random pedestal fluctuations are effectively selected. Typically the H.E.S.S. I analysis uses thresholds of $t_1 = 10$ pe and $t_2 = 5$ pe which is optimized for typical NSB values during observations. In the analysis presented later it will, however, be necessary to change the threshold definition.

	Image Amplitude	Center of Gravity	MSCL	MSCW
Preselection	> 80 pe	< 0.525 m	-	-
Postselection	-	-	-2 to $+2$	-2 to 0.9

Table 2.1: γ-ray event selection criteria for pre- and postselection used in this thesis if no other criteria are explicitly given. Preselection criteria apply to every telescope individually. The postselection is applied to averaged quantities derived from data obtained from telescopes which pass the preselection. The center of gravity criterion is understood as the maximal distance of the center of gravity of the camera image to the camera center. For a sketch of the geometry of the H.E.S.S. cameras see fig. 16 in appendix B.

2.6.2 Background Suppression and Event Reconstruction

In a first step after cleaning an image from NSB and electronic noise effects, the so called Hillas parameters (Hillas [1985]) are calculated as moments of the intensity distribution in the camera. In detail, the quantities that are used are

- the Hillas length L and width W as the second order moments of the signal intensity distribution in a camera (see f.i. Eidenmueller [2002] for a detailed discussion of the Hillas parameter calculation),
- the total image amplitude in a camera (equal to the zero order moment of the signal intensity distribution)
- and the distance of the center of gravity (first order moment of the signal intensity distribution of the image intensity to the camera edge.

In order to guarantee a good reconstructability of the image parameters, only camera images that have a reasonable total intensity after image cleaning (typically 80 pe for standard H.E.S.S. I selection criteria used in this thesis) and whose center of gravity is far away from the camera edges are considered in a preselection step. The typical data rates are reduced by this (standard H.E.S.S. I) preselection by a factor of $2-3$ from typically ~ 200 Hz to ~ 80 Hz. The usage of the stereoscopic trigger condition[14] makes the reconstruction of the direction of the triggering shower possible: The prolongations of the major axes of each reconstructed Hillas ellipse intersect in the direction of the shower. The shower direction can be reconstructed with a typical standard deviation of 0.1°.

Assuming that the images of a given event are due to a primary γ-ray, the γ-ray energy can be reconstructed by the comparison of the image intensity in a camera, the distance of the shower to the camera (obtained from the direction reconstruction) and the zenith and azimuth angle under which the event is observed from the camera with Monte Carlo

[14] The stereoscopic trigger condition is that a minimum of two telescopes is triggered in an event. Direction reconstruction is also possible with only one telescope. For a discussion of direction reconstruction algorithm in one telescope observations see f.i. Murach [2012].

simulations of γ-ray showers employing the same telescope configuration (telc) and a similar (equal up to the muon correction discussed later) optical configuration (optc). The energy that best fits the reconstructed event intensity in a camera, distance to the camera as well as zenith and azimuth angles can be attributed as the energy of the event under the assumption that it is triggered by a primary γ-ray. The event energy is to a first approximation proportional to the image intensity in a camera which in turn depends on the reflectivity of the telescope mirrors. The mirror reflectivity changes in time due to material aging. This is in a standard H.E.S.S. analysis accounted for by scaling the reconstructed event energy in a given camera by a correction factor that compensates for differences between the mirror reflectivity at time of data taking and the mirror reflectivity used for the Monte Carlo simulation. The correction factor is obtained by comparing the radius and image intensity of ring or partial ring images generated by the Cherenkov emission of high energy muons passing the telescope at small distance (see H.E.S.S. Col. [2006] for more information). If not explicitly stated differently, the 'muon correction' is used in this form in the analysis presented below. The energy of the event under the assumption that a primary γ-ray triggered the detected particle shower is the average of all triggered camera energy estimations. Obviously, the energy resolution depends on the number of triggered telescopes in a multi-telescope array. In cases where good energy resolution is crucial, typically only 4 telescope and possibly also 3 telescope trigger events are selected and the energy resolution compared to 2 telescope events is typically increased by a factor $\sqrt{4/2} \sim 1.4$ and $\sqrt{3/2} \sim 1.2$ respectively. The assumption that a given event is due to a γ-ray shower is, however, typically not fulfilled and a discrimination between γ-ray events and CR events is necessary for background suppression. As outlined above, differences in the shower development between CRs and γ-rays lead to different image shapes in the cameras. Hadronic showers tend to have more circular camera images than γ-ray showers that tend to be more elliptic leading to differences between hadronic shower images and γ-ray images in the Hillas width that can be used for γ/hadron separation. This method based on the Hillas parameters width W and length L has been described in Hillas [1985]. Subsequently (HEGRA Col. [1999]) it became clear that the scaled parameters, defined as

$$SCx_i = \frac{x_i - \langle x_i \rangle}{\sigma(x_i)},$$

are more effective to use. Here

- x_i can be the Hillas length L or Hillas width W and
- $\langle x_i \rangle$ and $\sigma(x_i)$ are the mean and root mean square of the Hillas parameter x_i as obtained for γ-rays at the reconstructed energy, distance to the telescope and zenith/azimuth pointing in Monte Carlo simulations of γ-ray showers and their camera images.

The usage of scaled parameters accounts for the correlation of the bare Hillas parameters with the shower distance and primary γ-ray energy (see Fegan [1997] for more information). The average of the scaled parameters obtained for every telescope gives

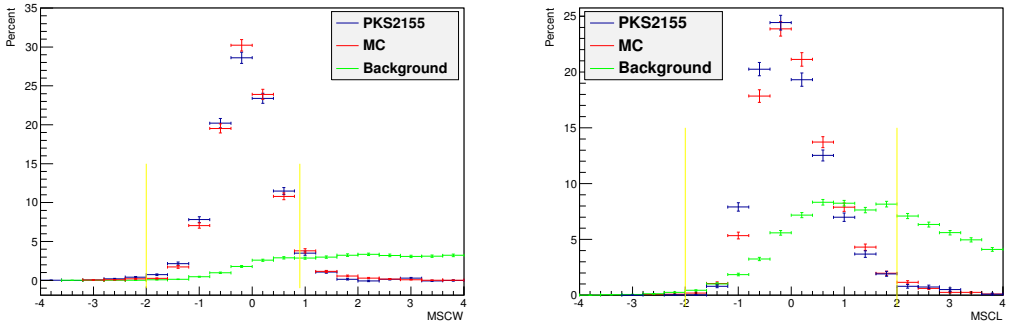

Figure 2.5: Mean scaled parameters (width left and length right) for γ-ray events in H.E.S.S. data (blue), MC simulated γ-ray events (red) and background events from H.E.S.S. data (green). The yellow vertical lines indicate the standard γ-ray cuts used in this work. The γ-ray events are from an almost clean γ-ray event dataset (PKS2155 flare, H.E.S.S. Col. [2011]). Nevertheless, the background shown in green datapoints is subtracted with the reflected background subtraction and the corresponding exposure normalization. The MC simulated γ-ray events are selected to be compatible in the zenith angle and event offset from camera center range with the data events.

two discriminants (mean scaled width and length) that are in practice used for the γ-hadron separation. Obviously, the absolute value of the mean scaled parameters of a γ-ray shower should not be much larger than one as this would suggest that the scaled parameters differ from the mean scaled parameter of a γ-ray by much more than the typical root mean square for a γ-ray. In practice, standard selection criteria on the mean scaled length (MSCL) from -2 to 2 and on the mean scaled width (MSCW) on -2 to 0.9 (see also fig. 2.5) are used to extract γ-ray events out of the H.E.S.S. data in the analysis presented below. This cut reduces the preselected event rate of $\mathcal{O}(80\text{Hz})$ to $2-5$ Hz. In total, the event pre- and postselection, i.e. the cuts on the image quality and mean scaled parameters, suppress the CR background by two orders of magnitude while having a typical γ-ray efficiency of $\sim 50\%$. Table 2.5 summarizes the event selection criteria that are applied later in the thesis. The remaining background after cuts is to a large fraction composed of electron CRs whose shower development largely mimics the shower development of γ-rays. This remaining CR background has to be accounted for by background subtraction methods. Note that the background suppression technique based on Hillas parameters is not the only known technique for a γ/hadron separation. The method has, however, the advantage to be simple, robust and in use for many years. Alternative methods (see Fiasson et al. [2010] for an overview) do not necessarily share those advantages and are therefore not used in the analysis presented later.

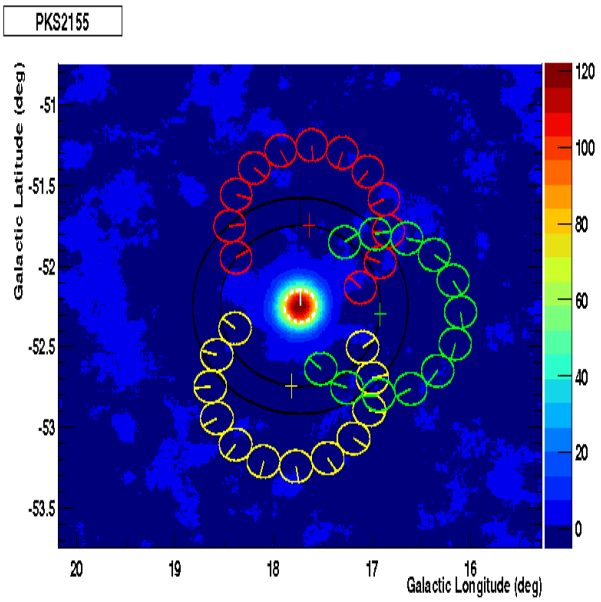

Figure 2.6: Significance skymap for the PKS 2155-304 region in galactic coordinates. Shown are the 0.1° signal region around the nominal position of PKS 2155-304 (white circle), ring background algorithm background region (black circles), the three pointing positions for the three runs (colored crosses) and reflected background algorithm background regions (circles with colors corresponding to the color representing the pointing position).

2.6.3 Standard Background Subtraction

There are multiple background subtraction methods for the analysis of H.E.S.S. data available. A short description of the two most frequently used algorithms for the analysis of point-like or moderately extended sources is given below (see also fig. 2.6). In general, both methods estimate the background in a signal region within the field of view by measuring the number of events within a suitable control region in the same field of view. Given the limited field of view of H.E.S.S. I, it is obvious that both methods fail for the investigation of very extended γ-ray emission regions.

- For the ring background method (see also fig. 2.6), the number of events in a ring around the source position is counted. The ring is placed symmetrically around the signal region which is typically a circle and the inner radius of the ring is chosen to be much larger than the signal region radius. The outer radius of the ring is typically determined by the request of having a factor of $1/\alpha = 7$ larger area in the ring than in the signal region to improve the statistical precision of the background estimation. When counting N_{ON} events in the signal region and N_{OFF} events within the ring around the signal region, the number of excess events in the signal region is given by

$$N_{\mathrm{Excess}} = N_{\mathrm{ON}} - \alpha N_{\mathrm{OFF}} \,. \tag{2.1}$$

  The statistical significance of the excess is calculated using Li and Ma [1983]. The ring background method gives typically a rough estimation of the excess in the signal region. It suffers in general from the problem that the acceptance of H.E.S.S. I to γ-ray events and to CRs after background suppression cuts is dependent on the radial distance to the camera center in a non-linear way. Therefore, the average acceptance to background and γ-rays within the background region ring is only to a first approximation the same as in the signal region which leads to a systematic error. Additionally, the ring background method is often not applicable in regions where many γ-ray source candidates are found as the ring around one signal region intersects possibly with another γ-ray source in this case. In general, the ring background method is, however, applied to obtain sky-maps, i.e. the spatial distribution of excess events or excess event significance within the telescope array field of view in sky-regions without too dense γ-ray source populations. The ring background method gives a good impression of the morphology of a possible γ-ray source. In contrast to the background subtraction technique discussed next (reflected region algorithm), the ring algorithm has also the ability to subtract the background in the center of the field of view.

- The reflected region background subtraction algorithm (see also fig. 2.6) assumes that the acceptance of H.E.S.S. to γ-rays and CRs after background suppression cuts is rotationally symmetric around the center of the array field of view. Background regions of the same shape as the signal region for a given source region are constructed on a ring around the observation position which must not be spatially

coincident with the source region. Exclusion regions where no background region must be placed are defined, typically at places where γ-ray sources are known. If it is possible to place $1/\alpha = N$ background regions within the field of view, the number of excess events is again given by formula 2.1. The reflected region background algorithm is typically used to obtain γ-ray source spectra, i.e. the energy dependence of the γ-ray flux. It is more precise than the ring background method if the knowledge of the source environment is sufficient to accurately place exclusion regions. However, for geometric reasons, the algorithm cannot be applied to signal regions that are spatially coincident with the pointing position making the method not well suited for the production of skymaps and for the search for new γ-ray sources.

The ring- and reflected region background subtraction algorithm are typically applied to H.E.S.S. data taken in the so called 'wobble' observation mode. This means that a signal region under investigation is not observed by pointing the telescope array into the signal region but by pointing the array with a 'wobble' offset from the region of interest. The offset makes the application of the reflected region background subtraction possible. Typically, the offset direction is also altered between different observations of a region of interest to average out systematic effects. More information on the mentioned background algorithms and also other methods (f.i. the 'template algorithm') that are occasionally used in the standard H.E.S.S. data analysis can be found in Berge et al. [2007].
It is obviously not possible to apply the discussed background subtraction methods to regions of interest with a size comparable to the H.E.S.S. field of view. The investigation and development of background subtraction methods suitable for this case is a main topic in this thesis and discussed later.

3 Weakly Interacting Massive Particles: Current Status

Weakly interacting massive particles (WIMPs) have been motivated as viable cold particle dark matter candidate in the introduction. This chapter gives a more detailed motivation from the particle physics point of view where the existence of WIMP like particles is discussed as prediction of theories beyond the standard model of particle physics. The focus is on the motivation for the extension of the standard model of particle physics with two classes of models (Supersymmetry and Kaluza-Klein theories) that have received much attention in the past and lead naturally to candidates for WIMPs. In the second part of the chapter, the current experimental status is summarized to enable a comparison and discussion of the results on WIMP searches in the Milky Way Halo with Cherenkov telescopes discussed later in this thesis.

3.1 Theory

Supersymmetric and Kaluza-Klein WIMPs are introduced and motivated as particle dark matter candidates. The foundation of supersymmetry is the extension of the physical three dimensional space by fermionic, i.e. anti-commuting, variables. The Kaluza-Klein theory and variants of it extend the space on the other hand by ordinary bosonic, i.e. commuting, space variables that are, however, compactified. Supersymmetry and Kaluza-Klein theory are not the only models that predict the existence of particle dark matter candidates. However, the mass and interaction scale is for supersymmetric and Kaluza-Klein models naturally on the weak scale without further fine-tuning. In case of supersymmetric models, the solution of the hierarchy problem predicts the mass scale of the dark matter particle to be on the weak scale (GeV-TeV). For Kaluza-Klein and related theories, the mass scale is tightly constrained to be on the weak scale by relic density arguments. Thus, in contrast to other models, it is naturally predicted that the particle dark matter candidate has a weak scale mass in both models. For the specific dark matter search method presented later to be sensitive, it is a necessary condition that the mass of the dark matter particle is on the weak scale. Therefore the mentioned two models are highlighted in this chapter.

3.1.1 Supersymmetric Dark Matter

The relativistic energy-momentum conservation, $E^2 - p^2c^2 = m^2c^4$, leads with the momentum $p = -i\hbar\partial_i$ and energy $E = i\hbar\partial_t$ to the Klein-Gordon equation[1]. The Klein-Gordon field, i.e. the field that fulfills the Klein-Gordon equation, is naturally (second) quantized by commutation relations (see f.i. Peskin and Schroeder [1995]). This means that the particles that correspond to the fields that propagate according to the Klein-Gordon equation are bosons.
Something interesting happens when the Klein-Gordon equation is linearized, i.e. an equation is derived that only depends on first order time and momentum. The problem of linearizing the Klein-Gordon equation is essentially equivalent to the problem of finding the square root of the squared Hamiltonian operator $H^2 = E^2 - p^2c^2$ which is not straight forward as it is an operator equation. The ansatz $H = \gamma^0 E + \vec{\gamma} \cdot \vec{p}c$ leads, however, to the desired result if $\gamma^\mu = (\gamma^0, \vec{\gamma})$ is a four vector which fulfills $\{\gamma_\mu, \gamma_\nu\} = 2g_{\mu\nu}$ for the anti-commutator , with the 'west coast metric' $g_{00} = 1$, $g_{ii} = -1$ for $i = 1...3$ and $g_{\mu\nu} = 0$ for off-diagonal elements. Interesting about the resulting Dirac equation is that its (second) quantization is not possible with commuting fields but only with anti-commuting fields (see f.i. Peskin and Schroeder [1995]). In other words the particles that correspond to the fields that propagate according to the Dirac equation are fermions. Obviously the power of the Hamiltonian involved in the establishment of a wave equation is connected to the spin statistics of the resulting fields after second quantization. The foundation of supersymmetry can be seen as the investigation of this dependence.
The 'square root' of the squared Hamiltonian $H^2 = E^2 - p^2c^2$ is $H = \gamma^\mu p_\mu$ with the energy-momentum vector $p_\mu = (E, \vec{p}c)$. Is it possible to investigate the meaning of finding the square root of some power of the Hamiltonian by finding the square root of the Hamiltonian itself? An ansatz would be $H = \gamma^\mu p_\mu = QQ^\dagger$ with

$$Q = A + B\gamma^\mu p_\mu \, .$$

and complex A, B. Evaluation of the ansatz gives

$$QQ^\dagger = AA^\dagger + BA^\dagger\gamma^\mu p_\mu + AB^\dagger\gamma^\mu p_\mu + BB^\dagger(\gamma^\mu p_\mu)^2 \, ,$$

i.e. $AA^\dagger = BB^\dagger = 0$ and $BA^\dagger = AB^\dagger = 1/2$. Obviously A and B cannot be ordinary complex numbers. However, the algebra can be represented by complex 'Grassman numbers'. Grassman numbers (θ) are essentially anti-commuting numbers, $\{\theta_1, \theta_2\} = 1$, from which follows immediately $\theta^2 = 0$. Let $B = \theta$ be a complex Grassman number, i.e. real and imaginary part of θ are Grassman numbers. Then $BB^\dagger = 0$ by definition. Additionally let

$$A = \frac{\partial}{\partial\theta^\dagger} := \partial_{\bar{\theta}} \, .$$

[1] The approach to supersymmetry presented in this chapter is to a large fraction inspired by a lecture on 'supersymmetry and grand unification' by Lennard Susskind in Stanford. For a different treatment that goes far beyond the material presented here, see Martin [2013].

Then $BA^\dagger = AB^\dagger = 1$ and $AA^\dagger = 0$ because no non-zero function can depend on a product of a complex Grassman number with its conjugate as this function would vanish by definition. After consideration of the normalization, the surprising result of the attempt to find the square root of a general relativistic Hamiltonian is thus

$$Q = \frac{1}{\sqrt{2}}(\partial_{\bar{\theta}} + \theta\gamma^\mu p_\mu)$$

with $QQ^\dagger = \gamma^\mu p_\mu = H$ and $\{Q, Q^\dagger\} = 2\gamma^\mu p_\mu$. The operator Q can be interpreted as mixing space-time dimension translation generators (p_μ) with additional Grassman (or fermionic) dimension translation generators in a very non-trivial way.
How does Q act on a field? Consider a massless fermion field ψ_a, where $a = 1, 2$ is the chirality component corresponding to a left- and right handed fermion. In general, Q can act differently on each ψ_a and thus gains an index Q_a. This operator acts on the Grassman space spanned by $(\theta_a, \bar{\theta_a}, \theta_b, \bar{\theta_b})$, i.e. on a four dimensional 'fermionic' space. The action of Q_a on ψ_a is given by

$$Q_a\psi_a = (\partial_{\bar{\theta_a}} + \theta_a\gamma^\mu p_\mu)\psi_a = \partial_{\bar{\theta_a}}\psi_a$$

where the Dirac equation for a massless fermion, i.e. $\gamma^\mu p_\mu = 0$ is used. The additional application of the Klein-Gordon operator ∂_μ^2 gives

$$\partial_\mu^2(Q_a\psi_a) = \partial_\mu^2(\partial_{\bar{\theta_a}}\psi_a)\,. \tag{3.1}$$

This is the Klein-Gordon operator applied to a derivative of the fermion field in the new fermionic space. For a massless bosonic field ϕ the action of Q_a is on the other hand

$$Q_a\phi = (\partial_{\bar{\theta_a}} + \theta_a\gamma^\mu p_\mu)\phi\,.$$

Additional application of the Dirac operator $\gamma^\mu p_\mu$ gives

$$\gamma^\mu p_\mu(Q_a\phi) = \gamma^\mu p_\mu(\partial_{\bar{\theta_a}}\phi)\,. \tag{3.2}$$

This is the Dirac operator applied to the derivative of the boson field in the new fermionic space.
In other words, if it were possible to extend the space-time dependence of the fields $\psi = \psi(x^\mu)$ and $\phi = \phi(x^\mu)$ by additional fermionic dimensions which are constructed such that $\partial_{\bar{\theta_a}}\phi = \psi_a$ is a massless fermion field and $\partial_{\bar{\theta_a}}\psi_a$ is a massless boson field the operators Q_a would essentially transform between massless fermionic and bosonic fields as equations 3.1 and 3.2 show. This is an interesting hint, however, it leads to conceptional problems. A small modification of this approach is, however, to combine fermionic and bosonic fields into one 'superfield' which is defined in 'superspace'. Consider for this a 'superspace' spanned by two complex Grassman variables θ_1 and θ_2. The most general (scalar) function in superspace is then

$$\Phi = \phi + \theta_1\bar{\psi} + \theta_2\bar{\chi} + \theta_1\theta_2 F_1 + \bar{\theta_1}\theta_2 F_2 \;+\; \text{h.c.}\,. \tag{3.3}$$

Here, the coefficients $\phi = \phi(x^\mu)$, $\bar{\psi} = \bar{\psi}(x^\mu)$ etc. are interpreted as ordinary fields defined on space-time which qualifies Φ as being a 'superfield'. The application of Q_a to Φ changes the number of Grassman variables for a given field coefficient by one unit (see Martin [2013], the proof is straightforward but lengthy). If one assigns bosonic fields to even number of Grassman variables and odd numbers of Grassman variables to fermionic fields respectively, the operator Q_a is essentially interchanging fermionic and bosonic components of the superfield. This is what is often symbolically written by $Q|\text{fermion} >= |\text{boson} >$ and vice versa.
An obvious phenomenological problem with the claim that nature is supersymmetric is that there is not a single fermion which has a bosonic partner particle of equal mass and vice versa. Nature can thus not be supersymmetric. On the other hand, it would have not only aesthetic but also conceptional advantages if nature were supersymmetric. The conceptional advantage is that supersymmetric theories give a simple solution to the 'hierarchy problem' which is in general the question why the weak scale, ~ 100 GeV, is so small in energy compared to the fundamental Planck scale, $\sim 10^{15}$ GeV. More specifically, the hierarchy problem is the question why the standard model Higgs particle mass (~ 125 GeV)[2] is so small although its Yukawa coupling to fermions ($\sim m_{\text{fermion}}$) should lead to large loop corrections for the squared Higgs mass, primarily from the top quark due to the large mass of the top quark (see Peskin and Schroeder [1995]). The supersymmetric explanation for this effect not to be existent is that the fermion loop corrections to the squared Higgs mass cancel with bosonic corrections stemming from the supersymmetric partner to a given fermion. This mechanism only works exactly if particles and their supersymmetric partners have exactly the same mass, as supersymmetry predicts (see Martin [2013]). However, there is some space in the argument as long as the loop corrections to the Higgs mass are only demanded to be small on the weak scale. In this case, supersymmetry can be an approximate symmetry on the weak scale, i.e. there exists a superpartner to every particle and the mass differences between particle and superparticle are on the weak scale, i.e. some 100 GeV to TeV. There are different studied mechanism of how supersymmetry can be broken to an approximate symmetry on the weak scale, in case of the scalar superpotential given above they are f.i. connected with the F_1 and F_2 terms in eq. 3.3 (see Martin [2013], Argurio [2011]). Instead of discussing the details of possible supersymmetry breaking mechanisms (of which a large number is discussed in literature), the phenomenological consequences are quickly summarized below. No particular literature is given below but the material is discussed in much more detail in Martin [2013] and Argurio [2011].
The particle content of the simplest supersymmetric extension of the standard model of particle physics, the Minimal Supersymmetric Standard Model or MSSM, is given by the standard model particles and their superpartners and an, in comparison to the standard model, more complicated Higgs sector. Instead of one superpartner for the one physical standard model Higgs particle, it is necessary to build a model based on at least two complex Higgs doublets in the particle sector to cancel anomalies as well as to generate

[2] Assuming that the recently discovered new boson (see CMS Col. [2012b] and ATLAS Col. [2012b]) is the standard model Higgs boson. Currently all indications point towards this direction.

a mass for up- as well as down type quarks in a way consistent with supersymmetry. After spontaneously breaking the enlarged Higgs sector with two complex SU(2) Higgs doublets (8 degrees of freedom), the physical particle content of the Higgs sector are 2 CP even neutral Higgs particles (H,h), one CP odd neutral Higgs particle (A) and two charged Higgs particles ($H^{\pm}$). All of the supersymmetric particles have spin zero, like the usual standard model Higgs particle. The masses of the different Higgs particles are connected at tree level with simple relations which in turn decreases the number of free parameters in the MSSM Higgs sector at tree level to two - usually denoted by $\tan\beta$ and one Higgs mass, usually m_A. In addition to the enlarged Higgs sector, a new symmetry is usually added to the MSSM to prevent the model from the prediction of the existence of certain unobserved particle reactions, f.i. the decay of the proton. The new continuous $U(1)$ symmetry is called R-symmetry. R-symmetry is in practice broken to an R-parity that assigns a multiplicative quantum number (± 1) to every particle ($+1$ by convention) and its supersymmetric partner (-1 by convention) and must be conserved. The conservation of the R-parity stabilizes as a side result also the lightest neutralino, i.e. the lightest of the four electrically neutral superpositions of the two neutral CP even Higgs particles as well as superpartners of the Z-boson (zino) and the photon (photino). The lightest neutralino is thus (if it is additionally equivalent to the lightest of all electrically neutral supersymmetric particles) stabilized against decays into standard model particles (by R-parity) as well as decay into other supersymmetric particles (by energy conservation). In other words, the lightest neutralino is a natural candidate for particle dark matter. The neutralino is by construction a spin 1/2 particle that is its own antiparticle, i.e. the neutralino is a Majorana fermion. The neutralino must be its own antiparticle because if the anti-neutralino were different from the neutralino, then the boson that corresponds to the anti-neutralino via the supersymmetry transformation would also be different from the boson that corresponds to the neutralino via the supersymmetry transformation which makes no sense. A practical problem is that the full parameter space of the MSSM has 124 dimensions which does not particularly simplify the experimental falsification. A reduction of the number of independent parameters of the MSSM is possible by postulating that the mass (m_0) of all scalar particles in the model is the same at some very high energy scale usually chosen to be the Planck scale of $\sim 10^{19}$ GeV. Similarly, the mass of all fermionic particles ($m_{1/2}$) is postulated to be the same at a high energy scale. In this constrained MSSM (cMSSM), the number of free parameters is reduced to five and experimental results are often given in the gaugino/sfermion or $m_{1/2}/m_0$ plane where the other three parameters which are two real numbers and one sign are fixed.

3.1.2 Kaluza-Klein (and related) Dark Matter

In 1921 Theodor Kaluza reported on the outcome of an attempt to express Einstein's field equations in 5 instead of 4 space-time coordinates (Kaluza [1921]). The additional dimension was assumed to be space-like and the result was that Einstein's field equations split into three parts. One part was equivalent to the usual Einstein equations in 4 dimensional space-time, one part was equivalent to the Maxwell equations and one part

described an additional new scalar field. This was obviously an interesting calculation. However, no observational support for the existence of a new scalar field could be found at that time and the existence of a fourth space like dimension seemed even more problematic. However, Oskar Klein found a method to prevent the new space-like dimension to be observable (Klein [1926]). The trick was to 'compactify' the fourth space dimension such that moving within this dimension is equivalent to moving on a circle (therefore 'compact') with very small radius (therefore unobservable).
The resulting theory is a model for a unification of gravitation and electromagnetism that predicts the existence of a new scalar field. The investigation of the decay and composition of atomic nuclei that started to become more systematically performed around the same time led, however, eventually to the introduction of new forces. A simple unification of all known forces in a Kaluza-Klein model seemed not to be easy and the very successful advent of quantum field theoretical methods to describe the new forces and especially electromagnetism gave further reason to move large parts of the main research engagement away from extensions of space-time. Left from the original ideas from Kaluza and Klein was the possible existence of one or more small and compactified space - or universal extra - dimensions which is still debated (see f.i. Bringmann [2005]). A putative simple consequence of the existence of universal extra dimensions (UED) can be derived for bosons when the Klein-Gordon equation is reformulated for UEDs. For one UED, y, compactified to a radius R, the Klein-Gordon equation for a boson field $\phi(x_\mu, y)$ reads

$$\left(\partial_\mu^2 + \frac{1}{R^2}\partial_y^2 - m^2\right)\phi(x_\mu, y) = 0\,.$$

The compactification of the UED enables the boson field to be Fourier decomposed into $\phi(x_\mu, y) = \phi(x_\mu, R\theta) = \sum_k \phi_k(x_\mu)\exp(ik\theta)$. This in turn lets each mode of the Fourier decomposition satisfy the Klein-Gordon equation with a replaced mass of

$$m(k) = \sqrt{m^2 + \left(\frac{k}{R}\right)^2}\,.$$

This means that the masses of the bosons increase with the UED excitation state k. The equivalent argument for fermions is more subtle due to the σ-matrices in the Dirac equation which need to be generalized. However, consistent constructions for fermions exist (see Hooper and Profumo [2007] and references therein). If all usual particles in the standard model correspond to the UED ground state ($k = 0$), the model predicts the existence of heavier excitation modes of every standard model particle. Additionally, the 'Kaluza-Klein parity' $(-1)^k$ must be a conserved quantity (see Hooper and Profumo [2007]) in a theory with UED. The conservation of Kaluza-Klein parity is an additional constraint that avoids the prediction of the existence of the additional scalar field that arises when the Einstein equations are formulated in five dimensional space time (see Bringmann [2005]). Kaluza-Klein parity conservation ensures that a single particle in an excited state (f.i. $k = 1$) is forbidden to move into the Kaluza-Klein ground state ($k = 0$) due to the differing Kaluza-Klein parity. However, the annihilation of two particles in the same Kaluza-Klein state into the ground state is possible. The $k = 1$

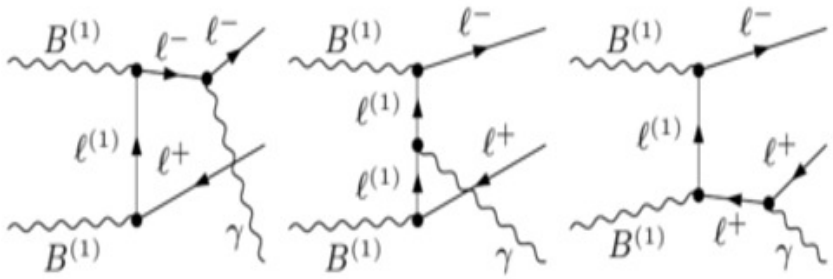

Figure 3.1: $B^{(1)}$ annihilation mediated by first Kaluza Klein excited leptons generates light standard model leptons ($e^{\pm}$, $\mu^{\pm}$) with final state (left and right panel) and virtual internal (middle panel) bremsstrahlung. This dominates the continuous annihilation photon spectrum at the highest energies, $E_\gamma \sim m_{B^{(1)}}$. See Bergstrom et al. [2005] from which also the figure is taken from.

Kaluza-Klein excitation of the standard model particles is therefore predicted to be a stable particle with the possibility to annihilate into the ground state. The lightest first Kaluza-Klein excitation of all electrically neutral standard model particles is therefore an interesting candidate for particle dark matter. A natural candidate for the lightest first Kaluza-Klein excitation is obviously the first excitation of the standard model photon which has the predicted mass $1/R$ in case of one UED. The excitation of the photon into the Kaluza-Klein mode changes, however, the electroweak mixing angle such that the first Kaluza-Klein excitation of the standard model photon is essentially the first excitation of the hypercharge boson, $B^{(1)}$ (see Hooper and Profumo [2007] or Bringmann [2005]). Note that the spin statistics of a particle is not changed in transitions between different Kaluza-Klein states, i.e. the WIMP is expected to be a boson for Kaluza-Klein models which stands in contrast to supersymmetric models where the WIMP is expected to be a (Majorana) fermion. It is interesting to note that this particle dark matter candidate can satisfy the dark matter relic density constraint by WMAP CMB measurements only in a very narrow mass range around 0.9 TeV to 1.2 TeV (Servant and Tait [2003]). This results from the velocity averaged $B^{(1)}$ annihilation cross section to be inversely proportional to $m^2_{B^{(1)}}$ (Hooper and Profumo [2007]) which is essentially (via its dependence on the compactification radius) the only free parameter of the model. Heavy (light) $B^{(1)}$ thus lead to an under (over) production of dark matter in the early universe and the size of the allowed range is essentially determined by the WMAP error-band of the dark matter abundance measurement. In contrast, supersymmetric dark matter candidates are scattered on much larger allowed mass ranges because the supersymmetric interactions depend on many additional parameters. As will be discussed later, the allowed $B^{(1)}$ mass range agrees with the mass range where Cherenkov telescopes have the highest sensitivity for WIMP annihilation searches. The annihilation branching ratios for two $B^{(1)}$ are different from the annihilation of supersymmetric neutralino

WIMP dark matter. The dominant annihilation products are leptons with $\sim 20\%$ per family followed by up-type quarks with $\sim 10\%$ per family (see Hooper and Profumo [2007]). The direct annihilation products lead among other standard model particles to the production of photons or, for $m_{B^{(1)}}$ being large enough, γ-rays. Compared to the scale given by the $B^{(1)}$ mass, the highest energy photons are generated by either virtual or final state bremsstrahlung (see also fig. 3.1). The semi-hadronic decays of τ leptons dominate intermediate photon energies and only low energy photons are dominantly created in the fragmentation of the quark final states (see Bergstrom et al. [2005]). Supersymmetric (Majorana) neutralino WIMP γ-ray spectra are in contrast typically dominated by quark fragmentation spectra for all energies as the annihilation into light leptons is helicity suppressed which leads in practice to τ leptons as the only open leptonic channel (see Bertone et al. [2005] and Hooper and Profumo [2007]).

3.2 Experimental Situation

The experimental status on supersymmetric and Kaluza-Klein models as extensions of the standard model of particle physics is on one hand very simple, on the other hand very complicated. Very simple, because there is yet no convincing, i.e. reproduced and unique (in the sense of cannot be explained by other effects), hint for either of the two models to be realized in nature. The status is on the other hand very complicated because many conceptually different experimental approaches are used to search for effects predicted by models beyond the standard model of particle physics. Some experiments indeed find significant effects that are expected from extensions of the standard model but either they are not unique, i.e. can also be explained by other effects as f.i. the positron excess (PAMELA Col. [2009], Fermi Col. [2012]), or other experiments rule out the observed effects (see f.i. the 'DAMA annual modulation effect', Bernabei et al. [2004]). In some cases effects are even both, not unique and ruled out as for instance the 'EGRET excess' (see Boer et al. [2006]) or the 'ATIC peak' (see Chang et al. [2008]).
The situation is even more complicated because even if a specific effect beyond the standard model of particle physics were observed, it would be in general difficult to say which particular model is validated or outruled. Consider for example the case that a significant excess is observed by a Cherenkov telescope observing towards a direction where a high density of dark matter is suspected in the line of sight and the excess cannot be explained by usual astrophysical γ-ray emission. Then, in general at least the two models introduced in the theory section of this chapter, supersymmetry and Kaluza-Klein like extensions, are plausible candidates to explain this excess in a dark matter annihilation interpretation. The differences in the predicted γ-ray spectra for Kaluza-Klein dark matter on the one hand and supersymmetric dark matter on the other hand are in general too small to make a resilient statement on the nature of the dark matter particle without a very precise measurement of the γ-ray spectrum. Precise measurements of γ-ray spectra are, however, only possible with highly significant effects which are unlikely to be obtained in a first analysis.
Very similar to the situation for Cherenkov telescopes is also the situation with other ex-

perimental techniques, in particular as concerns the discrimination between Kaluza-Klein and supersymmetric models. In general there are three large branches of experimental approaches to test for physics beyond the standard model and for Kaluza-Klein and supersymmetric particles. 'Direct' and 'indirect' searches are experiments that search for interactions of particle dark matter. 'Direct searches' operate detectors which 'directly' detect the interaction of a dark matter particle with detector material. 'Indirect searches' aim at the detection of standard model messenger particles that are produced in interactions of particle dark matter in space. Indirect and direct searches are both equally important and in fact complementary as they probe different parameters with respect to the dark matter particle properties as well as the dark matter density. Accelerator searches on the other hand could directly produce dark matter particles but also other new particles that are not part of the standard model of particle physics. In general this allows to obtain a more complete picture of physics beyond the standard model but has the drawback that even if physics beyond the standard model is discovered and a dark matter particle candidate is found, it needs to be confirmed that this candidate is indeed responsible for the astrophysical observations that initially led to the introduction of the dark matter paradigm. This can not be accomplished with accelerator experiments and thus all three methods are important and complementary for the solution of the dark matter problem.
A general discussion of the three approaches to search for physics beyond the standard model and particle dark matter in particular is given below without claim for completeness but with a focus on the general technical realization and on key results.

3.2.1 Direct Searches

As stated above, 'direct search' experiments probe the 'direct' interaction of dark matter particles with detector material. Astrophysical considerations (f.i. the measurement of the number of tracer stars as a function of the distance perpendicular to the galactic disc at the position of the earth, Weber and de Boer [2010]) give an astrophysical motivation for the presence of dark matter at the position of the earth with a density of $\sim 0.3\,\mathrm{GeV/cm^3}$. Figure 3.2 show examples of Feynman diagrams for the interaction of Kaluza-Klein and supersymmetric particle dark matter candidates with matter. Consider a dark matter particle interacting f.i. via the diagrams in fig. 3.2 with quarks in a detector on earth. The dark matter particle as well as the interacting quark are both elementary particles, the interaction is thus elastic and energy is transferred between the two particles. In the rest frame of the detector, the atomic nucleus in which the quark is embedded will thus in general receive energy from the collision. The experimental task of direct particle dark matter search experiments is to measure this energy transfer and discriminate it from background events.
Background events can be caused by all sorts of standard model particles that enter the detector and interact with its material. For instance cosmic rays and particles produced in the interaction of cosmic rays with the earth atmosphere (for example muons) are candidates for particles that generate background events. Direct dark matter search experiments have to install their detectors in underground laboratories (f.i. the XENON

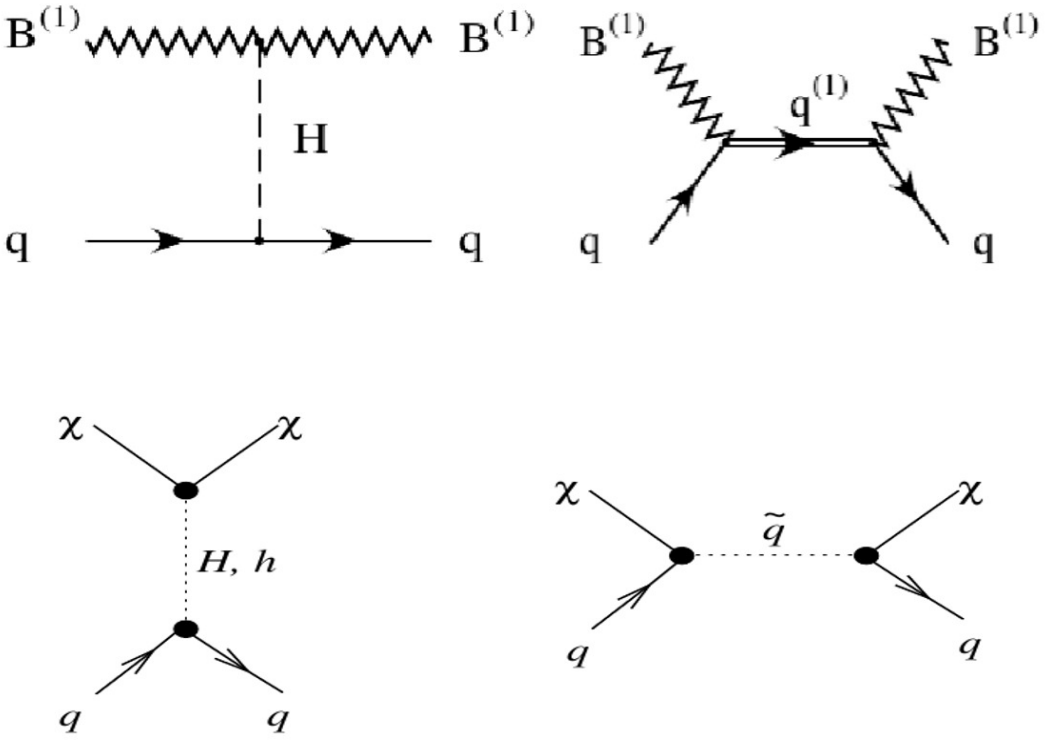

Figure 3.2: Example tree level Feynman diagrams relevant for the direct detection of Kaluza-Klein (upper two plots) and supersymmetric (lower two plots) particle dark matter. The upper two plots (taken from Servant and Tait [2002]) show the t-channel Higgs exchange and the s-channel exchange of a first KK quark mode for the interaction of the first KK mode of the hypercharge boson $B^{(1)}$ with a quark in a detector material. The lower two plots (taken from Jungmann et al. [1996]) show the t-channel exchange of the two CP even Higgs particles of the MSSM and the s-channel squark exchange of a neutralino interacting with a quark in a detector material. The diagrams indicate the phenomenological similarity of Kaluza-Klein and supersymmetric dark matter particles.

experiment is operated in the Gran Sasso massive with ~ 3.5 km water equivalent shielding) to suppress cosmic ray background. Also natural radioactivity in the environment or the detector itself generates particles that lead to background events. Electrons and γ-rays from radioactive decays in the vicinity of the detector or the detector material itself interact typically with the electrons of the material, in contrast to particle dark matter which interacts with the nucleus. It is thus desired to discriminate between electronic and nuclei interactions in the detector. Protons, neutrons and α-particles generated in radioactive decays interact with the nuclei of the detector material and have to be suppressed by ultra-clean materials, shielding and active vetos on charged particles. The main background is in fact currently due to neutrons as they are electrically uncharged and mimic the behavior of particle dark matter interactions. It is evident that a very detailed understanding of the background is needed to perform a successful direct search for particle dark matter.
Currently there are $\mathcal{O}(20)$ direct detection experiments running. The suppression of background events is in all cases technically highly non-trivial and the concrete methods depend on the experimental approach, i.e. the detector medium and the detection principle. Most of the currently operating experiments aim to measure the nuclear recoil in a WIMP-quark interaction where typically ~ 1 keV energy is transferred for a ~ 10 GeV WIMP mass by measuring one or two of the following three quantities.

- When a WIMP scatters on a nucleus which is part of a solid state detector (typically germanium or silicon), phonons are excited and in turn the temperature of the detector increases. The increase in temperature can be measured with typically highly advanced techniques (f.i. the measurement of electrical resistance changes of either a highly doped semiconductor whose resistance-temperature curve is very steep or the operation of a superconductor on the turning point between super- and normal conducting state). It is obvious that the detector must be cooled to nearly absolute zero temperature and this temperature must be kept stable over a science run, i.e. typically many months.

- In certain liquid (f.i. xenon) and solid state (f.i. NaI doped with thalium) materials, a nucleus can induce the emission of scintillation light if it is hit by a WIMP and thus recoiling (see Chepel and Araujo [2012]). The principle is also used for the detection of high energy neutrons in nuclear physics. The scintillation light can be measured by optical detectors (f.i. photomultipliers). It is not necessary to cool down the detector for the use of this effect and thus large detectors can be realized.

- The ~ 1 keV recoil of a nucleus hit by a WIMP can induce a band gap transition of valence electrons in semiconductors, typically germanium (band gap ~ 0.7 eV) or silicon (band gap ~ 1.2 eV). Free electrons that can be generated by recoiling nuclei after a WIMP collision are employed in liquid noble gas (typically xenon or argon) detectors, see Chepel and Araujo [2012]. Either the charges in the conduction band or the free electrons can be electronically detected.

As stated, current direct detection experiments use typically two distinct detection principles in coincidence to increase the discrimination power of signal from background.

The quantity that is directly measured by direct detection experiments is the number of recorded events or the event rate respectively. The event rate is supposed to contain a fraction of signal events from WIMP interactions among background events. In practice, the WIMP-nucleon scattering cross section is either inferred from a significant signal measurement or an upper limit on the cross section is derived. A distinction is made between the 'spin dependent' and the 'spin independent' WIMP-nucleon cross section. Consider the Feynman diagrams in fig. 3.2. The exchange of a scalar Higgs boson between a WIMP candidate and a quark will lead to a spin independent or scalar interaction. On the other hand, the exchange of fermions depends on the relative spin of WIMP and quark and leads in general to a spin independent (scalar and possibly vector) and a spin dependent (axial vector) contribution. Note that vector interactions are helicity suppressed for Majorana fermions such as supersymmetric neutralino WIMPs but not for Kaluza-Klein $B^{(1)}$. For more information on the direct detection cross section see Servant and Tait [2002] and Jungmann et al. [1996] or Bertone et al. [2005] for Kaluza-Klein and supersymmetric WIMPs respectively. The spin independent WIMP scattering cross section is roughly proportional to the number of nucleons squared but the spin dependent cross section is only proportional to the total nucleon spin (see Jungmann et al. [1996]). Experiments are therefore typically much more sensitive to the spin independent WIMP scattering cross section (only a material with large atomic number has to be chosen) than to the spin dependent cross section (nuclear spins tend to be small due to spin pairing between nucleons).
To derive a statement on the WIMP-nucleon scattering cross section based on the number of detected signal events in a direct detection experiment it is necessary to input among information on the scattering kinematics and nuclear form factors (which are measured) also astrophysical parameters. Most important are the local dark matter density and the velocity distribution of WIMPs in the detector. Both parameters are subject to intensive discussions. The local dark matter density is in general assumed to be $\sim 0.3\,\mathrm{GeV/cm^3}$, however, the error on this quantity is sometimes argued to be $\sim 10\%$ (Weber and de Boer [2010]) or $\sim 1\%$ (Catena and Ullio [2010]). The WIMP velocity distribution is (usually) taken to be a Maxwell-Boltzmann distribution, $f(v) \sim 1/v_{\mathrm{RMS}}^3 \exp(-(v-v_0)^2/(2v_{\mathrm{RMS}}^2))$, where $v_0 \sim 220\,\mathrm{km/s}$ is the velocity of the earth moving around the galactic center and $v_{\mathrm{RMS}} = v_0/\sqrt{\beta}$ where $\beta \sim 1-2$ depends on the WIMP density distribution in the galactic halo via the Jeans equation (see Peter [2011]). The underlying assumption of a Maxwell-Boltzmann velocity distribution is strictly speaking only valid for a collisionless ideal gas with constant density and pressure and thus already intrinsically assumes a specific, i.e. constant, WIMP density distribution. Computer simulations predict, however, that the WIMP density is increasing towards the center of galaxies and thus deviations from a Maxwell-Boltzmann distributions for the WIMP velocity. The influence of this effect can be significant (factor $0.2-6$, Baushev [2011]) but depends on the detector properties, see also Peter [2011], Kuhlen et al. [2010]. Figure 3.3 summarizes the current experimental status of direct detection searches with respect to the spin independent WIMP-nucleon scattering cross section. The signal detections by CoGeNT and DAMA are in obvious conflict with the upper limits of most notably XENON100. The measured DAMA signal is compatible to two different regions in the parameter

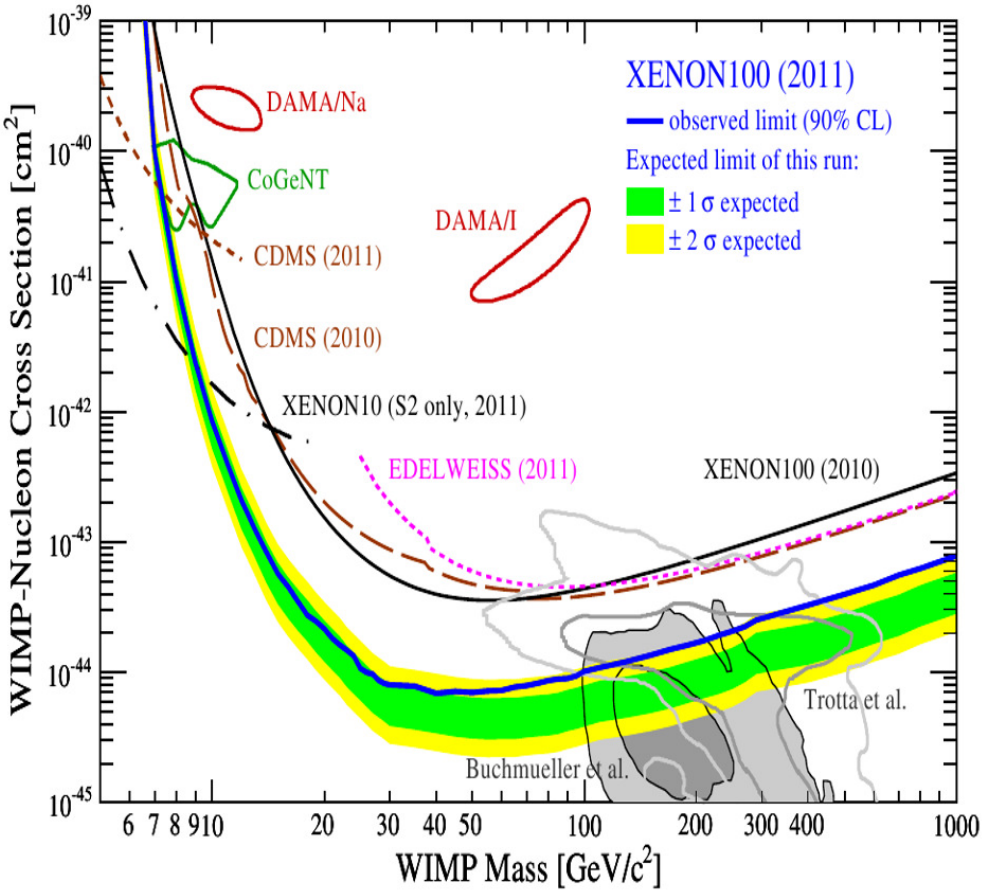

Figure 3.3: Current status of spin independent WIMP-nucleon cross section measurements as a function of the WIMP mass. The results of different experiments are shown (colored) together with predictions of supersymmetric models (grey). Closed colored lines indicate significant detections (CoGeNT and DAMA). The figure is taken from Aprile et al. [2011]. Note that the plot does not contain the hint for a positive signal ($\sim 3\sigma$) reported from CDMS-II (CDMS Col. [2013]) for a WIMP mass of ~ 8.6 GeV with a spin independent cross section of $\sim 1.9 \cdot 10^{-41}$ cm^2.

space plotted in fig. 3.3. One of the allowed regions is in the vicinity to a region allowed by the CoGeNT detection. Especially the DAMA signal which is the annual modulation of the WIMP-nucleon scattering rate while the earth is moving around the sun is highly significant (overall $\sim 9\sigma$ detected over 7 annual cycles, Bernabei et al. [2010]) and carefully checked for systematics (Bernabei et al. [2000]). A theoretical explanation of this effect and the non detection in other experiments is challenging, mainly 'inelastic' dark matter is currently discussed (see f.i. Smith and Weiner [2001]). The inelastic dark matter scenario assumes the WIMP to have intrinsic degrees of freedom (f.i. through a higher Kaluza-Klein state or mixed supersymmetric states) and absorb energy if the interaction momentum transfer is large enough. In this way the XENON100 measurement (typically sensitive to ~ 40 keV recoil energies) and the DAMA measurement (typically sensitive to ~ 3 keV recoils) can be made compatible. However, much more detailed investigations and independent cross checks are necessary to reach conclusive statements in this issue. Not shown in fig. 3.3 are predictions of spin independent cross sections for Kaluza-Klein WIMPs which are typically $\sim 10^{-46}\,\mathrm{cm}^2$ (see Servant and Tait [2002]). The figure shows that direct detection experiments and especially XENON100 are starting to constrain the supersymmetric WIMP parameter space but do not yet reach the necessary sensitivity to constrain Kaluza-Klein models.

3.2.2 Accelerator Searches

Production of Dark Matter Particles

The CMS and ATLAS experiments at the LHC (Large Hadron Collider) in Geneva have collected data from which the currently most constraining collider limits on the production of dark matter particles can be derived. The LHC is a ring accelerator with two equal energy proton beams which move in opposite directions. At certain points in the collider, the two proton beams are colliding in the center of multi purpose particle detectors. In practice not two protons but two constituents (partons) of the proton, one out of each colliding proton pair, are interacting due to the large collision energies (design center of mass energy 14 TeV). Partons can be quarks of any flavor (but with a dominance of up over down quarks for a proton), antiquarks of any flavor (always less abundant than quarks in a proton) and gluons (large abundance especially at low momentum transfer but less at high momentum transfer due to the 'asymptotic freedom' (see Peskin and Schroeder [1995]) of the QCD). The method employed to search for signatures of produced dark matter particles is to search for quark-antiquark collisions with large 'missing', i.e. not detected, energy in the final state from undetected dark matter particles and a single energetic jet or photon from initial state gluon/photon radiation (CMS Col. [2012a], ATLAS Col. [2012a]). The number of detected events with this signature is measured and compared to the number of expected background events, f.i. from quark-antiquark annihilation into neutrinos via Z-boson exchange with initial state radiation. On the other hand, the number of expected signal events can be calculated using an effective field theory approach under the assumption that the particle that mediates the annihilation of quark and antiquark to a pair of dark matter particles

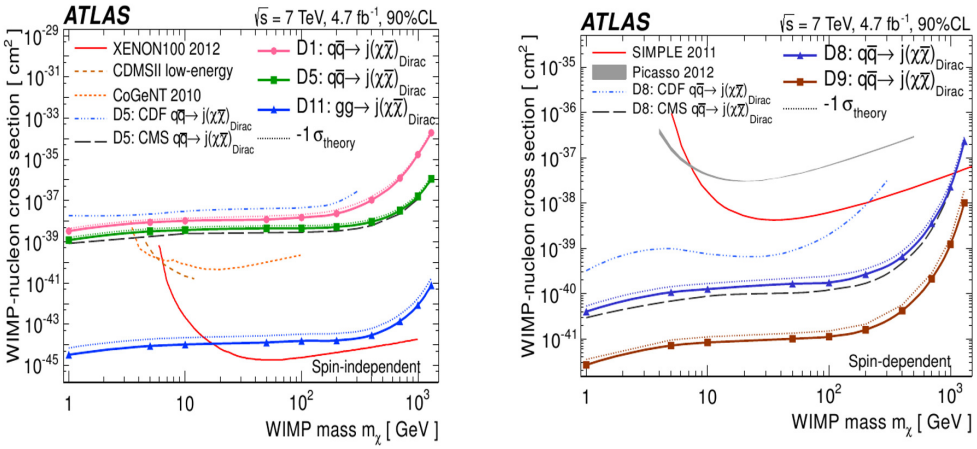

Figure 3.4: Spin independent (left panel) and spin dependent (right panel) WIMP-nucleon scattering cross section upper limits derived from a negative search result for the production of WIMP pairs at the LHC from ATLAS, CMS and CDF at Fermilab. Important are the lines corresponding to D1 (scalar) and possibly D5 which holds only for Dirac fermions but not for Majorana fermions (f.i. supersymmetric neutralinos) in the left panel. In the right panel the lines corresponding to D8 (axial vector) are of primary interest. For comparison the upper limit on the spin dependent WIMP scattering cross section derived from direct detection experiments (XENON100, CDMS, PICASSO, SIMPLE) is plotted. The plot is taken from ATLAS Col. [2012a].

is much heavier than the initial state quarks and final state dark matter particles. The most important effective field theory Lagrangian terms that are investigated under the assumption of heavy mediator particles (mass scale M) are a scalar interaction (D1 in the following), a vector interaction (D5 in the following) and an axial-vector interaction (D8 in the following), for the exact definitions see ATLAS Col. [2012a]. The effective interaction terms can be translated to an effective spin independent (D1 and D5) or spin dependent (D8) cross section which can be compared to the corresponding quantities measured in direct detection experiments (see Goodman et al. [2010] for the exact translation). Figure 3.4 shows the result of the corresponding ATLAS search (ATLAS Col. [2012a]) based on 4.7fb^{-1} data recorded at a center of mass energy of $\sqrt{s} = 7$ TeV. Equivalent results have been obtained from a CMS analysis (CMS Col. [2012a]). It is seen that the sensitivity of ATLAS to the spin independent cross section is currently worse compared to XENON100 for DM masses larger than ~ 10 GeV. For smaller masses, the sensitivity of XENON100 is worse because such small DM masses produce nuclear recoils which are typically below the XENON100 detection threshold. In comparison with fig. 3.3 it is also obvious that the LHC sensitivity after a currently performed upgrade resulting in an increased center of mass energy and luminosity should be able to test the

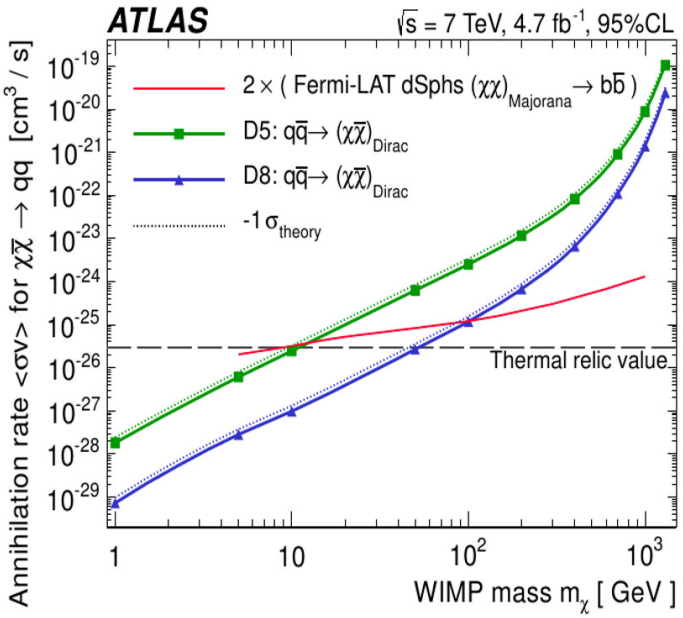

Figure 3.5: Velocity averaged annihilation cross section upper limit derived from LHC data by the ATLAS collaboration. The line corresponding to D5 (D8) holds for vector (axial vector) interactions between WIMPs and quarks. For comparison an upper limit derived from data recorded by the Fermi-LAT experiment and the canonical expectation value for a thermal relic WIMP (see eq. 1.4) is shown. The plot is taken from ATLAS Col. [2012a].

DAMA and CoGeNT signal detections which will be very interesting (an improvement of 2 orders of magnitude in sensitivity to the spin independent cross section is within the discovery reach of a similar analysis conducted at $\sqrt{s} = 14$ TeV, see Rajaraman et al. [2011]). It will be very challenging for currently debated WIMP models (f.i. inelastic dark matter, see above) that explain the positive DAMA/CoGeNT signal measurements and the constraining upper limits from XENON100 at the same time if the LHC will not detect a signal in the preferred DAMA and CoGeNT spin independent cross section and WIMP mass regions. Figure 3.4 also shows that the sensitivity of collider searches to spin dependent WIMP interactions is by far superior to the sensitivity of current direct detection experiments.

Figure 3.5 shows a translation of the negative search result obtained from LHC data to the velocity averaged annihilation cross section defined in eq. 1.4. The figure compares the obtained limit on $\langle \sigma v \rangle$ with a limit derived in an indirect search with the Fermi-LAT detector that is described later in this text. Fermi-LAT performed a search for a Majo-

rana WIMP annihilation in outer space where always two WIMPs annihilate dominantly into bottom quarks. The assumptions of the Fermi-LAT search fit well to a search for a supersymmetric neutralino WIMP which is by construction a Majorana particle, i.e. its own antiparticle. The Fermi-LAT result can be modified to the corresponding result for a Dirac fermion by a multiplication with 2 which is already done in fig. 3.5. This factor two accounts for the fact that a given Dirac WIMP in space cannot annihilate with every other WIMP but on average only with every 2nd WIMP and thus the expected annihilation rate is by a factor of 2 smaller than for Majorana WIMPs which translates approximately to a factor of 2 weaker upper limit on $\langle \sigma v \rangle$. To read fig. 3.5 for a supersymmetric WIMP, the line corresponding to D5 is vanishing (Majorana fermions have helicity suppressed vector coupling), the line corresponding to D8 is essentially unaltered (see also Fox et al. [2012]) and the line corresponding to the Fermi-LAT upper limit has to be divided by two. The Fermi-LAT sensitivity to neutralino WIMP is then larger above $\sim$ 60 GeV than the current LHC sensitivity. Below $\sim$ 60 GeV the LHC sensitivity is larger, respectively. It can, however, be expected that the LHC sensitivity will improve significantly after the currently performed energy and luminosity upgrade.

Other Collider Searches

Besides the direct production of WIMP particles in collider experiments, there are other methods to possibly gain hints for the existence and nature of WIMP dark matter. The two most important strategies are precision measurements of quantities that are tightly constrained by standard model calculations (f.i. branching ratios or magnetic moments of electrons and muons) and the search for particles whose existence is not predicted by the standard model of particle physics (f.i. an enlarged Higgs sector with more than one Higgs boson as predicted by supersymmetric extensions of the standard model). Deviations of measured observables from standard model predictions hint obviously towards the interaction not being adequately described by the standard model. In turn, models beyond the standard model of particle physics with enlarged parameter space and particle content are candidates to explain the deviations of observables from standard model predictions. A strong hint for the existence of dark matter particles would be found if a certain candidate model for physics beyond the standard model can be found that is compatible with the measurements and the model does predict the existence of dark matter particles. An incomplete list of three examples of observables that have recently gained particular interest is

- the $h \to \gamma\gamma$ branching fraction for the decay of the Higgs boson (assumed to be the recently discovered boson with $\sim$ 125 GeV mass, CMS Col. [2012b]). Currently ATLAS observes a branching fraction relative to the standard model prediction of $1.65 \pm 0.24_{\text{stat}} \pm 0.21_{\text{sys}}$ (presented at Moriond 2013 conference) which is within systematical and statistical errors compatible with the standard model prediction at the $\sim 2\sigma$ level and CMS measures a result compatible with the standard model prediction within 1σ (presented at Moriond 2013 conference).

- The decay of the 'strange B meson', $B_s = (\bar{b}s)$ consisting of a bottom antiquark and a strange quark into two muons ($B_s \rightarrow \mu^+\mu^-$) is almost forbidden in the standard model due to helicity suppression. Hints for the presence of the decay have been recently observed (at $\sim 3.5\sigma$) and deviations from the standard model prediction have been searched for with LHCb without success (see LHCb Col. [2013]). Specific regions in the MSSM parameter space were in turn ruled out but 'substantial room for the SUSY parameters' is left (see Arbey et al. [2013]). The precision measurement of B meson branching fractions is of particular interest for the search for physics beyond the standard model because B mesons have typically a mass that is large enough to open decays into many channels that are suppressed by the standard model but at the same time the mass is small enough to enable production of B mesons at current collider energies.

- The magnetic moment of the muon has been measured to be incompatible with the standard model prediction at the level of $\sim 3\sigma$ (see f.i. Jegerlehner and Nyffler [2009]). The measured discrepancy is not yet significant enough to allow a resilient conclusion on its nature but is discussed as one of the most interesting hints for physics beyond the standard model.

3.2.3 Indirect Searches

Indirect searches for particle dark matter use in general standard model messenger particles that are expected to be produced in the annihilation or decay of dark matter particles in outer space. The messenger particles can be detected with earth based or satellite detectors. It is obvious that an indirect search for particle dark matter has always the problem of a discrimination between standard model particles that are produced in dark matter interactions and standard model particles that are of usual astrophysical nature, f.i. cosmic rays. There are multiple experimental approaches in different energy regimes with different standard model messenger particles used for indirect dark matter searches. One possibility to classify the different approaches is to discriminate first between the employment of neutral and electrically charged standard model messenger particles. Indirect dark matter searches with electrically charged standard model messenger particles aim typically at the measurement of anti-particle fluxes (positrons, anti-protons, anti-deuterium etc.) because the astrophysical background for particle fluxes is obviously larger than for anti-particle fluxes which primarily result from cosmic ray interactions in the interstellar medium and are thus a second order effect. One notable exception for the general tendency to search for anti-particles is the precise measurement of the electron spectrum and the comparison of the result with model predictions. The uncertainty in the model predictions is, however, typically large and deviations of the measured spectrum cannot clearly be associated with new physics. Another approach is the measurement of anisotropies in the electron spectrum which is currently performed with increasing intensity. However, even if anisotropies in the electron flux were detected, it would be challenging to discriminate between a modeling with nearby pulsars on the one hand and dark matter interactions in the local dark matter halo on the other hand. The

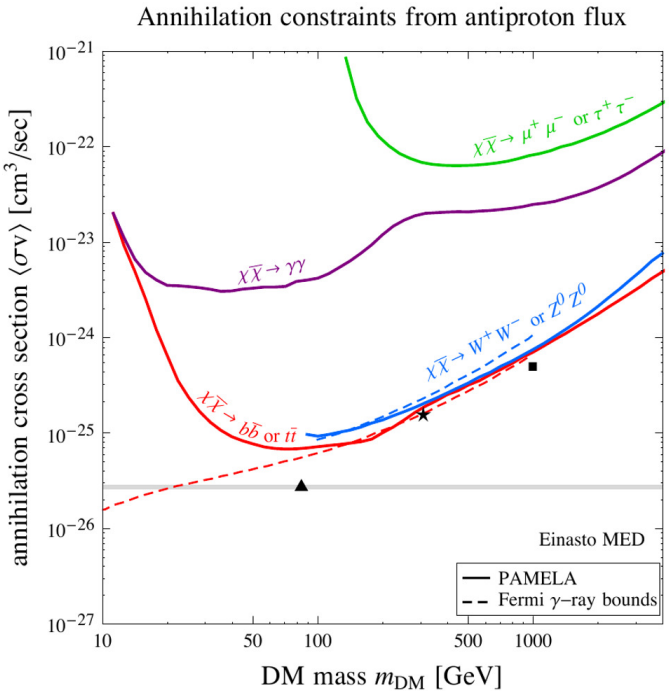

Figure 3.6: Upper limits on the velocity averaged annihilation cross section as a function of the dark matter particle mass as derived from the anti-proton flux measurement from PAMELA (solid lines for different dark matter annihilation channels). The dotted lines are obtained from Fermi/LAT γ-ray measurements. The plot is taken from Cirelli and Giesen [2013].

following list gives an incomplete overview of recent key results obtained from indirect dark matter searches with electrically charged standard model messenger particles.

- The ATIC collaboration found evidence for a peak in the electron spectrum around 400 GeV (Chang et al. [2008]. An analysis of H.E.S.S. data ruled out a peak but confirmed a broad excess in the electron spectrum in the energy range $\sim$ 300 GeV to $\sim$ 800 GeV above the standard electron background model (H.E.S.S. Col. [2009]). The electron spectrum measured by HESS is compatible with a broken power law with a spectral break around 900 GeV.

- The positron fraction in the cosmic ray electron plus positron flux has been measured recently with independent experiments (PAMELA Col. [2009], Fermi Col. [2012], AMS-II Col. [2013]). All experiments confirm an increasing positron fraction in the energy range $\sim$ 8 GeV ($\sim$ 5%) to at least $\sim$ 200 GeV ($\sim$ 15%). The positron fraction beyond $\sim$ 200 GeV is not yet measured but results can be expected from AMS-II. The measured positron fraction is within errors compatible

with being directionally isotropic. The amplitude for the dipole anisotropy is constrained to be smaller than 3.6% at 95% C.L. which is not yet enough to rule out the modeling of the result with known nearby pulsars (f.i. the Monogem and Geminga pulsars) for which a dipole anisotropy at the level of arrival direction of around 1% or even smaller is predicted (Linden and Profumo [1996]). If no dipole anisotropy is found that is larger than $\sim 0.5\%$, the explanation of the result being due to the superposition of multiple pulsars that are in part not yet discoverd but would produce a smaller dipole anisotropy than a single pulsar source if distributed randomly would still be hard to discriminate from a dark matter scenario. A dark matter origin of the positron fraction increase would predict a very small anisotropy whose exact value depends on the dark matter distribution in the galaxy.

- Annihilating or decaying dark matter particles can produce hadrons and, among them, anti-protons. The anti-proton flux is measured f.i. with PAMELA (Adriani et al. [2010]) and happens to agree well with the model predictions for secondary anti-protons produced f.i. in reactions of cosmic rays with the interstellar medium (see Evoli et al. [2012] for a description of the modeling). The agreement between the measured flux and the model predictions constraints the velocity averaged dark matter cross section (see fig. 3.6) and the lifetime of the dark matter particle (Cirelli and Giesen [2013]). The upper limits derived from the PAMELA data are one to two orders of magnitude larger than the canonical value for thermal relic dark matter particles in the mass range from ~ 100 GeV to ~ 3 TeV. More precise measurements are expected from AMS-II. However, as in the case of the positron fraction, the putative detection of an excess flux above the background model for the astrophysical anti-proton flux would be hard to uniquely connect with the presence of dark matter particles as the precision of the astrophysical background anti-proton flux predictions is difficult to quantify.

At least as complex as the indirect search for particle dark matter with electrically charged messenger particles is the indirect search with neutral standard model messenger particles. A neutral standard model particle that is useful for the indirect dark matter search must obviously be stable on cosmological time scales which already excludes all known particles except photons and neutrinos. Photons and neutrinos are indeed used in practice and a further classification of the different indirect searches with photons and neutrinos is possible with a distinction of the targets used for the dark matter search. A promising target for a dark matter search with neutrinos or photons is in practice always a compromise between large dark matter content (i.e. large mass to light ratio), small distance (the neutrino or photon particle flux generated in particle dark matter interactions decreases with the inverse square of the distance) and small background flux, i.e. flux of the same particle type as is used for the dark matter search but caused by known astrophysical effects. Additionally to the target used for the dark matter search, a further classification of the different experimental strategies is possible by dividing between searches for the continuous emission of photons or neutrinos that is f.i. generated in the fragmentation of hadronic final states for the annihilation of dark

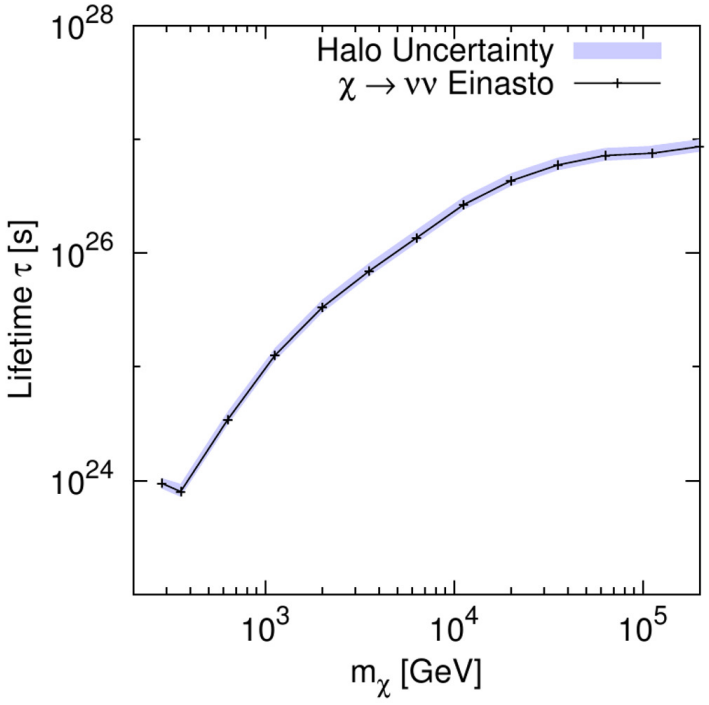

Figure 3.7: Lower limit on the lifetime of a WIMP dark matter particle as a function of the WIMP mass as obtained from IceCube data on the galactic halo. The lower limit should be compared to the age of the universe ($\sim$ 13.8 billion years or $\sim 4 \cdot 10^{17}$ s) as the WIMP is required to be stable on cosmological timescales and to the lifetime of a $\sim$ 200 GeV WIMP that is necessary to model the 'positron excess' measured by PAMELA and other experiments (see above) of $\mathcal{O}(10^{26}\,\mathrm{s})$ (see Pohl and Eichler [2010]). The plot is taken from IceCube Col. [2011].

matter particles and the search for narrow lines of neutrinos or photons as f.i. possibly produced in the direct annihilation of dark matter particles into neutrinos or photons. The direct annihilation or decay of dark matter particles into photons is not possible on tree level but loop suppressed which reduces the expected annihilation rate. On the other hand, the astrophysical background for the production of photon lines is, especially in the GeV or higher energy ranges, small.
The following list gives an incomplete overview of indirect dark matter searches with neutrinos as messenger particles.

- The sun is a well known target to search for (muon-) neutrinos that possibly result from the annihilation of WIMPs that are captured in the sun by WIMP-proton scattering (see IceCube Col. [2013a] for details, especially a discussion of the background for the measurement). The most recent analysis is performed with data

accumulated with the IceCube detector. No significant signal has been detected and upper limits on the spin-dependent and spin-independent WIMP-proton scattering cross sections, whose value are controlling the concentration of WIMPs in the sun, were derived. Especially the upper limit on the spin-dependent cross section is more constraining than results obtained from earth based direct detection experiments. However, the ATLAS and CMS accelerator (see fig. 3.4) bounds for the spin-dependent WIMP-proton cross section are still more constraining in most of the investigated WIMP mass range.

- The extended dark matter halo of the Milky Way and its central region have been investigated with data from the IceCube detector (see IceCube Col. [2011] for the halo and IceCube Col. [2013b] for the central region). No significant neutrino excess over the background estimation was found and upper limits on the velocity averaged WIMP annihilation cross section as well as lower limits on the WIMP decay lifetime were derived for WIMP masses in the range $\sim$ 200 GeV to $\sim$ 10 TeV. The upper limits on the velocity averaged annihilation cross section are not competitive ($\sim$ 3 orders of magnitude worse than current HESS limits (H.E.S.S. Col. [2011a]) but the lower limit on the WIMP lifetime derived from the observation of the extended dark matter halo is among the most constraining results that currently exist (see fig. 3.7). The analysis of the extended dark matter halo of the Milky Way for decaying dark matter particles benefits from the large field of view of the IceCube instrument. For annihilating dark matter, the large field of view is not helpful because the expected signal is assumed to be highly peaked towards the galactic center region due to the squaring of the dark matter density distribution.

In the following, a collection of three important indirect dark matter searches with photons is given. The list focuses on the high energy photon, i.e. γ-ray, searches and only results that are of particular importance in general or for the following text are discussed.

- Using data recorded with the Fermi γ-ray satellite, evidence for the emission of a 'tentative γ-ray line' with energy $\sim$ 130 GeV was found towards the galactic center region (Weniger [2012], post trial significance $\sim 3.2\sigma$). The analysis used a signal (dark matter profiles resulting from N-body computer simulation) to noise (diffuse γ-ray background, especially in the galactic plane) optimized search region. 'Strong evidence' for the same line signal ($\sim$ 130 GeV) and an additional weaker line signal at $\sim$ 110 GeV was found little later in an analysis that assumed the signal region shaped like a Gaussian whose center was left as a free fit parameter found to be offset from the galactic center region by $\sim -1.5^\circ$ in longitude (Finkbeiner and Su [2012], post trial significance for the 130 GeV line of more than 5σ). However, the significance of the offset of the Gaussian signal region from the galactic center is difficult to quantify, the best fit FWHM of the used Gaussian is $1.4^\circ (-0.4^\circ)(+1.6^\circ)$ and an offset in latitude was not searched for. The result is currently heavily debated as an astrophysical origin of a γ-ray line with $\sim$ 100 GeV appears unlikely and the appearance of two γ-ray lines of similar energy is well compatible with the

loop suppressed annihilation of WIMPs into two γ-rays on the one hand and into one γ-ray and one Z-boson on the other hand. Besides discussions on the putative origin of the line feature near 130 GeV, also the reality of the signal is heavily discussed. The Fermi collaboration finds a local significance for the signal of 3.3σ which reduces to only 1.6σ after the consideration of trial factors (Fermi-LAT Col. [2013]). An independent cross check of the result is hopefully possible in the near future with the HESS phase II instrument (Bergstrom et al. [2012]).

- The Fermi satellite recorded data towards 14 dwarf galaxies to search for an excess signal that could indicate annihilations of dark matter particles in the dwarf galaxies which result in a continuous γ-ray spectrum up to some energy determined by the mass of the dark matter particle. No significant signal was found from any of the observed dwarf galaxies and upper limits were derived on the velocity averaged WIMP annihilation cross section (Fermi Col. [2010]). The 'stacked', i.e. combined, analysis of the 7 dwarf galaxies whose observation resulted in the most constraining individual limits did also not result in a significant γ-ray excess but a constraining upper limit on the velocity averaged WIMP annihilation cross section was derived from the non observation of a signal (Geringer-Sameth and Koushiappas [2011]). The stacked analysis rules out a WIMP of cross section larger than the canonical value of $3 \cdot 10^{-26}\,\mathrm{cm}^3/\mathrm{s}$ for WIMP masses in the range from 10 GeV to 20 GeV or from 10 GeV to 40 GeV for the exclusive annihilation of WIMPs into $\tau^+\tau^-$ and $b\bar{b}$ respectively. The analysis presents the first result that is sensitive to the thermal relic WIMP annihilation cross section.

- The H.E.S.S. collaboration searched for a γ-ray excess towards the vicinity of the galactic center (1° radius signal region around the galactic center, see H.E.S.S. Col. [2011a]). Known γ-ray sources as well as the galactic plane ($|b| < 0.3^\circ$), which is known to be a source of diffuse γ-ray emission and possibly contains yet unresolved γ-ray sources, were excluded from the analysis. A version of the 'reflected region' background algorithm (see chapter 2) has been developed to subtract the cosmic ray background despite of the signal region being large in comparison with the H.E.S.S. phase I field of view ($\sim 2^\circ$ radius). No significant excess signal has been found and upper limits on the velocity averaged WIMP annihilation cross section were derived. The upper limits are the most constraining results for WIMPs in the mass range from ~ 300 GeV to ~ 10 TeV. However, the sensitivity is still one order of magnitude above the canonical velocity averaged annihilation cross section for thermal relic WIMPs of $\sim 3 \cdot 10^{-26}\,\mathrm{cm}^3/\mathrm{s}$. The analysis will be discussed in detail in the next chapter.

To summarize the current status of indirect dark matter searches with neutral messenger particles, it can be concluded that there is yet no convincing signal with the very notable exception of the putative γ-ray line signal(s) with energies around $\sim$ 130 GeV. The sensitivity of the current searches for γ-ray and neutrino lines as well as for continuous γ-rays or neutrino emission resulting from dark matter particle interactions was improving in the last years. It will be discussed in the next chapter whether new approaches in γ-

ray astronomy with Cherenkov telescopes can improve the detection potential of particle dark matter in the Milky Way.

4 Search for WIMPs Towards the Milky Way Center Region with H.E.S.S.

This chapter discusses different technical approaches to search for WIMPs in the Milky Way halo with the H.E.S.S. array. Assumptions on WIMPs concerning their distribution and annihilation are discussed in the introduction together with the measurement principle and technical analysis aspects that are of general interest for the chapter. The subsequent data analysis section starts with the discussion of the rotated pixel background subtraction method. An algorithm that is very similar to the rotated pixel method has already been described in H.E.S.S. Col. [2011a] before the start of this thesis. Two datasets are analyzed with the rotated pixel method. The first dataset analysis is an independent re-analysis of a H.E.S.S. dataset whose investigation has already been described in H.E.S.S. Col. [2011a] before the work presented in this thesis started. The development and application of new background subtraction methods (On/Off and driftscan) that are presented later in the data analysis section and the comparison of the sensitivity of the different approaches in the final section of the chapter is a central part of this thesis.

4.1 Introduction

4.1.1 Dark Matter Distribution in the Milky Way

The distribution of dark matter in the Milky Way is of central importance for any indirect search for a WIMP annihilation signal in the Milky Way Dark Matter Halo. Consider a small volume with dark matter density ρ. For a WIMP with mass M, there are on average $N = \Delta V \rho / M$ dark matter particles in the considered volume ΔV. The probability that an annihilation occurs in the volume is proportional to the number of possible combinations of two particles that can annihilate. For Majorana ('self annihilating') WIMPs this is $\binom{N}{2} = N(N-1)/2 \sim N^2/2$ for large number of particles N in the volume. For Dirac WIMPs in contrast, the number of possible combinations is smaller than for Majorana WIMPs. Given that N Dirac particles are in a volume, there are on average $N/2$ particles and $N/2$ antiparticles and the number of combinations is $N^2/4$. As a consequence of a WIMP annihilation, N_γ γ-rays are assumed to be created isotropically. The fraction $d\Omega/4\pi$ of the created γ-rays is emitted in the solid angle $d\Omega$. The expected flux of γ-rays created in WIMP annihilations and observed in the field of view $d\Omega$ is obtained by integrating many of the considered small volumes of dark matter

density $\rho(s)$ over the line of sight ds,

$$d\Phi = N_\gamma \frac{\langle \sigma v \rangle}{2} \frac{d\Omega}{4\pi} \int ds \left(\frac{\rho(r(s))}{M} \right)^2 , \tag{4.1}$$

where the proportionality constant $\langle \sigma v \rangle$ is called the 'velocity averaged annihilation cross section'. For Dirac WIMPs, eq. 4.1 has to be divided by an additional factor of two[1]. Given a line of sight from an observer on earth towards a direction with angle α to the galactic center, the distance $r(s)$ from a point s on the line of sight to the galactic center is given by

$$r(s) = \sqrt{r_E^2 + s^2 - 2 r_E s \cos(\alpha)} \, .$$

Here, $r_E \sim 8.5$ kpc is the distance between the earth and the galactic center. The dependence of the expected signal strength on the squared dark matter density along the line of sight motivates a discussion of the current knowledge of the dark matter distribution in the Milky Way. Apart from details, there are two different approaches to gain information on the dark matter distribution in the Milky Way. Unfortunately both methods lead to two different predictions. This is sometimes called the 'core/cusp problem' in literature.

Computer Simulations

Computer simulations are used to solve the N-body problem for a large set of 'particles' that interact gravitationally starting from a nearly flat matter distribution with some seed density fluctuations in a realistic cosmology at the recombination epoch. Here, 'particles' is used as a general term that denotes a mass unit in the simulation. The mass unit used for a simulation depends in general on the resolution, i.e. spatial scale, that is investigated. The large scale structure of the universe with the dynamics of galaxy clusters is simulated with particles that are much more massive than for example the galaxy scale structure. To investigate the matter density distribution on galaxy scales, a full simulation of a universe with low spatial resolution is typically considered and the formation of galaxies of a given size is searched for. Selected seed galaxies are then simulated in more detail with a higher spatial resolution and lower 'particle' masses. In the following, the current main results from the investigation of Milky Way size galaxies are itemized.

- The dark matter distribution in a Milky Way size galaxy is neither spherically symmetric nor smooth. In other words, a substantial amount of substructure on top of a smooth component is predicted by N-body simulations.

- The smooth component of the dark matter density can be well fitted by universal

[1] It appears as if a substantial amount of confusion about the factors of 2 in eq. 4.1 exist in the literature. No reference for a justification argument like the one given above could be found.

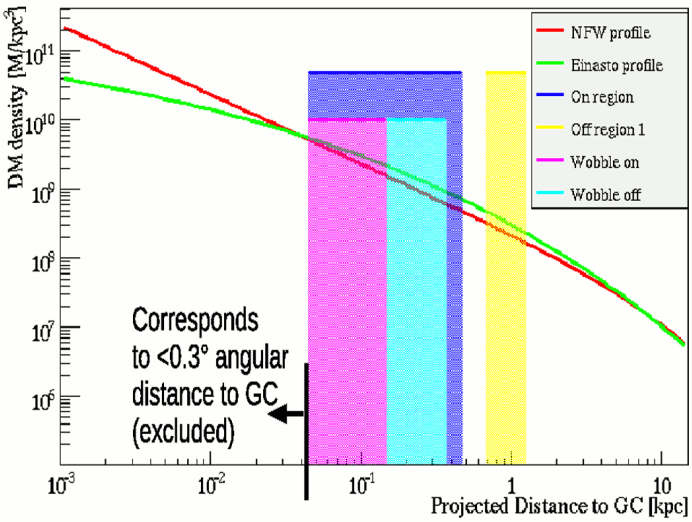

Figure 4.1: Einasto and NFW parametrizations of the dark matter density as a function of the distance to the galactic center for the Milky Way. Parameters are adapted from Pieri et al. [2011]. The colored regions indicate the signal and background regions of the rotated pixel (signal region in pink, background region in green) and the On/Off method (signal region in blue and background region in yellow) discussed later in this text.

and simple functions. The Einasto profile with $\alpha = 0.17$,

$$\rho_{\mathrm{Einasto}}(R) = \rho_s \, \exp\left(-\frac{2}{\alpha}\left(\left(\frac{R}{r_s}\right)^{\alpha} - 1\right)\right) ,$$

describes the result of the Aquarius simulation and the Navarro Frenk White (NFW) profile,

$$\rho_{\mathrm{NFW}}(R) = \frac{\rho_s}{\frac{R}{r_s}\left(1 + \frac{R}{r_s}\right)^2} ,$$

fits the Via Lactea II simulation results (see Pieri et al. [2011] and references therein).

In both cases, r_s and ρ_s are the scaling radius and scaling density which are fit parameters respectively and R is the distance to the center of the galaxy. It is obvious that the dark matter density predicted by the mentioned N-body simulations is increasing towards the center of a galaxy where a 'cusp' is expected. In the vicinity of the center of a galaxy, the smooth component of the dark matter density predicted in N-body simulations is dominant and the subhalo component is negligible. Figure 4.1 compares the Einasto and the NFW parametrization of the dark matter density profile with parameters taken from[2] Pieri et al. [2011] that lead to the dark matter density in the vicinity of the sun to be $\sim 0.3\,\mathrm{GeV/cm^3}$.

Observations

The presence of dark matter in galaxies is inferred from investigations of the dynamics of galaxy constituents. Especially the flatness of the velocity curves of spiral galaxies hints towards the presence of dark matter in the investigated spiral galaxies. For the velocity $v(R)$ of a test mass around the mass $M(< R)$ enclosed within the radius R it holds in general that

$$v(R) \sim \sqrt{\frac{M(< R)}{R}} .$$

To obtain a constant velocity curve $v(R)$, the density profile must follow $\rho(R) \sim 1/R^2$ as this leads to $M(< R) = 4\pi \int_0^R dr\, r^2 \rho(r) \sim R$. This means that the dark matter density distribution must follow $\rho(R) \sim 1/R^2$ far away from the center of the galaxy, i.e. outside of the luminous radius of a galaxy where most of the visible mass resides. The density distributions quoted above that fit the results of N-body simulations are compatible with this behavior. Unfortunately it is very difficult to obtain conclusive information on the dark matter density distribution within the optical radius of a spiral galaxy through observations. The measurement of the velocity curves of investigated spiral galaxies is not precise enough to distinguish between different proposed density profiles. Especially,

[2]The parameters from the given reference are also used in the analysis presented below. They are $\rho_s = 8.1 \cdot 10^6\,\mathrm{M_{Sun}/kpc^3}$ and $r_s = 21\,\mathrm{kpc}$ for the NFW profile and $\rho_s = 2.8 \cdot 10^6\,\mathrm{M_{Sun}/kpc^3}$, $r_s = 20.0$ kpc and $\alpha = 0.17$ for the Einasto profile.

the precision is not sufficient to distinguish between a cusped profile motivated by N-body simulations and a profile with constant or nearly constant density within the optical radius of a spiral galaxy. An example for a dark matter density distribution with nearly constant density within the optical radius r_0 and a $\rho(R) \sim 1/R^2$ dependence outside of the optical radius is the Burkert profile

$$\rho_{\text{Burkert}}(R) = \rho_0 \frac{r_0^3}{(R + r_0)(R^2 + r_0^2)} \,.$$

Gentile et al. [2004] investigate five spiral galaxies which are similar to the Milky Way and conclude that the velocity curves are better fit by Burkert profiles but a cusped profile like NFW cannot be ruled out. As discussed in Strigari [2012], the situation is very similar for the investigation of Milky Way Dwarf galaxies where cusped profiles appear also less preferred than cored profiles. In particular for the Fornax and Sculptor Dwarf galaxies, a NFW dark matter density profile is disfavored at a confidence level of 96% and 99%, respectivly, and in both cases cored profiles give compatible descriptions (Walker and Penarrubia [2011]).
Obviously there is a hint for a conflict between the prediction for dark matter density distributions from N-body simulations and the observational results. Possible sources for this and other discrepancies such as the missing satellite problem, which is the mismatch between the small number of observed Milky Way dwarf galaxies and the large predicted number (see Strigari [2012] for a discussion), are

- the possible failure of the ΛCDM cosmology that is underlying the N-body simulations (see Strigari [2012] for a discussion) or on a less fundamental scale

- the disregard of baryons in N-body simulations. Most N-body simulations neglect the influence of baryonic matter and the complicated physics associated with f.i. supernovae explosions and star formation with the argument that galaxies are dominated by dark matter. Most older attempts to include baryonic effects in the N-body simulation predicted that the central dark matter density becomes even steeper than for dark matter particles only (see Abazajian and Harding [2012] and references therein). However, very recently the opposite conclusion, i.e. that the inclusion of baryons is flattening the central dark matter density distribution, was drawn (see Governato et al. [2012]). Those results indicate an attractive solution for the 'core/cusp problem', i.e. the hint for a discrepancy between the cusped dark matter density distribution predicted by N-body simulations of only gravitationally interacting particles and the observations that tend to prefer cored dark matter density distributions. Additionally, the abundance of substructure in form of dark matter subhalos is predicted to be reduced when baryons are included in N-body simulations which is also in better agreement with the observational data (see Governato et al. [2012]).

Conclusion

Currently, it appears impossible to draw a definite conclusion on the dark matter density distribution in general galaxies and in the Milky Way in particular. For the concrete case of the Milky Way, three different possible dark matter density profiles are conceivable.

- A steep dark matter density profile which is singular towards the galactic center. Figure 4.1 shows the Einasto and NFW dark matter density distribution with parameters adopted from Pieri et al. [2011] for the Milky Way. For distances larger than ~ 45 pc to the galactic center, both characterizations obtained from different N-body simulations agree within a factor of two.

- The dark matter density distribution follows in general a parametrization as obtained from N-body simulations. However, the impact of baryons lead in the vicinity of the galactic center to a flattening of the dark matter density distribution. Governato et al. [2012] find that this leads to a nearly constant dark matter density within the inner ~ 500 pc of a galaxy (corresponding to $\sim 3 - 4^\circ$ angular distance to the galactic center for an observer on earth when the Milky Way is considered).

- The dark matter density distribution of the Milky Way follows a Burkert profile and is thus constant up to the optical radius of the Milky Way.

A search for WIMP annihilation in the Milky Way halo should consider the uncertainty in the dark matter density profile as far as possible. The methods that are discussed below are not necessarily sensitive to all of the listed dark matter distributions. In particular, no sensitivity at all can be achieved in the case of a constant dark matter density distribution up to the optical radius parametrized by the Burkert profile.

4.1.2 WIMP Annihilation γ-Ray Spectra

Consider two WIMPs with negligible relative velocity annihilating into two standard model particles via the exchange of some gauge particle. The total energy of the two final state standard model particle is determined by the WIMP mass and does not depend on the details of the gauge particle that mediates the annihilation. The allowed and preferred final state particles will, however, in general depend on the WIMP candidate via the coupling to annihilation mediating gauge particles. In all cases, the direct annihilation into γ-ray is loop suppressed. The search for the loop suppressed γ-ray line features from the annihilation of WIMPs is discussed in H.E.S.S. Col. [2013] for energies between ~ 500 GeV and ~ 25 TeV and in Ackermann et al. [2012a] for energies between ~ 5 GeV and ~ 250 GeV. A strong hint for the emission of two γ-ray lines with energies of ~ 110 GeV and ~ 130 GeV in the vicinity of the galactic center is presented in Finkbeiner and Su [2012] and can be interpreted as resulting from WIMP self annihilation into $Z\gamma$ and $\gamma\gamma$ final states. The prospects of testing the presence of those line features with Cherenkov telescopes is shortly discussed in Bergstrom et al. [2012]. However, instead of line features, the work presented in this chapter aims at the detection

of continuous γ-rays that are produced in subsequent reactions of the standard model particles resulting from the WIMP annihilation. The continuous WIMP annihilation γ-ray spectrum depends on the allowed final states for the WIMP annihilation and thus on the WIMP model and mass. However, the maximal possible γ-ray energy is in any case the WIMP mass. This point motivates a generic WIMP search that is explained in the next section. In the case that no WIMP signal is found in a WIMP search, an upper limit on the velocity averaged WIMP annihilation cross section $\langle \sigma v \rangle$ is typically derived. This derivation is in general model dependent and depends in particular on the assumed γ-ray spectrum resulting from the WIMP annihilation. In this work, two different γ-ray spectra are used.

- The 'Bergstrom spectrum' assumes the annihilation of the WIMPs into W and Z gauge bosons. Obviously, the WIMP mass must be above $\sim$ 200 GeV to make this annihilation channel possible. Additionally, the annihilation into electroweak gauge bosons is not allowed for spin conservation reasons for the (bosonic) Kaluza-Klein candidate. However, for large mass neutralinos, this annihilation channel is possibly realistic for a large class of models. Bergstrom et al. [1998] parametrized the γ-ray spectrum obtained in PYTHIA simulations of WW and ZZ pairs of a given total energy (double WIMP mass, $2M$) and found a sufficient fit to the resulting γ-ray spectra by

$$\frac{dN_\gamma}{dE} = \frac{1}{M} \frac{0.73}{(E/M)^{1.5}} \exp(-7.8E/M) \, .$$

- The 'Tasitsiomi spectrum' (see Tasitsiomi and Olinto [2002] for the following) is not obtained from a fit to a standard model particle WIMP annihilation final state Monte Carlo simulation γ-ray output. Instead, it is derived by assuming that the final state standard model particles of a WIMP annihilation hadronize exclusively into pions. The starting point is an empirical fit ($N_h \sim \sqrt{E}$) of the number of hadrons N_h produced in a jet as a function of the jet energy E as obtained from PETRA data (Wiik and Mess [1982]). The fit is combined with a guess ($dN_h/dx \sim (1-x)^2$) on the dependence of the number of hadrons dN_h/dx in a given jet with energy fraction x for large $x \to 1$. The hadron spectrum in a given jet has to lead to the total number of hadrons in the jet as a function of the jet energy via $\int_{\epsilon(E)}^1 dx \, dN_h/dx = N_h(E) \sim \sqrt{E}$ with an infrared cut off $\epsilon(E) \sim 1 \text{ GeV}/E$. This leads to the prediction for the spectral dependence of hadrons in a jet to be $dN_h/dx = \text{Norm} \, x^{-3/2}(1-x)^2$. The normalization is fixed to Norm = 15/16 by energy conservation in the form of the first moment of the spectral distribution to be $\int_0^1 dx \, x dN_h/dx = 1$. This spectrum was first derived in Hill [1983] for the decay of bound states of magnetic monopoles and anti monopoles (Monopolium) into hadrons.
  Assuming as stated by Tasitsiomi and Olinto [2002] that a WIMP annihilates into standard model particles which hadronize exclusively into pions, one out of three pions is on average neutral and decays into two γ-rays. The γ-ray spectrum for

the annihilation of two WIMPs of mass M is then given by

$$\frac{dN_\gamma}{dE} = \int_{E/M}^{1} dy \, \frac{2}{y} \frac{1}{3} \frac{dN_h}{dy} = \frac{1}{M} \left(\frac{10}{3} + \frac{5}{12} \left(\frac{E}{M} \right)^{-1.5} - \frac{5}{4} \sqrt{\frac{E}{M}} - \frac{2.5}{\sqrt{E/M}} \right) .$$

The convolution factor $2/y$ is a factor that accounts for the probability of a neutral pion with energy $E_\pi > E_\gamma \gg m_\pi$ to produce a photon with energy E_γ in the decay. Note that in the case of a hadron fragmentation spectrum, the resulting photon spectrum is not the same as the original hadron spectrum. This is in contrast to the typical high energy astrophysics situation where a power law proton spectrum produces a neutral pion decay γ-ray spectrum with same spectral index as the original proton spectrum.

In practice, both γ-ray spectra that are listed above are only very approximately realistic for a generic WIMP candidate. More precise parametrizations in certain energy ranges exist (Cembranos et al. [2011]) for special annihilation channels but the precision in the description of a special annihilation channel is on the expense of the precision in the description in other annihilation channels or energy ranges. Additionally, many authors have investigated whether the helicity suppression for the annihilation of Majorana (f.i. supersymmetric neutralino) WIMP dark matter into light fermions could be circumvented by the radiation of a photon (Bringmann et al. [2008]) or W/Z bosons (Bell et al. [2011]). The lifting of the helicity suppression of the WIMP annihilation is, however, found to be a very model dependent effect and will not be investigated here. Instead, in this chapter, WIMP annihilation γ-ray spectra are only used for generic sensitivity predictions and the usage of the 'benchmark' spectra given above appears thus justified in order to enable comparisons with other works assuming the same spectra. Once a significant γ-ray signal from WIMP annihilation is found, it will, however, be important to fit (probably superpositions) of precise spectra in certain annihilation channels to the signal to investigate which WIMP model can best explain the γ-ray excess.

4.1.3 Measurement Principle

The general idea of the measurements that are presented below is to measure the number of γ-ray candidate events, i.e. the number of H.E.S.S. I events after applying standard γ-ray event selection criteria, towards a region where a large amount of dark matter is expected along the line of sight. The signal region, where the expected amount of dark matter along the line of sight is large, is the galactic center region in this chapter. However, when pointing the telescopes of the H.E.S.S. array towards the galactic center region, the majority of events are caused by cosmic ray air showers, even after application of standard γ-ray event selection cuts. As outlined in the last chapter, a background subtraction technique is necessary to estimate the number of background events in the signal region. For this, a background region is defined and the number of events in the background region is measured. In order to be sensitive to a γ-ray flux from WIMP annihilation, the background region must be chosen such that the expected amount of

dark matter along the line of sight in the background region is smaller than for the signal region. More precisely, the so called astrophysical factor

$$J = \frac{1}{\Delta\Omega} \int_{\Delta\Omega} d\Omega \int_{\mathrm{LoS}} ds\, \rho^2(r(s)) \,, \tag{4.2}$$

i.e. the squared dark matter density integrated over the line of sight (LoS) and averaged over the field of view $\Delta\Omega$ must be larger for the signal than for the background field of view.
In consequence, the most important condition for the method that is discussed in this section to work is that the dark matter density distribution is peaked towards the galactic center region. As outlined above, there are hints based on N-body simulations that suggest this behavior but it is also possible that the dark matter density distribution is cored, i.e. roughly constant from the center to the optical radius of the Milky Way. If this is the case, all measurements that are discussed below are not sensitive to a WIMP annihilation flux in the Milky Way halo. Additionally, there can be the case that the central few hundred parsec around the Milky Way center have a dark matter density distribution that is significantly affected by the presence of baryonic matter with respect to either the dark matter density peak location (Kuhlen et al. [2013]) or the dark matter density distribution as such (Governato et al. [2012]) or both. Depending on the situation, not all of the methods presented below remain sensitive to a WIMP annihilation flux towards the Milky Way center region.

4.1.4 Exposure Ratio

The analysis of H.E.S.S. data with a background subtraction algorithm relies in general on the measurement of the number of events N_{ON} in the signal and N_{OFF} in the background region. An excess, $\Delta = N_{\mathrm{ON}} - \alpha N_{\mathrm{OFF}}$, is calculated where α is the ratio of the exposures of the signal and background region. Typically, a measurement of a γ-ray excess is performed with a large dataset that consist of multiple smaller sub-datasets - usually (f.i. in the case of the rotated pixel and driftscan method) multiple observation runs. In general, the method employed for the background subtraction gives a prediction for the value of α individually for every subdataset. In the following, α_i, i.e. the exposure ratio for a specific subdataset, is discussed in detail. The combination of multiple subdataset exposure ratios is discussed afterwards.

Exposure Ratio for One Subdataset

To understand the significance and the precise meaning of α_i, consider the case where N_i^{ON} and N_i^{OFF} are the number of events that pass standard γ-ray event selection criteria in the signal and background region of a subdataset i, respectively. In general, $N_i^{\mathrm{ON}} = N_i^{\mathrm{ON,sig}} + N_i^{\mathrm{ON,bkg}}$ and $N_i^{\mathrm{OFF}} = N_i^{\mathrm{OFF,sig}} + N_i^{\mathrm{OFF,bkg}}$, i.e. the number of events in the signal and background region is the sum of the number of background events $N_i^{\mathrm{ON/OFF,bkg}}$ that are selected as γ-ray event candidates but in reality are background events and the number of real γ-ray events $N_i^{\mathrm{ON/OFF,sig}}$.

The excess,

$$\Delta_i = N_i^{\mathrm{ON}} - \alpha_i N_i^{\mathrm{OFF}} = N_i^{\mathrm{ON,sig}} + N_i^{\mathrm{ON,bkg}} - \alpha_i N_i^{\mathrm{OFF}} \,, \tag{4.3}$$

is in an ideal case intended to be equal to the number of signal events in the signal region, i.e.

$$\Delta_i = N_i^{\mathrm{ON,sig}} \,. \tag{4.4}$$

This condition defines the exposure ratio as

$$\alpha_i = \frac{N_i^{\mathrm{ON,bkg}}}{N_i^{\mathrm{OFF}}} \,. \tag{4.5}$$

The given definition of the exposure ratio is precise but in practice only useful as a starting point for further considerations because the number of background events that pass γ-ray event selection criteria in the signal region, $N_i^{\mathrm{ON,bkg}}$, is not measurable independently from $N_i^{\mathrm{ON,sig}}$. As a first step, the exposure ratio is defined such that eq. 4.4 is fulfilled only on average, i.e. $\langle \Delta_i \rangle = \langle N_i^{\mathrm{ON,sig}} \rangle$. This is possible with

$$\alpha_i = \frac{\langle N_i^{\mathrm{ON,bkg}} \rangle}{N_i^{\mathrm{OFF}}} \tag{4.6}$$

which leads to statistical fluctuations of $\Delta_i = N_i^{\mathrm{ON,sig}} + N_i^{\mathrm{ON,bkg}} - \langle N_i^{\mathrm{ON,bkg}} \rangle$ around $\langle \Delta_i \rangle = \langle N_i^{\mathrm{ON,sig}} \rangle$.
A further step is to approximate N_i^{OFF} in the exposure ratio by $\langle N_i^{\mathrm{OFF,bkg}} \rangle$ which in general changes the γ-ray excess to be

$$\langle \Delta_i \rangle = \langle N_i^{\mathrm{ON,sig}} \rangle - \alpha_i \langle N_i^{\mathrm{OFF,sig}} \rangle \tag{4.7}$$

on average with the exposure ratio

$$\alpha_i = \frac{\langle N_i^{\mathrm{ON,bkg}} \rangle}{\langle N_i^{\mathrm{OFF,bkg}} \rangle} \,. \tag{4.8}$$

A meaningful measurement is thus only possible if $\langle N_i^{\mathrm{ON,sig}} \rangle > \alpha_i \langle N_i^{\mathrm{OFF,sig}} \rangle$, i.e. typically if the γ-ray flux per solid angle in the signal region is larger than in the background region.
In the following, the background acceptances $\mathfrak{A}_i^{\mathrm{ON}}$ and $\mathfrak{A}_i^{\mathrm{OFF}}$ for the signal and background region are introduced by

$$\langle N_i^{\mathrm{ON,bkg}} \rangle = \mathfrak{A}_i^{\mathrm{ON}} \Omega_i^{\mathrm{ON}} T_i^{\mathrm{ON}} \tag{4.9}$$

and

$$\langle N_i^{\mathrm{OFF,bkg}} \rangle = \mathfrak{A}_i^{\mathrm{OFF}} \Omega_i^{\mathrm{OFF}} T_i^{\mathrm{OFF}} \tag{4.10}$$

where

- Ω_i^{ON} and Ω_i^{OFF} are the field of views of the signal and background region observations,

- T_i^{ON} and T_i^{OFF} are the livetimes, i.e. the dead time corrected observation times, of the signal and background region observations.

This leads to the preliminary expression for the exposure ratio

$$\alpha_i = \frac{\Omega_i^{\mathrm{ON}} T_i^{\mathrm{ON}}}{\Omega_i^{\mathrm{OFF}} T_i^{\mathrm{OFF}}} \frac{\mathfrak{A}_i^{\mathrm{ON}}}{\mathfrak{A}_i^{\mathrm{OFF}}} \tag{4.11}$$

in which all quantities except the acceptances for the signal and background region observation are determinable. A background subtraction algorithm will typically construct the signal and background regions such that the acceptance in the signal and background region are equal and the acceptance ratio cancels thus out in the exposure ratio. The equality of the acceptance in the signal and the background region will, however, in general only hold up to a systematic error which in turn introduces a systematic error $\sigma_{\alpha(i)}$ in the exposure ratio that has to be estimated from case to case. Statistical fluctuations of the number of signal and background events lead to statistical fluctuations of the excess around its average value (eq. 4.7). The statistical fluctuations of the excess around its average value are of the order of magnitude of

$$\sigma_{\Delta(i)} \sim \sqrt{N_i^{\mathrm{ON}} + \alpha_i^2 N_i^{\mathrm{OFF}}} \tag{4.12}$$

if the exposure ratio α_i is known to have a negligible error $\sigma_{\alpha(i)}$. The error on the exposure ratio is in general negligible if

$$\sigma_{\alpha(i)} N_i^{\mathrm{OFF}} \ll \sigma_{\Delta(i)} \,, \tag{4.13}$$

i.e. if the statistical error on the excess due to fluctuations of the number of signal and background events is much larger than the error on the excess introduced due to the finite precision with which the exposure ratio is known. Note that the systematic error on the excess, $\sigma_{\alpha(i)} N_i^{\mathrm{OFF}}$, scales linearly with the number of events in the background region but the statistical error on the excess due to Poisson fluctuations of the number of signal and background events scales only with the square root of the number of background events.
Traditionally the significance of an excess measured with a Cherenkov telescope is calculated with the method described in Li and Ma [1983]. This method is, however, not able to treat a systematic error on the exposure ratio. A modification that is capable of treating systematic errors is described in appendix D. If no significant excess is measured, an upper limit on the γ-ray event excess is usually derived. The method described in Feldman and Cousins [1998] is known to have very good frequentist coverage properties but can on the other hand not treat a systematic error on the exposure ratio. Alternatively, the method described in Rolke et al. [2005] is known to be in general over-covering but can consider a systematic error on the excess.

Combination of Multiple Subdatasets

Consider now the situation that multiple subdatasets $i = 1..K$ are to be combined. The combination of the dataset has to state the significance of a putative signal measurement. This would in principle be possible with a likelihood ratio method similar to the one applied in Li and Ma [1983] when a likelihood function for the combined measurement is defined as the product of the likelihood functions for the individual subdataset. This is possible because all measurements are assumed to be independent but it leads to a log-likelihood ratio which is asymptotically behaving like a χ^2 distribution with K degrees of freedom if no signal is present. In contrast, the same method for only one subdataset leads in the same situation (no signal present) to a log-likelihood ratio which is asymptotically behaving like a χ^2 distribution with only one degree of freedom, i.e. like the absolute value of a standard normal random variable. This is obviously much easier to interpret. Apart from that there are other practical problems, the most problematic being that it is in general intended to determine a γ-ray flux in case of a significant signal or, in case that no significant signal is measured, an upper limit on the γ-ray flux. This is in practice only possible if a γ-ray excess is measured and leads to the necessity to combine the individually measured γ-ray excesses Δ_i for every subdataset into one combined γ-ray excess Δ. In practice, it is argued that the individual subdatasets are combined by summing up the number of signal and background events, $N^{\mathrm{ON}} = \sum_i N_i^{\mathrm{ON}}$ and $N^{\mathrm{OFF}} = \sum_i N_i^{\mathrm{OFF}}$. The combined excess is then given by

$$\Delta = N^{\mathrm{ON}} - \alpha N^{\mathrm{OFF}} \tag{4.14}$$

with a new exposure ratio α for the combined dataset. A consideration similar to the one given above for only one subdataset leads to the expression for the exposure ratio

$$\alpha = \frac{\sum_i \Omega_i^{\mathrm{ON}} T_i^{\mathrm{ON}} \mathfrak{A}_i^{\mathrm{ON}}}{\sum_i \Omega_i^{\mathrm{OFF}} T_i^{\mathrm{OFF}} \mathfrak{A}_i^{\mathrm{OFF}}} \,. \tag{4.15}$$

One interesting point to note here is that the average excess, $\langle\Delta\rangle$, is given by

$$\langle\Delta\rangle = \langle N^{\mathrm{ON}}\rangle - \alpha\langle N^{\mathrm{OFF}}\rangle = \langle N^{\mathrm{ON}}\rangle - \sum_i \alpha_i \langle N_i^{\mathrm{OFF}}\rangle = \langle \sum_i \Delta_i\rangle \tag{4.16}$$

by means of the definitions 4.9 and 4.10 and the rewriting of eq. 4.15 in the form

$$\alpha = \frac{\sum_i \alpha_i \, T_i^{\mathrm{OFF}} \Omega_i^{\mathrm{OFF}} \mathfrak{A}_i^{\mathrm{OFF}}}{\sum_i T_i^{\mathrm{OFF}} \Omega_i^{\mathrm{OFF}} \mathfrak{A}_i^{\mathrm{OFF}}} \,. \tag{4.17}$$

Equation 4.16 means that the average combined excess is equal to the average of the sum of the excess for every subdataset, a result that is supported by intuition. However, the exposure ratio defined in eq. 4.15 is not a simple quantity. The primary reason for the complexity of the general exposure ratio is that even if a suitably chosen background subtraction algorithm manages to gain perfectly equal acceptances in the signal and background region for every single subdataset, $\mathfrak{A}_i^{\mathrm{ON}} = \mathfrak{A}_i^{\mathrm{OFF}}$, the subdataset accep-

tances do not cancel out of the exposure ratio. The cancellation would only hold if the acceptances were additionally equal for every subdataset which is highly unrealistic[3]. In practice, there are only two ways out of this situation.

- One can try to construct the signal and background regions such that $\alpha_i \sim \text{const.}$ In that case, the average $\bar{\alpha} = 1/K \sum_i \alpha_i$ can be used and the exposure ratio for the combined dataset becomes trivially $\alpha = \bar{\alpha}$. This method can be applied if the RMS of the α_i, $\text{RMS}(\alpha_i)$, fulfills

$$\text{RMS}(\alpha_i) N^{\text{OFF}} \ll \sqrt{N^{\text{ON}} + \alpha^2 N^{\text{OFF}}} \,. \tag{4.18}$$

  Alternatively, a systematic error on the exposure ratio must be considered.

- The other option is to argue that the acceptances $\mathfrak{A}_i$ do not vary too much from subdataset to subdataset. In that case, the average $\bar{\mathfrak{A}}$ is used and the exposure ratio becomes

$$\alpha = \frac{\sum_i \Omega_i^{\text{ON}} T_i^{\text{ON}}}{\sum_i \Omega_i^{\text{OFF}} T_i^{\text{OFF}}} \tag{4.19}$$

  up to an error

$$\sigma(\alpha) \sim \sqrt{2}\alpha \, \frac{\text{RMS}(\mathfrak{A}_\text{i})}{\bar{\mathfrak{A}}} \,. \tag{4.20}$$

  Again $\sigma(\alpha) N^{\text{OFF}} \ll \sqrt{N^{\text{ON}} + \alpha^2 N^{\text{OFF}}}$ must hold or a systematic error on the exposure ratio has to be considered.

For the case where the exposure ratio, α_i, for every subdataset is only known up to a non-negligible systematic error, $\sigma_{\alpha(i)}$, it is of central importance that the systematic error $\sigma_{\alpha(i)}$ is of random nature and not biasing towards a preferred direction. For instance for the first of the two options considered above with almost equal exposure ratios for every subdataset, $\alpha_i = \bar{\alpha}$, and almost equal systematic error for the exposure ratio for every subdataset, $\sigma_{\alpha(i)} = \sigma_{\bar{\alpha}}$, the random nature of the systematic error leads to an on average smaller systematic error on the exposure ratio $\alpha = \bar{\alpha}$ for the combined dataset, i.e. $\sigma_\alpha = 1/\sqrt{K}\sigma_{\bar{\alpha}}$. This means that the systematic error on the excess introduced by the systematic error on the exposure ratio scales with the number of subdataset K like $\sqrt{K}$, i.e. like the statistical error on the excess. If the systematic error were in contrast not random, the systematic error on the excess introduced by the systematic error on the exposure ratio would scale directly with K and at some point limit the potential to improve the sensitivity by means of increasing the number of subdataset.

4.1.5 Exclusion Regions

As outlined in the previous chapters, it is well known that γ-rays are generated in the vicinity of galactic astrophysical environments such as for instance some pulsar wind

[3] Consider for instance a dataset consisting of two subdataset, one taken with a 2 telescope array and one with a four-telescope array. It is obvious that the acceptances for the two subdataset would not be the same in this frequently occurring situation.

nebulae or some of the remnants of supernovae. A search for γ-rays generated in reactions subsequent to WIMP annihilation faces the problem that it must be excluded that a measured γ-ray signal is created in other astrophysical γ-ray sources. In case that a search for a γ-ray signal generated in WIMP annihilations does not find a signal, it must still be excluded that the background region contains γ-ray sources of astrophysical origin and just balances a γ-ray signal due to WIMP annihilation in the signal region. In practice, the validity of both points is not easy to guarantee and typically it is argued that known astrophysical sources are to be excluded from a data analysis for a WIMP annihilation signal by suitably choosing exclusion regions from within events are disregarded in the analysis. For the region of $\sim 5^\circ$ around the galactic center, the known astrophysical VHE γ-ray sources are

- HESS J1745-290 (see H.E.S.S. Col. [2009]) which is a strong γ-ray source that is spatially coincident with the galactic center position, i.e. $l = 0^\circ$, $b = 0^\circ$. The source is not yet identified, i.e. no source class has been attributed, and the source is detected with H.E.S.S. without significant angular extension given the H.E.S.S. point spread function.
- HESS J1747-281 or G0.9+0.1 (see H.E.S.S. Col. [2005a]) is a γ-ray source that is associated with a pulsar wind nebula located in a shell type supernova remnant ('composite supernova remnant'). The source is detected in H.E.S.S. data at galactic coordinates $l = 0.9^\circ$, $b = 0.1^\circ$ without significant extension given the H.E.S.S. point spread function.
- HESS J1745-303 (see H.E.S.S. Col. [2008]) is an extended ($\sim 0.2^\circ$) γ-ray source at $l = 358.7^\circ$, $b = -0.6^\circ$ in galactic coordinates. The source association is unclear.
- HESS J1741-302 (see Tibolla et al. [2008]) is also an extended and unidentified γ-ray source at $l = 358.4^\circ$ and $b = 0.2^\circ$ in galactic coordinates.
- HESS J1747-248 or Terzan 5 (see H.E.S.S. Col. [2011b]) is an extended ($\sim 0.2^\circ$) γ-ray source at $l = 3.7^\circ$, $b = 1.7^\circ$ in galactic coordinates. The source could be associated with the globular cluster Terzan 5.

Additionally, the vicinity of the galactic center region is known to be the origin of diffuse γ-ray emission (H.E.S.S. Col. [2005b]). The statement that known astrophysical γ-ray sources must be excluded from a search for a WIMP annihilation signal will be refined below as a consequence of the 'rotated pixel method' analysis.

4.1.6 Calculation of an Upper Limit on $\langle \sigma v \rangle$

Based on the outcome of the analysis presented below it will be frequently necessary to calculate an upper limit on the velocity averaged annihilation cross section. For a self-annihilating WIMP, the expected γ-ray flux due to the annihilation of WIMPs with mass M is given by

$$\frac{d\Phi}{dE} = \frac{\Delta\Omega J}{4\pi M^2} \frac{\langle \sigma v \rangle}{2} \frac{dN_\gamma}{dE} \,. \tag{4.21}$$

This equation can be easily derived from eq. 4.1 with the definition of the astrophysical factor J (eq. 4.2). The expected number of γ-ray events detected in one subdataset i due to the annihilation of WIMPs is thus

$$N_i(M) = \frac{\Delta\Omega_i T_i J_i}{4\pi M^2} \frac{\langle\sigma v\rangle}{2} \sum_\kappa \text{Exposure}_i(\kappa) \int_{T(\kappa)}^{M} dE \, \text{A}_{\text{Eff}}(\kappa, E) \frac{dN_\gamma}{dE} \, . \tag{4.22}$$

In the analysis presented below, $\text{Exposure}_i(\kappa)$ is in practice a five dimensional histogram which is normalized to unity ($\sum_\kappa \text{Exposure}(\kappa) = 1$) and contains for every event recorded in the field of view $\Delta\Omega$ the

- zenith and azimuth angle of the array pointing in the horizon system,
- the offset of the event from the observation position
- and the array configuration (arrangement and number of operating telescopes) as well as the optical configuration characterizing the mirror reflectivity.

It is obvious that the energy threshold of the array, $T(\kappa)$, and the effective area, $\text{A}_{\text{Eff}}(\kappa)$, depend on the parameters listed above. In none of the analyses presented below, a significant difference in the upper limit on the velocity averaged WIMP annihilation cross section is observed if the zenith and azimuth angle of the reconstructed event is used to build $\text{Exposure}(\kappa)$ instead of the zenith and azimuth angle of the array pointing. For multiple observation runs i, the sum of eq. 4.22 is to be taken over all runs in a dataset. If no significant excess is obtained in an analysis, upper limits $\hat{N}(E_0 < E_i)$ on the number of excess events in the energy range $[E_0 : E_i]$ are derived with a suitable method. In practice, the method described in Rolke et al. [2005] is applied in the later analysis to set upper limits on the number of excess events at 95% CL. The energy values E_i are chosen such that the bin width $E_{i+1} - E_i$ is larger than the energy resolution at E_i and E_0 is the smallest energy threshold of the dataset. Based on the upper limit on the number of excess events calculated at a certain confidence level, $\hat{N}(E_0 < E_i)$, an upper limit on the velocity averaged annihilation cross section, $\langle\hat{\sigma v}\rangle$, for a WIMP of mass M can be inferred at the same confidence level. For this, the number of expected γ-ray excess events after background subtraction is calculated using eq. 4.22, i.e.

$$\Delta = \sum_i \Delta_i = \sum_i \left(N_i^{\text{ON}}(M) - \alpha_i N_i^{\text{OFF}}(M) \right) \, , \tag{4.23}$$

where the index i is running over all considered subdatasets and eq. 4.16 is used. It holds further that

$$\begin{aligned} \alpha_i N_i^{\text{OFF}}(M) &\sim \frac{\Delta\Omega_i^{\text{ON}} T_i^{\text{ON}}}{\Delta\Omega_i^{\text{OFF}} T_i^{\text{OFF}}} \Delta\Omega_i^{\text{OFF}} T_i^{\text{OFF}} J_i^{\text{OFF}} \\ &= \Delta\Omega_i^{\text{ON}} T_i^{\text{ON}} J_i^{\text{OFF}} \, . \end{aligned} \tag{4.24}$$

Additionally, a suitable background subtraction algorithm has to ensure that the zenith and azimuth pointing angles as well as the radial acceptance and the mirror reflectivity and the array configuration are approximately equal for the signal and background region

measurement within one subdataset. In other words, Exposure(κ) is approximately equal for the signal and background region measurement and it holds

$$\begin{aligned} \text{Exposure}_i^{\text{ON}}(\kappa) &\sim \text{Exposure}_i^{\text{OFF}}(\kappa) \sim \tfrac{1}{2}\left(\text{Exposure}_i^{\text{ON}}(\kappa) + \text{Exposure}_i^{\text{OFF}}(\kappa)\right) \\ &=: \text{Exposure}_i(\kappa)\,. \end{aligned} \tag{4.25}$$

Together it follows for the expected γ-ray excess

$$\Delta = \frac{\langle\sigma v\rangle}{8\pi M^2} \sum_i \Delta\Omega_i^{\text{ON}} \left(J_i^{\text{ON}} - J_i^{\text{OFF}}\right)\, \text{PF}_i\,, \tag{4.26}$$

where

$$\text{PF}_i := T_i^{\text{ON}} \sum_\kappa \text{Exposure}_i(\kappa) \int_{T(\kappa)}^{M} dE\; \text{A}_{\text{Eff}}(\kappa, E) \frac{dN_\gamma}{dE}\,. \tag{4.27}$$

For the datasets considered below, the variation of the product $\Delta\Omega_i(J_i^{\text{ON}} - J_i^{\text{OFF}})$ from dataset to dataset is very small. It is thus appropriate and in practice much easier to approximate eq. 4.26 by

$$\Delta = \frac{\langle\sigma v\rangle}{8\pi M^2} \overline{\Delta\Omega_i^{\text{ON}} \left(J_i^{\text{ON}} - J_i^{\text{OFF}}\right)} \sum_i \text{PF}_i\,, \tag{4.28}$$

where $\overline{\Delta\Omega_i^{\text{ON}} \left(J_i^{\text{ON}} - J_i^{\text{OFF}}\right)}$ is the average of $\Delta\Omega_i^{\text{ON}}(J_i^{\text{ON}} - J_i^{\text{OFF}})$.
Equation 4.28 is used to infer an upper limit on $\langle\sigma v\rangle$ from an upper limit on the excess via

$$\hat{\langle\sigma v\rangle}(M) = 8\pi M^2\, \frac{\hat{N}(E_i = M)}{\overline{\Delta\Omega_i^{\text{ON}} \left(J_i^{\text{ON}} - J_i^{\text{OFF}}\right)} \sum_i \text{PF}_i}\,. \tag{4.29}$$

The method described above relies essentially on eq. 4.22 which holds in general only approximately and has especially to be adapted for the case of driftscan observations which is discussed below. The approximation that goes into eq. 4.22 is that the 'astrophysical factor' is decoupled from the exposure integration. In practice, a given small solid angle element is f.i. observed under a fixed offset from the observation position if the celestial pointing is kept constant. It is then more precise to calculate the astrophysical factor towards the direction of the considered small solid angle and the corresponding 'particle physics factor',

$$\text{PPF}_{\psi(l,b)} = \frac{\langle\sigma v\rangle}{2M^2} \sum_\kappa \text{Exposure}(\kappa|\psi = \psi(l,b)) \text{A}_{\text{Eff}}(\kappa, E) \frac{dN_\gamma}{dE} \tag{4.30}$$

where the exposure histogram is evaluated at the offset $\psi(l,b)$ corresponding to the direction of the solid angle element and the pointing direction of the array. Eventually, the integration over all small solid angle elements leads to a coupling of the 'astrophysical'

and 'particle physics' factors via

$$N_i(M) = \frac{T_i}{4\pi} \int_{\Delta\Omega_i} d\Omega \, \mathrm{LoS}(l,b) \, \mathrm{PPF}_{\psi(l,b)} \tag{4.31}$$

where

$$\mathrm{LoS}(l,b) = \int_{\mathrm{LoS}} ds \, \rho^2(r(s)) \tag{4.32}$$

is the line of sight integral over the squared dark matter density towards the direction defined by (l,b). A blueprint for a more general and precise derivation of statements on $\langle\sigma v\rangle$ is given in appendix E but not used below. The problem with a general and precise treatment of the problem is that the methods become increasingly complicated and non-standard. On the other hand, the gain in precision of the more complicated methods is to be expected at the level of $\sim 10\%$ to $\sim 20\%$ which is small compared to the dependence of any statement concerning $\langle\sigma v\rangle$ on models for the γ-ray spectrum resulting from WIMP annihilation and the distribution of dark matter along the line of sight. It is therefore concluded that the method to derive upper limits on $\langle\sigma v\rangle$ that is presented above is of great value due to its comparatively simple implementation and logic. It would be desirable to compare the results with more complicated but precise methods described in appendix E which is, however, not performed in the analysis below.

4.2 H.E.S.S. Data Analysis

Three methods (rotated pixel, On/Off and driftscan) to search for the presence of WIMPs towards the galactic center region with H.E.S.S. observations are discussed in this section. The rotated pixel method is very similar to the method described in H.E.S.S. Col. [2011a]. In order to test the implementation of the method, it is first applied to the very same dataset as has been done in H.E.S.S. Col. [2011a]. Later, a different dataset will also be considered. The On/Off and the driftscan method employ data-taking in very special observation modes that have up to now not been investigated with the precision presented in this section.

4.2.1 Rotated Pixel Method

The rotated pixel method is very similar to the method described in H.E.S.S. Col. [2011a]. The sensitivity of the method relies on the steepness of the predicted dark matter density profile in the vicinity of the galactic center and the assumption of the H.E.S.S. I instrumental acceptance to be rotationally symmetric around the pointing position. A signal region of 1° angular radius around the galactic center is defined and subdivided into many pixel, i.e. bins, each of which has a side length that is much smaller (0.01°) than the angular resolution of H.E.S.S. I ($\sim 0.1^\circ$). For a given observation run pointing in a constant direction in celestial coordinates, each pixel in the overlap of the signal region and the field of view is then rotated out of the signal region at constant angular distance to the pointing position to construct the background region for a run. A pixel in the

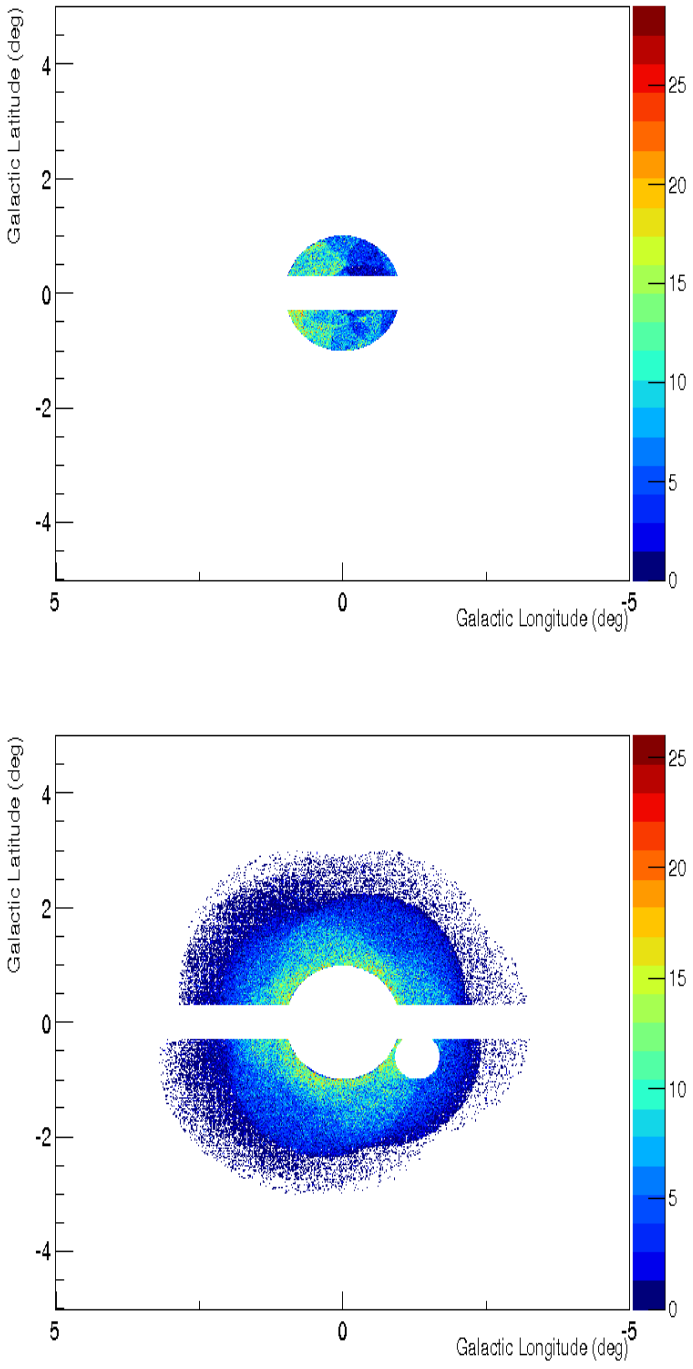

Figure 4.2: Rotated pixel signal (upper plot) and background (lower plot) region. Shown are the number of events per pixel on the color scale for a H.E.S.S. I dataset in the galactic coordinate system. The dataset contains 244 observation runs with different observation positions. Apparent inhomogeneities in the number of detected γ-ray events are due to different regions having different exposures. Clearly visible are the exclusion of the galactic plane and the known γ-ray source HESS J1745-303.

signal region is only considered if four[4] different pixels in the background region that are not used as background pixel for another signal pixel of the considered run can be found. In practice, a given pixel in the signal region is rotated by random angles around the observation position of a given run until four independent background pixels are found that are not used before. Astrophysical γ-ray sources, the galactic plane ($|b| < 0.3^\circ$) and signal pixels for which no four independent background pixels can be constructed for geometrical reasons with the explained method are excluded from the analysis. The exclusion regions for astrophysical γ-ray sources depend in general on the considered dataset and will be detailed below. The exclusion of the galactic plane intends primarily to avoid that the integrated γ-ray emission of yet unresolved astrophysical γ-ray sources, which are concentrating in the galactic plane, is affecting the measurement. At the same time, the dark matter density distribution predicted by two different large scale N-body simulations agrees for distances to the galactic center larger than $\sim 0.3^\circ$ within a factor of two (see fig. 4.1). Thus, the resulting sensitivity to a WIMP annihilation γ-ray flux is less dependent on specific dark matter distribution models within the results of N-body simulations that neglect the presence of baryons. Figure 4.1 shows additionally the projected distances to the galactic center covered in the signal (magenta, tagged 'wobble on') and background (turquoise, tagged 'wobble off') region. The construction of the background region ensures that the signal region is always closer in angular distance to the galactic center than the background region and the predicted average dark matter density in the signal region is thus larger than in the background region. A search for a particle dark matter annihilation signal is thus possible by comparing the number of events detected in the signal region with the number of events detected in the background region.

The rotated pixel method has the advantage that H.E.S.S. data obtained in standard observation runs can be used. This results in a large available dataset after ~ 10 years of H.E.S.S. I observations. However, a disadvantage is that the application of the rotated pixel background subtraction algorithm limits the angular extension of the signal region by the demand to fit signal and background region into one H.E.S.S. I field of view. A larger signal region could, depending on the signal to background ratio, increase the sensitivity of H.E.S.S. I to a WIMP self annihilation γ-ray flux from the galactic dark matter halo. Without the constraint due to the rotated pixel background subtraction, the maximal signal region could be increased to be the complete H.E.S.S. I field of view. The maximal distance of the background region to the galactic center is also limited by the applied background subtraction technique. If the background region were constructed much farther away from the galactic center than possible with the rotated pixel technique, the expected γ-ray flux due to WIMP self annihilation in the background region would be smaller and the sensitivity would thus increase. Additionally, the sensitivity to WIMP annihilations in the Milky Way halo in the case where the dark matter

[4] The number of background pixel to be employed in the analysis depends in general on the size of the signal and the background region. The number of four background pixel is motivated by considering a region of $\sim 1^\circ$ around the galactic center with a field of view of $\sim 2^\circ$ radius leading to $2^2/1^2 = 4$ background pixel. Of course, this is only a back on the envelope estimation and the optimal number of background pixel depends in general also on the pointing position.

density does not follow the distribution predicted by N-body simulations without inclusion of baryons could possibly be enhanced. As outlined above, there are hints that the existence of baryons in the galactic center region is affecting the dark matter density towards an almost constant density within the $\sim$ 500 pc (or $\sim 3^\circ$) around the galactic center (see Governato et al. [2012]). This would imply that the rotated pixel method has no sensitivity to a WIMP annihilation flux from the galactic center region as the background region would have approximately the same astrophysical factor as the signal region. The same would hold if there were a significant ($\sim 1^\circ$ to $\sim 2^\circ$) offset of the maximum dark matter density from the galactic center as recently predicted in N-body simulations involving baryons (Kuhlen et al. [2013]).

Analysis of Dataset 1

Figure 4.3 illustrates the analysis outlined in H.E.S.S. Col. [2011a]. The 'rotated pixel method' for the background subtraction employed in this section is up to small modifications equal to the method applied in this reference. More precisely, the differences are:

- The rotated pixel method as applied in this section does not rotate individual pixels (or bins) of the signal region by multiples of 90° around the pointing position to construct the background region but rotates by a random angle.
- The rotation by a random angle is repeated until either a maximum number of trials is reached or four independent and allowed background pixels are found. The method applied in H.E.S.S. Col. [2011a] does in contrast also use signal pixels for which not four background pixels but only a smaller number could be constructed.

In order to test the implementation and the rotated pixel method as described in this section, a similar dataset as used in H.E.S.S. Col. [2011a] is reanalyzed in a first step. For this, a dataset of 140h livetime H.E.S.S. phase I four-telescope data that consists of multiple (329) observation runs with pointing positions in the vicinity of the galactic center up to a maximal pointing position distance of 1.5° to the galactic center was used. Each individual analyzed observation run passes standard H.E.S.S. data quality checks. A further observation run selection is performed by only analyzing observation runs with mean pointing zenith angle below 30°. This selection criteria serves to reduce the energy threshold as well as to reduce possible deviations of the instrumental acceptance from rotational symmetry due to zenith angle gradients across the field of view[5]. The zenith angle selection criteria reduces the number of analyzed observation runs from 329 to 244 and the livetime of the dataset from 140h to 103h[6]. The mean pointing zenith

[5] The H.E.S.S. I trigger rate scales approximately with $\cos(\theta)$ where θ is the pointing zenith angle. The trigger rate is an approximate measure for the instrumental acceptance and the zenith angle dependence of the trigger rate leads thus to the prediction that the gradient of the acceptance within the H.E.S.S. field of view caused by the fact that different parts of the field of view point towards different zenith angles is the larger the larger the pointing zenith angle is.

[6] The livetime values used for the rotated pixel analysis are all calculated with the standard H.E.S.S. method, not with the method described in appendix A.

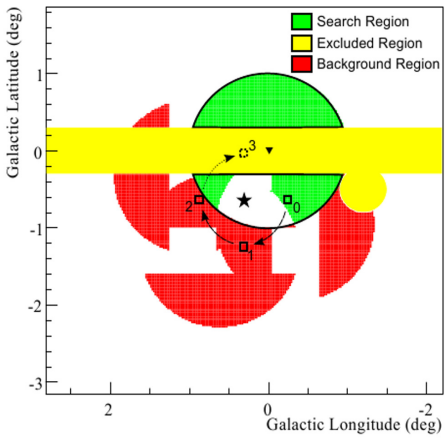

Figure 4.3: Illustration of the background subtraction method employed in H.E.S.S. Col. [2011a] from where also the plot is taken. The signal region around the galactic center is shown in green an the background regions (shown in red) are constructed by rotating individual pixels in the signal region by 90°, 180° and 270° around the pointing position (black star). Yellow regions are excluded from the analysis. White regions in the signal region are not used for the analysis because no background region could be constructed.

angle of the selected dataset is 14°. Background suppression is performed using the Hillas technique with standard image cleaning ('0510') and image intensity (80 pe per analyzed camera image) selection criteria. Additionally, events are only analyzed if their offset from the observation position is smaller than 2°. This avoids the analysis of events that are detected in regions of the H.E.S.S. I field of view where the acceptance drops below $\sim$ 40% of the peak acceptance (see H.E.S.S. Col. [2006]). The dataset and the event selection are very similar to the one described in H.E.S.S. Col. [2011a] where a dataset with pointing positions within 1.5° around the galactic center, pointing zenith angles below 30°, a livetime of 110h and a mean zenith angle of 14° was analyzed. The only remarkable difference between the two datasets and the event selections is that the livetime of the dataset considered in H.E.S.S. Col. [2011a] is by 7h larger than for the dataset considered here. Exclusion regions are chosen to be in agreement with the choice in H.E.S.S. Col. [2011a]. In particular, the galactic plane ($|b| < 0.3°$) is excluded from the analysis and

- The galactic center is excluded with a radius of 0.2°,
- the composite supernova remnant G0.9+0.1 is excluded with a radius of 0.2°,
- the region around the globular cluster Terzan 5 is excluded with a radius of 0.2°,
- the unidentified source HESSJ1745-303 is excluded with a radius of 0.4° and

- the unidentified source HESSJ1741-302 is excluded with a radius of 0.2°.

The size of the exclusion regions is chosen to be in visual agreement with the yellow regions shown in fig. 4.3.
The application of the rotated pixel algorithm to the described dataset gives a total number of detected signal events that pass γ-ray selection criteria of $N_{\mathrm{ON}} = 154905$. The corresponding number of events in the background region is $N_{\mathrm{OFF}} = 621311$ and the exposure ratio is $\alpha = 0.25005$. The exposure ratio is calculated as the mean over the subdataset exposure ratios justified by the RMS[7] of the exposure ratio within the subdataset sample being $\sigma_\alpha \sim 10^{-5}$ and thus negligible as $N_{\mathrm{OFF}}\sigma_\alpha \sim 10$ which is much smaller than the statistical error $\sigma_\Delta \sim 440$ on the excess $\Delta \sim -451$. The significance of the measured γ-ray excess is -1.2σ and the excess is thus compatible with zero. The fit of the distribution of the runwise significances to a Gaussian gives a mean that is compatible with zero, $(3\pm7)\cdot10^{-2}$, and a width that is compatible with unity (1.11 ± 0.05). Significant systematic differences in the signal and background acceptance would lead to a significance distribution that is compatible with a Gaussian with vanishing mean but width that is larger than unity (see also appendix D). It is thus concluded that no significant difference between the acceptance in the signal and background region exists and no systematic error on the excess has to be taken into account.
The result of an energy dependent analysis is shown in fig. 4.4 where the γ-ray excess for events above the energy threshold is shown as a function of the event energy. The energy threshold is defined as the larger value of the trigger energy threshold or the minimal energy bias threshold (see chapter 2). No significant excess is found in the investigated energy range. Eventually upper limits on the velocity averaged WIMP annihilation cross section are derived with the method described in the introduction. Figure 4.5 shows the resulting exclusion lines for different γ-ray spectra and dark matter density distributions. Additionally, the upper limit published in H.E.S.S. Col. [2011a] is shown as the magenta line. As outlined above, the used dataset and the applied data analysis is very similar for the results obtained in this section and in H.E.S.S. Col. [2011a]. The comparison of the corresponding upper limits derived in both analyses (magenta for H.E.S.S. Col. [2011a] and black for the result obtained with the analysis described in this section) shows a good agreement for large WIMP masses (larger than ~ 2 TeV). For lower WIMP masses, the black exclusion line is more constraining. The reason for this is very probably to be found in the energy dependent analysis applied in the analysis that is described in this section but not in the analysis described in H.E.S.S. Col. [2011a]. The upper limit on the number of excess events that contributes linearly to the upper limit on $\langle\sigma v\rangle$ (see eq. 4.29) is for low WIMP masses M only calculated for events with energies E up to $E = M$ which leads in general to a more constraining upper limit on the number of excess events and thus on $\langle\sigma v\rangle$ with decreasing WIMP mass. Apart from that, the overall agreement between the upper limit inferred from the analysis described in this section and the one

[7] A finite width of the subdataset exposure ratio distribution is introduced despite of the demand for exactly four independent background pixel per signal pixel because the exposure ratio is given by $\alpha_i = \sum_{l\in\text{signal}} \cos(b_l) / \sum_{l\in\text{background}} \cos(b_l)$ and the b_l in the signal and background region are varying from observation run to observation run.

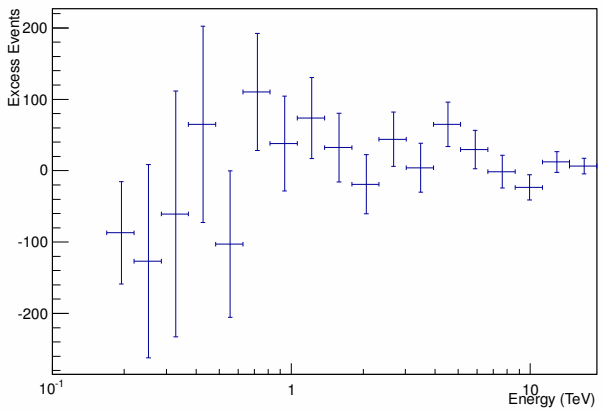

Figure 4.4: Rotated pixel analysis γ-ray excess differential in reconstructed event energy. No significant deviations from a vanishing excess are found.

derived in H.E.S.S. Col. [2011a] is very good. Given that differences in the rotated pixel analysis (number of requested background pixels), the way the upper limit is derived (via flux measurements and self developed methods in H.E.S.S. Col. [2011a] and via excess event measurements and the algorithm described in Rolke et al. [2005] here) as well as possibly the detailed run selection exist, the good agreement is not trivially to be expected. This supports the reliability of the result published in H.E.S.S. Col. [2011a] as well as the methods described in this section. The derived upper limits on $\langle \sigma v \rangle$ are the most constraining limits with respect to the benchmark models investigated in fig. 4.5 and for WIMP masses larger than ~ 400 GeV. The analysis of the dataset has up to now tried to resemble the analysis published in H.E.S.S. Col. [2011a] to compare the results and investigate their reliability. It is argued in the introduction to this chapter that a viable analysis for WIMP annihilation towards the galactic center region that relies on a background subtraction method must

- make sure that astrophysical γ-ray sources in the signal region are not responsible for a putative signal, and that
- astrophysical sources in the background region are not responsible for the subtraction of a WIMP annihilation signal present in the signal region.

The exclusion of the astrophysical sources is in practice to be handled based on a skymap of the region that is created with the investigated dataset. The ad-hoc exclusion of any known γ-ray source is not recommended because the investigated dataset may not be large enough to detect all known γ-ray sources or the dataset may be so large that γ-ray sources are detected which were unknown before. A significance map for the considered dataset, that is generated with a ring background algorithm and correlated with a radius of 0.1°, is shown in fig. 4.6. Exclusion regions as defined above for the analysis have been applied. These regions are not used to estimate the background and appear as blanked

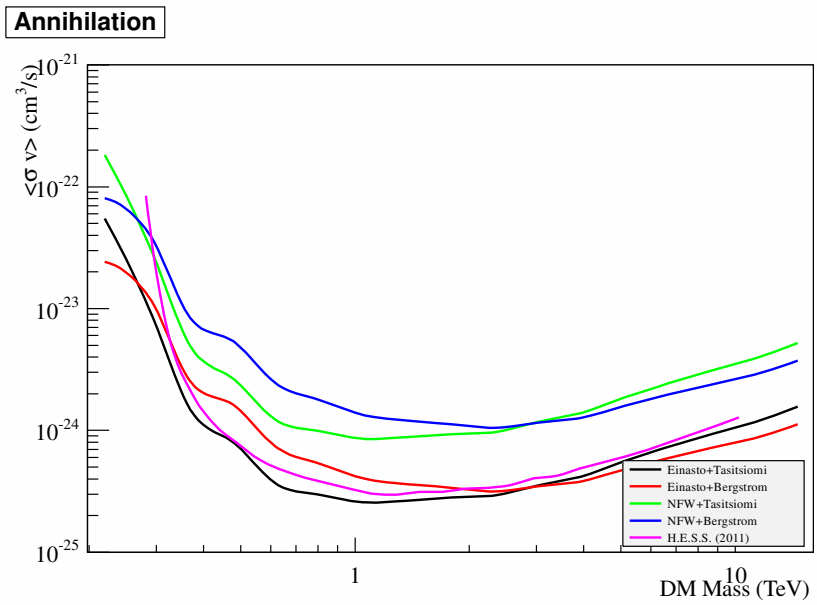

Figure 4.5: Upper limits for the velocity averaged WIMP annihilation cross section as a function of the WIMP mass inferred from the rotated rotated pixel analysis assuming different γ-ray spectra and dark matter density parametrizations. The magenta line shows the upper limit as derived under the assumption of a Tasitsiomi γ-ray spectrum and an Einasto parametrization of the dark matter density in H.E.S.S. Col. [2011a].

in the skymap. Additionally, the signal region of 1° around the galactic center is shown as a black circle in fig. 4.6. Although no single point in the skymap marks a significant excess, the exclusion of the galactic plane in the signal region with $|b| < 0.3°$ appears insufficient as does the radius of 0.4° for the exclusion of the γ-ray source HESSJ1745-303 at $l = 358.7°$, $b = -0.6°$. This could, depending on the exposure distribution, lead to the situation where the γ-ray signal detected due to the insufficient exclusion regions in the signal and the background region balance by chance and no signal is found in total. It could even lead to the case where the γ-ray signal detected due to the insufficient exclusion of a source in the background region and the γ-ray signal detected due to the insufficient exclusion of the signal region plus a γ-ray signal generated by WIMP annihilations in the signal region are balancing each other by chance.
In order to claim a non-detection of a signal, the most important point is to make sure that the background region is as free of a signal flux as possible. For the case considered here, this can be best achieved by

- increasing the exclusion radius for HESSJ1745-303 from 0.4° to 0.8° and
- additionally only considering the regions below and above the signal region in latitude, i.e. $|b| > 1°$ as background regions.

The last item concerns the potential presence of a large scale diffuse γ-ray signal from the galactic plane which could not be detected with a local background algorithm, such as the ring background method that is used to generate fig. 4.6. The presence of such a signal is expected because the material present in form of dust and gas in the galactic plane acts as target material for hadronic cosmic rays. Additionally, the increased intensity of low energy photon fields generates a target for the up-scattering of low energy photons via the inverse Compton scattering of high energy electrons in the galactic plane. The large scale diffuse emission from the galactic plane is investigated in more detail in the next chapter. At this point it is sufficient to state that it is in general expected that the large scale diffuse emission is decreasing with latitude, essentially because the target material density of the galactic disc is decreasing with latitude. However, inhomogeneities of the large scale galactic diffuse emission within the galactic plane are potentially present. To exclude the balancing of putatively present signals with inhomogeneities of the galactic large scale diffuse emission, the background estimation for the signal region is conservatively only to be obtained from below or above the galactic plane.
It has been investigated in detail that the re-analysis of the dataset described above with an increased radius (0.8°) for the exclusion of HESSJ1745-303 as well as the consideration of background events only from above and below the galactic plane ($|b| > 1°$) does not yield a significant γ-ray excess. In numbers, $N_{\mathrm{ON}} = 90216$ signal and $N_{\mathrm{OFF}} = 360820$ background events are detected for an exposure ratio of $\alpha = 0.25001$ which leads to a γ-ray excess of 7 events and a statistical significance of 0.05σ. It is concluded at this point that the analysis of the considered dataset is indeed sensitive to the benchmark models investigated in fig. 4.5.

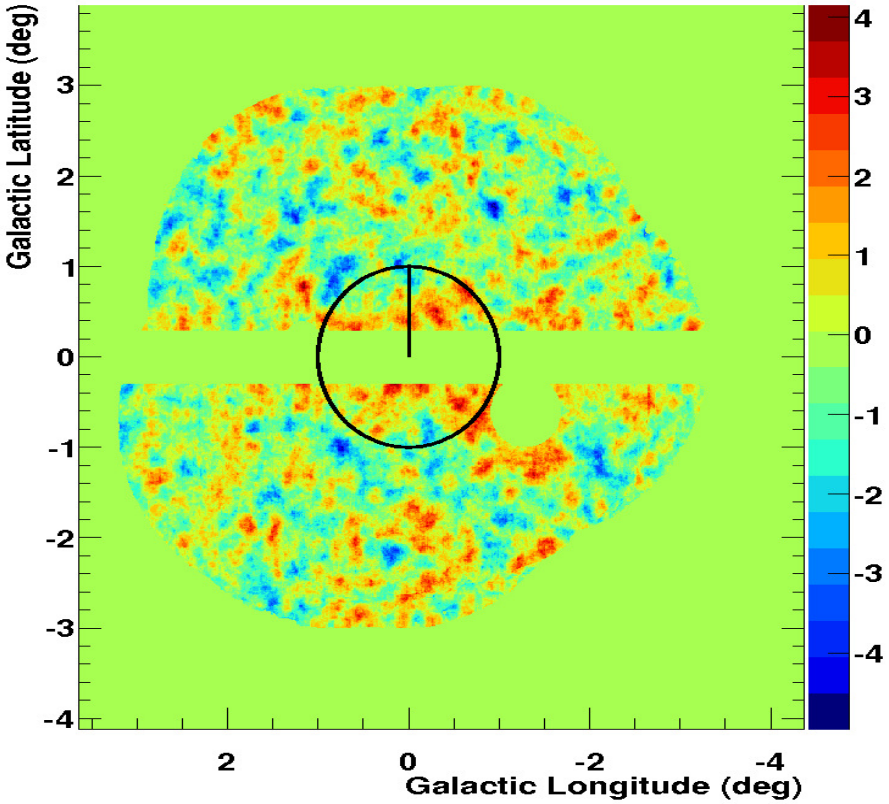

Figure 4.6: Significance map generated with a ring background algorithm with an integration radius of 0.1° for the dataset 1 discussed in the rotated pixel analysis section. The black circle marks the signal region of the rotated pixel analysis, regions left blank have either no exposure or are excluded from the analysis.

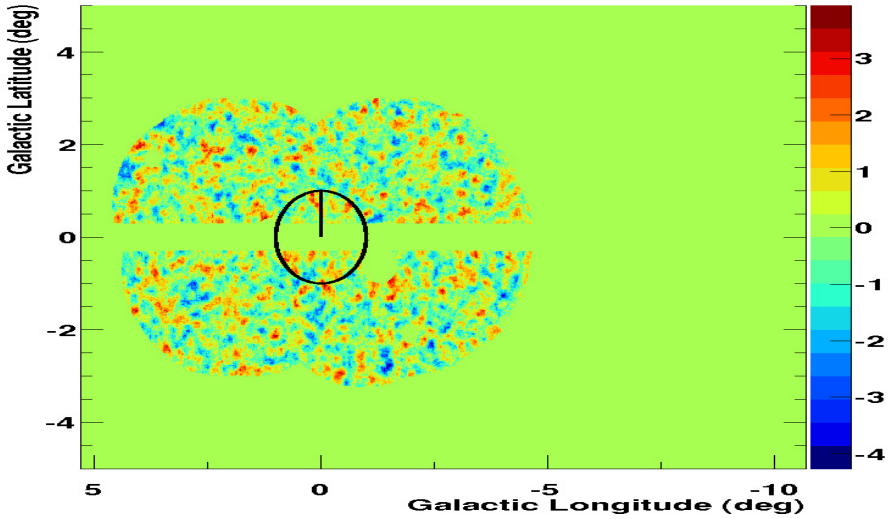

Figure 4.7: Significance map generated with a ring background algorithm with an integration radius of 0.1° for the dataset 2 discussed in the rotated pixel analysis section. The black circle marks the signal region of the rotated pixel analysis, regions left blank have either no exposure or are excluded from the analysis.

Analysis of Dataset 2

The dataset analyzed in the previous section (dataset 1) is selected such that the maximal allowed distance of the pointing position of an observation run to the galactic center is 1.5°. Indeed the majority of the pointing positions of the observation runs considered in dataset 1 is within 1° around the galactic center, i.e. within the signal region. It is interesting to investigate what follows if this constraint is relaxed to a maximal distance that only guarantees that the signal region of 1° around the galactic center is in the field of view of 2° around the pointing position. In practice this can be achieved by demanding that the maximal distance of the pointing position of a run is within 2.8° around the galactic center. To concentrate on the differences compared to dataset 1, a small dataset 2 with observation run pointing positions within 1.5° and 2.8° angular distance to the galactic center is investigated in the following. The total livetime of dataset 2 is 23 h distributed over 55 four-telescope observation runs each of which passes standard data quality checks. Figure 4.7 shows a significance map (correlation radius 0.1°) created with a ring background subtraction algorithm and the same exclusion regions that are also used for the analysis of dataset 1. No regions with a significant signal are apparent on the significance map. Figure 4.8 shows the resulting event maps for the signal (upper panel) and background region (lower panel) of a rotated pixel analysis of dataset 2 that is performed in complete similarity to the analysis of dataset 1. In total, $N_{\mathrm{ON}} = 19029$ signal and $N_{\mathrm{OFF}} = 73724$ background events have been recorded. Selection criteria

on the event energy (energy threshold etc.) have not been applied in this analysis because no energy dependence is investigated. The minimal reconstructed event energy in dataset 2 is ~ 200 GeV. The average exposure ratio of the dataset is $\alpha = 0.25008$ and the RMS of the exposure ratio distribution is negligible ($\sim 10^{-5}$). The total number of γ-ray excess events is $\Delta = 592$ corresponding to a significance of $S_{\mathrm{LiMa}} = 3.8\sigma$. The mean zenith angle of the investigated dataset is $\sim 21^\circ$ but the dataset contains runs with average zenith angle of more than 30°. If only observation runs whose mean zenith angle is smaller than 30° are considered, the livetime is reduced from 23 h to 13 h and the significance of the excess is reduced to 2.7σ. If the full dataset is considered but only background events that originate from below or above the galactic plane according to $|b| > 1^\circ$ are used for the background estimation, a total of $N_{\mathrm{ON}} = 17928$ events in the signal region and $N_{\mathrm{OFF}} = 68601$ events in the background region are observed which corresponds to an excess measurement of $\Delta = 770$ events with statistical significance of 5.2σ. The blanking of the galactic plane in the background region with $|b| > 1^\circ$ can be motivated with the argument that putatively present diffuse γ-ray emission should be decreasing in intensity with increasing distance to the galactic plane, i.e. with increasing $|b|$. For the quantitative motivation of the cut in latitude, see also the next chapter. It is unlikely that the hint for an excess towards the galactic center region that results from the rotated pixel analysis of dataset 2 is due to a software problem as this has been checked in depth with Monte Carlo generated input. It is also considered as unlikely but cannot be ruled out that deviations of the acceptance from a rotational symmetry around the observation position are causing the result. In the case of dataset 1, a significant deviation of the rotational symmetry of the acceptance would lead to a fitted Gaussian width of the runwise significance distribution that is larger than unit. Because this is not observed, it is concluded that the acceptance of an observation run in dataset 1 is with sufficient precision rotationally symmetric within the considered ranges of event offsets from the observation position. Figure 4.9 shows in the upper panel the distribution of the offsets of the considered signal and background events (both distributions are by construction equal) from the observation position shown for dataset 1 and 2. Both distributions are not differing significantly. The presence of the rotational symmetry of the acceptance for a given observation run across the field of view in dataset 1 suggest that deviations of the acceptance from rotational symmetry are unlikely to cause the hint for an excess in dataset 2.

The analysis of dataset 1 and 2 do not necessarily contradict each other because the average distance of the background region to the galactic center is larger for dataset 2 than for dataset 1. This is explicitly shown in fig. 4.9 where in the lower panel the normalized distribution of distances between employed background pixel and the galactic center is shown. Background pixel for the analysis of dataset 1 are typically within 2° around the galactic center but outside of the 2° radius in the analysis of dataset 2. The application of additional selection criteria to match the shape and location of the signal and background regions of dataset 1 and 2 has been investigated but is found to be inconclusive due to the limited amount of data and the overall low significances.

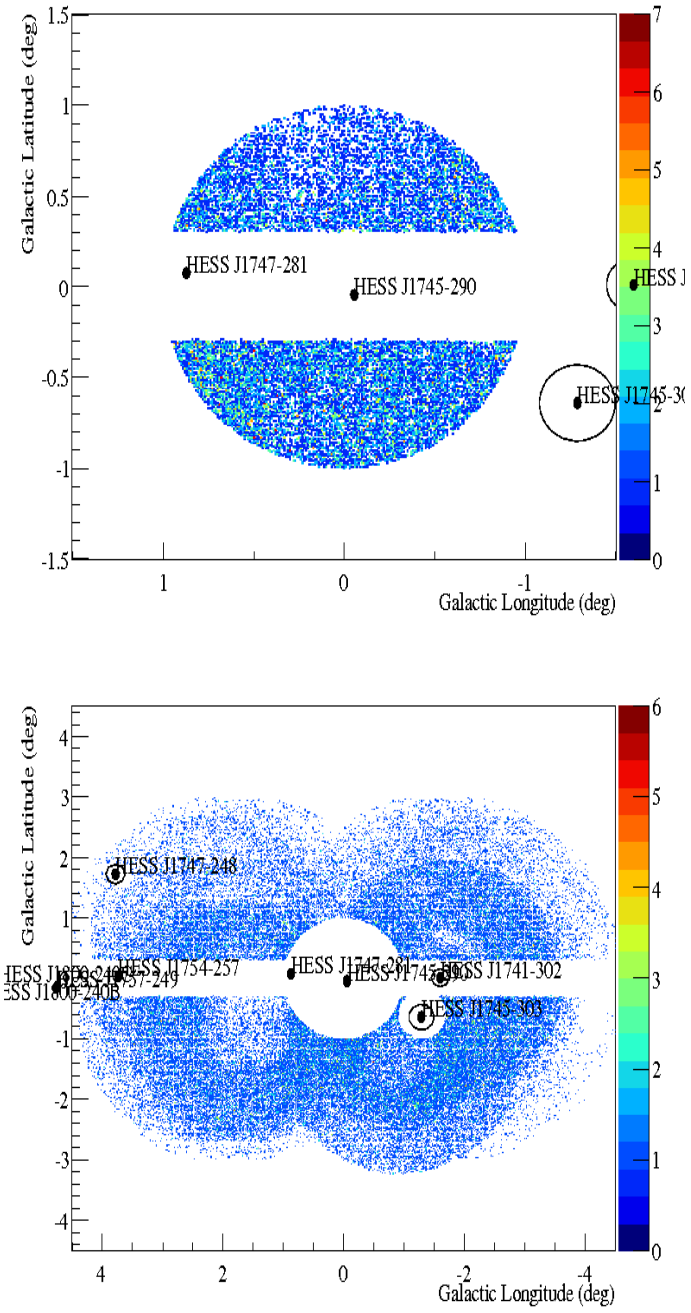

Figure 4.8: Reconstructed event positions in the signal (upper panel) and background region (lower panel) for the rotated pixel analysis of dataset 2.

No final conclusion on the situation will be given here[8] but the results and discussion of the analysis of dataset 2 should indicate that the rotated pixel analysis is possibly more complicated than the result of the analysis of dataset 1 suggests. Especially the possible presence of a band of diffuse γ-ray emission towards the galactic plane must be taken into account when results of a rotated pixel analysis for the presence of WIMP annihilations in the center of the Milky Way dark matter halo are interpreted. The non detection of a γ-ray excess can only lead to a limit on a WIMP model related quantity if it is assumed that a putatively present WIMP annihilation signal is not by chance balanced by a diffuse emission signal of possibly complicated morphology. It is, however, very unlikely that this happens in dataset 1.
What concerns the results of the analysis of dataset 1 with respect to the upper limits on $\langle \sigma v \rangle$ it is concluded that the results derived above and previously in an independent analysis (H.E.S.S. Col. [2011a]) are stable but should be quoted with the stated restriction with respect to the possibility that a WIMP signal is balanced by a diffuse γ-ray signal from the galactic plane.
The results of the analysis of dataset 1 and 2 should be kept in mind for the discussion of an analysis for the presence of large scale diffuse γ-ray emission from the galactic plane presented in chapter 5.

4.2.2 On/Off Method

Figure 4.10 shows H.E.S.S. I γ-ray events passing standard γ-ray event selection criteria in three different field of views. The galactic center region is observed as a signal region (fig. 4.10 upper plot). Symmetrically offset in right ascension are the two background regions (fig. 4.10 lower plot). Suitably chosen exclusion regions are mutually applied to all observed field of views respectively. The observation of the regions shown in fig. 4.10 is performed with a particular pointing strategy where always three H.E.S.S. I standard observation runs are taken consecutively such that the zenith and azimuth pointing angle range is always equal for each run within a sequence of three runs. This is guaranteed by starting one observation sequence with the 33 min runlength observation of a background region with -35 min offset in right ascension from the signal region pointing position. The array pointing moves forward by 35 min in right ascension immediately after the end of the first observation within a realistic run transition time of 2 min. The second run of the sequence observes then the signal region for 33 min. The third observation

[8] Note that also the On/Off analysis presented later will not lead to a conclusion on the presence or non presence of a γ-ray excess in dataset 2. The On/Off analysis applied as described below but with a signal region limited to 1° around the galactic center and exclusion regions similar to the one discussed for dataset 1 and 2 does not lead to a significant excess. The 'diffuse exposure' of the signal region, i.e. the product of signal region field of view and livetime summed over all considered observation runs is ~ 21 ssr for dataset 2 and ~ 5 ssr for the On/Off analysis. It is thus expected that the significance of the On/Off analysis is reduced by a factor of $\sim \sqrt{5/21} \sim 1/2$ when compared to the result of the analysis of dataset 2. This neglects corrections due to differing offsets and zenith angles. Additionally, the On/Off analysis faces problems with systematic effects that are described below and prevent any conclusion concerning the excess that occurs in the rotated pixel analysis of dataset 2.

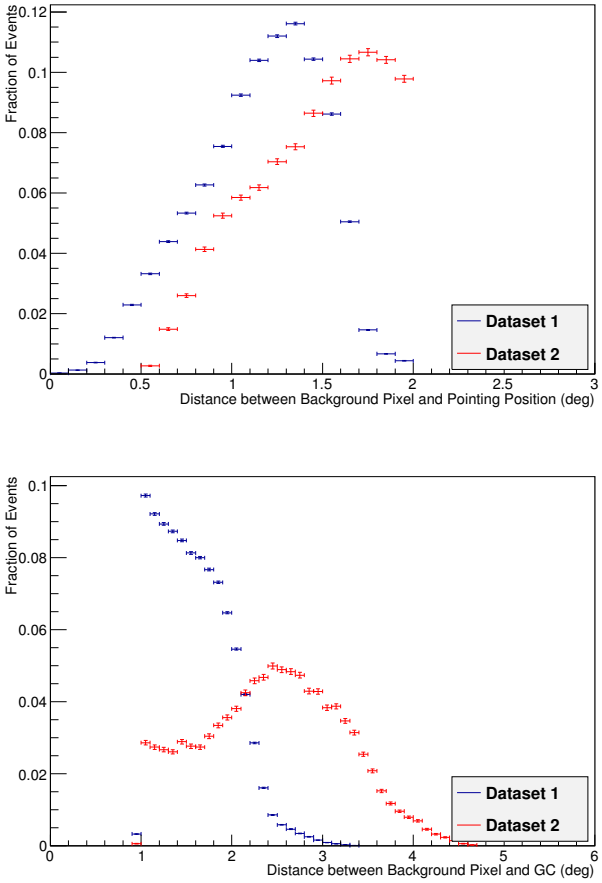

Figure 4.9: Distribution of the distance of background pixels from the observation position (upper panel) and of the distance of background pixels to the galactic center (lower panel). Shown in blue and red are the distributions for dataset 1 and 2, respectively. The distribution of the distance of the used background pixels to the observation position is very similar for both dataset. In contrast, the distribution of the distance of the used background pixels to the galactic center differs. For dataset 1, only few background pixels have a distance of more than 2° to the galactic center. The opposite holds for dataset 2. In both cases, no background pixels are used with a distance of less than 1° to the galactic center, i.e. from the signal region.

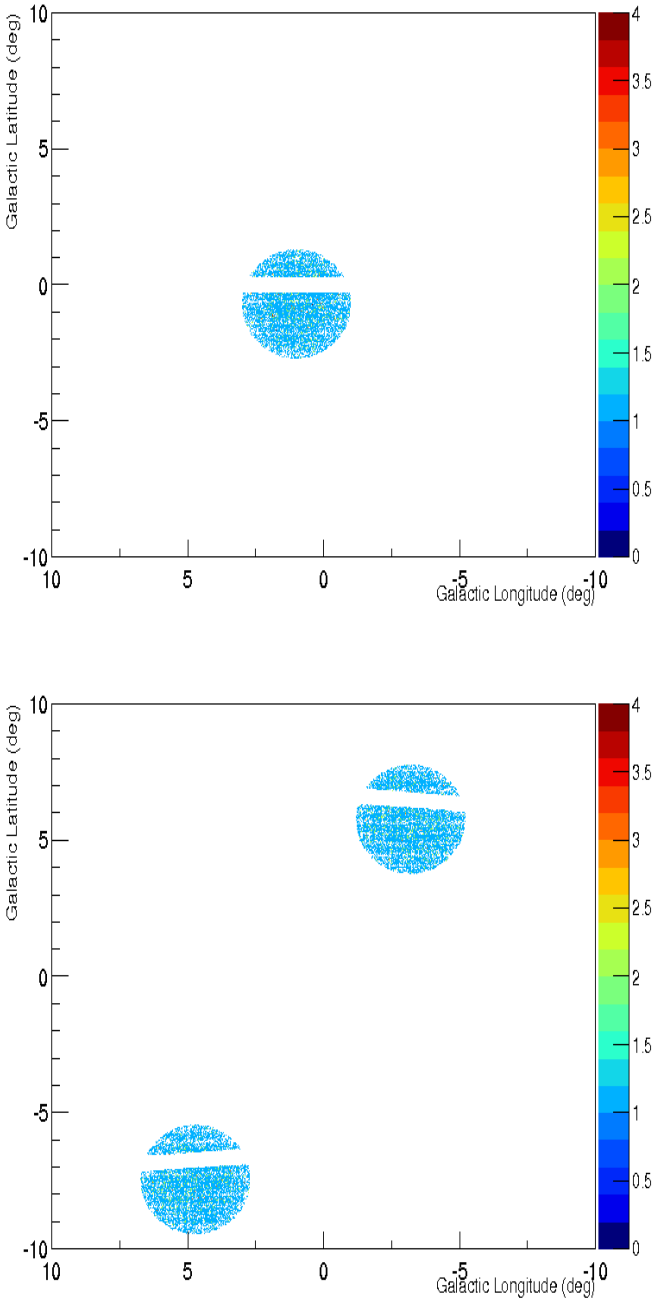

Figure 4.10: H.E.S.S. I events (color scale) for the observation of a signal region with the full H.E.S.S. I field of view (upper plot) and two background regions (lower plot) in galactic coordinates. The pointing positions for the background regions have a symmetric offset (±35 min) in right ascension to the pointing position of the signal region. All exclusion regions are mutually applied to all observation regions in the field of view system.

is again scheduled for 33 min immediately after the second observation by moving the array pointing by 35 min forward in right ascension within 2 min. Finally, the number of events after the application of standard γ-ray event selection criteria in the signal region and the corresponding number of events in the background region can be compared and the γ-ray excess can be calculated. The observation strategy ensures, as stated, that the zenith and azimuth pointing angle range is always the same for every run within a run sequence. The strong dependence of the H.E.S.S. I acceptance on the pointing zenith and azimuth angle does in consequence not influence the calculation of a γ-ray excess as the dependence is the same for the signal and the background region. The advantage of this method compared to the rotated pixel method is that obviously the signal region can be as large as the H.E.S.S. field of view and that the background regions are further away from the signal region (see also the blue and yellow region in fig. 4.1). The result is that the expected WIMP self annihilation γ-ray flux in the background region is smaller than for the rotated pixel method. This leads in turn to the expectation that the sensitivity of the On/Off observations to a WIMP annihilation γ-ray flux in the Milky Way halo is larger than for the rotated pixel background subtraction technique. On the other hand, the method needs 2/3 of the total observation time for the estimation of the expected number of background events in the signal region where the rotated pixel algorithm can use the complete observation time. It is a non trivial question which of the two competing factors is eventually dominant and a detailed investigation is presented later.

Dataset Description and Pointing Compatibility

In total, a dataset containing six triples of H.E.S.S. I four-telescope observation runs is considered in this section. Each run triple contains, as described above, two observations of OFF regions with ± 35 min offset in right ascension from the signal region center at RA = 17h50min, Dec = $-28.3°$. All regions, the ON region and the two OFF regions, within a run triple are observed consecutively with a run transition time of ~ 2 min for ~ 33 min. The total observation livetime, i.e. the dead time corrected runtime, spent in each region is ~ 3 h. Each single considered observation run passes standard H.E.S.S. data quality criteria.
The background regions used in the On/Off analysis presented in this section have not been observed with H.E.S.S. before and it is thus unclear whether or not γ-ray sources are contained within the background regions. Figure 4.11 shows a significance map for events that pass standard Hillas γ-ray event selection criteria of the two background regions respectively. It is concluded that no local γ-ray source is detected within the background regions. The signal region used for the On/Off analysis is well known and as for the rotated pixel method, the galactic plane ($|b| < 0.3°$) is excluded from the later analysis. It is visible in fig. 4.12 that the exclusion of the galactic plane is already sufficient to exclude all significantly detected regions, i.e. the galactic center source and G0.9+0.1 from the later analysis of events that pass standard γ-ray selection criteria.
As stated above, the particular observation strategy ensures that the array pointing position as a function of time in the horizon system, i.e. the pointing zenith and azimuth angle, is the same for all three runs within a run triple. In practice, this works very well

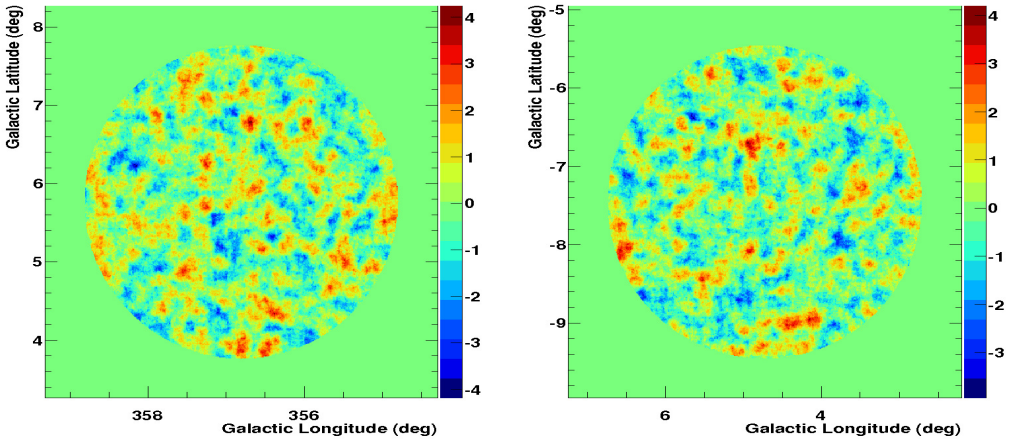

Figure 4.11: Significance skymaps for the OFF1 (left panel) and OFF2 (right panel) dataset used for the background estimation in the On/Off analysis. The skymaps have been created with the ring background algorithm and signal and background map are correlated with a correlation radius of 0.1° respectively. The field of view is limited to 2° around the observation position in both cases. No significant excess is visible in the skymaps. The significance distribution is in both cases compatible with being standard normal.

(see fig. 4.13 for one On/Off run triple and the similar plots in appendix B for the other considered run triples). It follows that differences in the H.E.S.S. array acceptance to γ-ray and background events that are caused by the dependence of the H.E.S.S. acceptance on the array pointing position in the horizon system are negligible. Despite of the array pointing position in the horizon system as a function of the observation time being compatible within a run triple, the array trigger rate[9] does vary significantly from observation run to observation run within a run triple (see the R_{Trig} column in table 4.1 as well as the rate-over-time plots in appendix B). This shows that the observation under equal array pointing positions in the horizon system does not suffice to guarantee equal instrumental acceptance. Instead, it must be investigated which physical effects cause the acceptance changes from run to run. Note that the trigger rates given in table 4.1 are calculated without application of any exclusion regions. Events originating from the γ-ray sources in the signal region do thus contribute to the signal region trigger rate. However, the event rate before application of any event selection criteria as well as the preselected event rate is completely dominated by background events and as a consequence, the small flux of γ-ray events from γ-ray sources in the signal region does not significantly influence the measured event rates.

[9]Event rates (R) are calculated from a fit of the distribution of time differences (Δt) between consecutive events to an exponential ($\exp(-R\Delta t)$) in the range $\Delta t > 1$ ms (far away from the telescope dead time of $\sim 400 - 800\ \mu$s) to $\Delta t < 0.1$ s in this section. See also appendix A.

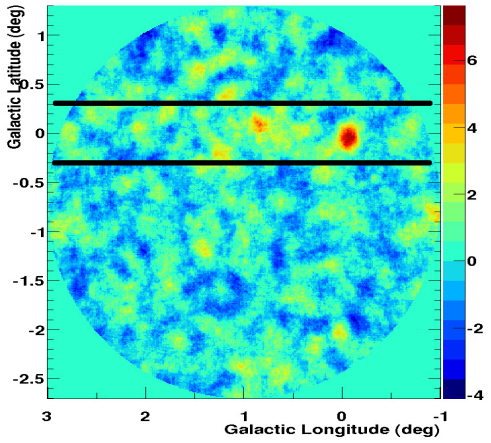

Figure 4.12: Significance skymap for the ON dataset in the On/Off analysis. The skymap has been created with the ring background algorithm and signal and background map are correlated with a correlation radius of 0.1° respectively. The field of view is limited to 2° around the observation position. The region within the two horizontal black lines is excluded from the On/Off analysis. Clearly visible within the excluded region are the galactic center source HESS J1745-190 and the composite supernova remnant G0.9+0.1.

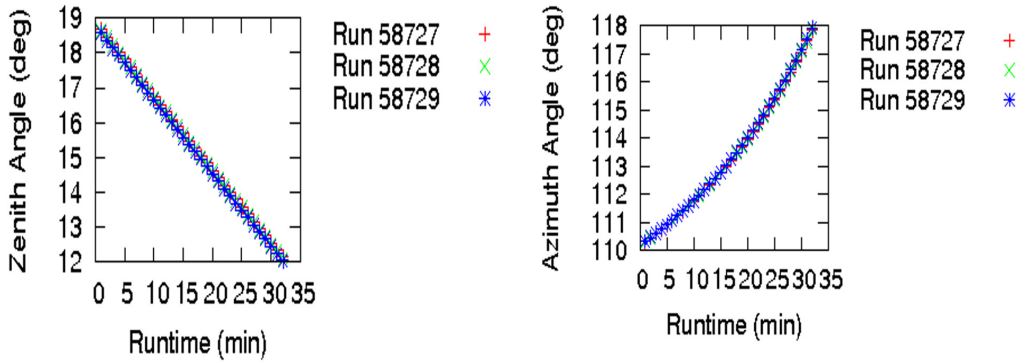

Figure 4.13: Horizon system pointing compatibility in zenith (left panel) and azimuth (right panel) for one On/Off observation run triple. The plot shows that the horizon system pointing compatibility is very good within the considered run triple. For the other run triples of the full On/Off dataset, see the equivalent plots in appendix B.

Run	Type	DS	T_{Live} (s)	R_{Trig} (Hz)	R_{Presel} (Hz)	BrPixel
58727	OFF1	1	1737.8 ± 0.4	$177.4 \pm 0.3 \pm 0.03$	53.8 ± 0.2	123
58728	ON	1	1733.8 ± 0.6	$180.4 \pm 0.3 \pm 0.06$	53.2 ± 0.2	182
58729	OFF2	1	1730.8 ± 0.4	$182.4 \pm 0.3 \pm 0.03$	53.5 ± 0.2	154
58801	OFF1	2	1754.3 ± 0.7	$162.7 \pm 0.3 \pm 0.06$	49.1 ± 0.2	131
58802	ON	2	1758.4 ± 0.4	$158.7 \pm 0.3 \pm 0.02$	48.2 ± 0.2	138
58803	OFF2	2	1760.3 ± 0.8	$157.3 \pm 0.3 \pm 0.07$	47.6 ± 0.2	130
58804	OFF1	3	1767.5 ± 0.4	$152.0 \pm 0.3 \pm 0.01$	46.0 ± 0.2	152
58805	ON	3	1765.0 ± 1.3	$153.9 \pm 0.3 \pm 0.1$	46.2 ± 0.2	153
58806	OFF2	3	1753.2 ± 0.4	$163.5 \pm 0.3 \pm 0.03$	48.5 ± 0.2	170
58828	OFF1	4	1733.7 ± 1.0	$180.7 \pm 0.3 \pm 0.1$	52.3 ± 0.2	221
58829	ON	4	1730.8 ± 1.6	$184.9 \pm 0.3 \pm 0.2$	53.5 ± 0.2	208
58830	OFF2	4	1725.8 ± 1.5	$187.6 \pm 0.3 \pm 0.3$	54.7 ± 0.2	164
58859	OFF1	5	1707 ± 5	$204.4 \pm 0.4 \pm 0.6$	60.3 ± 0.2	151
58860	ON	5	1705 ± 6	$206.4 \pm 0.4 \pm 0.7$	59.3 ± 0.2	177
58861	OFF2	5	1704 ± 8	$207.5 \pm 0.4 \pm 1.0$	60.1 ± 0.2	171
58886	OFF1	6	1708 ± 6	$202.1 \pm 0.4 \pm 0.4$	60.0 ± 0.2	164
58887	ON	6	1709 ± 5	$204.2 \pm 0.4 \pm 0.7$	59.1 ± 0.2	163
58888	OFF2	6	1709 ± 5	$202.5 \pm 0.4 \pm 0.6$	59.1 ± 0.2	185

Table 4.1: Detailed description of the On/Off dataset. Equal subdatasets (DS) entries denote runs that belong to the same On/Off run triple. The livetime (T_{Live}, calculated as described in appendix A) and the trigger (R_{Trig}) as well as the preselected event rate (R_{Presel}) are calculated considering only events where the number of triggered telescopes is equal to the number of read out telescopes and the time difference to the previous event is larger than 1 ms. For further details on the calculation of the livetime and the given error on the livetime that increases with the trigger rate, see appendix A. The preselected event rate is calculated for events which pass '0710' image cleaning additional to the preselection event criteria (see text). The number of broken pixels (BrPixel) is the number of pixels in all 4 telescopes which never triggered with a positive signal during the runtime. The given error on the trigger rate is $\pm$ statistical error $\pm$ systematic error. The error on the preselected event rate is statistical only as the systematic error is much smaller in all cases.

Night Sky Background Compatibility

In between the three regions observed for every run triple, the night sky background (see chapter 2) differs. It cannot be ruled out that this effect influences the acceptance. Figure 4.14 shows relative differences for the pixel intensities of all four-telescopes for events that pass preselection criteria between one On/Off run triple. Similar plots for the other considered run triples are given in appendix B. For pixel intensities that are larger than 7 pe, the differences between the number of times a given pixel intensity is measured in the array are non-zero but almost constant. In contrast, a non-constant difference is observed for pixel intensities smaller than 7 pe in fig. 4.14 and in the corresponding figures given in appendix B. The effect is very probably a consequence of differing night sky background levels between the signal and the two background regions. In favor of this conclusion is the fact that the difference between the number of times a given pixel intensity smaller than 7 pe is measured is always smaller than the approximately constant difference measured for intensities larger than 7 pe in the case of ON-OFF1. The opposite holds for ON-OFF2, i.e. when the signal region and the second background region are compared. Here, the differences in the number of times a pixel triggers with an intensity that is smaller than 7 pe is always larger than for intensities larger than 7 pe. The choice of the background region is thus responsible for the differences in the number of times a pixel triggers with an intensity that is smaller than 7 pe. No background region dependence is visible for pixels that trigger with intensities that are larger than 7 pe where the approximately constant difference can be well explained with the overall preselected rate differences between the ON and the OFF observation runs. Only events that pass '0710' image cleaning criteria, i.e. a pixel is selected for the further analysis if it has at least 10 pe intensity and at least one neighboring pixel with at least 7 pe intensity. All pixels with intensities smaller than 7 pe are thus not considered in the following. Additionally, only events that pass standard H.E.S.S. preselection criteria are considered. Of course the standard H.E.S.S. effective area has to be recalculated for the analysis of data with the increased image cleaning thresholds. Figure 4.15 shows a comparison of the H.E.S.S. I four-telescope effective area at 20° zenith angle between standard '0510' and the modified '0710' image cleaning. The modified image cleaning leads, as expected, to an energy dependent but in general moderate decrease of the effective area. The higher image cleaning level together with the event preselection suppress possible effects of night sky background differences between the regions observed within a run triple. However, even after night sky background effects are suppressed, the acceptance of the H.E.S.S. array is not identical for runs within a On/Off run triple. This is visible in the R_{Presel} column of table 4.1 that holds the preselected event rates after '0710' image cleaning. The preselected event rates after '0710' image cleaning are obviously not compatible within a run triple considered for the On/Off analysis. The same effect is also already visible in fig. 4.14 where also differences for the '0710' image cleaned pixel intensities between ON and OFF runs are apparent. However, it is unlikely that this effect is caused by night sky background differences because the relative pixel intensity differences for pixels with large intensities (f.i. 100 pe) are as large as for pixels with small intensities (f.i. 10 pe). Night sky background effects are expected to have

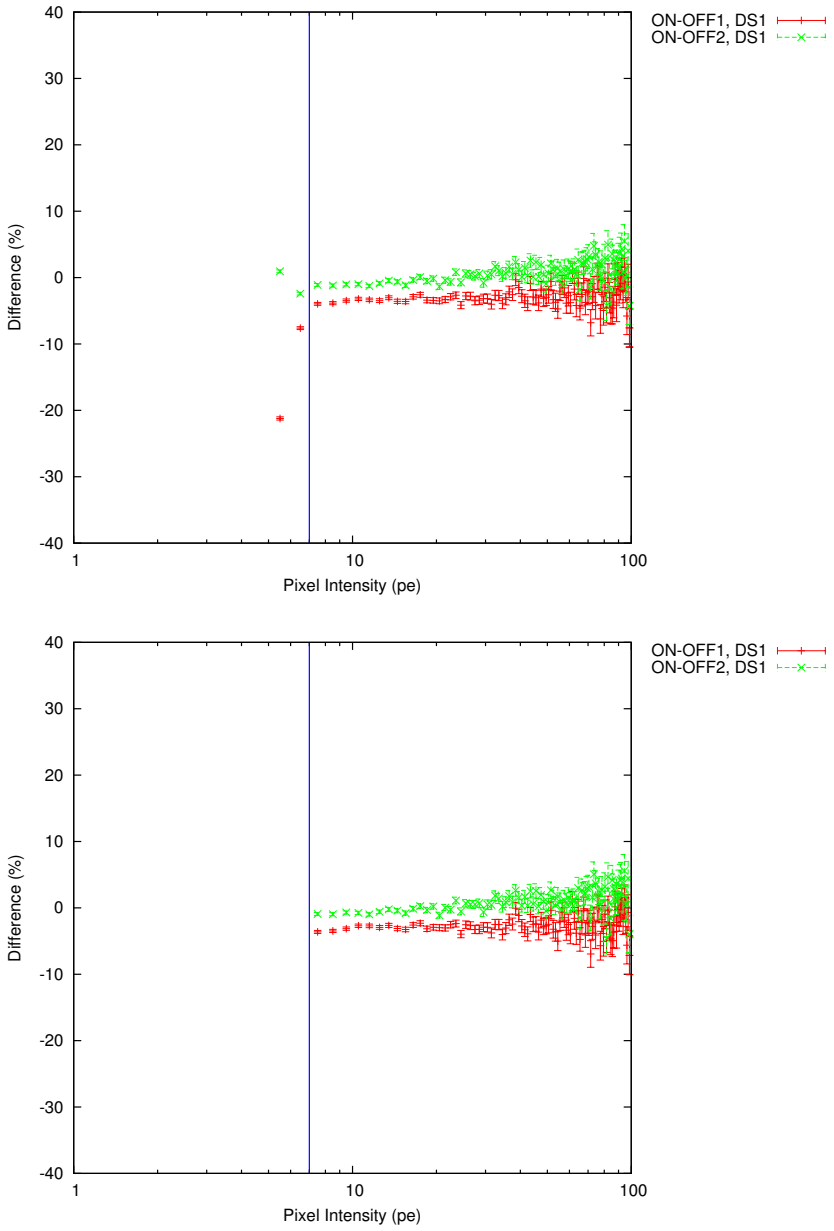

Figure 4.14: Relative pixel intensity difference, i.e. relative difference in the number of times a given intensity is measured in one of the array pixels (all four cameras), for one On/Off run triple (dataset 1 in table 4.1). Shown in green is the relative pixel intensity difference for ON-OFF1 and in red ON-OFF2. The blue line indicates 7 pe. The upper panel is for preselected events passing standard '0510' image cleaning. Large differences in the number of pixels with intensity below 7 pe are visible in the upper plot. The lower plot shows the same data but passing '0710' image cleaning. In the lower plot, the differences are non-zero but constant over the considered pixel intensity range. The constant shift can be explained by the constant (preselected) rate shifts between the On and the Off data runs (see also table 4.1). See also the similar plots for the full On/Off dataset in appendix B.

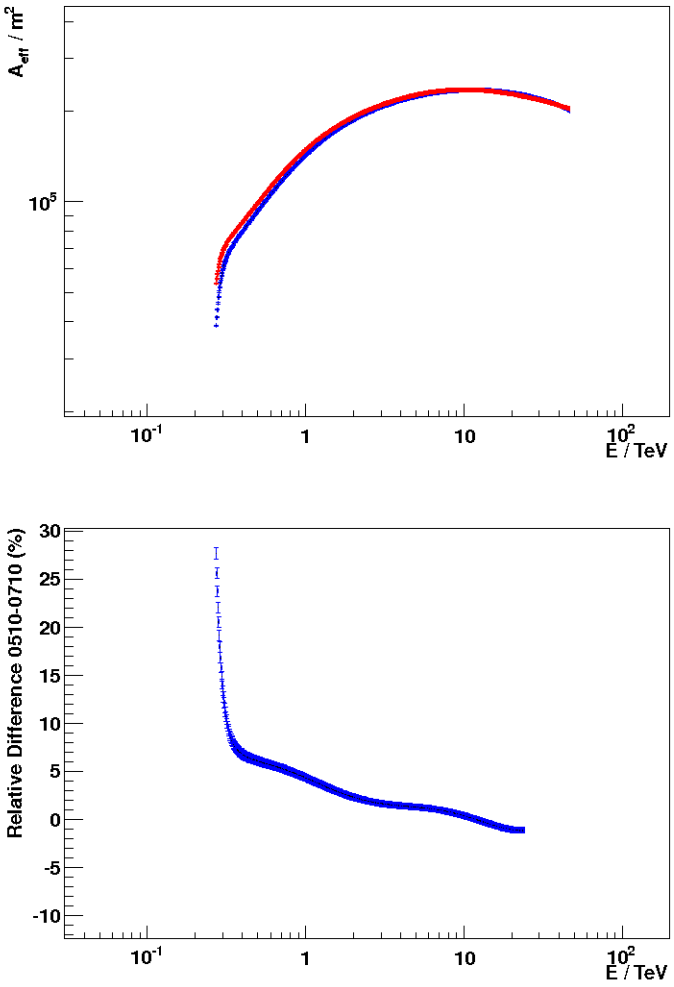

Figure 4.15: Comparison of the H.E.S.S. I four-telescope effective area at 20° zenith angle and 0.5° event offset from the field of view center for standard '0510' and '0710' image cleaning. The upper panel shows the absolute effective areas ('0510' in red and '0710' in blue). The lower panel shows the relative effective area differences for '0510' and '0710' image cleaning. Differences in the effective area decrease with event energy and are only larger than $\sim 10\%$ below the typical analysis energy reconstruction threshold.

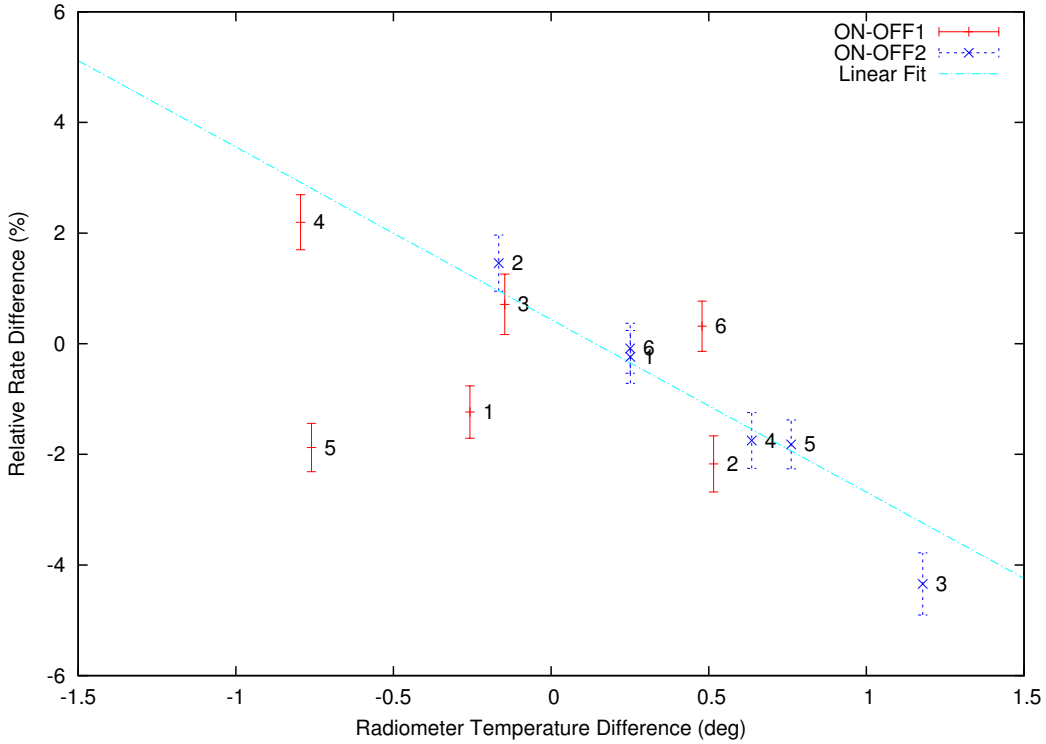

Figure 4.16: Relative preselected and '0710' image cleaned event rate difference for the ON and OFF pointing. Shown in red (blue) are the relative differences for the ON region with the OFF1 (OFF2) region as a function of the radiometer temperature difference. The light blue function is a linear fit to the dependence of the relative preselected event rate difference on the radiometer difference excluding datapoints (ON-OFF1 datasets 1 and 5) where a significant influence of the rate difference by differences in broken camera pixels is supposed.

more impact on small than on large pixel intensities. Additionally, the difference does not systematically depend on the observed OFF region which would also be expected if they were caused by night sky background effects. Other reasons for the different instrumental acceptances that result in the different '0710' cleaned event rates have thus to be searched.

Preselected Rate Compatibility: Atmospheric Effects and Broken Pixels

An obvious additional source for acceptance differences between ON and OFF observation runs are changes in the average atmospheric state during the two observation runs and changes in the number of broken camera pixels. The consecutive data taking aims at minimizing these effects but it is not a priori clear whether this is sufficient. Figure

4.16 shows the relative event rate difference[10] between signal and background observation runs for events passing the '0710' image cleaning and preselection as a function of the radiometer temperature difference between the runs. The figure shows again explicitly that despite the suppression of night sky background effects by the increased image cleaning thresholds, the event rates and thus the instrumental acceptance for runs taken consecutively and with the same zenith and azimuth pointings are incompatible. The level of incompatibility varies from run pair to run pair and no significant preference for the rate difference to be positive or negative is observable. A typical magnitude for the incompatibility is $\sim 2\%$. In addition to the existence of (preselected) event rate differences at the level of $\sim 2\%$ between two runs taken consecutavly and with equal zenith and azimuth pointing, fig. 4.16 also shows the radiometer temperature differences[11] between two considered runs. Within the errors on the event rate, there is no significantly positive rate difference when the radiometer temperature difference is positive. Excluding the red datapoints labeled by (1) and (5) in fig. 4.16, there is also within event rate errors no significantly negative rate difference for negative radiometer differences in the considered dataset. Ignoring for the moment the excluded datapoints which are discussed later, this apparent anti-correlation of the event rate with the radiometer temperature motivates a (linear) fit of the relative rate difference to the radiometer difference between two runs. Also from the physics point of view, an anti-correlation between the event rate and the radiometer temperature is expected. This is because an increasing radiometer temperature indicates an increasing amount of atmospheric material (primarily water vapor[12]) in the radiometer field of view. As a result, the Cherenkov light absorption is expected to be increasing with increasing radiometer temperature and thus the event rate is expected to be decreasing. However, this effect has up to now only been investigated on a qualitative level. The blue line in fig. 4.16 shows the result of a linear fit of the data excluding the mentioned datapoints to ($\Delta R = a\Delta T + b$) with $a = (-3.2 \pm 0.5)\%/\Delta T$ and an offset parameter that is compatible with zero, $b = (0.4 \pm 0.3)\%$. A linear fit without offset gives $a = (-2.8 \pm 0.5)\%/\Delta T$). However, the χ^2/NDF for the fits are 21/8 and 26/9 for the fit with and without offset, respectively. The χ^2/NDF and the up to yet excluded red datapoints labeled (1) and (5) in fig. 4.16 indicate strongly that the radiometer temperature is not the only physical quantity that influences the event rate difference for a given pair of runs out of an On/Off data run triple. Besides the night sky background from the observation region itself and the atmosphere between the instrument and the shower, the only likely source is the Cherenkov array itself. As

[10] The relative event rate difference is defined as 1-rate(off)/rate(on) where rate(off) can be either the event rate of the off1 or the off2 region

[11] The radiometer temperature difference is calculated by first averaging the radiometer temperature measured with the radiometer of a given telescope (CT1, CT2 or CT4 - the radiometer of CT3 appeared to have frequent technical problems for the considered dataset). In a second step, the difference between the radiometer temperature of the same radiometer in two different runs is calculated. Eventually, the three calculated differences (which agree typically at the level of 0.2° which is the nominal precision of the employed radiometers) are averaged.

[12] Note that also the correlation of the event rate differences with observation level humidity (and air pressure as well as camera and ambient temperature) has been investigated but no dependence of the two quantities was found.

stated, all considered runs are four-telescope runs and each run passes individually all standard H.E.S.S. data quality checks. Obvious instrumental effects like mirror aging and the malfunction of one or several telescopes can be ruled out. However, the number of broken pixels in an observation run[13] is typically not the same for runs taken in an On/Off run triple sequence (see also table 4.1 and the corresponding plots in appendix B). On the other hand, the up to now excluded red data points labeled with (1) and (5) in fig. 4.16 correspond to runs where differences in the number of broken pixels exist but the differences in the number of broken pixels are not significantly larger than in other considered datasets (see table 4.1 and appendix B). A difference for runs corresponding to the red datapoints labeled (1) and (5) in fig. 4.16 exist, however, with respect to the distribution of the number of broken pixels in the camera. In the special case of the two runs corresponding to the red datapoint labeled (1) and (5) in fig. 4.16, two complete drawer modules, each with four times four pixels, are not operating in the signal run in CT3 (see also the corresponding plots in appendix B for details). It appears thus as if the malfunction of a large number of spatially connected pixels, i.e. a cluster of pixels, does have a $\sim 2\%$ influence on the preselected event rate. For all run pairs except the ones that correspond to the datapoints labeled (1) and (5) in fig. 4.16, the size of the largest cluster of broken pixels is similar or equal (see appendix B). However, the number of isolated broken pixels and small clusters of broken pixels is not in general equal as f.i. visible in table 4.1 and appendix B. The influence of isolated and small clusters of broken pixels depends on the location of the broken pixel in the field of view and in case of several connected broken pixels (f.i. four broken pixels in a row due to a broken ARS ring sampler module) also on the morphology and size of the broken pixel cluster. These effects have been investigated but it was not possible to derive conclusive results due to the small dataset size. In the following it will be sufficient to say that it is likely that the remaining physical influences that primarily cause the bad χ^2/NDF of the linear fit of the relative preselected event rate differences between ON and OFF runs to the corresponding radiometer differences are caused by isolated and small clusters of broken pixels which result in typically $\sim 0.3\%$ shifts in the preselected image cleaned event rate. This effect is by one order of magnitude smaller than the effect of atmospheric changes and differences in the number of operating drawers which cause $\sim 2\%$ rate shifts between consecutive ON and OFF observations.

Rate Shift Correction and Cut Efficiency Compatibility

The presence of significant differences in the preselected rate between observation runs that belong to the same On/Off run triple as discussed in the last section are one aspect that needs to be considered in the calculation of the exposure ratio. In practice it is possible to correct for differences in the preselected event rate as will be shown later. However, apart from differences in the preselected event rate, it might also be possible that the background cut efficiency from preselected to selected events, i.e. the ratio of

[13] In the following, the number of broken pixels in a given time interval is the total number of photomultipliers in all operating cameras that are never detecting a positive signal in the considered time interval.

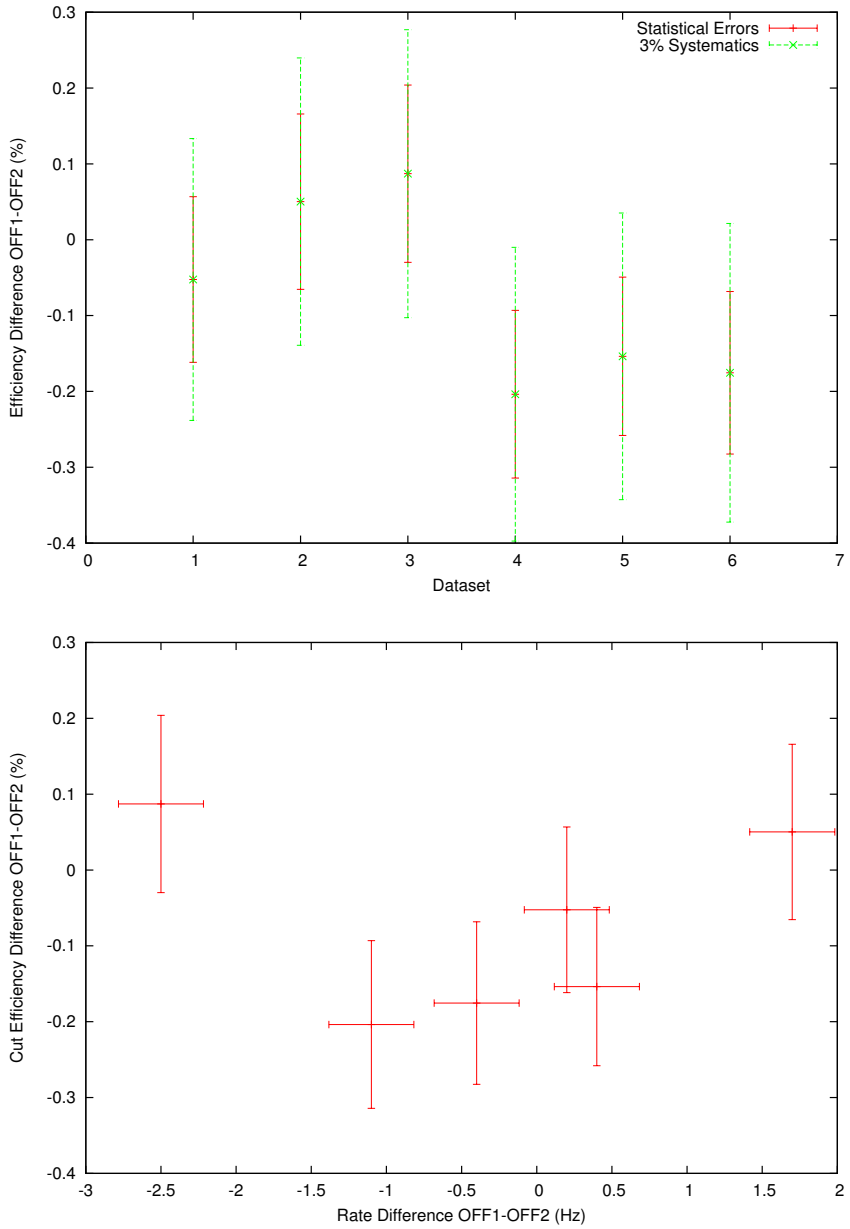

Figure 4.17: Upper Panel: Cut efficiency (from preselected to selected events) differences between OFF1 and OFF2 observation for each of the six On/Off run triples (datasets) investigated in this section. The red datapoints correspond to the cut efficiency difference where the error on the difference is calculated just from the statistical errors of the contributing efficiencies. The error on the green datapoints is calculated assuming a 3% systematic error on each of the two contributing efficiencies. Lower panel: Scatter diagram of the (preselected) event rate difference and the (preselected to selected) cut efficiency difference (with statistical errors only) for each of the OFF1 and OFF2 observations considered in this section.

the number of background events selected as γ-ray events and the number of preselected events, is differing from observation run to observation run within an On/Off run triple. Figure 4.17 shows in the upper panel the difference between the measured cut efficiency in the two background region observations (OFF1-OFF2) that belong to one On/Off run triple. Shown in red is the statistical error (propagated binomial errors) on the cut efficiency difference. A χ^2 test for the compatibility of the red datapoints with zero gives $\chi^2/\mathrm{NDF} = 12/6$. The large value for χ^2/NDF points towards an additional systematic error for the cut efficiencies. The fluctuations of the datapoints for the cut efficiency differences around zero do not support a bias of the cut efficiency that depends on the observed region but point instead to an underestimation of the error on the cut efficiency. Shown in green in the upper panel in fig. 4.17 are the same cut efficiency differences as discussed before but with the error $\sigma(\delta)$ on the difference $\delta = \epsilon^{\mathrm{OFF1}} - \epsilon^{\mathrm{OFF2}}$ estimated by

$$\sigma(\delta) = 3\%\sqrt{(\epsilon^{\mathrm{OFF1}})^2 + (\epsilon^{\mathrm{OFF2}})^2}\,.$$

This corresponds to the effect of a 3% systemtic error on the cut efficiency propagated into the cut efficiency difference. The compatibility of the corresponding datapoints with zero is very good ($\chi^2/\mathrm{NDF} = 4/6$). Based on the limited amount of data it is difficult to conclude whether the introduction of a 3% systematic error on the cut efficiency is necessary or not. In any case it is conservative and will in the following be considered.
The lower panel of fig. 4.17 shows the cut efficiency difference between two background region observations that belong to the same On/Off run triple as a function of the corresponding preselected event rate difference. Based on the limited amount of data, no correlation between the cut efficiency and the preselected event rate is visible. This is important because a putative correction of preselected event rate differences in the exposure ratio can lead to wrong exposure ratios if, f.i., the cut efficiency would be anti-correlated with the event rate and in turn a higher preselected event rate is balanced by a lower cut efficiency.
The agreement of the cut efficiencies between the two background regions at the level of $\sim 3\%$ within the same On/Off run triple suggests that also the background cut efficiencies for one signal region (ON) and one background region (OFF1 or OFF2) agree at the level of $\sim 3\%$. This will be important below.

Analysis of Individual Subdatasets

The number of events that pass standard γ-ray event selection criteria in the signal region observation run and the corresponding number of events in the two background observation runs is measured for every individual subdataset. Events that are reconstructed within an exclusion region or more than 2° away from the pointing position are not considered. In practice, the exclusion region is the galactic plane ($|b| < 0.3^\circ$) in the signal region and the corresponding region in the field of view system of the two background regions.

The exposure ratio for every subdataset is argued above to be given by

$$\alpha_i = \frac{\Omega_i^{\mathrm{ON}} T_i^{\mathrm{ON}} \mathfrak{A}_i^{\mathrm{ON}}}{\Omega_i^{\mathrm{OFF1}} T_i^{\mathrm{OFF1}} \mathfrak{A}_i^{\mathrm{OFF1}} + \Omega_i^{\mathrm{OFF2}} T_i^{\mathrm{OFF2}} \mathfrak{A}_i^{\mathrm{OFF2}}} \,. \tag{4.33}$$

The acceptance can be expressed as

$$\mathfrak{A}_i^k = \epsilon_i^k R_i^k \tag{4.34}$$

where k can be ON, OFF1 or OFF2 and ϵ_i^k is the cut efficiency, i.e. the ratio of the number of background events selected as γ-ray events after application of γ-ray event selection criteria and the number of events that contribute to the event rate R_i^k. In practice R_i^k can for instance be the trigger rate or the preselected event rate. Preselected event rates and the corresponding cut efficiencies are in general preferred because differences in night sky background between the different observed regions (ON/OFF1/OFF2) do not lead to significant differences in the '0710' image cleaned preselected event rate as argued above. For the remaining part of this section, R_i^k is thus the ('0710' image cleaned) preselected event rate measured in the region k. As argued above, the preselected event rate R_i^k as well as the corresponding cut efficiency ϵ_i^k are in general not equal for differing k within an equal subdataset i but subject to a random systematic error. The difference in the preselected event rate can be corrected for by writing the exposure ratio with eq. 4.33 and 4.34 as

$$\alpha_i = \frac{\Omega_i^{\mathrm{ON}} T_i^{\mathrm{ON}} R_i^{\mathrm{ON}} \epsilon_i^{\mathrm{ON}}}{\Omega_i^{\mathrm{OFF1}} T_i^{\mathrm{OFF1}} R_i^{\mathrm{OFF1}} \epsilon_i^{\mathrm{OFF1}} + \Omega_i^{\mathrm{OFF2}} T_i^{\mathrm{OFF2}} R_i^{\mathrm{OFF2}} \epsilon_i^{\mathrm{OFF2}}} \,. \tag{4.35}$$

The cut efficiencies ϵ_i^k in this equation are not known but it is argued above that they are equal ($\epsilon_i^k = \epsilon_i$) up to a random systematic error of $\sigma(\epsilon_i)/\epsilon_i = 3\%$ within a subdataset i and thus cancel out of the exposure ratio on average. The exposure ratio is in turn only known up to a systematic error estimated to be

$$\sigma(\alpha_i) = \sqrt{\sum_k \left(\frac{\partial \alpha_i}{\partial \epsilon_i^k} \sigma(\epsilon_i^k) \right)^2} = \sqrt{2} \alpha_i \frac{\sigma(\epsilon_i)}{\epsilon_i} = 3\% \, \sqrt{2} \alpha_i \,. \tag{4.36}$$

The given systematic error on the exposure ratio neglects errors on the preselected event rate and the livetime because those errors are smaller ($\sim 0.5\%$, see table 4.1) than the systematic error on the cut efficiency. Table 4.2 summarizes the results of the analysis of the individual On/Off subdatasets. The number of signal N_{On} and background $N_{\mathrm{OFF}} = N_{\mathrm{OFF1}} + N_{\mathrm{OFF2}}$ events that pass standard γ-ray selection criteria and '0710' image cleaning is calculated. No selection criteria on the event energy (f.i. energy threshold) have been applied. The exposure ratio is calculated using the method described above. No significant excess is found in any of the subdatasets.

DS	N_{ON}	N_{OFF}	α	Δ	S_{LiMa}	S_{Mod}
1	3849	7609	0.50 ± 0.02	45	0.6σ	0.3σ
2	3554	7053	0.50 ± 0.02	28	0.4σ	0.2σ
3	3391	6903	0.49 ± 0.02	9	0.1σ	0.1σ
4	3953	7831	0.50 ± 0.02	38	0.5σ	0.2σ
5	4177	8678	0.49 ± 0.02	-75	-1.0σ	-0.4σ
6	4383	8740	0.50 ± 0.02	13	0.2σ	0.1σ

Table 4.2: Results of the analysis of the individual On/Off subdatasets. Each subdataset (DS) consists out of one On/Off run triple. The exposure ratio α for a given subdataset is calculated as described in the text. Δ is the γ-ray excess measured in the corresponding subdataset. The Li and Ma (Li and Ma [1983]) significance (S_{LiMa}) and a modified significance (S_{Mod}, see appendix D) that takes the systematic error on the exposure ratio into account is given.

Analysis of the Combined Dataset

More interesting than the analysis of the individual subdataset presented above is of course the analysis of the total or combined On/Off dataset which is discussed in this section. In total $N_{\mathrm{ON}} = 23307$ events that pass standard γ-ray event selection criteria and '0710' image cleaning have been detected in the signal region before application of energy threshold cuts. The corresponding number of events in the background regions is $N_{\mathrm{OFF}} = 46814$. Figure 4.10 shows the reconstructed event positions in the signal region (upper panel) and the background regions (lower panel) as well as the exclusion of the galactic plane which is applied in the respective field of view system to all background regions. Additionally it is visible in fig. 4.10 that only events with a maximal offset of 2° from the respective pointing position are considered. The exposure ratio of the combined dataset is obtained as the mean of the exposure ratios of the individual subdataset (table 4.2) to be $\alpha = 0.496 \pm 0.005_{\mathrm{RMS}} \pm 0.01_{\mathrm{sys}}$ where the first error is the estimated variance of the sample of the individual subdataset α. The second error is obtained from the 6 random systematic errors of the subdataset exposure ratios to be $0.02/\sqrt{6} = 0.01$. The RMS error on the exposure ratio (0.005), that is caused by the non-vanishing width of the distribution of the individual subdataset exposure ratios, is still small compared to the systematic error on the combined exposure ratio (0.01) resulting from the random systematic error on the individual subdataset exposure ratios. The RMS error is in the following neglected. If a larger dataset were considered, the RMS error would increase and at some point become dominant over the systematic error. In that case it is recommended to artificially truncate the runtime of the observation runs such that the exposure ratios for the individual subdatasets are better compatible.
The total excess measured in the combined analysis is $\Delta = 87$ with a statistical significance of $S_{\mathrm{LiMa}} = 0.5\sigma$ or $S_{\mathrm{Mod}} = 0.2\sigma$ when the systematic error on the exposure ratio is considered. It is concluded that no significant excess is measured.
In a further step, an energy dependent analysis is performed. Additionally to the event selection criteria discussed above, only events with a reconstructed energy larger than

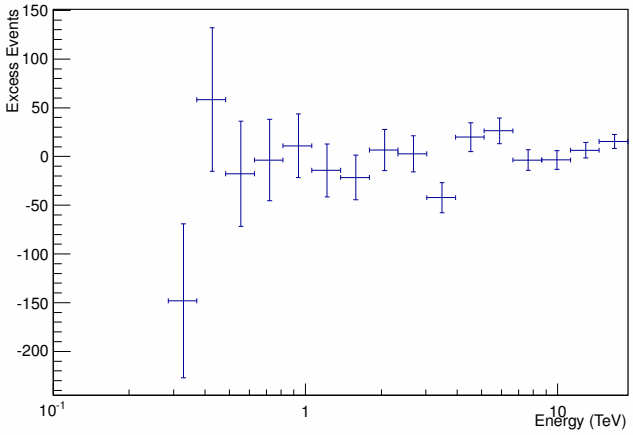

Figure 4.18: On/Off analysis excess events as a function of event energy. The error-bars are statistical only. No significant excess is observable.

the energy threshold are analyzed. The energy threshold is in that case defined as the larger value of the trigger energy threshold and the minimal energy bias threshold (see chapter 2). In order to reconstruct the event energy, the image amplitude in all cameras that contain data is necessary. Each image amplitude is scaled with the muon correction (see chapter 2) for the telescope. The muon correction itself is for every telescope taken to be the average of the 18 muon corrections measured in the 18 observation runs contained in the On/Off dataset that is investigated here. This is justified because all runs considered here were taken within the short period of 5 days in July 2010 and significant changes in the reflectivity are thus not expected. Variations of the muon correction coefficients at the level of 2% from run to run are considered as statistical fluctuations. The Hillas parameters and the '0710' image cleaning have been calculated with and without every camera pixel intensity being scaled with the corresponding muon coefficient but no significant differences in the analysis results where found. Figure 4.18 shows the number of excess events for the analysis of the combined On/Off dataset for energies larger than the energy threshold of ~ 300 GeV. The size of the intervals is $\sim 30\%$ of the central bin energy to avoid correlations within the histogram due to the finite energy resolution of $\sim 20\%$. No significant excess is visible in any of the energy intervals.
Eventually upper limits on the velocity averaged WIMP annihilation cross section are derived based on the non-detection of a significant signal in the On/Off dataset. The method described in the introduction is applied to gain upper limits on $\langle \sigma v \rangle$ at 95% C.L. assuming different models for the dark matter density distribution in the Milky Way (Einasto and NFW parametrization, see introduction) as well as different models for the γ-ray spectrum resulting from the annihilation of WIMPs (Tasitsiomi and Bergstrom spectrum, see introduction). A $2\% = 0.01/0.49$ Gaussian systematic error on

the event collection efficiency in the algorithm is assumed[14]. The upper limits on $\langle\sigma v\rangle$ are shown in fig. 4.19 as a function of the WIMP mass. The different lines shown indicate the dependence of the upper limit of $\langle\sigma v\rangle$ on the different models that are investigated. The best exclusion limit on $\langle\sigma v\rangle$ is obtained for the combination of the Tasitsiomi γ-ray spectrum and the Einasto dark matter parametrization with $\langle\sigma v\rangle < 4.7 \cdot 10^{-25}\,\mathrm{cm}^3/\mathrm{s}$ at a WIMP mass of 1.8 TeV.
Figure 4.1 shows that the On/Off method does also have a potential to detect annihilating WIMPs towards the galactic center if the dark matter density profile is not as steep towards the galactic center as is suggested by the results of N-body simulations. A recent N-Body simulation considers the effects of the presence of baryons and predicts that the dark matter density in the central ~ 500 pc around the galactic center is constant and steeply falling only for distances that are larger than ~ 500 pc (see Governato et al. [2012]). In that case, the On/Off method is still able to test the presence of WIMPs in the galactic center region. This is one central advantage of the On/Off method in comparison to the rotated pixel method that is, however, hard to quantify because no numerical predictions for the dependence of the dark matter density as a function of the distance to the galactic center is given in Governato et al. [2012].

4.2.3 Driftscan

Figure 4.21 shows events recorded in driftscan observations of the galactic center region. Driftscan runs are scheduled at a constant zenith and azimuth angle array pointing. The celestial pointing at the beginning of a run is chosen such that the galactic center region 'drifts through' the field of view after approximately half of the 68 min observation time. The observed region is divided into many pixels, i.e. bins, each of which is much smaller than the H.E.S.S. I angular resolution. Each run is divided in time into one signal region enclosing the galactic center and one background region. Two arguments that lead to the exposure ratio are given below. The first argument is rather complicated but useful in order to become familiar with the driftscan analysis.
The division of a driftscan run into two halves can be realized with a method that is indicated in fig. 4.22. The upper panel of fig. 4.22 shows black rectangles indicating a segment of 2° in right ascension (half of the used H.E.S.S. I field of view radius) and 4° in declination (full used H.E.S.S. I field of view). Indicated in blue is half of a used H.E.S.S. I field of view drifting (indicated by black arrows) through the black segments. Consider first the process that is labeled with A in the upper panel of fig. 4.22. Here, half of the H.E.S.S. I field of view drifts out of a black segment. The situation is equivalent to the first 2° in right ascension observed in the driftscan. In the last two degrees in right ascension observed in the driftscan, the same process occurs time reversed (see fig. 4.22 label C). The first and last 2° in right ascension of a 68 min runtime driftscan

[14] In practice the 'SetPoissonBkgGaussEff(non, noff, eff, $1/\alpha$, σ(eff))' routine of the TRolke ROOT package described in Rolke et al. [2005] is used. eff = 1 is the assumed event collection efficiency with a Gaussian error of σ(eff) = 0.02. This is in practice equivalent to a 2% Gaussian error on the exposure ratio α.

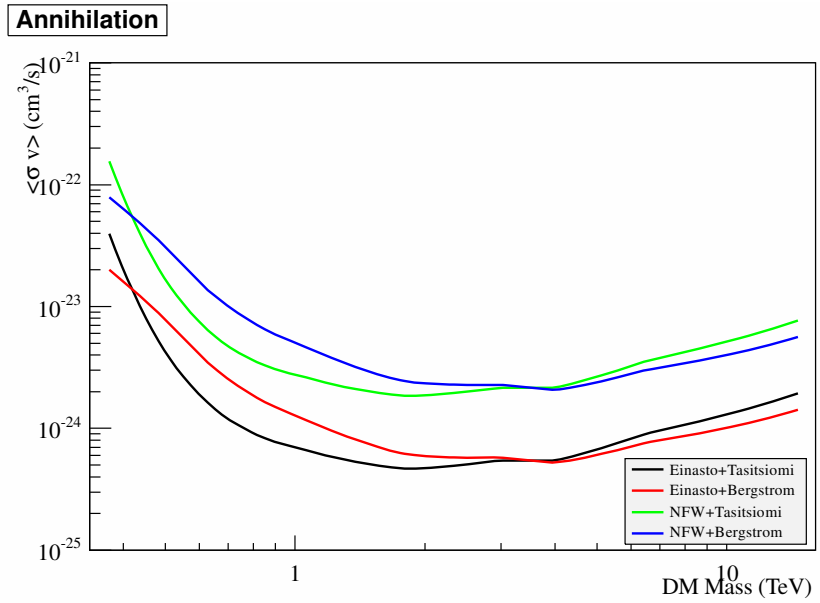

Figure 4.19: 95% CL upper limit on the velocity averaged WIMP annihilation cross section as infered from the analysis of the On/Off dataset. The color code for the different upper limit lines corresponding to different models for the dark matter density parametrization in the Milky Way and the γ-ray spectrum resulting from the annihilation of WIMPs is given in the lower right box. The spread between the different lines indicates the order of magnitude of the model dependence of the upper limits.

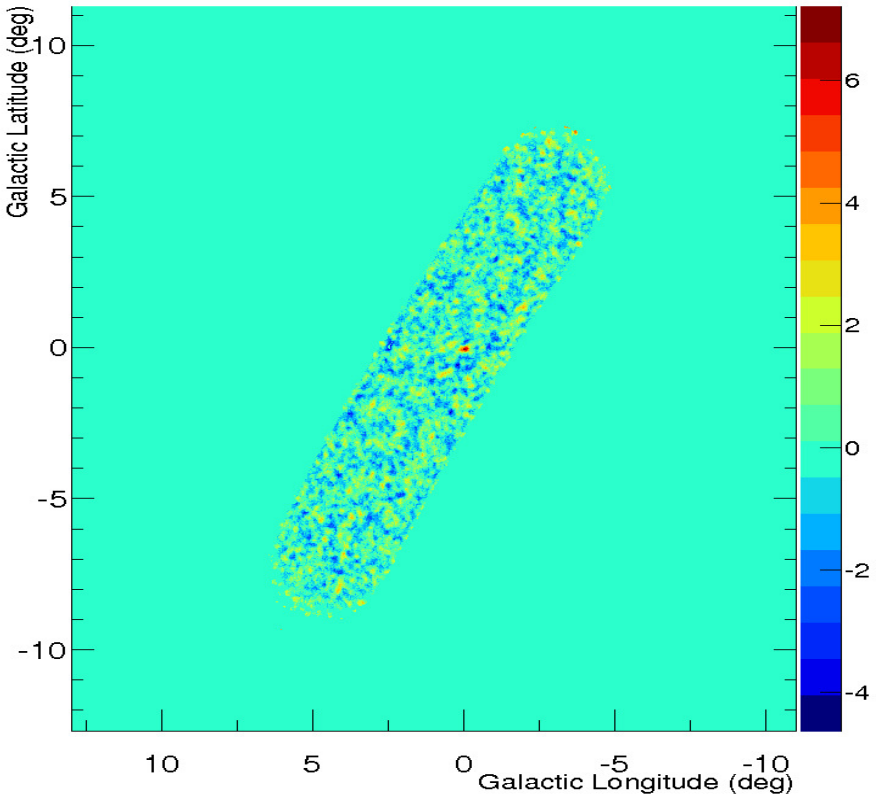

Figure 4.20: Significance skymap for the considered driftscan dataset of $\sim$ 9.5 h livetime (9 observation runs with 68 min observation time) in galactic coordinates. The ring background subtraction method has been used to create the map which is correlated with a radius of 0.1°. The galactic center source is clearly visible.

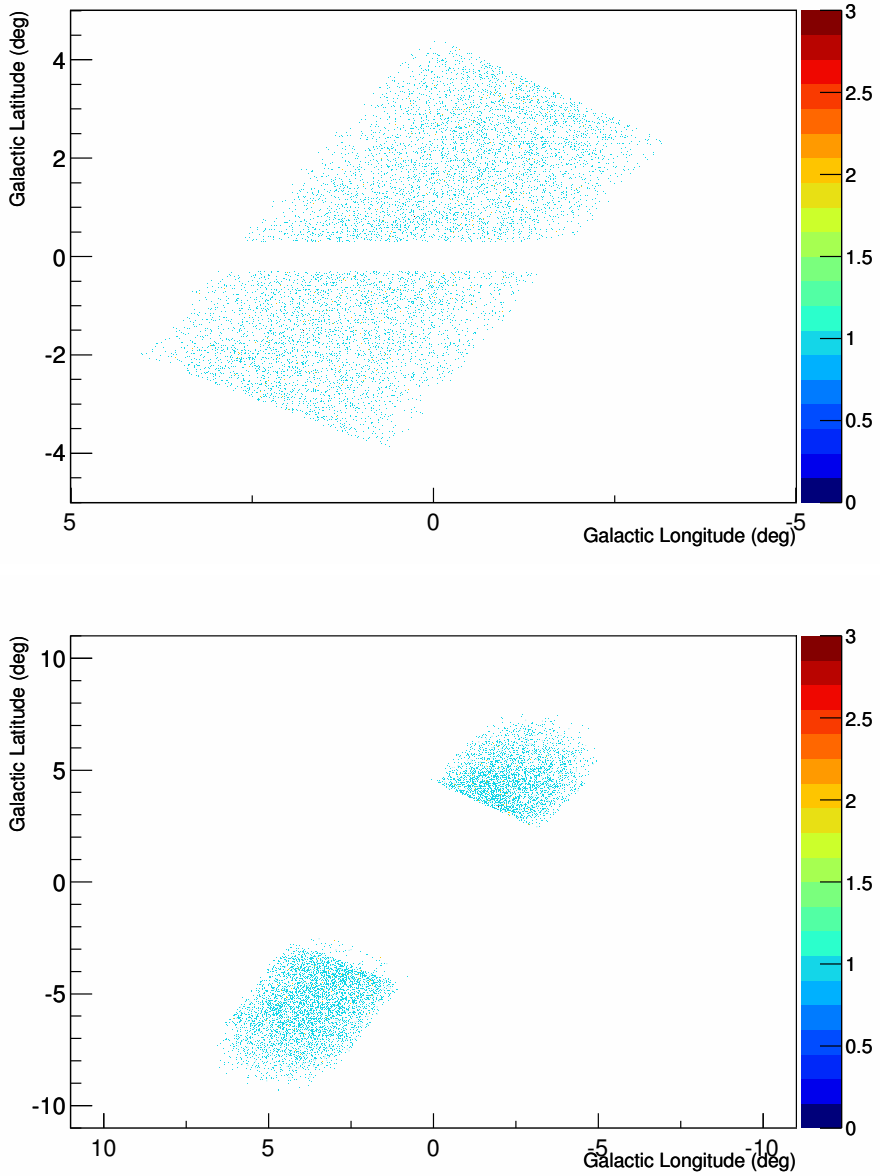

Figure 4.21: H.E.S.S. I events (colorscale) for the driftscan observation of the Milky Way dark matter halo in galactic coordinates. The data is recorded with a constant zenith and azimuth pointing of the array. The galactic center region 'drifts' through the field of view after approximately half of the observation time. Each run is subsequently divided into two parts, the signal region enclosing the galactic center region in the upper panel and the background region in the lower panel. Known γ-ray sources and the galactic plane ($|b| < 0.3°$) are excluded. Excluded regions are treated with a special method (see text) to guarantee the same total instrumental acceptance in the signal and background region.

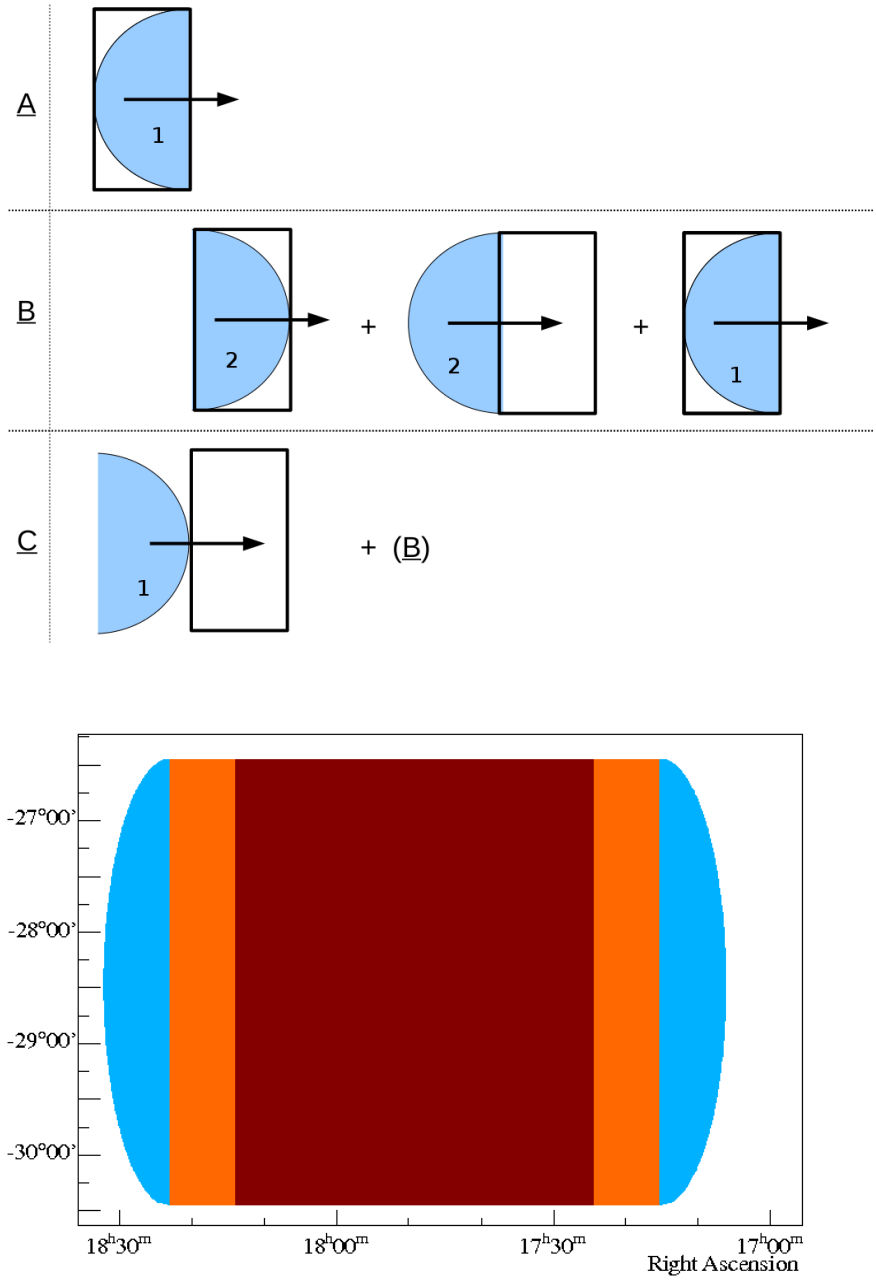

Figure 4.22: Exposure ratio calculation for the driftscan. The upper panel shows two elementary drift processes (labeled by 1 and 2) as well as the corresponding time reversed process. The integrated acceptance corresponding to the processes is ① and ② respectively (see text). The lower panel shows in color the driftscan field of view for a 68 min observation. The blue, orange and red regions correspond to the process labeled by A, B and C in the upper panel respectively.

observation are colored in blue in the lower panel of fig. 4.22. The integrated acceptance of each of the processes is ①. The second and next to last 2° in right ascension are colored in orange in the lower panel of fig. 4.22. Here, the process labeled with B in the upper panel of fig. 4.22 occurs. Half of the H.E.S.S. I field of view moves out of the black segment and at the same time the other half of the H.E.S.S. I field of view moves in. The integrated acceptance for each of the processes - one process being again the time reverse of the other - is ②. The last half of the field of view moves eventually out of the black segment. This is equivalent to the process labeled with A in fig. 4.22 and thus the total acceptance of process B in fig. 4.22 is ① + 2②. Finally, all other segments of 2° in right ascension are colored in red in the lower panel of fig. 4.22. The process here is the same as for the orange labeled segment but additionally the first half of the H.E.S.S. field of view moves into the segments and the total acceptance of every red colored segment of 2° in right ascension is thus 2(① + ②). Assuming that the signal region in the vicinity of the galactic center is completely in the acceptance region colored in red in the lower panel of fig. 4.22, the total acceptance in units of the acceptances of the processes labeled in the upper panel of fig. 4.22 for the signal region is

$$\mathrm{A_{ON}} = 2(① + ②)\frac{\Delta L}{2}$$

where ΔL is the length of the signal region in right ascension in degrees. Then, the total acceptance for the background region in the same units is given by

$$\mathrm{A_{OFF}} = \frac{L - 4^\circ - \Delta L}{2}\, 2\,(① + ②) + 2\,①\frac{2^\circ}{2} + 2\,(① + 2②)\,\frac{2^\circ}{2} = (L - \Delta L)(① + ②)$$

where L is the total interval covered in right ascension by array pointings, i.e. the range colored by orange and red in the lower panel of fig. 4.22. Eventually, the ratio of the signal region to the background region acceptance is for a runlength L and signal region size ΔL given by

$$\alpha = \frac{\mathrm{A_{ON}}}{\mathrm{A_{OFF}}} = \frac{\Delta L}{L - \Delta L}\,. \tag{4.37}$$

For instance, if $\alpha = 1$ is requested for a 68 min runtime driftscan observation, the resulting signal region pointing range in right ascension is with 34 min the same as for the background region. However, the background region has a larger total field of view than the background region - a result of the total acceptance of the first and last four degrees covered in the field of view being smaller than for the rest of the field of view.
A simpler argument that leads to eq. 4.37 is to state that due to the constant horizon system pointing position, the exposure ratio has to be the ratio of the observation time T_{Run} spent in the signal ($T_{\mathrm{Run}}^{\mathrm{ON}} = \Delta L$) and background region ($T_{\mathrm{Run}}^{\mathrm{OFF}} = L - \Delta L$).
Equation 4.37 holds if the assumption of constant instrumental acceptance is exactly fulfilled during the runtime. It is in practice to be expected that differences in the night sky background lead to trigger rate differences which in turn lead to differences for the livetime in the signal and background region. Additionally, atmospheric changes are expected which lead to acceptance differences between the signal and the background

region. This leads in practice to deviations from eq. 4.37 for the exposure ratio and to the necessity for respective corrections.
The method described above (eq. 4.29) to infer statements on the velocity averaged WIMP annihilation cross section, $\langle \sigma v \rangle$, is not directly applicable to the driftscan data because it is more complicated to say what f.i. the field of view, $\Delta\Omega_i^{\mathrm{ON}}$, of the signal region in a driftscan analysis or the livetime of the signal region observation is. A precise and general treatment of this problem is given in appendix E and involves a time dependent field of view direction in celestial coordinates. The problem is that in general the astrophysical factor is obviously changing with observation time. An approximate treatment that translates the situation into a case that is described with eq. 4.21 is possible by dividing the signal region resulting from the full driftscan observation into many small regions. The average astrophysical factor in the signal and background region is calculated and the difference $J_i^{\mathrm{ON}} - J_i^{\mathrm{OFF}}$, which is necessary to evaluate eq. 4.29, is obtained. The livetime of the signal region observation, which is also necessary to evaluate eq. 4.29, is in that case, however, not the full livetime but smaller. In practice, the effective signal region livetime is approximated by the mean length in right ascension that a small solid angle in the signal region stays in the field of view of the instrument[15]. The overall picture of the approach is to use that the observation of a drifting region of which only a small part can be seen in every point of time is equivalent to the observation of the whole region for a reduced time. This reduced time is the average time a small element of the full region stays in the field of view corrected for dead time effects.

Dataset and Data Quality

A dataset of 11 driftscan observation runs, each with ~ 68 min length is investigated in this section. Figures 18 and 19 in appendix C show the array trigger rate and the temperature of one radiometer as a function of runtime for each considered run. In two cases, the radiometer temperature variation during the run is very large, i.e. larger than $\sim 1^\circ$ and the runs are discarded in the following. Additionally, in three of the nine remaining runs, almost one complete telescope was not operational (see fig. 20 in appendix C). These runs are also discarded in the following, however, they have been used to generate the skymap in fig. 4.20. The significance map is generated for a driftscan dataset of ~ 9.5h livetime with the ring background algorithm and an integration radius of 0.1°. The map shows that no previously unknown γ-ray source is detected in the considered driftscan dataset within the regions below and above the galactic plane that have not been systematically observed before. The livetime of the dataset considered here is so small that only the galactic center source is detected as a γ-ray source with a local background algorithm and thus the exclusion of the galactic plane ($|b| < 0.3^\circ$) is sufficient for the further analysis. All exclusion regions are within the region colored in red in fig. 4.22. Excluded pixels within the red region in fig. 4.22 are shifted mutually in right ascension between signal and background region at constant declination. This special treatment guarantees that the shifting of the exclusion regions does not imbalance

[15]The mean is calculated involving only pixels that are not excluded from the analysis.

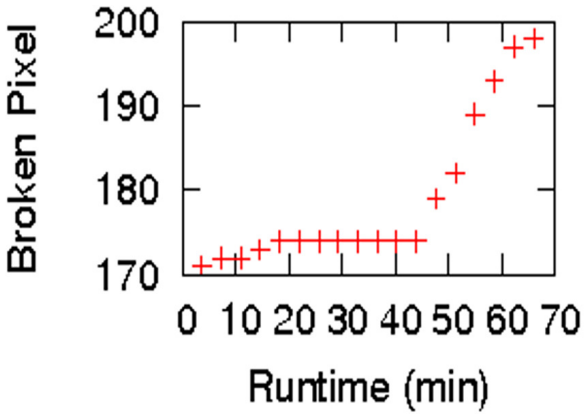

Figure 4.23: Number of broken pixels in all four cameras as a function of observation time for one analyzed driftscan observation run (run number 58862). For similar figures that belong to the other considered observation runs, see fig. 21 in appendix C.

the instrumental acceptance of signal and background region as the acceptance is by construction constant for constant declinations within the red region in fig. 4.22. To minimize the expected γ-ray flux from WIMP annihilation in the background region, every pixel excluded in the signal region is shifted along right ascension and constant declination as close as possible to the edge of the background region. Similarly, every pixel excluded in the background region is shifted as close as possible to the edge of the signal region to maximize the expected γ-ray flux from WIMP annihilation in the signal region.
Out of the six remaining runs, three runs have an unusually large number of broken pixels in the four cameras (see fig. 21 in appendix C for details). Typically, 400-600 pixels are broken in these runs which is $\sim 10\%$ of the total number of pixels in the four cameras and compares to the typical number of 100-200 or $\sim 2-5\%$ broken pixel in typical observation runs. The respective runs are also discarded from the analysis. For the remaining three runs, the number of broken pixels is significantly increasing after ~ 40 min of observation time (see fig. 4.23 and fig. 21 in appendix C). For a driftscan analysis as described above, this means in practice that the number of broken pixels in the background region is systematically larger (by typically ~ 10 pixels on average) than in the signal region. This stands in contrast to the situation in the On/Off analysis where the number of broken pixels in the background and signal region are not equal but no systematic preference for one region to have more or less broken pixels exists. The reason for the increase in the number of broken pixels is very probably that the region in the south of the galactic center, that is in the field of view when the number of broken pixels is increasing in the driftscan observation runs, has a larger density of stars than other regions of the sky.

The systematic increase of the number of broken pixels with time in the background region will eventually lead to a systematic difference of the γ-ray event acceptance in the signal and the background region. Based on the very small number of three observation runs that are finally analyzed it is, however, very difficult to quantify or correct for the increasing number of broken pixels in the background region. In the following, the dataset of three driftscan observation runs is analyzed under the assumption of a 5% systematic error on each of the runwise exposure ratios. A motivation for the numerical value of the systematic error on the exposure ratio is derived based on the experience from the analysis of the On/Off dataset that is discussed above. There, it has been found that:

- Atmospheric changes and differences in the number of broken pixels lead to a typical change of $\sigma(R)/R = 2\%$ on the preslected event rate. This can be corrected for.
- The systematic cut efficiency difference between the ON and OFF observation data from preselected to selected events is $\sigma(\epsilon)/\epsilon = 3\%$. This can not easily be corrected for.

In the following, no correction for the 2% change in the preselected event rate is applied for simplicity in the driftscan data analysis. The total systematic error on the exposure ratio for every observation run is estimated to be

$$\sigma(\alpha_i) = \sqrt{2}\alpha_i \sqrt{\left(\frac{\sigma(R)}{R}\right)^2 + \left(\frac{\sigma(\epsilon)}{\epsilon}\right)^2} \sim 5\%\alpha_i \,. \tag{4.38}$$

The estimation of the systematic error on the exposure ratio is similar to the estimation of the systematic error on the exposure ratio for the On/Off analysis (see eq. 4.35). This is justified because the time difference between the signal and background region observation ($\lesssim 30$ min) as well as the order of magnitude of the difference in the number of broken pixel ($10-20$, see fig. 4.23) is similar for the driftscan as well as for the On/Off analysis. However, due to the expected systematic bias in the number of broken pixels between the signal and the background region observation, the systematic error on the exposure ratio is not assumed to become smaller when multiple driftscan observation runs are considered. In other words, it is not assumed that systematic differences in the γ-ray event acceptance average out when multiple driftscan runs are analyzed and the systematic error on the exposure ratio is thus decreasing with $1/\sqrt{K}$ where K is the number of analyzed driftscan observation runs. The fact that the systematic error on the exposure ratio is not decreasing will eventually limit the sensitivity of the driftscan method.

Data Analysis and Results

Table 4.3 summarizes the results of the individual analyses of the three driftscan observation runs that pass the data quality criteria discussed above. No significant excess is observed. The average observation time a pixel in the signal region is observed is 859.5

Run	N_{ON}	N_{OFF}	α	Δ	S_{LiMa}	S_{Mod}
58862	2927	2823	1.00 ± 0.05	104	1.4σ	0.6σ
58889	2886	2708	1.00 ± 0.05	178	2.4σ	1.1σ
58965	2869	2866	1.00 ± 0.05	3	0.04σ	0.02σ

Table 4.3: Results of the analysis of the individual driftscan observation runs. Δ is the γ-ray excess, α the exposure ratio, N_{OFF} the number of background events above energy threshold and N_{ON} the number of signal events above energy threshold. The Li and Ma (Li and Ma [1983]) significance (S_{LiMa}) and a modified significance (S_{Mod}, see appendix D) that takes the systematic error on the exposure ratio into account is given.

s for all three runs and the total size of the signal region is $8.3 \cdot 10^{-3}$ sr which is more than twice the size of a region observed with a 2° radius H.E.S.S. I field of view, i.e. $2\pi(1 - \cos(2°)) \sim 3.8 \cdot 10^{-3}$ sr.
The analysis of the combined dataset does also not result in a significant γ-ray excess. For the combined dataset, $N_{\mathrm{ON}} = 8682$ events are detected in the signal region and $N_{\mathrm{OFF}} = 8397$ events are detected in the background region above the energy threshold of $\sim$ 300 GeV. The exposure ratio of the combined dataset is assumed to be the mean of the sub dataset exposure ratios but the error on the exposure ratio is not assumed to become smaller for the combined dataset than it is for the sub datasets , i.e. $\alpha = 1.00 \pm 0.05$. The corresponding γ-ray excess is $\Delta = 285$ with a significance of $S_{\mathrm{LiMa}} = 2.2\sigma$ or $S_{\mathrm{Mod}} = 0.7\sigma$ when a 5% systematic error on the exposure ratio is assumed. Figure 4.24 shows the uppers limit for $\langle \sigma v \rangle$ that are inferred[16] from the analysis of the combined dataset for different models for the γ-ray spectrum resulting from the WIMP annihilation and the dark matter distribution in the Milky Way. The best limit is achieved for a combination of the Tasitsiomi γ-ray spectrum and the Einasto parametrization of the dark matter density distribution for a WIMP mass of $\sim$ 1.8 TeV at the level of $\langle \hat{\sigma v} \rangle \leq 4 \cdot 10^{-24}\,\mathrm{cm}^3/\mathrm{s}$.

4.3 Comparison of the Sensitivity to a Benchmark Model

The analysis methods presented in this section have been implemented in the course of the thesis work into a special software environment that is available to the H.E.S.S. collaboration. The software input are either H.E.S.S. data events passing the post-selection γ-ray criteria or Monte Carlo simulated events resembling post-selected H.E.S.S. data events. In either case, a special binary data format file is read in that contains for every event information on few parameters of interest, f.i. event energy and direction as well as telescope pointing position in celestial and horizon coordinates. If real H.E.S.S. data are to be processed, the input file can be generated in the usual H.E.S.S. data processing

[16] A 5% Gaussian systematic error is assumed to derive the upper limits which are calculated at 95% confidence level using TRolke. For details, see the similar derivation of the upper limits in the analysis of On/Off data discussed above.

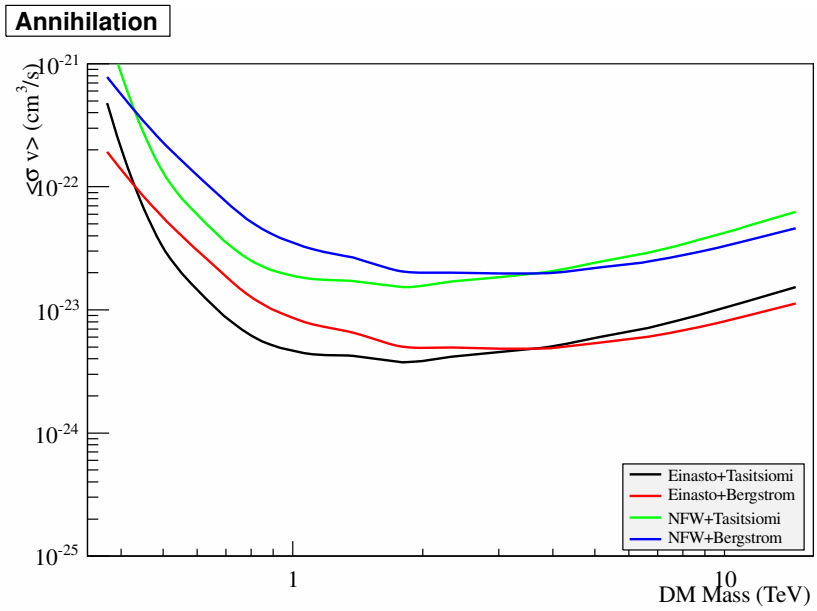

Figure 4.24: 95% C.L. upper limits on the velocity averaged WIMP annihilation cross section as a function of the WIMP mass. The limits are derived from the analysis of a ~ 3 h driftscan dataset. Different upper limit lines correspond to different combinations of the assumed γ-ray spectrum resulting from the WIMP annihilation and the dark matter distribution in the Milky Way.

chain. Monte Carlo input data are on the other hand generated by simulating the result of H.E.S.S. observations. For this,

- a realistic event rate (typically 2 Hz within a H.E.S.S. field of view with 2° radius as inferred from H.E.S.S. data taken at $\sim 20°$ zenith angle pointing towards regions without γ-ray source, i.e. 'offdata') for H.E.S.S. I events passing standard γ-ray event selection criteria is simulated for a variable observation time. A dead-time as is typical for offdata ($\sim 7\%$) is assumed to calculate the livetime of the simulation.

- Event coordinates in celestial coordinates are simulated such that they are rotationally symmetric around the assumed telescope array pointing position. The rotational symmetry of the H.E.S.S. I acceptance is an assumption that is underlying many H.E.S.S. data analysis results, especially all results that make use of the 'reflected region' background subtraction algorithm. Additionally to the rotational symmetry of the acceptance, a realistic radial acceptance for H.E.S.S. I events that pass standard γ-ray selection criteria, i.e. the dependence of the acceptance at a point in the field of view on the radial distance of that point to the center of the field of view, is taken into account. This is realized by first simulating event coordinates uniformly in latitude and longitude over the H.E.S.S. field of view. For a given simulated event, the angular distance to the simulated array pointing position is compared to a desired angular distance for an event to be accepted. The desired angular distance is randomly chosen from the distribution of offsets to the pointing position for γ-ray candidate events recorded in real H.E.S.S. offdata.

- Similarly, the event energy distribution is simulated to be compatible with the energy distribution of recorded H.E.S.S. I offdata events passing standard γ-ray event selection criteria.

The possibility to have realistic simulated data input opens the possibility to test the software under perfect conditions, i.e. without the existence of systematic effects.
Additionally, it is possible to compare different background subtraction techniques with respect to their sensitivity to a WIMP annihilation γ-ray flux under equal conditions with simulated data. This is interesting because the datasets used for the analysis presented above are differing with respect to their effective area (f.i. via differing pointing zenith angles) and livetime. The upper limits on $\langle \sigma v \rangle$ that are inferred above from the analysis of the rotated pixel, the On/Off and the driftscan dataset can thus hardly enable conclusions on the relative sensitivity of the respective methods. Three comparable Monte Carlo generated background event datasets, one for the rotated pixel method, one for the On/Off method and one for the driftscan method are therefore investigated in the following. For each of the datasets, a total observation time of 150 h is simulated using the same distribution for the radial acceptance, the background event energy distribution and the pointing zenith angle. In detail

- for each of the three On/Off pointing positions discussed above, a total observation time of 50 h is simulated in different runs of 30 min length.

Method	J_{ON}	J_{OFF}	Ω_{ON} (sr)	T_{ON} (h)
Rotated Pixel	4135 ± 329	2117 ± 300	$(3.4 \pm 1.2) \cdot 10^{-4}$	150
On/Off	2170	388/200	$3.2 \cdot 10^{-3}$	50
Driftscan	1570	339	$8.2 \cdot 10^{-3}$	30

Table 4.4: Detailed parameters for the comparison of the different background subtraction methods. Shown is the astrophysical factor in the signal (J_{ON}) and background (J_{OFF}) region as well as the signal region size (Ω_{ON}) and observation time (T_{ON}). All astrophysical factors are given for the Einasto parametrization of the dark matter density distribution in units of $\mathrm{GeV}^2/\mathrm{cm}^6\mathrm{kpc}$. In case of the rotated pixel method, the astrophysical factors for the signal and background region as well as the signal region size depend on the pointing position. The average of the respective distribution over the simulated dataset is given together with the RMS. For the On/Off method, the two background region astrophysical factors correspond to the OFF1 (above the galactic plane) and OFF2 (further away from the galactic center than the OFF1 region and below the galactic plane) region, respectively.

- A total dataset of 150 h of driftscan data has been simulated. The first observation position of each simulated observation run is equal to the first observation position of the driftscan observation runs discussed above. The runlength is set to 68 min and the pointing position is simulated to be drifting in right ascension after each simulated event by $dt = 68/N$ min where $N = \mathrm{Poisson}(2\,\mathrm{Hz}\,68\,\mathrm{min})$ is the number of simulated events.

- For the rotated pixel method, a dataset of 150 h observation time divided into 30 min observation runs is generated. The pointing position is randomly chosen such that 90% of the pointing positions are within a circle of 1° around the galactic center, i.e. within the signal region.

For each of the datasets, the analysis as described above for the respective method is performed and an upper limit on the γ-ray excess is derived assuming that the galactic plane ($|b| < 0.3°$) is the only region that is to be excluded from the analysis. In order to enable cross checks of the analysis, relevant parameters of the respective datasets are summarized in table 4.4. The average upper limits obtained from multiple simulations assuming the Einasto parametrization of the Milky Way dark matter density and the Tasitsiomi γ-ray spectrum are shown in fig. 4.26. It is concluded that the On/Off method is the most sensitive method followed by the driftscan and the rotated pixel method. However, all methods are comparable in sensitivity within the regime of statistical fluctuations of the upper limit. The driftscan method is investigated here with $\alpha = 1$, i.e. with equal ΩT in the signal and the background region. Smaller values of α, possible to realize by the limitation of the signal region field of view, have also been investigated and lead in general to marginally improved sensitivities of the method with respect to the investigated benchmark models. However, the improvement of the driftscan method to

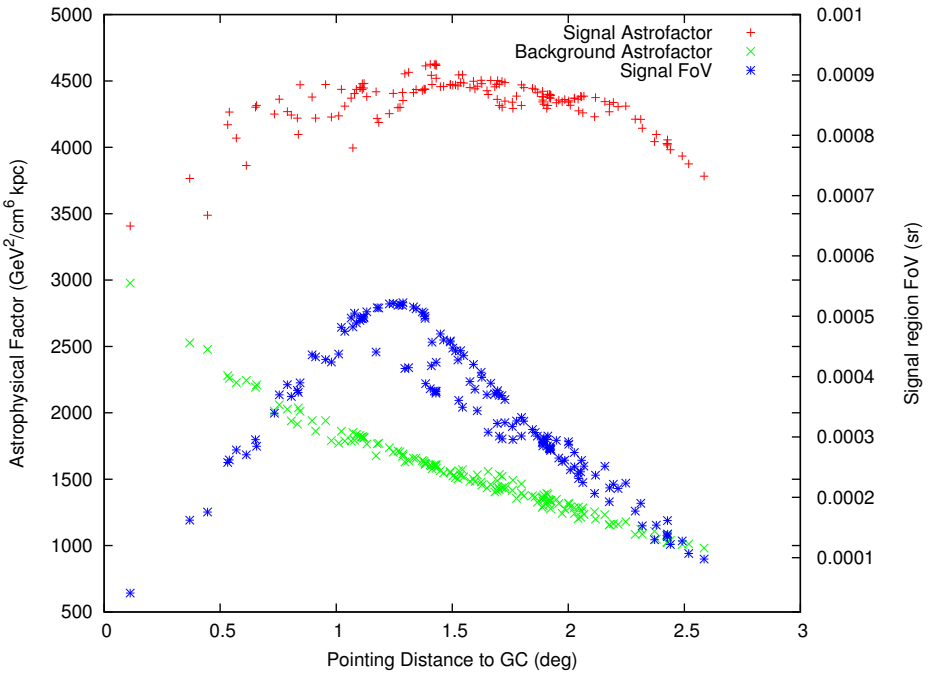

Figure 4.25: Left axis: Dependence of the astrophysical factor (assuming an Einasto profile) in the signal (red) and background (green) region on the pointing distance to the galactic center in the rotated pixel analysis. Right axis: Dependence of the effective signal region size (blue) on the pointing distance to the galactic center for the rotated pixel analysis. To gain an optimal sensitivity to WIMP annihilations for the Einasto dark matter density parametrization, a pointing distance of 1° to 1.3° to the galactic center is recommended for a signal region of 1° around the galactic center.

benchmark models with WIMP density distributions that are peaked towards the galactic center region (Einasto and NFW) comes along with a decrease in sensitivity to other models with non standard parametrizations of the WIMP density distribution. Similarly the distribution of pointings simulated in the dataset used for the estimation of the sensitivity of the rotated pixel method is not optimized. Figure 4.25 shows the astrophysical factors calculated for an Einasto parametrization of the dark matter density distribution for the signal and background region of the rotated pixel method as a function of the distance to the galactic center. The difference between the signal and the background region astrophysical factor is typically maximized for pointing distances between 1° and 2°. Additionally shown in fig. 4.25 is the size of the resulting signal field of view. This is maximized within 1° and 1.3° pointing distance to the galactic center. Also the radial acceptance of the H.E.S.S. I array is steeply decreasing for distances larger than $\sim 1.3°$ where the acceptance is still $\sim 75\%$ of the peak acceptance (see H.E.S.S. Col. [2006]). It is concluded that the with respect to the Einasto parametrization of the dark matter density distribution optimal pointing distance is within 1° and 1.3° from the galactic center. This is, however, typically not realized for standard γ-ray source observations of the galactic center where the only constraint on the pointing position is to maximize the radial acceptance (i.e. pointing distances within 0° and 0.7° to the galactic center) and observe with a non vanishing offset to enable a reflected region background subtraction. Statistical fluctuations of the astrophysical factors and the size of the signal region as seen in fig. 4.25 are caused by the random nature of the construction of the signal and background region for the rotated pixel method, i.e. the rotation of signal pixels by random angles to construct the background region.
Note that additionally to self annihilating WIMPs also the potential to search for decaying WIMPs towards the galactic center region has been investigated. It is, however, concluded that the sensitivity of an analysis of a 150 h dataset for a decaying WIMP is not competitive to the results derived with current large field of view and duty cycle neutrino observatories. Depending on the background subtraction method, a lower limit on the WIMP livetime of $\sim (2-6) \cdot 10^{22}$ s can be expected in the best case (i.e. assuming a γ-ray spectrum according to Tasitsiomi and Olinto [2002] and the Einasto parametrization of the WIMP density in the Milky Way). IceCube already inferred a lower limit between $\sim 10^{24}$ s and $\sim 10^{27}$ s depending on the WIMP mass between ~ 300 GeV and ~ 10 TeV (see IceCube Col. [2011] or fig. 3.7 in chapter 3).

4.4 Summary and Conclusion

Three different methods to search for a γ-ray signal resulting from WIMP annihilation towards the galactic center region have been discussed in this chapter. Independent H.E.S.S. datasets have been analyzed with all three methods. No signal has been found in any analysis and upper limits on the velocity averaged WIMP annihilation cross section at the level of up to $3 \cdot 10^{-25}\,\mathrm{cm}^3\mathrm{s}$ for WIMP masses around 1.8 TeV have been inferred for certain benchmark models with respect to the dark matter density distribution and the γ-ray spectrum expected from the annihilation of WIMPs. The comparison of the

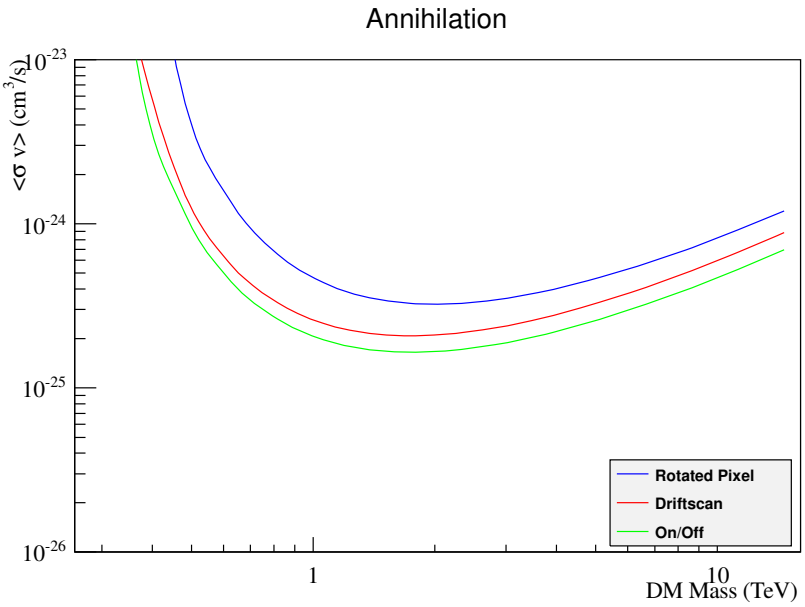

Figure 4.26: Comparison of the sensitivity of the rotated pixel, the On/Off and the driftscan method to the velocity averaged WIMP annihilation cross section assuming the Einasto parametrization of the dark matter density and the Tasitsiomi γ-ray spectrum. The sensitivity for the driftscan method holds for $\alpha = 1$. A total dataset of 150 h of observation time at a zenith angle of 20° is assumed in each case.

sensitivities as shown in fig. 4.26 supports the conclusion that searches for WIMPs should be carried out with the On/Off method to guarantee the maximal sensitivity. However, data obtained for the On/Off method is to 2/3 background data that is uninteresting for other γ-ray analyses. In principle, data taking with only one OFF observation per ON observation would be possible. This is, however, disfavored because the control of systematic errors is improved with two independent OFF region observations. Data obtained for the application of the rotated pixel method is in contrast usual H.E.S.S. data that can also be used to investigate astrophysical γ-ray sources that are present in the galactic center region. Given that the sensitivity of the rotated pixel method as shown in fig. 4.26 is only marginally reduced compared to the On/Off method, the multi purpose character of the data obtained for the rotated pixel method favors this method over the On/Off method. On the other hand, the comparison of the sensitivities as shown in fig. 4.26 does only hold for the assumed benchmark model. In particular the sensitivity of the rotated pixel method strongly relies on the steepness of the dark matter density profile in the vicinity of the galactic center. The On/Off and the driftscan method do provide a sensitivity to detect WIMP annihilation towards the galactic center region even if the dark matter density distribution in the central few hundred parsec of the Milky Way is almost constant. This is a very advantageous property of the On/Off and the driftscan method. The driftscan method suffers from a reduced sensitivity to steep dark matter profile benchmark models and additional problems caused by regions of large star density in the south of the galactic center that cause a significant amount of camera pixels to be switched off during part of the observation and lead to a systematic bias of the γ-ray event acceptance in the signal region compared to the γ-ray event acceptance in the background region. For those reasons, data taking in driftscan mode is in general not recommended.

A good observation strategy to search for a γ-ray signal caused by WIMP annihilation towards the galactic center region is thus to observe mostly in wobble mode which enables the rotated pixel method to be applied and is anyway of interest also for the analysis of other γ-ray sources in the galactic center region. Parts of the observations could be complemented by OFF data taking with a pointing strategy similar to the one discussed above, i.e. two OFF region observations offset by ± 35 min in right ascension. This would enable a future analysis to derive constraining benchmark limits with the rotated pixel method and additionally have a limited sensitivity to non-standard parametrizations of the dark matter density profile.

Note that the techniques that are developed and investigated in this chapter are also of great interest for the confirmation or falsification of the presence of the ~ 130 GeV γ-ray line signal that has recently been detected in the analysis of data taken with the Fermi satellite (see chapter 3). The new H.E.S.S. II array is sensitive to γ-ray events with an energy that is smaller than 130 GeV and can thus be used to search for the presence of the signal. However, the location of the γ-ray line emission is currently only constrained to a probably extended region in the vicinity of the galactic center region. Given that the field of view of H.E.S.S. II is smaller than for H.E.S.S. I, it will be of possible interest to search for γ-ray line emission in the galactic center region in On/Off observations. For the particular case of a line search with a fixed energy of ~ 130 GeV,

it is not necessary to have two OFF regions symmetric in right ascension around the signal region observation as discussed above for a search for a continuous signal. The systematic changes of the atmosphere and the number of broken pixels between the signal and the background region observation can instead be estimated by considering events with energy much larger than 130 GeV. This will be an important future analysis.

5 Outlook: Large Scale Diffuse VHE γ-ray Emission in the Galaxy

This chapter gives an outlook on the potential to study sources of galactic diffuse γ-ray emission with CTA, the next generation Cherenkov telescope array that is briefly introduced in the first part of the chapter. The following section summarizes the potential of CTA to search for the presence of WIMPs in the Milky Way halo as it is currently discussed in the literature. A main hypothesis of this chapter is that it is important to investigate and understand astrophysical sources of galactic diffuse γ-ray emission in the TeV energy domain. The galactic diffuse γ-ray emission can be a potential foreground for WIMP searches with Cherenkov telescopes in the Milky Way halo but also a very interesting subject in its own. An analysis of data taken with the H.E.S.S. observatory and a search for a large scale diffuse TeV γ-ray emission signal from the galactic plane are presented. The results are not yet conclusive but improvements of the analysis as well as consequences are discussed. The last section sketches the technique and potential of a new background subtraction method that is based on the spherical harmonic expansion of event skymaps.

5.1 The Cherenkov Telescope Array

The Cherenkov Telescope Array (CTA, see Actis et al. [2011]) is the planned successor of current generation Cherenkov telescope arrays like VERITAS, H.E.S.S. and MAGIC. The approach is to distribute Cherenkov telescopes over a large ($\sim$ 1 km radius) area and to possibly build two independent arrays, one in the northern hemisphere primarily aiming for observations of extragalactic objects and one in the southern hemisphere focusing on galactic high energy astroparticle physics (see Actis et al. [2011] for details). The project is currently in its design phase where different technical realizations of the array are investigated and compared. The expected timeline is to start the construction of the array in $\sim$ 2015 and start data-taking with the full operational array in $\sim$ 2020. Different Monte Carlo based studies predict that the effective area for CTA will be larger than $10^5\,\mathrm{m}^2$ above 100 GeV and larger than $10^6\,\mathrm{m}^2$ above 1 TeV up to at least $\sim$ 100 TeV (Bernloehr et al. [2013], Paz Arribas [2008], Becherini et al. [2012]). In comparison with the H.E.S.S. experiment (H.E.S.S. Col. [2006]) this means at least an improvement of one order of magnitude in effective area for γ-rays in the energy range between 100 GeV and 100 TeV. Additionally, the sensitivity of CTA to γ-rays is extended towards energies below 100 GeV and above 100 TeV and the background suppression can potentially be improved compared to current generation IACTs. The sensitivity of the planned CTA observatory can be very roughly estimated from the sensitivity of the H.E.S.S. array by

assuming that the CTA observatory has the same energy threshold as H.E.S.S. but a factor of 10 increased effective area for γ-ray and background events. This results in a factor of $\sqrt{10} \sim 3$ increase in sensitivity compared to the H.E.S.S. array. In other words, it is estimated that the observation of a γ-ray signal with the CTA observatory yields a factor of ~ 3 larger excess significances than the observation of the same signal with the H.E.S.S. array for the same exposure. Alternatively, the exposure needed for CTA to detect a γ-ray signal at a given significance level is by an order of magnitude smaller than for the H.E.S.S. instrument. This approach is conservative as regards the sensitivity estimate for CTA as it neglects any sensitivity improvements caused by a reduced energy threshold.

5.2 Diffuse VHE γ-ray Emission with CTA

Figure 5.1 is taken from Doro et al. [2012] and shows the predicted sensitivity of CTA to a γ-ray flux that is generated from self annihilating WIMPs in the Milky Way dark matter halo. The assumed analysis methods are very similar to the methods that have been used in this thesis especially with respect to the assumption that the exclusion of the galactic plane with $|b| < 0.3°$ is sufficient to avoid the contamination from the diffuse γ-ray emission of the galactic plane despite of the improved sensitivity of the instrument. If the assumptions hold, CTA will have the ability to be significantly more sensitive to search for the presence of WIMPs in the galactic halo than current Cherenkov telescope experiments. In particular it will be possible to test WIMP models with velocity averaged WIMP annihilation cross sections that are below the canonical value for thermal relic WIMPs with masses of some 100 GeV, depending on the analysis method (see fig. 5.1). However, if the extension of the exclusion regions must be increased in galactic latitude because the increased sensitivity of CTA traces the diffuse emission of the galactic plane also at larger $|b|$, the sensitivity estimates in Doro et al. [2012] most be modified. The resulting sensitivity of CTA to search for WIMPs in the dark matter halo of the Milky Way will be worse than estimated. It is thus appropriate to not only study the potential of CTA to detect the faint diffuse γ-ray fluxes that putatively result from WIMP annihilations in the Milky Way halo but also the potentially more intensive diffuse γ-ray fluxes that have an astrophysical origin. In the next section, a search for a large scale diffuse γ-ray emission from the galactic plane with H.E.S.S. data is presented.

5.3 Search for Large Scale γ-Ray Emission from the Galactic Plane with H.E.S.S.

Introduction

The interaction of cosmic rays with interstellar material leads to the production of γ-rays in neutral pion decays and is a well known source for the emission of a diffuse band of γ-rays with energies below ~ 100 GeV from the galactic plane (see f.i. Ackermann

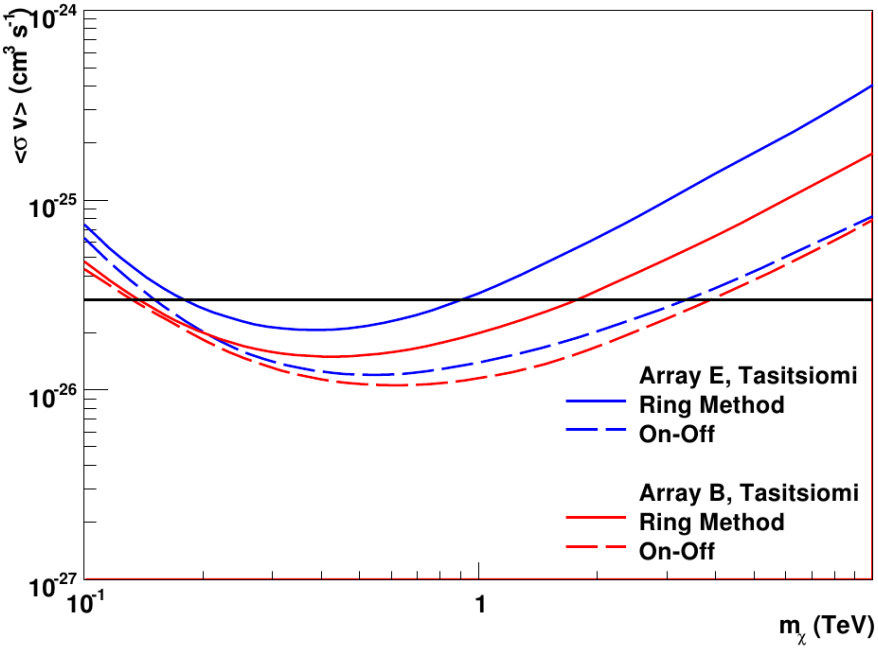

Figure 5.1: Estimated sensitivity of CTA to the velocity averaged annihilation cross section of WIMPs in the Milky Way dark matter halo as a function of the WIMP mass for different possible CTA design layouts (array E and B). The 'ring method' is similar to what is discussed as 'rotated pixel method' in this thesis. The On/Off method is assumed to have a similar pointing strategy as the On/Off method that is discussed in this thesis. A total of 100 h of observation time is assumed for the On/Off and the ring method. The horizontal black line indicates the canonical value for the thermal relic WIMP velocity averaged annihilation cross section. The plot is taken from Doro et al. [2012].

et al. [2012b]). Other equally well known sources for the emission of diffuse γ-rays from the galactic plane exist. One example is the inverse Compton up-scattering of low energy photon fields by high energy electrons. In the very high energy γ-ray regime, i.e. above ~ 100 GeV, diffuse γ-ray emission has by now been detected by two experiments. The extension of the diffuse γ-ray emission from the galactic center ridge as detected in H.E.S.S. data (H.E.S.S. Col. [2005b]) is with $|l| < 0.8°$ and $|b| < 0.3°$ in galactic longitude and latitude small compared to the extension of the galactic plane. The diffuse emission from the galactic center ridge can, however, be well modeled to be powered by hadronic interactions of cosmic rays with giant molecular clouds that lead to the creation of γ-rays in the decay of neutral pions (H.E.S.S. Col. [2005b]). Notably, the measured spectral index of the γ-ray emission (~ -2.3) as a tracer of the spectral index of the underlying hadron distribution excludes that the same population of cosmic rays that are detected on earth (spectral index ~ -2.7) is responsible for the generation of the diffuse γ-ray signal from the galactic center ridge. Additionally to the diffuse γ-ray emission from the galactic center ridge as observed with H.E.S.S., a large scale diffuse emission signal is also detected in data recorded with the Milagro water Cherenkov detector at ~ 15 TeV (Abdo et al. [2008]). However, only the dependence of the diffuse signal on galactic longitude and not on energy is investigated in Abdo et al. [2008].
The question emerges whether Cherenkov telescopes can be used to measure the spectral index of the large scale cosmic ray distribution of the Milky Way via the detection and spectral investigation of diffuse γ-ray emission from the galactic plane. The natural supposition (which is to be tested) is that the cosmic ray spectrum in the vicinity of the earth is not differing from the cosmic ray distribution in the rest of the galaxy and thus a soft spectrum (spectral index ~ -2.7) diffuse γ-ray signal from the galactic plane is to be searched for.
Regions in the galactic disc with high gas density are preferred target regions because the expected diffuse γ-ray flux is proportional to the line of sight integrated target material density distribution. A natural target is the molecular hydrogen (H_2) in the disc of the Milky Way because the H_2 molecule is only stable in regions of high density. In regions with a density below $\sim 10^3\,\mathrm{cm}^{-3}$ (Longair [2011]), the ambient UV radiation is dissociating or ionizing the H_2 molecule. The typical density of H_2 regions where dust or the outer hydrogen layers of the region itself shield the UV radiation and enable the presence of molecular hydrogen is $\sim 3 \cdot 10^3\,\mathrm{cm}^{-3}$ (Combes [1991]). For comparison, the average density of the giant molecular clouds that were traced via the diffuse γ-ray emission detected from the galactic center ridge in H.E.S.S. data (H.E.S.S. Col. [2005b]) is $\sim 10^4\,\mathrm{cm}^{-3}$ with peak values around $10^5\,\mathrm{cm}^{-3}$ (Wommer et al. [2008]). Regions where molecular hydrogen is present can be found indirectly via the detection of rotational transitions of CO that are excited in collisions with H_2 (see f.i. Longair [2011] for details). The CO concentration is maximal at $b \sim 0°$ and the scale height of the CO distribution perpendicular to he galactic disc is ~ 120 pc (FWHM) (Combes [1991]). In the projection onto galactic coordinates, the density of CO is decreasing with galactic latitude. At $|b| \sim 1°$ the CO density is about one order of magnitude smaller than the peak values at $b \sim 0°$ (see Combes [1991] but also the right panel of fig. 5.3). Predictions for the expected diffuse γ-ray flux from the galaxy based on assumptions for the cosmic

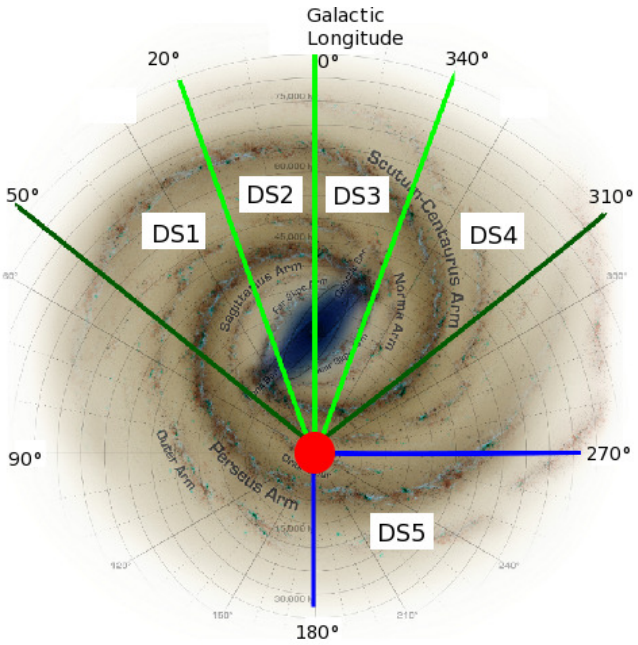

Figure 5.2: Schematic sketch of the Milky Way structure with galactic coordinates overlaid. The colored lines indicate the search regions (DS1 to DS5 for dataset 1 to dataset 5) as discussed in the text. Clearly visible are the galactic bulge (in the center the plot in blue) and the spiral arms. Note that the exact number and position of the spiral arms is a matter of intensive debate (see Hou et al. [2009] and references therein). The position of the sun is marked in red in between the Perseus and the Scutum-Centaurus arm. The figure has been adapted from Churchwell et al. [2009].

ray flux distribution within the galaxy (like f.i. that no flux and spectral variations exist within the galaxy (see Casanova et al. [2009]) or a full modeling of the cosmic ray diffusion in the galaxy (see Strong et al. [2009])) and measurements of the line of sight integrated CO emission are in general possible. However, they are based on either oversimplified assumptions or models with many parameters and lead in general only to order of magnitude estimations as long as no optimization based on measurements (see Ackermann et al. [2012b]) is performed. Given the large uncertainties in the flux predictions, it appears justified to perform a search for the presence of diffuse γ-ray emission at TeV energies from the galactic plane. The difficulties and prospects of such a search are outlined below.

Dataset and Data Analysis

As explained above, the density of molecular hydrogen as projected onto galactic coordinates is peaking around $b \sim 0°$ and decreasing with $|b|$. At $|b| \sim 1°$ the molecular hydrogen density is around one order of magnitude lower than the the peak value. Ad-

Dataset	$l_{\min}$	$l_{\max}$	Number of Runs	Total Livetime (h)	Mean Zenith Angle
1	20°	50°	848	363	32°
2	0°	20°	943	404	19°
3	340°	360°	823	352	27°
4	310°	340°	744	322	36°
5	180°	270°	505	214	33°

Table 5.1: Description of the datasets 1 to 5. The datasets 1 to 4 cover the signal region and dataset 5 is a control dataset where no signal is expected. $l_{\min}$ and $l_{\max}$ are the minimal and maximal covered longitude range.

ditionally, the density of molecular hydrogen in the galaxy is steeply decreasing for distances to the galactic center that are larger than the distance between the sun and the galactic center (see f.i. Longair [2011]). In other words, the density of the projection of the molecular hydrogen density onto galactic coordinates is steeply decreasing for galactic longitudes that exceed $|l| \sim 45°$.
In the following, the presence of a large scale diffuse γ-ray emission signal in the VHE regime is searched for in a region with an extension of $|b| < 1°$ in galactic latitude and $|l| < 50°$ in galactic longitude. A control region, where no signal detection is expected, is defined with $|b| < 1°$ and $180° \leq l \leq 270°$. Data that were taken with the H.E.S.S. I observatory with exposure in the signal and control region and pass standard H.E.S.S. data quality criteria is searched for. A total number of 3358 observation runs corresponding to 1441 h of livetime with a non-vanishing overlap between the observed field of view (defined as the region contained in a 2° radius around the pointing position) and the signal region are found. For the control region, a total number of 505 observation runs corresponding to 214 h of livetime are found. The total available dataset with exposure in the signal region is split into four smaller datasets that vary in the covered galactic longitude range. Table 5.1 gives a summary of the resulting five datasets and fig. 5.2 illustrates the covered pointing range for the different datasets graphically.
A rotated pixel analysis (see chapter 4) with four background pixels for each accepted signal pixel is performed for each of the resulting five datasets. Only events that pass standard H.E.S.S. γ-ray event selection criteria and are reconstructed within an angular distance smaller than 2° from the pointing position of the respective run are analyzed. The H.E.S.S. standard exclusion regions are used to define regions that are disregarded from the analysis.
Figure 5.3 shows in the left panel the distribution of the galactic latitude coordinates for γ-ray sources that were detected in the H.E.S.S. scan of the galactic plane (see Aharonian et al. [2006]). The histogram in the left panel of fig. 5.3 contains 46 entries of which 22 belong to sources with position within $|b| < 0.3°$. Motivated by this, the vicinity of the galactic plane ($|b| < 0.3°$) is excluded to prevent influences on the analysis results by unresolved γ-ray sources as well as by the imperfect exclusion of detected γ-ray sources. Note that the exclusion of resolved and unresolved sources is certainly the most complicated part of the analysis presented in this section. A perfect exclusion

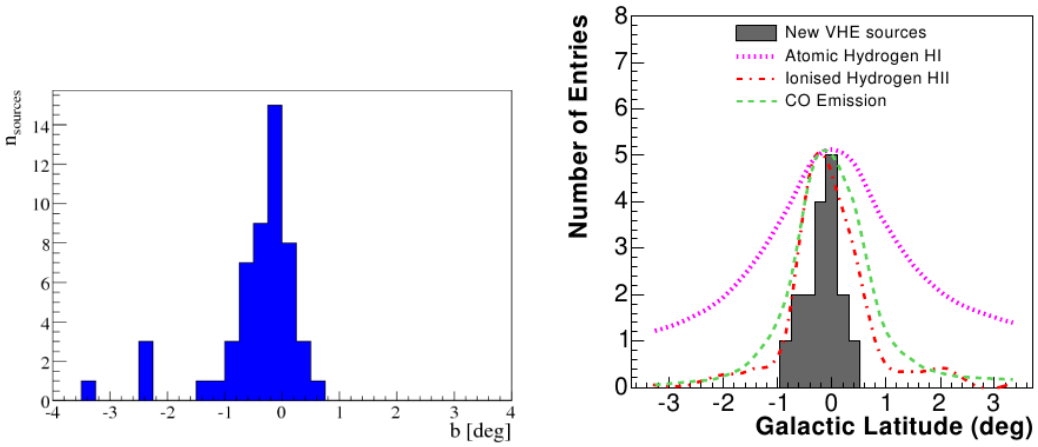

Figure 5.3: Left panel: Galactic latitude distribution of the VHE γ-ray sources detected in the H.E.S.S. galactic plane scan. The figure is taken from Chaves [2009]. Right panel: Same distribution in an older version supplemented by the latitude distribution of atomic, ionized as well as molecular hydrogen in arbitrary units. The plot is taken from Aharonian et al. [2006].

of resolved and unresolved γ-ray sources from the analysis is unrealistic and thus it must be investigated whether the result of an analysis is significantly influenced by imperfect exclusion regions. Note also that the search region for a diffuse emission signal, i.e. the region where high densities of H_2 are traced by the presence of CO emission, almost equals the region where most VHE γ-ray sources are found (see fig. 5.3 right panel). The spatial correlation between regions where VHE γ-ray sources are found and regions where diffuse VHE γ-ray emission is supposed is from the physical point of view not surprising because many of the known galactic VHE γ-ray sources (in particular SNRs and PWNe which make the majority of galactic VHE γ-ray sources) are powered by processes that set in at the end of the evolution of stars. However, stars are typically formed in regions of high ambient material density that does also act as target material for the hadronic generation of diffuse VHE γ-ray emission.

Results

Table 5.2 summarizes the results of the analysis of all five considered datasets. Significant γ-ray excesses are detected in the datasets one to four. No significant γ-ray excess is detected in dataset five. The result appears highly interesting as it is what would be expected from a diffuse γ-ray signal in the galactic plane. However, much more detailed investigations are necessary to conclusively claim a detection of a γ-ray signal. A first step towards a more detailed analysis is presented below for two of the considered datasets.

Dataset	$\sum \Omega T$ (ssr)	N_{ON}	N_{OFF}	α	Δ	S_{LiMa}
1	519	350941	1371100	0.25010	8031	12.2σ
2	538	470494	1834300	0.25012	11707	15.4σ
3	463	378576	1498073	0.25010	3904	5.7σ
4	456	339789	1323340	0.25012	8795	13.6σ
5	197	141070	564384	0.25014	-106	-0.3σ

Table 5.2: Results of the analysis of datasets one to five. Summarized are the total signal region exposure ($\sum_{\mathrm{runs}} \Omega T$), the number of signal and background events (N_{ON} and N_{OFF}), the exposure ratio (α) as well as the excess (Δ) and significance (S_{LiMa}). The exposure ratio is the mean of the exposure ratios of all analyzed observation runs within a dataset. The RMS of the runwise exposure ratio distribution is always smaller than $5 \cdot 10^{-5}$.

Detailed Analysis of Dataset 5

Figure 5.4 shows the distribution of recorded events that pass standard H.E.S.S. γ-ray selection criteria in the signal (upper panel) and background (lower panel) region. It is apparent that the exposure of dataset five is not homogeneous over the control region with $180^\circ < l < 270^\circ$ but most of the exposure is in the regions around $250^\circ < l < 270^\circ$. Figure 5.5 shows the significance map of the signal region as generated with the rotated pixel background subtraction. For this, a skymap of events that are accepted as signal events in the rotated pixel analysis is generated and the background events that are counted in the background region that is constructed from the rotated pixel algorithm are saved in a second skymap in the bin that corresponds to the considered signal bin. The two maps are eventually correlated with a radius of 0.1°, i.e. the number of events within a radius of 0.1° around a given bin is put into the respective bin. A third map that contains the exposure ratio entries for each signal bin, i.e. the ratio $\cos(b_{\mathrm{on}}) / \sum_{i=1}^{4} \cos(b_{\mathrm{off(i)}})$ where b_{on} is the signal bin galactic latitude value and $b_{\mathrm{off(i)}}$ with $i = 1..4$ are the four background pixel latitude values, is created. The significance of the γ-ray excess in each bin in the signal region skymap is calculated finally with the method described in Li and Ma [1983]. No single local region with a significant γ-ray excess is visible in fig. 5.5. The local significances are typically fluctuating between -4σ and $+4\sigma$.

Detailed Analysis of Dataset 1

The analysis of dataset one revealed the putative presence of a strong ($\sim 12\sigma$) γ-ray signal in the search region. The strength of the signal motivates an energy dependent investigation of the γ-ray flux from the search region. Figure 5.6 shows the energy dependence of the γ-ray flux (dN/dE) from the search region as well as a forward-folded fit (see Piron et al. [2001]) of the data to a power law $dN/dE = k\,(E/\mathrm{TeV})^{-\Gamma}$. The signal in the search region is detected above ~ 240 GeV up to ~ 5 TeV. The compatibility of the forward-folded fit result with the datapoints is excellent ($\chi^2/\mathrm{NDF} = 9.3/9$).

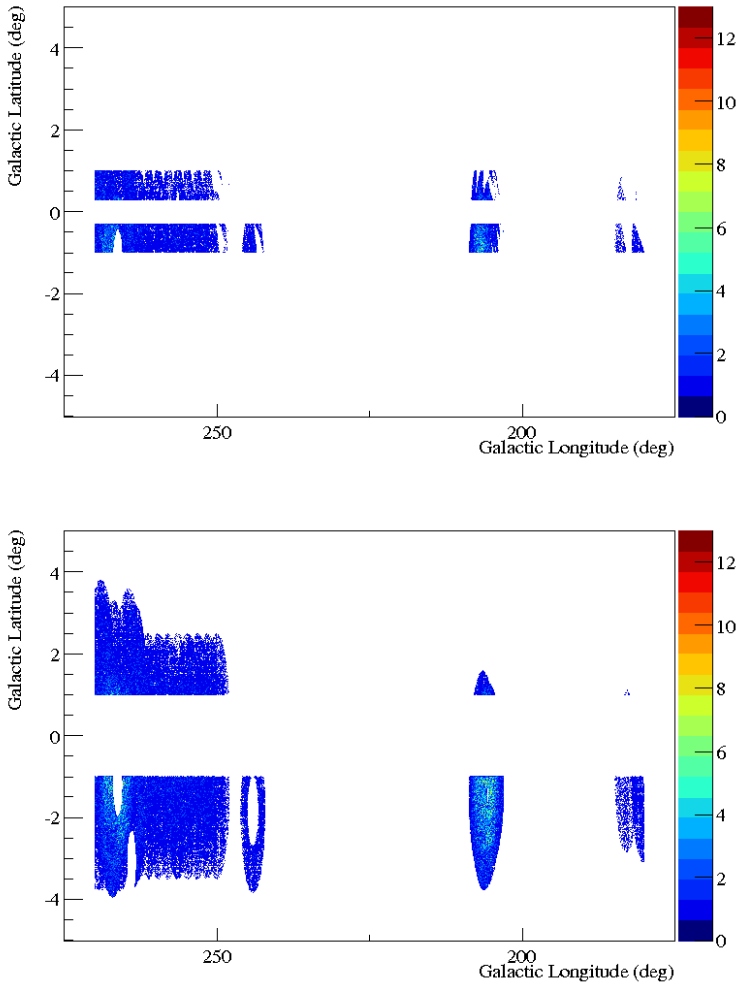

Figure 5.4: Number of reconstructed events in galactic coordinates for the dataset 5 signal (upper panel) and background (lower panel) region. White regions are either excluded from the analysis or have not been observed.

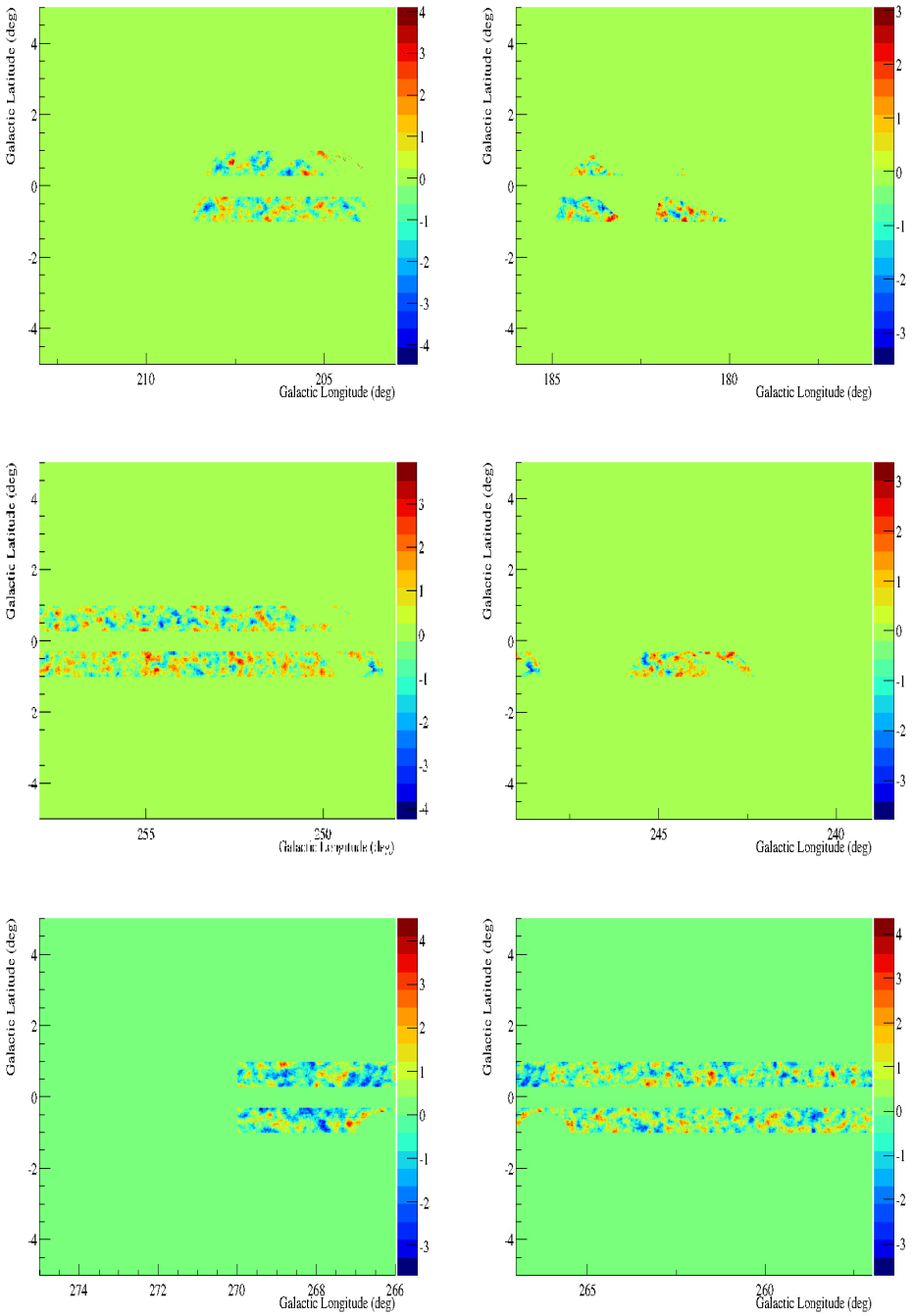

Figure 5.5: Significance map of the signal region of dataset 5 in galactic coordinates. The skymap is split into six partially overlapping regions in longitude. Only regions with non-vanishing exposure are shown. The map is generated with the rotated pixel algorithm for the background subtraction and correlated with 0.1°.

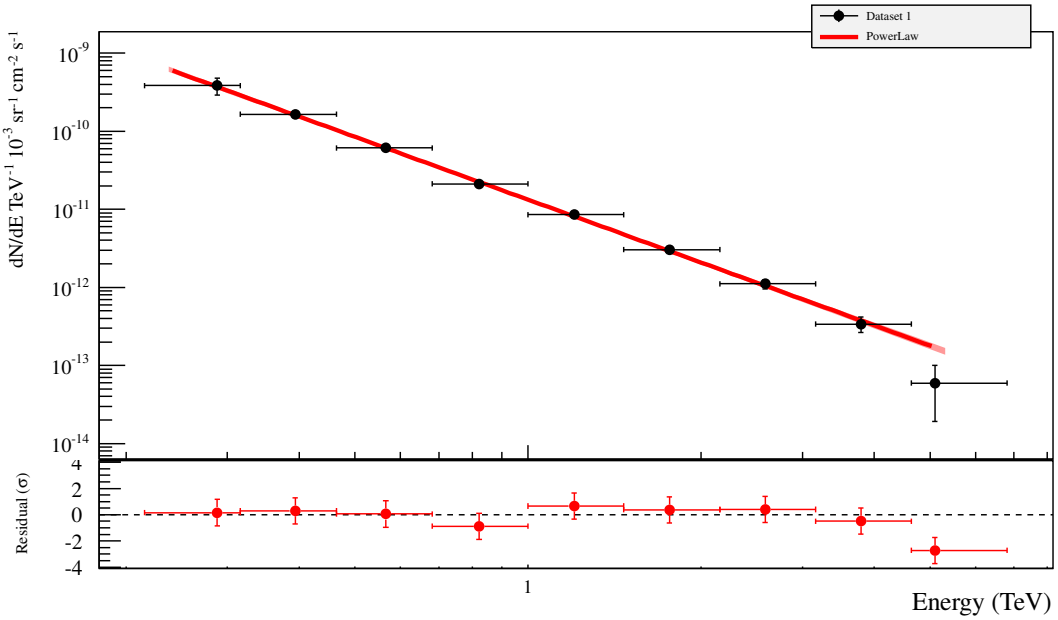

Figure 5.6: Energy dependence of the γ-ray flux detected in dataset 1 (black) and fit to a power law (red) in the upper panel as well as fit residuals in the lower panel. Shown are 1σ statistical errors.

The flux normalization[1] and spectral index as obtained from the fit are $k = (1.94 \pm 0.06_{\mathrm{stat}}) \cdot 10^{-8}\,\mathrm{TeV}^{-1}\mathrm{cm}^{-2}\mathrm{sr}^{-1}\mathrm{s}^{-1}$ and $\Gamma = 2.67 \pm 0.05_{\mathrm{stat}}$. Figure 5.7 shows the number of reconstructed events that are analyzed in dataset one for the signal and background region to get a visual impression of the distribution of signal and background events as well as the applied exclusion regions. A rather uniform exposure in the search region with galactic longitude in the range of $20° < l < 50°$ is visible. More detailed are the local significance maps shown in fig. 5.8. The significance maps are generated from the same rotated pixel analysis that is used to search for the presence of a signal in the total dataset but show only local significances, similar to the generation of the local significance map for dataset five as discussed above. As visible in fig. 5.8, there are spatially connected regions around some of the exclusion regions where the local excess significance is not fluctuating around zero but appears biased towards values larger than zero. This complicates the analysis considerably because two options to explain the pu-

[1] Note that no investigation of systematic errors on the inferred γ-ray flux besides a check of the stability of the results against the increase of the image cleaning threshold from '0510' to '0710' (see chapters 2 and 4) has been performed yet. The apparent stability of the results against increased image cleaning thresholds disfavors an explanation with night sky background gradients between the signal and background regions used in the analysis. However, this and other sources of systematic errors have to be studied in more detail. In particular, the flux normalization as inferred from the fit appears too large when compared with the flux normalization of the diffuse emission from the galactic center ridge of $(1.73 \pm 0.13_{\mathrm{stat}} \pm 0.34_{\mathrm{sys}}) \cdot 10^{-8}\,\mathrm{TeV}^{-1}\mathrm{cm}^{-2}\mathrm{sr}^{-1}\mathrm{s}^{-1}$, see H.E.S.S. Col. [2005b].

tative γ-ray excess detected in the analysis of dataset one are conceivable. The first is that a diffuse γ-ray emission signal from the galactic plane is detected that has the same energy spectrum as the cosmic ray TeV spectrum measured in the vicinity of the earth. The second is that an accumulation of γ-rays that are generated in usual astrophysical sources is detected. A proper solution of this problem is beyond the scope of this thesis but a possible method is sketched below.
Figure 5.10 shows VHE γ-ray sources that are detected with the H.E.S.S. instrument in the region covered by dataset one. The positions and spectral indices (as far as it is measured) of the 17 sources that are detected in the region are given in table 5.3. The table shows that $\sim 50\%$ of the γ-ray sources known in the region have a spectral index which is compatible with -2.7. Figure 5.9 shows the longitude distribution of the 8031 excess events (see table 5.2) detected in dataset one towards the galactic plane. The comparison of the longitude distribution of the excess signal (fig. 5.9) with the table of the positions and spectral indices of the known VHE γ-ray sources in the region (table 5.3) shows that a large fraction of the signal measured in dataset one is detected towards regions where γ-ray sources whose measured spectral index is compatible with -2.7 are present.
It is obvious that the strategy to search for a diffuse γ-ray emission signal from the galactic plane must be modified for a conclusive analysis. It is suggested that for a search of a diffuse γ-ray signal from the galactic plane with a soft spectrum (i.e. ~ -2.7 spectral index), very conservative exclusion regions must be placed around astrophysical γ-ray sources with unknown or soft spectral index (f.i. smaller than ~ 2.4). The exclusion regions in the vicinity of hard spectrum γ-ray sources can be arranged to be less conservative, similar to the exclusion regions considered in the analysis above. If the analysis is still showing the presence of a significant large scale excess signal with a soft spectral index, the insufficient exclusion of astrophysical sources appears disfavored as an explanation. A similar search can also be conducted for diffuse γ-ray emission with hard spectral index by conservatively excluding known γ-ray sources with hard spectrum. However, it is obvious that a detailed study of the γ-ray sources that are present in the field of view that is of interest is necessary as a starting point for a later search for a diffuse γ-ray emission signal. As stated, this is beyond the scope of this thesis.

Discussion and Conclusion

A first step towards a search for the presence of a large scale diffuse γ-ray signal from the disc of the Milky Way is discussed in this section. It is shown that the main problem of a diffuse emission search is the strong expected spatial correlation of regions with intense diffuse γ-ray emission and localized astrophysical γ-ray sources. A possible solution of this difficult problem is proposed by the search for a deviation of a putative large scale diffuse γ-ray spectrum from the spectra of the local astrophysical sources. An alternative approach is discussed in Egberts et al. [2013] where conservative exclusion regions are proposed. The exclusion of any region by 0.2° around a bin in a skymap whose γ-ray excess significance (calculated with a ring background algorithm) exceeds 4σ and a neighboring bin exists whose significance is exceeding 4.5σ as suggested in Egberts

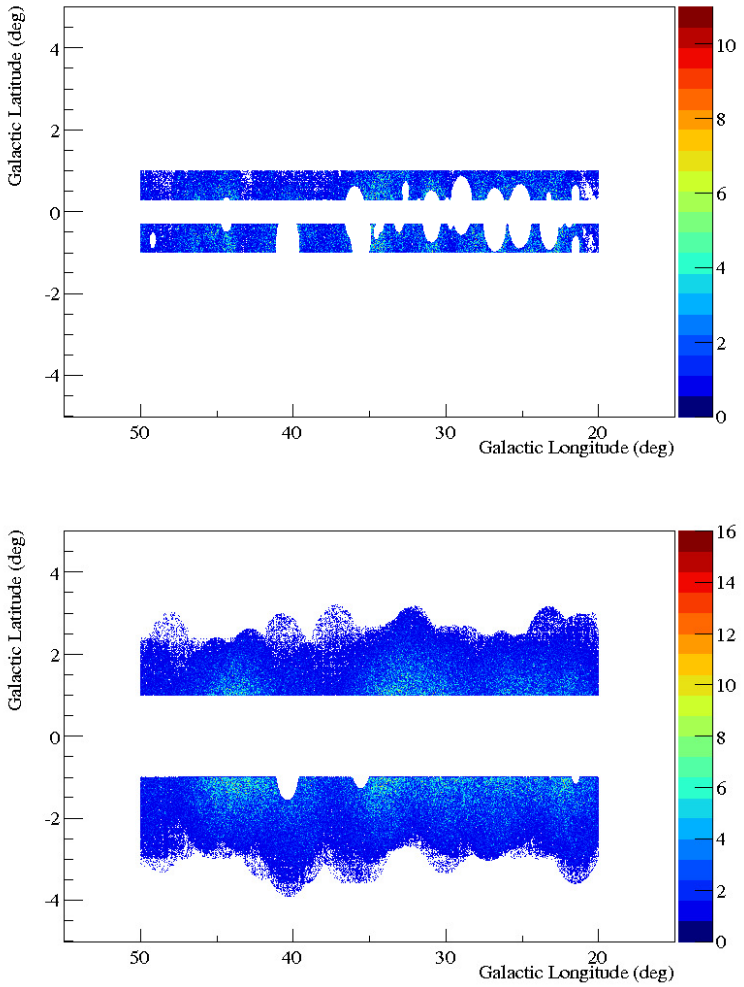

Figure 5.7: Number of reconstructed events in galactic coordinates for the dataset 1 signal (upper panel) and background (lower panel) region.

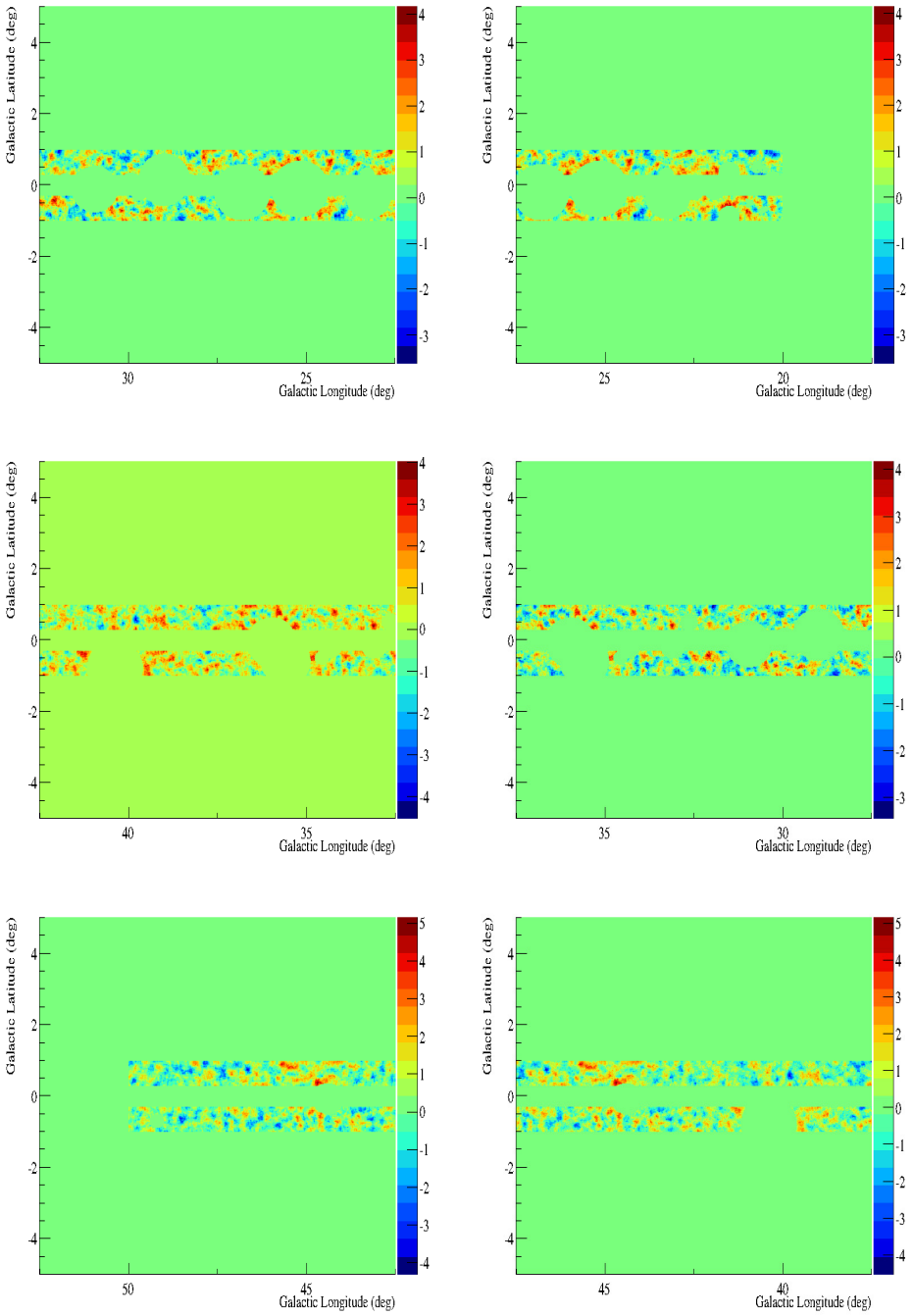

Figure 5.8: Significance map of the signal region of dataset 1 in galactic coordinates (split into six partially overlapping regions in longitude). The map is generated with the rotated pixel algorithm for the background subtraction and correlated with 0.1°.

Source	l	b	Γ	Reference
J1833-105	21.5°	−0.9°	$-2.08 \pm 0.22_{\mathrm{stat}} \pm 0.1_{\mathrm{sys}}$	Djannati-Atai et al. [2007]
J1831-098	21.9°	−0.1°	-2.1 ± 0.1	Sheidaei et al. [2011]
J1832-093	22.5°	−0.2°	$-2.6 \pm 0.3_{\mathrm{stat}} \pm 0.3_{\mathrm{sys}}$	Laffon et al. [2013]
J1834-087	23.2°	−0.3°	$-2.5 \pm 0.2_{\mathrm{stat}} \pm 0.2_{\mathrm{sys}}$	Albert et al. [2006]
J1837-069	25.2°	−0.1°	-2.27 ± 0.06	Aharonian et al. [2006]
J1841-055	26.8°	−0.2°	$-2.4 \pm 0.1_{\mathrm{stat}} \pm 0.2_{\mathrm{sys}}$	Aharonian et al. [2008c]
J1843-033	29.3°	0.5°	-	Hoppe [2008]
J1846-029	29.7°	−0.2°	-2.26 ± 0.15	Djannati-Atai et al. [2007]
J1849-000	32.6°	0.5°	-	Terrier et al. [2008]
J1848-018	31.0°	−0.2°	~ -2.8	Acero et al. [2013]
J1852-000	33.1°	5.1°	-	-
J1857+026	36.0°	−0.1°	~ -2.2	Hessels et al. [2008]
J1858+020	35.6°	−0.6°	-2.17 ± 0.12	Aharonian et al. [2008c]
J1908+063	40.4°	−0.8°	$-2.10 \pm 0.07_{\mathrm{stat}} \pm 0.2_{\mathrm{sys}}$	Aharonian et al. [2009]
J1911+090	43.3°	−0.2°	$-3.1 \pm 0.3_{\mathrm{stat}} \pm 0.2_{\mathrm{sys}}$	Chaves et al. [2008]
J1912+101	44.4°	−0.1°	$-2.7 \pm 0.2_{\mathrm{stat}} \pm 0.3_{\mathrm{sys}}$	Aharonian et al. [2008b]
J1923+141	49.1°	−0.6°	-	-

Table 5.3: Spectral indices of the known γ-ray sources that are present in the field of view of dataset one. No information could be found for fields marked with '-'.

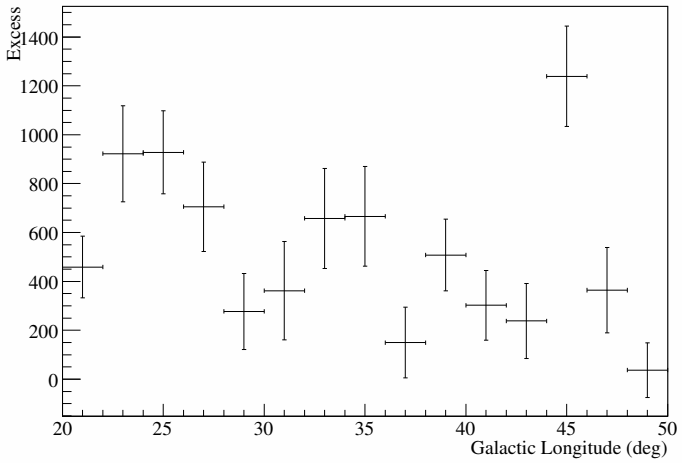

Figure 5.9: Longitude distribution of the 8031 γ-ray excess events detected in dataset one. The binning is 2° in longitude.

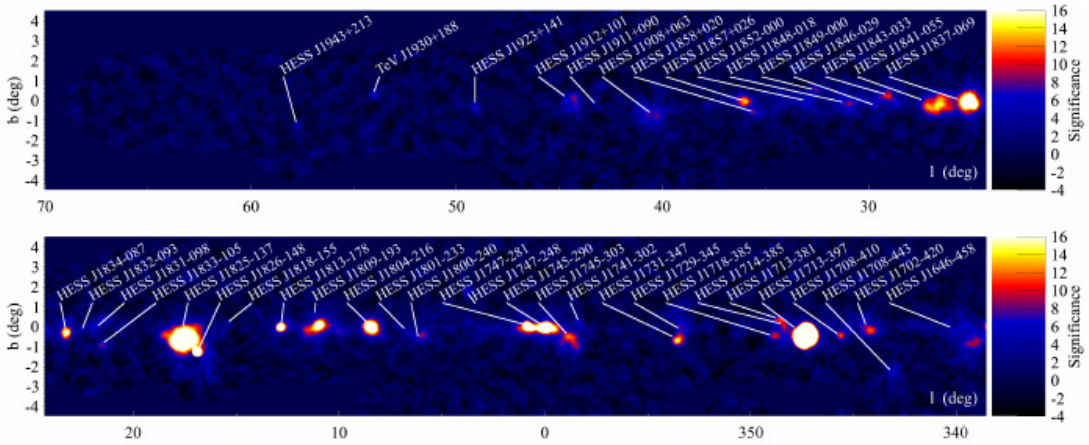

Figure 5.10: VHE γ-ray sources detected in the scan of the galactic plane in the region covered with exposure from dataset one. Shown is the post-trial significance in galactic coordinates. The figure is taken from Carrigan et al. [2013].

et al. [2013] leads to the conclusion that a residual large scale diffuse γ-ray spectrum is detected in an analysis of H.E.S.S. data. The spatial distribution of the signal in galactic latitude but not the energy spectrum of the residual flux is investigated in Egberts et al. [2013]. The inferred distribution of the residual γ-ray signal in galactic latitude exhibits a strong correlation with the galactic latitude distribution of known γ-ray sources, as is expected. Similar to the analysis presented above, it appears difficult to conclude based on the apriori selection of exclusion regions whose shape is determined by arbitrary significance levels that the residual γ-ray signal detected in Egberts et al. [2013] is caused by diffuse γ-ray emission of the galactic plane.
A conclusion can be drawn that is independent from the problem to determine whether the residual signal detected in the search for large scale diffuse emission from the galactic plane in data taken with the H.E.S.S. array are caused by the insufficient exclusion of known γ-ray sources or not. If the analysis of several 100 h of H.E.S.S. data reveals either the presence of diffuse γ-ray emission from the galactic plane or problems with the insufficient exclusion of γ-ray sources, the same problem must be handled for CTA in much smaller datasets. Consider the typical extension ($\Omega = 3.4 \cdot 10^{-4}$ sr, see chapter 4) of the signal region in a rotated pixel analysis for the presence of a γ-ray flux from WIMP annihilation as discussed in chapter 4. The extension of the signal region that is assumed for the 'ring method' in fig. 5.1 is typically similar. The exposure in one typical observation of $T = 30$ min length is $T\Omega \sim 0.6\,\mathrm{ssr/run}$. The sensitivity of the CTA observatory to the velocity averaged WIMP annihilation cross section in a search for a diffuse γ-ray emission towards the vicinity of the galactic center region is estimated in fig. 5.1 for 100 h of observation time. This corresponds to a diffuse exposure of $\sim 120\,\mathrm{ssr}$ or a factor of ~ 4 less than for the search region considered in this section (see table 5.2). Given that CTA is conservatively estimated to need one order of magnitude less exposure

than H.E.S.S. to detect a signal at the same statistical significance level, it appears to be very unlikely that the same analysis that has been performed with H.E.S.S. data in the galactic center region can also be performed with CTA data without the detection of a signal that is either due to diffuse emission from the galactic plane or due to astrophysical sources that are not sufficiently excluded. Given that the non-detection of a signal is an underlying assumption of the CTA sensitivity estimation for the velocity averaged WIMP annihilation cross section that is shown in fig. 5.1, it appears well motivated to further investigate the effects discussed in this section in the future.

5.4 Harmonic Background Subtraction

Motivation: The Fermi Bubbles

The background subtraction technique that is discussed in the following has been developed in the context of the discovery of an impressive large scale structure of γ-ray emission that is roughly symmetric to the galactic center in an analysis of data recorded with the Fermi γ-ray satellite (see Su et al. [2010] and Dobler et al. [2010]). In more detail, the first analysis results were (see Su et al. [2010] and Dobler et al. [2010]):

- The presence of two bubble shaped emission regions with extended γ-ray emission ($\sim$ 10 kpc or 50° in galactic latitude) towards the north and south of the galactic center.
- A hard energy spectrum of the γ-ray emission, that is compatible with a power law with spectral index -2 and flux normalization $3 \cdot 10^{-10}$ TeV^{-1}s^{-1}sr^{-1}cm^{-2}. The spectrum was initially measured up to $\sim$ 100 GeV.
- Uniform surface brightness of the bubbles. In other words, the initially measured flux did not vary significantly within the Fermi bubbles as seen in the projection to galactic coordinates.
- Partial spatial matches of the γ-ray bubbles with former detections of galactic large scale emission regions in other wavelength, especially in microwave (WMAP, Planck) and X-ray (ROSAT) measurements (see Su et al. [2010], Dobler et al. [2010], Dobler [2012], Planck Col. [2012] for a detailed discussion).

The theoretical modeling of the γ-ray emission was initially driven by the following scenarios:

- A hadronic model was proposed in Crocker and Aharonian [2011] and Crocker [2012]. The general outline of the model is that protons are accelerated via diffusive shock acceleration (1st order Fermi acceleration) in SNRs that are frequently produced in the vicinity of the galactic center as a result of a high star formation rate in that region. A wind drives the accelerated protons out of the galactic disc. The γ-ray emission is generated in the decay of neutral pions which result from the interaction of the accelerated hadrons with the inter stellar medium. The putative

microwave counterpart to the γ-ray bubbles can be explained with the synchrotron emission of electrons resulting from the decay of charged pions. Central predictions of the model are that no cut-off in the energy spectrum at photon energies above $\sim$ 150 GeV is present and that neutrino emission must also be generated as the result of the decay of charged pions.

- Two leptonic models were proposed. First order (or diffusive shock) acceleration of leptons from stars disrupted by a central black hole in the Milky Way was proposed in Su et al. [2010]. Alternatively, second order (or stochastic) Fermi acceleration of leptons on turbulent plasma waves within the bubble is proposed (Mertsch and Sarkar [2011]). In both cases, the accelerated leptons generate the emission of γ-rays via the inverse Compton up scattering of cosmic microwave, far infrared or optical photons. No emission of high energy neutrinos is predicted. Additionally, the γ-ray spectrum must have a cut-off at some 100 GeV.

The predicted cut-off in the energy spectrum triggered the investigation of the potential to use Cherenkov telescope arrays to discriminate between leptonic and hadronic models for the Fermi bubbles. If no signal towards the Fermi bubbles were detected with a Cherenkov telescope array with sufficient sensitivity, the hadronic models could be ruled out. If, on the other hand, a signal above some 100 GeV were detected, leptonic models would be ruled out. A similar approach is currently investigated with neutrino telescope data (Lunardini and Razzaque [2012]). Preliminary results from observations with the ANTARES neutrino observatory show no indication of a signal and set upper limits on the neutrino flux from the Fermi bubbles which are only a factor of ~ 2 larger than the expected flux in a simple hadronic model (see Kulilovskiy [2013]). The discrimination between hadronic and leptonic emission models for the Fermi bubbles with Cherenkov telescopes faces, however, problems with the application of known background event subtraction techniques. An obvious observation strategy is to point Cherenkov telescopes towards the edges of the Fermi bubbles and define a signal region as the overlap between the observed field of view and the Fermi bubbles and the background region as the remaining field of view[2]. However, the location of the Fermi bubbles is only inferred from Fermi γ-ray data with a precision of $\sim 2^\circ$ which is comparable to the field of view of current Cherenkov telescopes. A modified pointing strategy with three different pointing positions, one towards the location of the Fermi bubble edge as inferred from

[2]The Fermi bubble templates as discussed in Su et al. [2010] were kindly provided to me by Douglas Finkbeiner. The edges of the templates were in turn extracted and H.E.S.S. data with pointing positions in the vicinity of the extracted edges were searched for. More than 800 observation runs ($\sim$ 400 h livetime) of H.E.S.S. data that pass standard data quality criteria were found where the H.E.S.S. field of view overlaps with the Fermi bubble edges as extracted from the templates discussed in Su et al. [2010]. A rotated pixel analysis with this dataset for the signal region defined by the provided Fermi bubble template and excluding all known γ-ray sources as well as the galactic plane ($|b| < 0.3^\circ$) has been performed. No significant γ-ray event excess has been detected. However, the analysis is not conclusive as the precision of the determination of the location of the Fermi bubble edges is not sufficient to precisely define a signal region and no upper limit on the flux from the Fermi bubbles can be derived without precise knowledge of the size of the overlap between the observed field of view and the Fermi bubble emission region.

Fermi satellite data and two with an angular distance offset by $\pm 2^\circ$, has in the following been investigated. This strategy ensures that one or two pointings do have an overlap between the observed field of view and the Fermi bubble edge. However, it is not possible to define a signal and background region for the background subtraction based on the imprecise knowledge of the γ-ray Bubble edge position. Therefore, the harmonic background subtraction, that does not rely on the a priori definition of the location and shape of the signal and background region, has been developed.
Very recently published preliminary results from the Fermi Collaboration show a clear cut-off of the Fermi γ-ray bubble emission spectrum at $\sim$ 130 GeV (Franckowiak and Malyshev [2013]). The detection of a cut-off of the γ-ray spectrum strongly disfavors hadronic emission models for the Fermi bubbles and dilutes the motivation for the investigation of the Fermi bubbles with Cherenkov telescopes. The detection of a cut-off of the Fermi bubble spectrum at $\sim$ 130 GeV gives, however, an interesting hint towards a possible natural explanation for the presence of γ-ray line emission at an energy around 130 GeV (Finkbeiner and Su [2012]) by the insufficient background modeling as is discussed in more detail in Profumo and Linden [2012].
Although the initial motivation for the development of the harmonic background subtraction is by now diluted, new motivations are present. One of them is possibly the investigation of the presence of the emission of a γ-ray line at $\sim$ 130 GeV from a region in the vicinity of the galactic center whose shape and position is, however, as is the shape and position of the Fermi bubble edges, only known with a precision that is comparable to the field of view of current Cherenkov telescopes.

Spherical Harmonics and Background Subtraction

A central assumption of the rotated pixel and the more commonly applied reflected region background subtraction algorithm is the rotational symmetry of the background event acceptance around the observation position. A different perspective on the problem of background subtraction with rotationally symmetric background acceptance is to consider the number of events that are recorded towards a direction θ, ϕ on the unit sphere in one observation run whose pointing position is aligned with the z-axis of the coordinate system, i.e. $\theta = 0$, and expand in spherical harmonics, i.e.

$$\text{Events}(\theta, \phi) = \sum_{l=0}^{\infty} \sum_{m=-l}^{+l} a_{lm} Y_{lm}(\theta, \phi) \, . \tag{5.1}$$

Here, a_{lm} are complex coefficients given by

$$a_{lm} = \int_{S^2} d\Omega \text{Events}(\theta, \phi) Y^*_{lm}(\theta, \phi) = \int_0^{2\pi} d\phi \int_0^{\pi} d\theta \sin(\theta) \, \text{Events}(\theta, \phi) Y^*_{lm}(\theta, \phi) \, . \tag{5.2}$$

$Y_{lm}(\theta, \phi)$ are spherical harmonics,

$$Y_{lm}(\theta, \phi) = N_{lm} P_{lm}(\cos(\theta)) \exp(im\phi) \, , \tag{5.3}$$

where N_{lm} are normalization coefficients that are independent of the coordinates and $P_{lm}(\cos(\theta))$ are the associated Legendre polynomials (see Hassani [2002] and references therein). The expansion in spherical harmonics in the given coordinate system can be used to extract a component that is rotationally symmetric around the observation position,

$$\mathrm{Bkg}(\theta) = \sum_{l=0}^{\infty} a_{l0} Y_{l0}(\theta) \,, \tag{5.4}$$

with the help of the 'zonal harmonics' for $m = 0$, i.e.

$$Y_{l0}(\theta) = N_{l0} P_{l0}(\cos(\theta)) \,. \tag{5.5}$$

The difference

$$\mathrm{Sig}(\theta, \phi) = \mathrm{Events}(\theta, \phi) - \mathrm{Bkg}(\theta) \tag{5.6}$$

is in the following called the γ-ray signal after the subtraction of the rotationally symmetric background. It is investigated in this section whether a connection between this γ-ray signal definition and the usual γ-ray excess obtained from standard background subtraction algorithms exists. For this, important properties of the spherical harmonics that are used explicitly or implicitly in the following are itemized below.

- Most important is the orthonormality of the spherical harmonics, i.e.

$$\int_{S^2} d\Omega Y_{lm}(\theta, \phi) Y^*_{l'm'}(\theta, \phi) = \delta_{ll'} \delta_{mm'} \tag{5.7}$$

  with Kronecker deltas $\delta_{ll'}$ and $\delta_{mm'}$. Equations 5.1 and 5.2 are a direct consequence of the orthonormality.

- Consider the total number of events

$$\int_{S^2} d\Omega \mathrm{Events}(\theta, \phi) = \sum_{l=0}^{\infty} \sum_{m=-l}^{+l} a_{lm} \int_{S^2} d\Omega Y_{lm}(\theta, \phi) \tag{5.8}$$

  detected in an observation run. The lowest order spherical harmonic is

$$Y_{00}(\theta, \phi) = Y^*_{00}(\theta, \phi) = \frac{1}{\sqrt{4\pi}} = \mathrm{const} \tag{5.9}$$

  and it follows with the orthonormality of the spherical harmonics that

$$\frac{1}{\sqrt{4\pi}} \int_{S^2} d\Omega Y_{lm}(\theta, \phi) = \int_{S^2} d\Omega \, Y^*_{00} Y_{lm}(\theta, \phi) = \delta_{l0} \delta_{m0} \,. \tag{5.10}$$

  In other words, the total number of events detected in an observation run is given by

$$\int_{S^2} d\Omega \mathrm{Events}(\theta, \phi) = \sqrt{4\pi} a_{00} \tag{5.11}$$

  or essentially by the 'monopole moment' of the spherical harmonic expansion, i.e.

a_{00}. This already means that eq. 5.6 is different from the usual γ-ray excess obtained with standard background subtraction algorithms in the sense that the total signal measured in a run

$$\int_{S^2} d\Omega \mathrm{Sig}(\theta, \phi) = 0 \tag{5.12}$$

is always vanishing.

- The coefficients a_{lm} of the spherical harmonic expansion (eq. 5.1 or 5.2, respectively) are complex numbers. In total there are $2l + 1$ coefficients for every l but not all a_{lm} are independent. Using that $Y_{lm}(\theta, \phi) = Y^*_{l,-m}(\theta, \phi)$ (see f.i. Hassani [2002]) it follows that

$$a_{lm} = \int_{S^2} d\Omega \mathrm{Events}(\theta, \phi) Y^*_{lm}(\theta, \phi) = a^*_{l,-m} \,. \tag{5.13}$$

  In other words, for complex a_{lm} it is sufficient to only consider the $l+1$ coefficients with $0 \leq m \leq l$ because all but the coefficient a_{00} have an in general non-vanishing complex part and there are thus in total $2l + 1$ parameters.

In the following, the harmonic background subtraction will be investigated in practice with real H.E.S.S. data and numerical algorithms. The effect and meaning of eq. 5.12 will be addressed.

Algorithm

The numerical expansion of an event map is performed using the Healpix software library (see Gorski et al. [2005] and Hivon [1999]) that is also commonly applied for the analysis of CMB data. Essentially, Healpix offers a pixelization scheme that divides a unit sphere into bins of equal area. The pixelization scheme leads to computational and numerical advantages compared to a direct implementation of the spherical harmonic expansion with uniform bins in latitude ΔB and longitude ΔL where the pixel area $\Delta\Omega$ depends on latitude via $\Delta\Omega = \Delta L \Delta B \cos(B)$. The resolution of the Healpix maps needs to be selected and is controlled via the so called N_{Side} parameter. The number of equal area pixels on the unit sphere, N_{Pix}, is connected to the N_{Side} parameter via $N_{\mathrm{Pix}} = 12 N^2_{\mathrm{Side}}$ where N_{Side} must be a power of 2 (see Hivon [1999]). The solid angle that one pixel covers on the unit sphere is $\Delta\Omega = 4\pi / N_{\mathrm{Pix}}$ and can be translated into an effective radius R of the pixel via $\Delta\Omega = 2\pi(1 - \cos(R))$. The optimal choice of the parameter N_{Side} has been investigated for the algorithm described below and a good compromise between speed and resolution is found with $N_{\mathrm{Side}} = 1024$ corresponding to a typical pixel radius of $\sim 0.03°$. Additionally, Healpix provides highly efficient and well tested algorithms to perform the actual calculation of the spherical harmonic coefficients, a_{lm}, as well as the inverse transformation from a_{lm} to coordinate space (see Seljebotn [2012] for a discussion of the numerical approach). In practice, a maximal $l = l_{\mathrm{lmax}}$ has to be defined above which the spherical harmonic expansion is truncated. The total number of a_{lm} coefficients scales with l^2_{max} and should by order of magnitude match the number of

pixels $N_{\mathrm{Pix}} \sim N_{\mathrm{Side}}^2$ from which follows $l_{\mathrm{max}} \sim N_{\mathrm{Side}}$. For the algorithm described below, the Healpix recommendation $l_{\mathrm{max}} = 3N_{\mathrm{Side}} = 3072$ is used. Note that the computing time for the spherical harmonic expansion scales approximately with l_{max}^2 (see Seljebotn [2012] for more detailed scaling laws). The implicit usage of OpenMP[3] in the Healpix routines for the spherical harmonic transformations enables the parallel usage of multiple CPU cores which is of great value for the efficient analysis of data.
In the following, a schematic routine is described that is in practice implemented in a software environment which has been developed in the course of this thesis work. The input format is again the same binary input format that is also used in the analysis of H.E.S.S. data for a γ-ray flux created in subsequent reactions of annihilating or decaying WIMPs in the Milky Way halo (see chapter 4). The input file can be created from usual H.E.S.S. data in a standardized way. Additionally, also a Monte Carlo generator is implemented that simulates background events rotationally symmetric around a fixed celestial pointing position together with a user controlled fraction of localized signal events. The ability to process Monte Carlo generated input data is very useful for debugging. The subsequent items describe the basic algorithm and are to be understood as being applied within a loop over all observation runs within a dataset. The resulting $\mathrm{Sig}(\theta, \phi)$ and $\mathrm{Bkg}(\theta, \phi)$ event maps for each observation run are to be added after the observation run loop has finished.

- First, the reconstructed directions of all events that pass γ-ray selection criteria and whose angular offset to the observation position is smaller than a fixed maximal value ψ_{max} are filled into an event map. Typically $\psi_{\mathrm{max}} = 2^\circ$ is used for the analysis of H.E.S.S. data which is about the radius of the usable field of view of the H.E.S.S. array.

- A series of Euler rotations is applied to every bin in the resulting map such that the pointing direction of the observation run is matching the z-axis after the rotation. In other words, the event map is rotated such that it is centered on the north pole of a sphere. Special care has to be taken for differing direction and coordinate conventions between the Healpix and the H.E.S.S. software environment.

- The resulting event map is centered on the north pole and stretched over the whole unit sphere. For this, the z-coordinate of every bin in the event map is transformed according to
$$z \to \frac{2z - 1 - z_{\mathrm{min}}}{1 - z_{\mathrm{min}}} \tag{5.14}$$
where $z_{\mathrm{min}} = \cos(\psi_{\mathrm{max}})$. This prescription is the linear realization of a map that maps the north pole to the north pole ($z = 1 \to z = 1$) and z_{min} to the south pole ($z_{\mathrm{min}} \to -1$). The application of higher order maps has been investigated but no substantial advantage or disadvantage was found for a general analysis. The linear map is thus kept. The stretching of the event map over the whole unit sphere is in practice saving computation time as the resolution of the spherical harmonic expansion can be substantially reduced in this way.

[3] See http://openmp.org for more information.

- The expansion into spherical harmonics is performed, i.e. the coefficients a_{lm} are calculated with a Healpix routine. Signal coefficients, i.e. a_{lm} with $m \neq 0$, and background coefficients, i.e. a_{l0} are split and the signal and background map is calculated by inverting the spherical harmonic expansion with the corresponding coefficients. The computing time needed for the expansion of a skymap into spherical harmonics is for the stated parameters ($N_{\mathrm{Side}} = 1024$, $l_{\mathrm{max}} = 3072$) in the order of magnitude of 1 min when 5 modern Intel Xeon CPUs are used in parallel. The inverse transformation is much faster, ~ 10 s are needed for the calculation of the signal map and ~ 5 s for the calculation of the background map.

- The stretching of the event map over the whole sphere is in the following inverted as is the rotation of the pointing position to the north pole.

In order to get a better impression of the algorithm that is sketched above, a test skymap is analyzed with a harmonic background subtraction in a first step. The test skymap is centered at the galactic center and has entries

$$\mathrm{Events}(l, b) = \begin{cases} 1 & d \leq 2^\circ \\ 0 & d > 2^\circ \end{cases}$$

where d is the angular distance between the point l, b and the galactic center. The test skymap is analyzed with a harmonic background subtraction algorithm and the skymap that is resulting from the inverse spherical harmonic transformation of each coefficient a_{lm} is calculated. The figures 5.11 and 5.12 show the resulting skymaps for a selection of l and m. The first six zonal components of the harmonic background subtraction are shown in fig. 5.11. The rotational symmetry of the zonal components around the pointing position, i.e. the galactic center is clearly visible. Figure 5.12 shows the signal components for one dedicated $l = 7$ as an example. The graphical representation of the signal components reveals a similarity between the harmonic and the reflected background subtraction. The reflected background subtraction (see chapter 2) for a given event map can also be interpreted as the convolution of the event skymap of interest with a template that consists of a certain number of circles with defined radius that are symmetrically arranged around the pointing position such that the center of each circle has the same angular distance to the pointing position. Each bin in the template that is not within one of the circles must have zero as entry and the bins in all but one circle must have entry -1. Only the bins within one circle, the signal region for the reflected background subtraction, must have entries +1. Similarly, the harmonic background subtraction can be interpreted as a computationally efficient way to calculate the convolution of templates that are proportional to the ones exemplified in fig. 5.11 and fig. 5.12 with the eventmap. The absolute value of the a_{lm} coefficients for $m > 0$ are in other words a function of the deviation of the eventmap from rotational symmetry around the pointing position at a scale defined by l. The phase of the a_{lm}, which is only deviating from zero for $m > 0$, defines just a rotation of the spherical harmonic corresponding to a_{lm} around the pointing position.

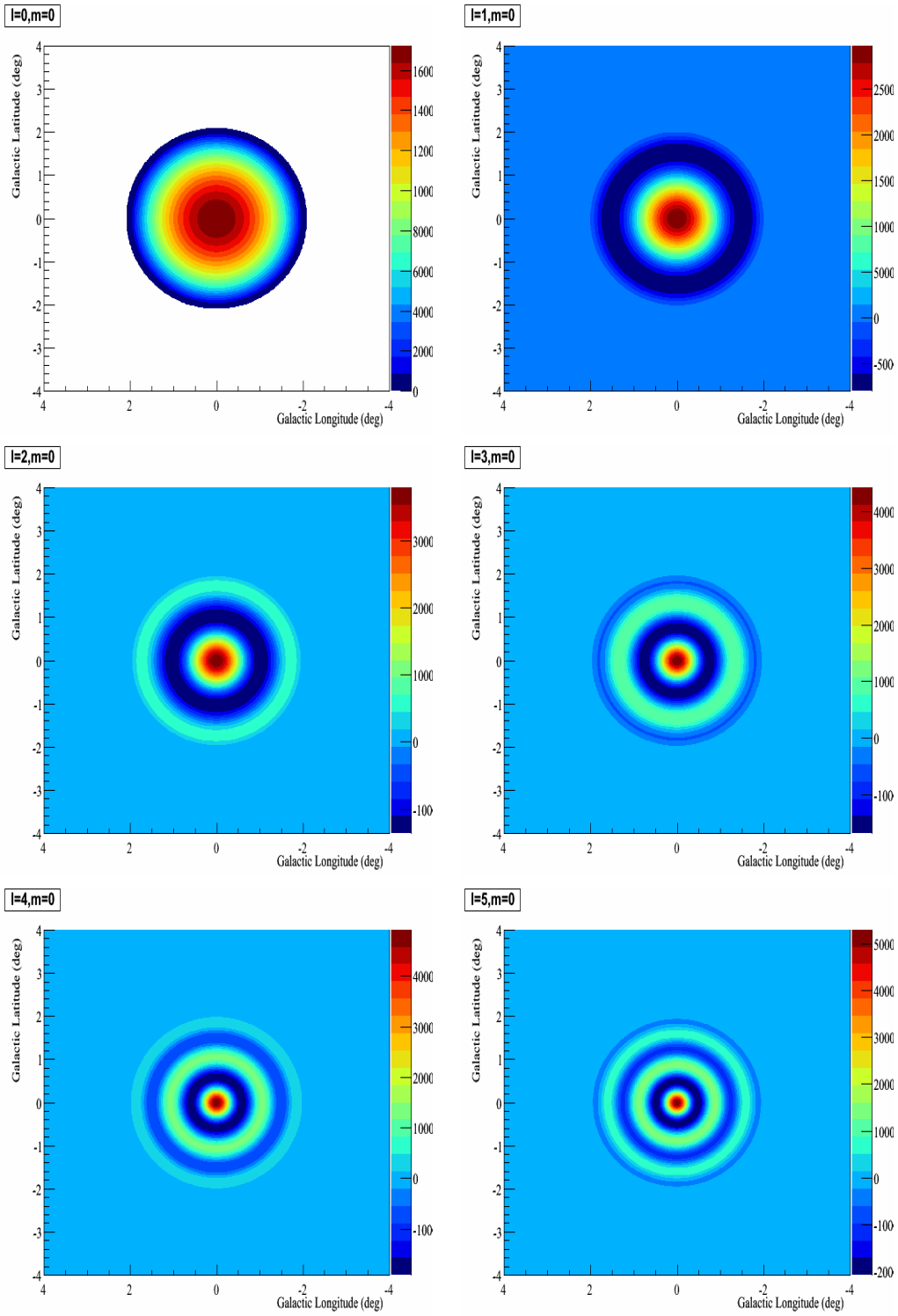

Figure 5.11: Graphical representation of the first six zonal ($l = 0$ to $l = 5$, $m = 0$) spherical harmonic components of the harmonic background subtraction for a 2° field of view around the galactic center.

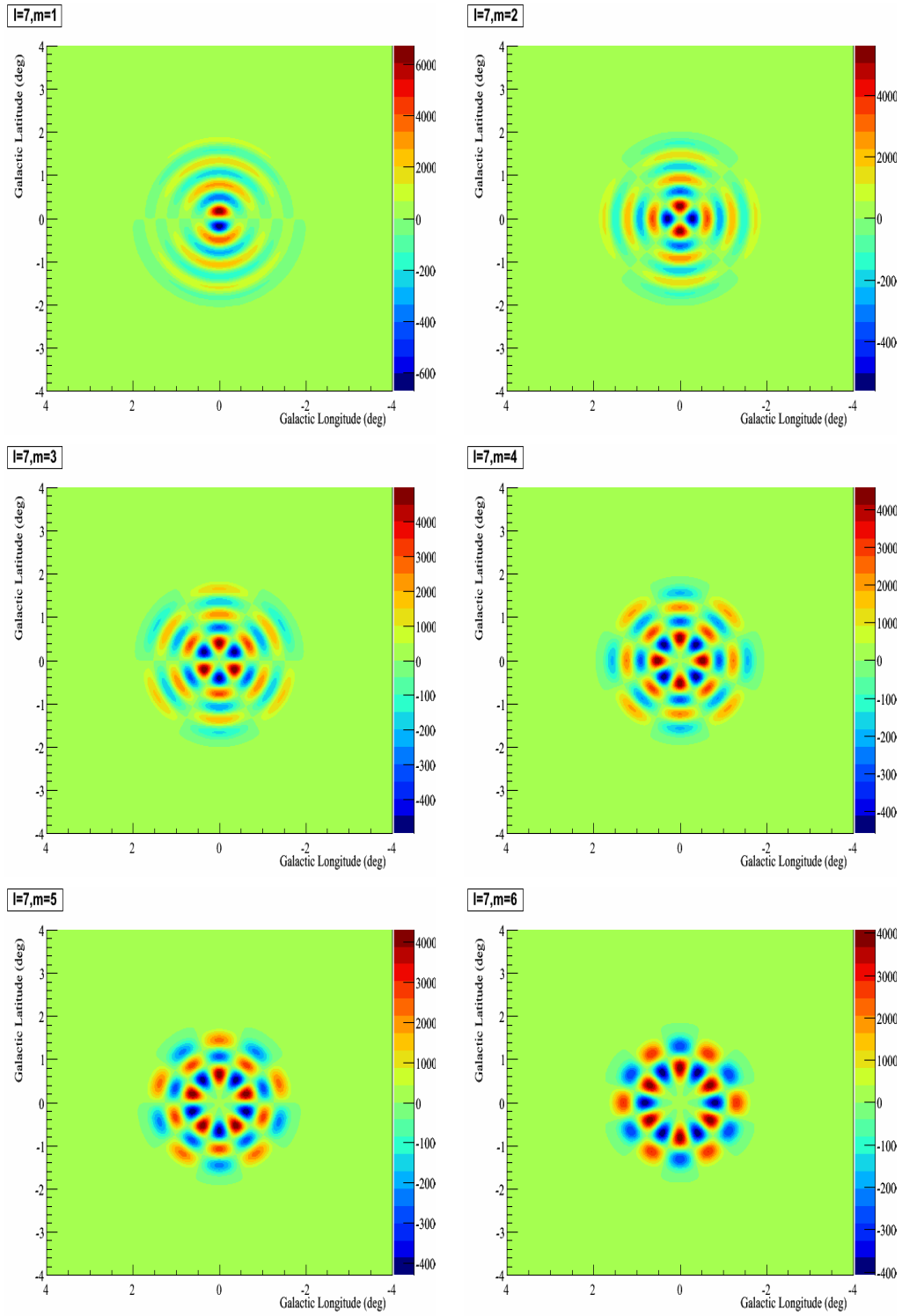

Figure 5.12: Graphical representation of the $l = 7$, $m = 1$ to $m = 6$ spherical harmonic components of the harmonic background subtraction for a 2° field of view around the galactic center.

First Results: Skymaps

Figure 5.13 shows in the left panel an excess map generated with the ring background method for one standard H.E.S.S. I observation run towards the Crab Nebula ($\sim$ 27 min livetime). For comparison, the signal component of the result of the harmonic background subtraction is shown in the right panel. A clear excess signal is visible in both figures at the nominal position of the Crab Nebula. Figure 5.14 shows the signal component of the harmonic background subtraction of the data recorded in 65 H.E.S.S. I observation runs (corresponding to a total livetime of $\sim$ 28 h) with different pointing positions in the vicinity of the supernova remnant Vela Junior. The peculiar shell morphology of the Vela Junior remnant is clearly visible and well compatible with the morphology published in Aharonian et al. [2007].
The signal skymaps created in the analysis of a small dataset of H.E.S.S. observation runs towards the Crab Nebula and a larger dataset of observation runs towards the Vela Junior supernova remnant show that it is in general possible to generate skymaps with the harmonic background subtraction algorithm. However, the generation of skymaps with the harmonic background subtraction algorithm is in practice not recommended for two reasons.

- The signal skymap as obtained from the subtraction of the zonal components of the harmonic expansion from the event map is equal to a skymap that is obtained by subtracting the recorded event map from an event map that is generated by rotating every single recorded event by a random angle around the pointing position. This 'symmetrized event map' is much quicker to calculate than the spherical harmonic expansion.

- The method has the drawback that although a clear signal is visible f.i. in the signal skymaps generated from H.E.S.S. data taken towards the Crab Nebula (fig. 5.13) or the Vela Junior supernova remnant (fig. 5.14), that the total magnitude of the signal is smaller than in the corresponding excess map generated with a ring background algorithm. This is clearly visible by comparing the scales in fig. 5.13 between the left and right panel. The reason for this is to be found in argument given in the previous item or eq. 5.12. The signal skymap as generated in the harmonic background subtraction differs from the excess map generated in an usual background subtraction f.i. with the ring background method because the quantity that is really shown is the deviation of the recorded event map from a 'symmetrized event map' as defined in the previous item.

Although the direct generation of signal maps with the harmonic background subtraction method is not useful in practice, the method does provide important information on the putative presence of a signal, i.e. a deviation of the event map from rotational symmetry around the observation position, if the spherical harmonic coefficients as such and not the corresponding event maps are considered.

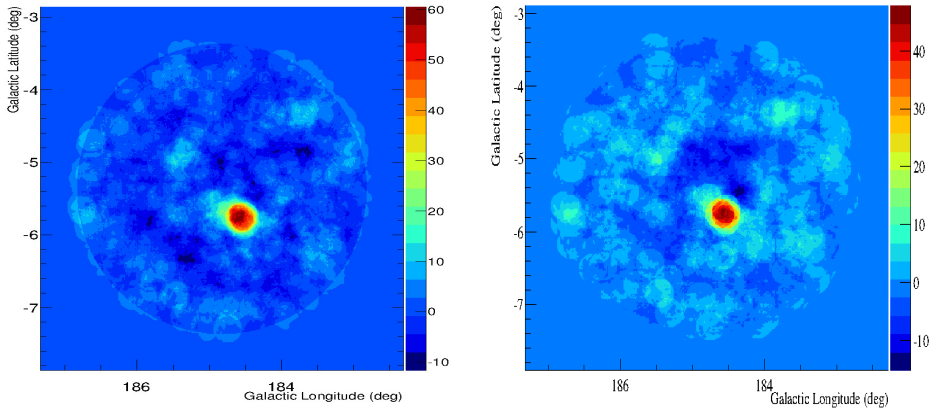

Figure 5.13: Left panel: Excess map generated with the ring background subtraction algorithm for one H.E.S.S. observation run towards the Crab Nebula. Right panel: Same observation run but the signal map as resulting from a harmonic background subtraction. Both maps are in galactic coordinates and correlated with 0.2° (the standard H.E.S.S. correlation radius for a point source analysis of 0.1° is not chosen to prevent the appearance of holes in the skymaps that are the result of the very limited amount of analyzed data). A clear excess signal is visible in both maps around the nominal position of the Crab Nebula ($l = 184.56°$, $b = -5.79°$).

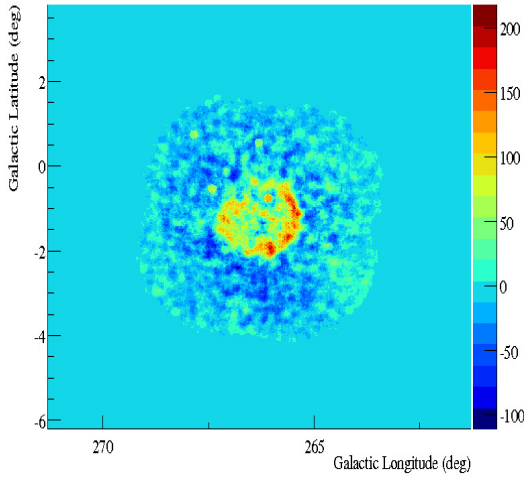

Figure 5.14: Signal map resulting from a harmonic background subtraction of H.E.S.S. data recorded in observation runs towards the Vela Junior region. The map is correlated with 0.1°. The Vela Junior supernova remnant is clearly visible with a shell-like morphology.

First Results: Signal Coefficients

It has already been outlined above that not all a_{lm} coefficients are independent. Consider for the moment complex a_{lm}. The real and imaginary part of the a_{lm} coefficients for $m > 0$ define a maximal set of independent coefficients because for negative m it holds that $a_{l,-m} = a^*_{lm}$. In the following it will be more convenient to use the absolute value of the a_{lm} coefficients and the phase. The absolute value of the a_{lm} coefficients obtained in a harmonic background subtraction for $m > 0$ is a measure for the deviation of the event map from the rotational symmetry around the pointing position. The phase is a parameter that is rotating the spherical harmonic component that corresponds to a_{lm} around the pointing position. In practice, it is useful to calculate the real (x_1) and imaginary (x_2) part of each a_{lm} coefficient for a given event map. The significance of the deviation of the absolute value obtained for the spherical harmonic coefficients for a given event map from the absolute value of the spherical harmonic coefficients that would be obtained for an event map that is rotationally symmetric around the pointing position due to statistical fluctuations is estimated with the quantity

$$Z = \left(\frac{x_1 - \bar{x_1}}{\sigma(x_1)}\right)^2 + \left(\frac{x_2 - \bar{x_2}}{\sigma(x_2)}\right)^2 . \tag{5.15}$$

Here

$$\bar{x_i} = \frac{1}{N}\sum_{k=1}^{N} x_{ik} \tag{5.16}$$

and

$$\sigma(x_i) = \sqrt{\frac{1}{N-1}\sum_{k=1}^{N}(x_{ik} - \bar{x_{ik}})^2} \tag{5.17}$$

are calculated from the spherical harmonic coefficients of N symmetrized event maps. In other words, the harmonic background subtraction is performed for a given event map to obtain x_1 and x_2 for each l and m. Afterwards, the harmonic background subtraction is repeated N times with an event map that is derived from the original event map by rotating each recorded event by a random angle around the pointing position. The quantity Z is distributed like $\chi^2(2)$ when no signal is present, the x_i are Gaussian distributed and N is sufficiently large. For a measured value of Z, the p-value for the observation of $Z' > Z$ in a $\chi^2(2)$ distribution can be translated into a Gaussian significance.
Figure 5.15 shows in the upper panel the inferred Gaussian significance of the absolute value of a_{lm} as a function of $0 < l \leq 300$ and $0 < m \leq l$ for a Monte Carlo generated input into the harmonic background subtraction where event coordinates are simulated rotationally symmetric around the pointing position. The number of symmetrized event maps that are calculated in order to infer $\bar{x_i}$ and $\sigma(x_i)$ is $N = 35$ which is found to be a good compromise between speed and precision. The corresponding significance distribution is compatible with being standard normal.
Also compatible with being standard normal is the distribution of the significances of the absolute value of the a_{lm} coefficients obtained in a similar analysis of a single H.E.S.S.

off-data observation run, i.e. an observation run where no known γ-ray source is present in the field of view. The corresponding scatter plot of the significance of the absolute value of a_{lm} as a function of $0 < l \leq 300$ and $0 < m \leq l$ is shown in fig. 5.15 in the lower panel. Note, however, that the majority but not all H.E.S.S. offdata observation runs show no indication for a deviation of the acceptance from rotational symmetry around the observation position. An analysis of a large set of H.E.S.S. offdata is, however, beyond the scope of this thesis. The significance of the absolute value of the a_{lm} coefficients can also be used to detect a signal. Figure 5.16 shows the scatter plot of the significance of the a_{lm} coefficients for $0 < l \leq 300$ and $0 < m \leq l$ for one H.E.S.S. I observation run towards the Crab Nebula in the left panel and the skymap as generated with a ring background subtraction for the same data in the right panel. The significance of the absolute values of the a_{lm} coefficients is larger than 5σ in an extended region in the (l, m) scatter plot around $l \sim 8$ and $m \sim 3$.
A similar result is visible for the much stronger γ-ray source that is present in the field of view of the H.E.S.S. observation taken during an exceptional flare of PKS2155-304 (see H.E.S.S. Col. [2011]). Figure 5.17 shows in the left panel the (l, m) scatter plot of the significance of the a_{lm} coefficient absolute value as obtained from the harmonic background subtraction of one H.E.S.S. observation run taken during the flare of PKS2155-304. Very large significances are again observed in an extended region of the scatter plot around $l \sim 8$ and $m \sim 3$. The significance map generated with the ring background method from the same data is shown in the right panel for comparison.

Conclusion and Outlook

The examples that were discussed in the last section show that it is in general possible to gain information on the presence of a γ-ray signal in H.E.S.S. data from the investigation of the significances of the absolute value of the a_{lm} coefficients. The examples are, however, simple and the method must certainly be developed further. It is especially necessary to investigate the following items:

- The $\bar{x_i}$ and $\sigma(x_i)$ values are inferred from a Monte Carlo simulation in the analysis discussed in the last section. It should be investigated whether they can also be calculated with less computational effort with the usage of special properties of the spherical harmonics or whether there is a more efficient way to express the significance of the absolute value of the a_{lm} coefficients. Given that each expansion of a symmetrized event map into spherical harmonics takes around 1 min when 5 modern Intel Xeon CPU cores are used in parallel, it is obvious that the analysis of one complete run with $N = 35$ symmetrized event maps takes more than 30 min which is reasonable but becomes a limiting factor when large datasets are investigated.

- A systematic analysis of offdata recorded with the H.E.S.S. array must be performed. The analysis should lead to important conclusions with respect to the presence of deviations from the rotational symmetry of the H.E.S.S. acceptance

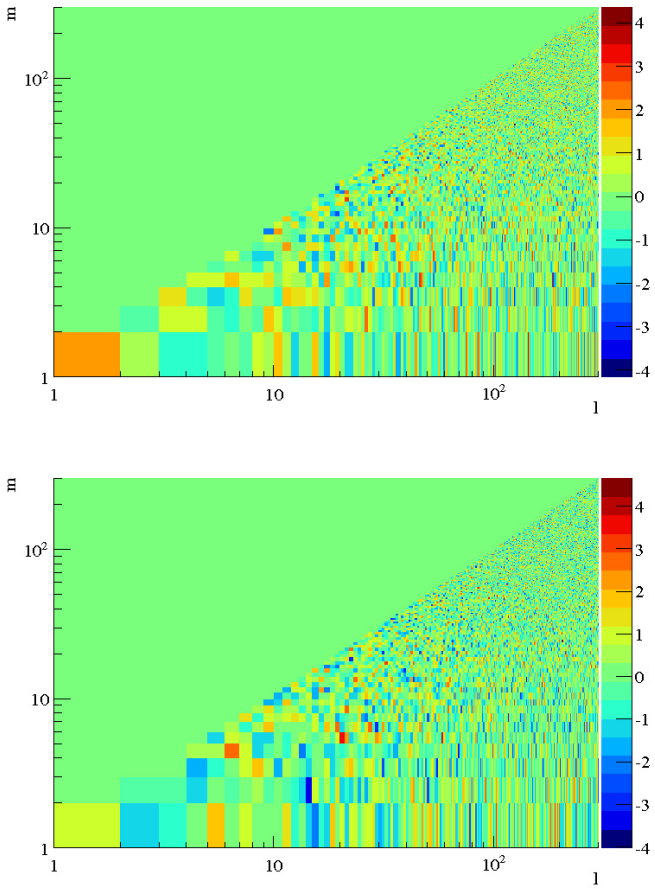

Figure 5.15: Significance of the absolute value of the spherical harmonic coefficients a_{lm} in the range $l = 0$ to $l = 300$ and $m \leq l$. Upper panel: Result for Monte Carlo generated background events whose directions are up to statistical fluctuations rotationally symmetric around the pointing position. Lower panel: Result for a H.E.S.S. observation run without γ-ray source in the field of view. No significant differences between the Monte Carlo generated and the H.E.S.S. observation dataset is apparent. The distribution of the significances is compatible with being standard normal in both cases.

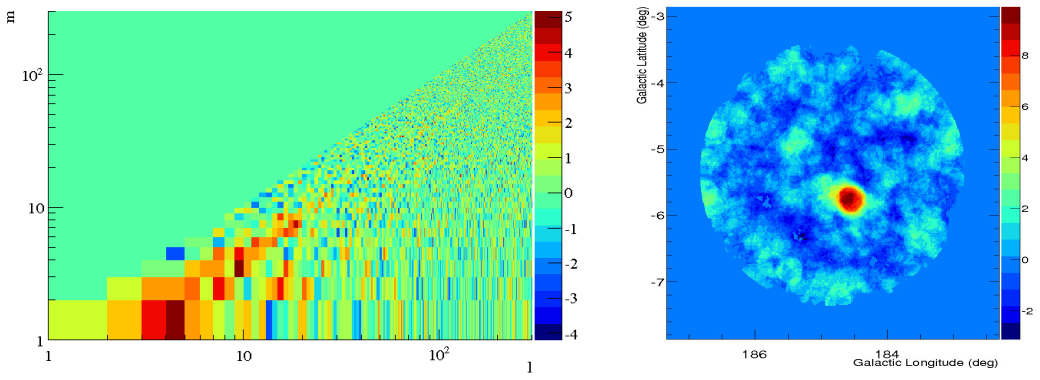

Figure 5.16: Left panel: Significance of the absolute value of the spherical harmonic coefficients a_{lm} in the range $l = 0$ to $l = 300$ and $m \leq l$ for one H.E.S.S. observation run ($\sim$ 27 min livetime) towards the Crab Nebula. Right panel: Significance skymap generated with the ring background algorithm for the same observation run with a correlation radius of 0.2°.

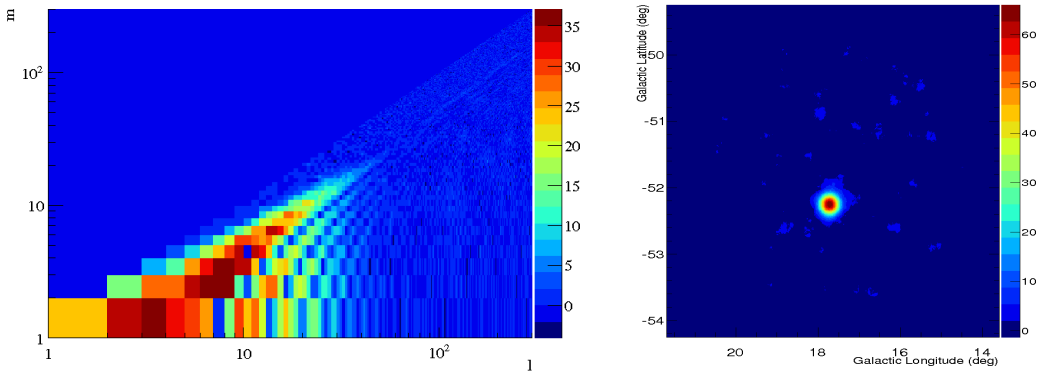

Figure 5.17: Left panel: Significance of the absolute value of the spherical harmonic coefficients a_{lm} in the range $l = 0$ to $l = 300$ and $m \leq l$ for one H.E.S.S. observation run taken during the exceptional flare of the source PKS2155-304 (see H.E.S.S. Col. [2011] and references therein for a description of the data). Right panel: Significance skymap generated with the ring background algorithm for the same observation run with a correlation radius of 0.1°.

around the pointing position as well as the dependence of the deviations on parameters such as the number of broken pixels and the pointing zenith angle.

- A method with which it is possible to correlate the bins in the (l, m) scatter plot of the absolute values for the a_{lm} coefficients would be of high value as it would reduce the trial factor for the significances in the scatter plot. Additionally or as an alternative it is to be investigated whether an additional limitation of the maximal l of the scatter plot is appropriate. Currently the unoptimized limitation to $l \leq 300$ is used. Large values of l correspond typically to small angular scales for the a_{lm} parameters. At some point the angular scale that corresponds to an a_{lm} parameter becomes smaller than the typical extension of the H.E.S.S. point spread function ($\sim 0.1^\circ$) which is not useful.

Apart from information on the deviations of the H.E.S.S. acceptance from rotational symmetry around the pointing position on different angular scales, the method of the harmonic background subtraction can potentially become very important for the search for the presence of γ-ray sources for which no detailed information on the signal region location and extension is available from independent measurements. One concrete examples of interest is the verification of the hint for the existence of the emission of a γ-ray line with an energy around 130 GeV from the vicinity of the galactic center region as derived from the analysis of data recorded with the Fermi observatory (see chapter 3). As discussed above (and f.i. in Bergstrom et al. [2012]), the confirmation of the presence of this signal is a highly interesting science topic for the CTA but also the H.E.S.S. II array. The potential ability of the harmonic background subtraction method to search for the presence of a γ-ray excess signal without a priori definition of a signal region offers an obviously interesting analysis possibility. Note, however, that the galactic center region is populated by well known γ-ray sources that would have to be excluded from the search for the presence of a γ-ray signal around 130 GeV with the harmonic background subtraction method. The exclusion of sources means usually that an exclusion region is defined around the γ-ray source that is to be excluded, i.e. events that are recorded within the exclusion region are not analyzed. For a harmonic background subtraction, the angular distance of the excluded points to the observation position is relevant. All events that are reconstructed with an angular distance to the pointing position that is equal to the angular distance of a point in the exclusion region to the pointing position must be excluded. A search for a line feature around event energies with 130 GeV could be realized with the harmonic background subtraction for a dataset of H.E.S.S. II observation runs with pointing positions in the vicinity of the galactic center with the following method. In a first step, only events with energies that are much larger than 130 GeV are to be analyzed and exclusion regions are suitably chosen such that no significant spherical harmonic coefficients remain in a harmonic background subtraction. A hint for the presence of a line like signal is found if the same analysis is applied to events with energies around 130 GeV and significant spherical harmonic coefficients are derived in a harmonic background subtraction.
Given the interesting prospects as concerns an analysis for the presence of a 130 GeV γ-ray line emission from the vicinity of the galactic center as well as the investigation of

deviations of the γ-ray event acceptance from rotational symmetry around the pointing position, a further investigation of the method is justified.

6 Summary

Three different observation strategies for the search for the presence of TeV mass WIMPs in the Milky Way halo have been compared in this thesis. The method to subtract residual cosmic ray background events, that are passing γ-ray event selection criteria, differs for all three considered observation strategies. In particular the sources of potential systematic effects differ for the background subtraction of data that were recorded in the On/Off and the driftscan observation mode as well as for the background subtraction with the rotated pixel method. The analysis of data that were recorded with the H.E.S.S. array with all three methods showed that from the viewpoint of systematic effects, both the On/Off observation as well as the rotated pixel background subtraction can be handled. To control systematic effects in the background subtraction for data that were recorded in the On/Off mode, it is important to schedule the observation of two background regions symmetric in right ascension around the signal region observation. However, for the special case of a search for a γ-ray line signal, an On/Off analysis with only one background region observation is possible when the systematic error on the exposure ratio is estimated in a control energy band without overlap with the considered γ-ray line energy. This will be of future interest for a falsification of the putative 130 GeV γ-ray line signal that has been detected recently in Fermi satellite data. The subtraction of background events in data recorded in driftscan observations suffers from systematic influences that are difficult to control. From the viewpoint of the sensitivity of the three different methods to search for the presence of WIMPs in the Milky Way halo, the On/Off method is in general preferred when compared to the rotated pixel method. However, the sensitivity of searches for the presence of WIMPs in the Milky Way depends strongly on the unknown distribution of dark matter in the Milky Way. When dark matter density distributions that result from currently discussed large scale N-body simulations of gravitationally interacting particles are assumed, the sensitivity of the three methods is comparable, i.e. almost equal within statistical fluctuations. However, this result relies on the steepness of the dark matter density distributions towards the galactic center region. N-body computer simulations that predict the steepness of the dark matter distribution towards the galactic center neglect important physical aspects, f.i. the presence of baryonic matter. The On/Off method is more sensitive to the presence of WIMPs in the Milky Way halo if general distributions of the dark matter density in the Milky Way that exhibit a less pronounced peak towards the galactic center are assumed. Such dark matter density distributions are predicted by very recent N-body simulations of gravitationally interacting particles that also consider the influences of baryonic matter.

Upper limits on the velocity averaged WIMP annihilation cross section, $\langle \sigma v \rangle$, have been derived in the framework of models for the distribution of dark matter in the Milky

Way and the creation of γ-rays in the annihilation of WIMPs. Depending on the used method and the exposure of the considered H.E.S.S. dataset, the best upper limits on $\langle\sigma v\rangle$ are at the level of $3 \cdot 10^{-25}\,\mathrm{cm}^3/\mathrm{s}$ at 95% confidence level for WIMP masses around 1.8 TeV. The canonical prediction for thermal relic WIMPs is that $\langle\sigma v\rangle$ is about one order of magnitude smaller than the derived limit.
An analysis strategy to search for diffuse TeV γ-ray emission from the galactic plane in H.E.S.S. data has been outlined. Additionally, a new background subtraction mechanism (harmonic background subtraction) that does not rely on the precise knowledge of the shape and position of a γ-ray signal region in an observed field of view has been developed and first results are discussed. The potential presence of large scale diffuse TeV emission from the galactic plane as well as the confusion of a diffuse TeV γ-ray flux with a flux from a population of local astrophysical γ-ray sources has been discussed as a possible limitation to increase the sensitivity of the planned CTA observatory in searches for the presence of WIMPs in the Milky Way.

Appendix A: Livetime Calculation for H.E.S.S. Data

This appendix summarizes the livetime calculation which is used in parts of the thesis. The general statistical discussion is in part inspired by Mueller [1973].
The recording of events in one observation run by the H.E.S.S. array is in an ideal case a Poisson process. Events occur at times $t_0, t_1, ..., t_i$ with time differences $\Delta_i = t_{i+1} - t_i$. The average time difference between two consecutive events is $1/R$ where R is the event rate and the probability density distribution for the time differences $p(\Delta t)$ is exponential,

$$p(\Delta t) = R \exp(-R\Delta t)\,, \tag{1}$$

and in this context also frequently called time difference distribution.
The given consideration holds for a Poisson process without instrumental dead time. Figure 1 shows the measured event time difference distribution for one run of standard H.E.S.S. data that passes standard data quality checks. Two observations are remarkable in fig. 1. The first is that the camera dead time quoted in chapter 3 to be $\mathcal{O}(400\,\mu\mathrm{s})$ is not visible as a sharp cut-off if visible at all. The second is that the distribution is obviously not exponential over the whole considered Δt range. Both observations are directly linked to the behavior of the H.E.S.S. I array trigger. When 4 telescopes are operating and it is requested that at least 2 telescopes participate in an array trigger, the total number of possible array configurations is 11. This number is the sum of the $\binom{4}{2} = 6$ two telescope, the $\binom{4}{3} = 4$ three telescope and the one four telescope configuration. Figure 2 shows two time difference distributions for events where only CT1 and CT4 (left panel) and only CT3 and CT4 (right panel) trigger the array. In contrast to fig. 1, a clear cut off of the time difference distribution is apparent. However, the cut off is different for the two configurations (at $\sim 475\,\mu$s in the case of CT1 and CT4 and $\sim 724\,\mu$s in the case of CT3 and CT4). A further investigation of the time difference distributions of the individual trigger configurations leads to the conclusion that the cut off is always $\sim 724\,\mu$s when CT1 is involved in an array trigger and always $\sim 475\,\mu$s if CT1 is not involved. The cut off in the time difference distribution is caused by the instrumental dead time of the array which is in turn a consequence of the camera read out time and the time for data transfer from a camera to the central data storage system. It is thus concluded that the sum of the time for the data transfer and the camera read out time is larger for CT1 than for the other telescopes. Note that the time difference distribution cut-off measured for all telescopes except CT1 ($475\,\mu$s) agrees reasonably with the time that was measured years ago in laboratory for the sum of the data transfer ($141\,\mu$s) and the camera read out ($273\,\mu$s) which is $446\,\mu$s (see Funk et al. [2004]).
If each of the individual telescope trigger configurations leads to a time difference dis-

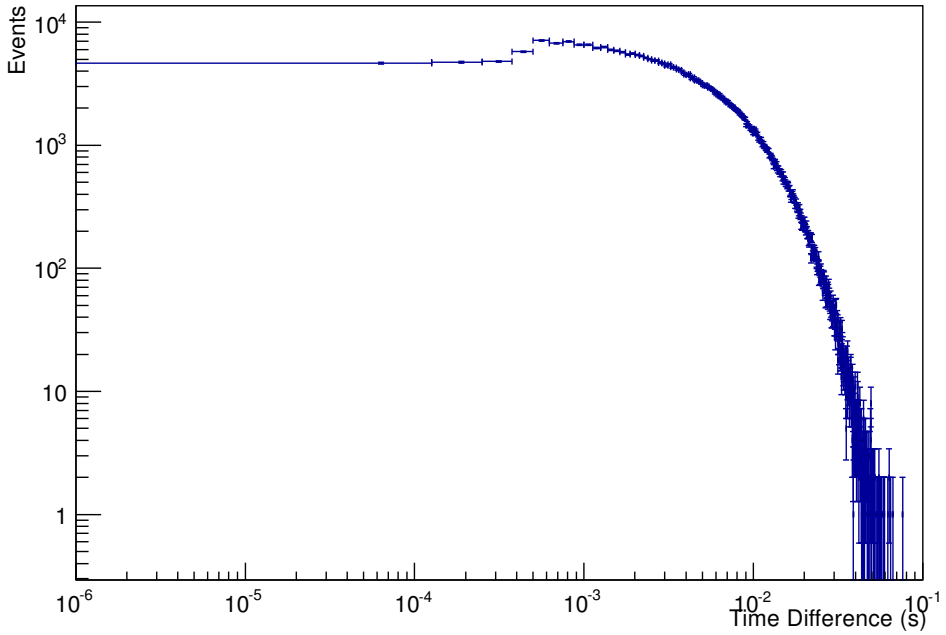

Figure 1: Time difference distribution for all events recorded in one H.E.S.S. I observation run (run 58727).

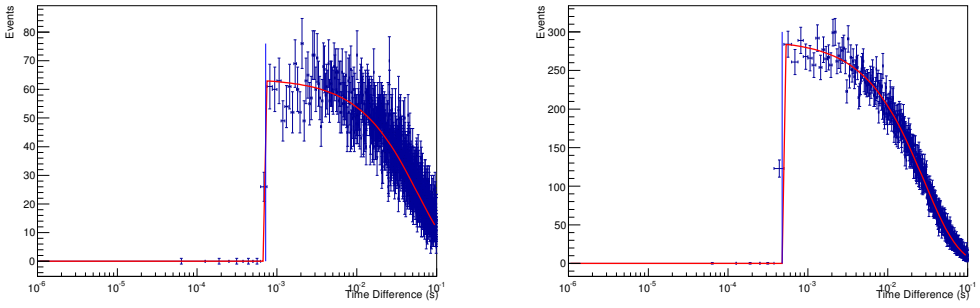

Figure 2: Time difference distributions for events that only trigger CT1 and CT4 (left panel) and for events that only trigger CT3 and CT4 (right panel). The distribution in the left panel has a sharp cut off at $\Delta t \sim 724\,\mu$s and the distribution in the right panel has a cut off at $\Delta t \sim 475\,\mu$s.

tribution with a sharp cut-off that represents the largest single telescope dead time that is involved in the array, how can the time difference distribution for all recorded events (fig. 1) not have a sharp cut-off? The reason is again to be found in the array trigger and concerns events where only two telescopes trigger the array. Consider an event that triggers two telescopes. The two telescopes are read out and cannot be read out again within the dead time that belongs to the telescope configuration under consideration. However, it is possible that the remaining two telescopes trigger without any dead time directly after the trigger of the first two telescopes. Figure 3 shows with green data points the time difference distribution of events where the triggered telescope configuration is completely read out for the same run that is also considered above. Blue data points show the (up to now not discussed) time difference distribution for events where the number of telescopes that are read out is smaller than the number of telescopes that triggered the event. This case will be discussed later. The blue vertical lines indicate the fitted dead times of the individual telescopes as obtained from the time difference distribution cut-off for different trigger configurations. The red line for $\Delta t > 1.5$ ms is a fit of of the green data points for time differences larger than the largest telescope dead time to an exponential distribution. The fit has a reasonable $\chi^2/\mathrm{NDF} = 462/405$. The light red line for $\Delta t < 724\,\mu$s is not a direct fit to the corresponding green data points. Instead it is tested whether the event time difference distribution for Δt smaller than the largest telescope dead time can be explained by the model indicated above. For $\Delta t < 475\,\mu$s, i.e. smaller than the smallest telescope dead time, only two telescope events can occur where the two telescopes that trigger and are read out are different from the two telescopes that have been read out in the event before. In between the smallest and largest individual telescope dead time, it is additionally possible that a certain telescope configuration triggers an event and the whole telescope configuration or a sub-configuration becomes ready to trigger and read out the next event. The light red line for $\Delta t < 724\,\mu$s in fig. 3 is thus the sum of all time difference distributions with trigger rates as obtained from the fits to all time difference distributions for $\Delta t > 724\,\mu$s for all 11 possible array configurations extrapolated to the case where an event triggers and another event triggers the same or another array configuration. It is obvious that the light red line is a reasonable approximation to the time difference distribution for $\Delta t < 724\,\mu$s. Thus it is concluded that the time difference distribution for events where all triggered telescopes are read out can be explained by the special array trigger. However, for time differences that are smaller than the largest individual telescope dead time, the probability for an event to trigger the read out depends in general on the telescope configuration of the event that triggered the event before. One strong condition for a stochastic process to be Poisson like is that all events occur independently from each other. This condition is not any more fulfilled for events that occur within a time period smaller than the largest individual telescope dead time. As a consequence, the process is not Poisson like in this regime.

Similar considerations hold for the blue data points in fig. 3, i.e. the event time difference distribution for events where the number of read out telescopes is smaller than the number of triggered telescopes. The H.E.S.S. trigger demands that at least two different telescopes trigger the array, but does not require any telescope to be read out. It is

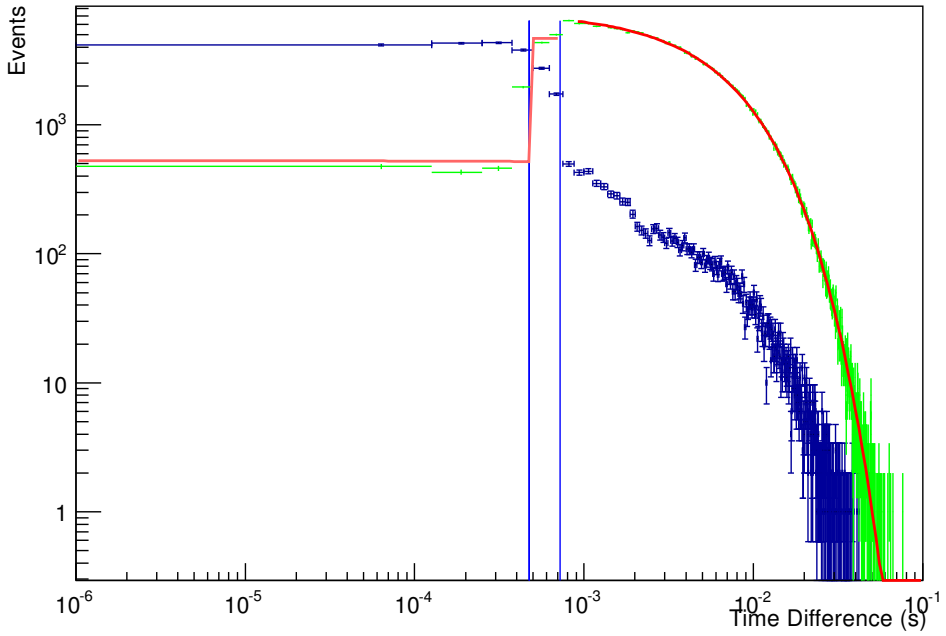

Figure 3: Time difference distribution for all events recorded in one H.E.S.S. I observation run (run 58727). The green data points show all events where all triggered telescopes are read out. The vertical blue lines indicate the fitted dead times of the individual telescope configurations. The red line right for $\Delta t > 724\,\mu$s is a fit of the green data points to an exponential distribution. The red line for $\Delta t < 724\,\mu$s is a prediction for the event time difference distribution with Δt smaller than the largest involved telescope dead time. The prediction holds only for events where all triggered telescopes are read out and is obtained from the time difference distributions for individual possible trigger configurations where also all triggered events are read out. The blue data points show the time difference distribution for events where the number of triggered telescopes is larger than the number of read out telescopes.

thus possible that an event triggers a telescope configuration where one or more of the telescopes cannot be read out. This is always possible if an event triggers at least one telescope that is different from the telescopes that triggered the event before. Additionally it is possible that an event triggers a telescope configuration where one or more of the telescopes that triggered the event before become ready to read out faster than the other triggered telescopes. This can explain the event time difference distribution for events where the number of read out telescopes is smaller than the number of triggered telescopes and where Δt is smaller than the largest individual telescope dead time. For the same events with Δt larger than the largest individual telescope dead time, no conclusive explanation is possible but it is very likely that those events suffered from occasional electronic problems. The total number of those events is, however, typically $\sim 1\%$[1] of the total number of all events and thus not very large. It can thus be concluded that also the event time difference distribution for events where the number of read out telescopes is smaller than the number of triggered telescopes can be explained with the exception of the case where $\Delta t > 724\,\mu$s. However, all events where the number of read out telescopes is smaller than the number of triggered telescopes suffer from either electronic problems ($\Delta t > 724\,\mu$s) or from the dependence of the detection probability on the trigger configuration of the event before. In all those cases, the process cannot be assumed to be Poisson like. Additionally, the effective area, the energy threshold and reconstruction as well as the direction reconstruction used in the analysis of those events are imprecise because the comparison of incompletely recorded events with Monte Carlo data that assumes always the complete read out of triggered events will obviously lead to systematic errors.
One could think that a clean analysis with a Poisson process with fixed dead time D assumed to be larger than the largest sub array dead time is now possible by cutting out all events with $\Delta t < D$ from the time difference distribution. Unfortunately, the situation is, however, more complicated. This will be discussed now with a comparison of two situations that differ in a subtle point.

- Consider a Poisson process that is observed with a detector that does not suffer from any dead time. Events are assumed to be recorded at times $t_0, t_1, t_2, ...$ with time differences between consecutive events of $\Delta_0 = t_1 - t_0$, ..., $\Delta_i = t_{i+1} - t_i$ and the time difference distribution is given by eq. 1.
  Consider now the case where events with $\Delta_i < D$ are not recorded. In total N events are assumed to be recorded in a runtime T_{Run} and the observed event rate $\rho = N/T_{\mathrm{Run}}$ will in general be lower than the true rate $R = N/T_{\mathrm{Live}}$ with the livetime T_{Live} because not all events that occur are observed. More precisely the fraction
  $$\frac{\int_D^\infty d\Delta t\, R \exp(-R\Delta t)}{\int_0^\infty d\Delta t\, R \exp(-R\Delta t)} = \exp(-RD) = \frac{\rho}{R} \tag{2}$$

[1] Occasiaonally this number can also be large, up to $\sim 30\%$ have been observed in data that pass usual H.E.S.S data quality checks.

of all events that occur is also recorded. Equation 2 leads to

$$T_{\mathrm{Live}} \exp\left(\frac{ND}{T_{\mathrm{Live}}}\right) = T_{\mathrm{Run}} \tag{3}$$

from which the livetime T_{Live} can be obtained numerically. On the other hand, the true event rate R can still be reconstructed from a fit of the time difference distribution between consecutive events for $\Delta t > D$.
A Monte Carlo simulation that simulates a true event rate between $R = 100$ Hz and $R = 300$ Hz in an observation time of $T_{\mathrm{Run}} = 1500\,\mathrm{s} = 25\,\mathrm{min}$ has been performed to check the consistency of the results presented above. The simulated number of events is assumed to be Poisson distributed with mean $\langle N \rangle = RT_{\mathrm{Run}}$. The time difference distribution of the simulated events is assumed to be exponential, $p(\Delta t) \sim \exp(-R\Delta t)$, with the mean time difference $1/R$. An event is assumed to be recorded if $\Delta t > D = 0.75\,\mathrm{ms}$, the number of recorded events (N) is counted. The resulting Δt distribution is fitted with a minimal χ^2 method to an exponential $C\exp(-r\Delta t)$ with fit parameters C and r in the range $\Delta t = [D, 0.1\,\mathrm{s}]$. As a result, the fitted rate r agrees with the true event rate R within errors $\sigma(r)$ obtained from the fit. However, multiple simulations show that the reconstructed event rate r is on average biased towards large rates because the quantity $(R-r)/\sigma(r)$ is on average not compatible with zero. The likelihood fit of the time difference distributions results in an unbiased estimate of the event rate with the quantity $(R-r)/\sigma(r)$ being compatible with standard normal. It is concluded that the true event rate can indeed be reconstructed from the time difference distribution via an exponential fit. A likelihood fit is preferred over a χ^2 fit. The livetime is calculated with eq. 3 and the true event rate is in turn estimated from the calculated livetime to be $r = N/T_{\mathrm{Live}} = N/(T_{\mathrm{Run}} - ND)$ with a statistical error of

$$\sigma(r) = \frac{\partial r}{\partial N}\sqrt{N} = \sqrt{N}\left(\frac{1}{T_{\mathrm{Live}}} - \frac{N}{T_{\mathrm{Live}}^2}\,\frac{\partial T_{\mathrm{Live}}}{\partial N}\right) . \tag{4}$$

The partial derivative of the livetime can be calculated using the implicit function theorem to be

$$\frac{\partial T_{\mathrm{Live}}}{\partial N} = -\frac{D}{1 - ND/T_{\mathrm{Live}}} \tag{5}$$

and results in the statistical error on the livetime,

$$\sigma(r) = \frac{\sqrt{N}}{T_{\mathrm{Live}}}\left(1 + \frac{ND/T_{\mathrm{Live}}}{1 - ND/T_{\mathrm{Live}}}\right) . \tag{6}$$

The result of the reconstructed event rate using the numerically derived livetime is compatible within errors with the true event rate. The quantity $(R-r)/\sigma(r)$ is standard normal distributed if the event rate is reconstructed from the numerically derived livetime with $\sigma(r)$ given by eq. 6. Note, however, that eq. 3 can have up to two real solutions for T_{Live}. It was not possible to find a general rule which solution

leads to the best estimate for the reconstructed event rate if multiple solutions for T_{Live} exist. In any case it is not always correct to use the solution that is better compatible with $T^{\star}_{\mathrm{Live}} = T_{\mathrm{Run}} - ND$ which is the unique solution for the livetime if the approximation $\exp(RD) = 1 + RD$ would be appropriate in eq. 3. As a general rule, one has thus to infer the true event rate based on a (likelihood) fit of the time difference distribution to an exponential and calculate the up to two possible real solutions for the livetime. The livetime that leads to an inferred rate that is compatible with the event rate inferred from the time difference distribution fit is eventually correct.

- For comparison consider the same case of a Poisson process with events occurring at $t_0, ..., t_i$ with the time difference between consecutive events of $\Delta_i = t_{i+1} - t_i$. In contrast to the situation discussed above consider now the case where consecutive events are not recorded unless $\sum_i \Delta_i > D$. To clarify the difference between this cut out criteria and the criteria discussed above, consider three events t_0, t_1, t_2 occurring consecutively with time difference $\Delta_0 = t_1 - t_0 < D$ and $\Delta_1 = t_2 - t_1 < D$ but $\Delta_0 + \Delta_1 > D$. The criteria discussed above would dismiss events t_1 and t_2 in contrast to the criteria discussed here which would only dismiss event t_1.
  The effect of the selection criteria $\sum_i \Delta_i > D$ is that after each event no event is recorded for the time D. Thus on average RD events are not recorded after each recorded event and the true event rate R is determined by the observed number of events N via
  $$R = \frac{N + NRD}{T_{\mathrm{Run}}} \tag{7}$$
  which leads with $R = N/T_{\mathrm{Live}}$ to
  $$T_{\mathrm{Live}} = T_{\mathrm{Run}} - ND\,. \tag{8}$$
  Note that eq. 8 and eq. 3 agree with each other when $\exp\left(ND/T_{\mathrm{Live}}\right) = 1 + ND/T_{\mathrm{Live}}$ is a sufficient approximation. The true event rate can thus be inferred from the livetime with a statistical error of
  $$\sigma(r) = \sqrt{N}\left(\frac{1}{T_{\mathrm{Live}}} - \frac{N}{T^2_{\mathrm{Live}}}\frac{\partial T_{\mathrm{Live}}}{\partial N}\right) = \frac{\sqrt{N}}{T_{\mathrm{Live}}}\left(1 + \frac{ND}{T_{\mathrm{Live}}}\right)\,. \tag{9}$$
  On the other hand, the true event rate can also be obtained from a fit of the distribution of the time differences Δt between recorded events away from the dead time, i.e. for $\Delta t > D$. This holds because the distribution of the time differences between recorded events is equal to the distribution of the time to the first arrival time of an event plus D where the distribution of the time to the first event is the same as the distribution of the time differences between consecutive events for a Poisson process.
  The results discussed here have been checked in a Monte Carlo simulation similar to the one discussed above for the other event selection criteria. It is found that the true event rate obtained from a χ^2 fit of the distribution of the time differences

between recorded events is biased in contrast to the results from a likelihood fit for which the quantity $(R - r)/\sigma(r)$ with the true rate R and the reconstructed rate r with statistical error $\sigma(r)$ is standard normal distributed. The quantity $(R-r)/\sigma(r)$ is also standard normal distributed if the true event rate R is estimated to be r using the number of recorded events and the livetime as calculated with eq. 8 if the error on the estimated rate is given by eq. 9.

This criteria for the acceptance of events, $\sum \Delta_i > D$, would be appropriate if there were a fixed hardware dead time for the complete H.E.S.S. array after every recorded event. The later implementation of this criteria in software would, however, only be possible if all events were recorded. To see this, consider again a sequence of events occurring at times t_0, t_1, t_2, t_3 with $\Delta_i = t_{i+1} - t_i$ and the case that $\Delta_0 < D$, $\Delta_1 < D$ and $\Delta_0 + \Delta_1 > D$ as well as $\Delta_2 > D$. The application of the event selection criteria $\sum \Delta_i > D$ would select events t_0, t_2 and t_3. But for the real H.E.S.S. trigger it can happen that the event at t_2 is not recorded because the event would trigger an array configuration that is still processing the event recorded at t_1.
A similar consideration also holds for the software implementation of the first criteria for accepting events, i.e. $\Delta_i < D$. If events occur at t_0, t_1, t_2 and $\Delta_0 < D$ and $\Delta_1 < D$ but $\Delta_0 + \Delta_1 > D$ and the event at t_1 is not recorded due to a hardware dead time effect, the software application of the criteria $\Delta_i > D$ based on the recorded data (t_0, t_2) would select the events at t_0 and t_2 which is not intended.
Because of the those effects, the true event rates inferred from livetimes calculated according to eq. 3 and 8, respectively, do not agree within statistical errors with the true event rates inferred from the (likelihood) fit of the time difference distribution. A clean solution for this problem would only be possible by developing a full model for the H.E.S.S. trigger (which appears highly non trivial) or to implement a hardware dead time in the array that is centrally vetoing camera triggers as long as not all cameras are operational. A workaround for the current data taking situation is to estimate a systematic error on the true event rate and in turn a systematic error on the livetime. In practice this means that the true event rate is inferred with one of the methods discussed above and only the events that are satisfying the connected event selection criteria are further processed. The event selection criteria that is best suited is certainly $\Delta_i > D$ because the fraction of events where the number of read out telescopes is smaller than the number of triggered telescopes is smaller with this criteria than with the criteria $\sum \Delta_i > D$. However, it must be noted that events with $\Delta_i > D$ and number of read out telescopes smaller than the number of triggered telescopes have to be further processed because it is found that otherwise the χ^2 probabilities for the exponential fits to the time difference distribution become very small. The systematic error on the true event rate, $\sigma_s(r)$, is in turn estimated to be the absolute difference between the true event rate r_1 inferred from the fit of the time difference distribution for consecutive events ($\Delta_i > D$ where D can in practice be as low as 0.75 ms) and the true event rate r_2 inferred from the exponential fit to the time difference distribution for events selected with the criteria $\sum \Delta_i > D$, i.e.

$$\sigma_s(r) = |r_1 - r_2| \,. \tag{10}$$

The livetime is estimated to be

$$T_{\mathrm{Live}} = N/r_1 \tag{11}$$

where N is the number of events selected with the criteria $\Delta_i > D$ and the systematic error on the livetime is estimated in the same way as the systematic error on the event rate to be

$$\sigma_s(T_{\mathrm{Live}}) = |N/r_1 - N/r_2| \,. \tag{12}$$

Whether or not the systematic error on the event rate and the livetime are relevant, i.e. larger than statistical errors, depends on the true event rate itself. The investigation of a large dataset shows that the systematic error on the livetime becomes relevant ($\sim 0.5\%$) if the true event rate is larger than ~ 180 Hz. For event rates that are much lower, the systematic errors on the event rates and livetimes are typically negligible.

Appendix B: ON/OFF Data Quality Plots

This appendix is a collection of detailed data quality plots for the ON/OFF dataset considered in this thesis. An 'OFF1 run' labels the observation run corresponding to an offset of -35 min in right ascension from the ON observation position. An 'OFF2 run' labels the observation run corresponding to an offset of $+35$ min in right ascension from the ON observation position.

- Figure 4 and fig. 5 show the compatibility of the horizon system pointing within an On/Off observation run triple.

- Figure 6 shows the incompatibility of the event rates as a function of time within an On/Off observation run triple. Event rates are biased and fluctuating from observation run to observation run. Each datapoint is obtained from a fit of the time difference distribution to an exponential far away from dead time effects.

- Figure 7 shows the incompatibility of the number of times a given pixel intensity is read out in the array between the ON and the OFF observation runs. For intensities below ~ 7 pe (indicated by the blue vertical line), the incompatibility is larger. Additionally the direction of the incompatibility is fluctuating for intensities above ~ 7 pe from dataset to dataset which points towards an effect that is not connected to the observed regions. This is not true for the direction of the incompatibility for intensities below ~ 7 pe. The plots justify the application of '0710' image cleaning as explained in the main text.

- Figure 8 shows the incompatibility of the '0710' image cleaned preselected event rate as a function of observation time for different On/Off runs that belong to the same On/Off run triple. The effect is smaller than the incompatibility of the raw event rate (fig. 6).

- Figure 9 and 10 show the radiometer temperature as a function of runtime for runs that belong to the same On/Off run triple. The two different radiometer measurements are biased but the temperature change relative to the start of the run agrees for different radiometers in the same observation run.

- Figure 11 shows the muon correction factors for every telescope and every run of the considered On/Off dataset. The analysis uses eventually the average of the muon corrections measured for each camera respectively. If this is not done, incompatibilities in the distributions of the events with respect to the reconstructed energy can result within an On/Off run triple.

- Figure 12 shows the change of the average PMT current in CT1 relative to the start of the run as a function of time. The average PMT current depends linearly on the night sky background (NSB) in the field of view (H.E.S.S. Col. [2004]). Given the constant pointing in celestial coordinates it is expected that no time difference of the average PMT current is observed. The observed change in time of the quantity is a measure for possible systematic errors for the measurement of the NSB as a function of time in a driftscan observation run. An average difference of 0.1 μA relative to the start of the run is translated into a NSB change of ~ 3 MHz. Figure 13 shows the measured average drawer module temperature as a function of time for CT1. No obvious correlation between the average drawer module temperature and the PMT currents is apparent.

- Figure 14 shows the number of broken pixel in the four telescope array for each of the observation runs considered in the On/Off dataset as a function of observation time. Differences in the number of broken pixel exist at the level of ~ 10 to ~ 50 pixels. Typically ~ 150 pixels are not operating in the whole array.

- Figure 15 shows the number of times a pixel triggers with a non vanishing intensity for all four cameras as well as the position of the pixel for one On/Off run triple of three observation runs. Most important is the comparison of the distribution of pixel triggers for CT3. The comparison of the distribution of pixel triggers for CT3 between run 58727 and 58728 shows that a difference in respect to two broken drawer exists. On the other hand, the number of broken drawers is differing by only one between observation run 58728 and 58729. It is argued in the main text that the event rate between run 58727 and 58728 differs by $\sim 2\%$ due to the difference in two broken drawer modules but by much less than 2% between run 58728 and 58729. Figure 16 shows the same plot but with a color code of red for a pixel that triggers at least once and green for a pixel that never triggers during a run. This is better suited to identify broken drawer modules. Figure 17 shows the size of clusters of broken pixels for all considered On/Off observation runs. Large ($\sim 2\%$) influences on the event rate are found to be not caused by individual broken pixel or small clusters of broken pixels. Relevant are differences in the size of the largest cluster of broken pixel of more than 50%. This occurs only in dataset 1 ON-OFF1 (upper left panel of fig. 17 green and red) and dataset 5 ON-OFF1 (lower left panel green and red data points).

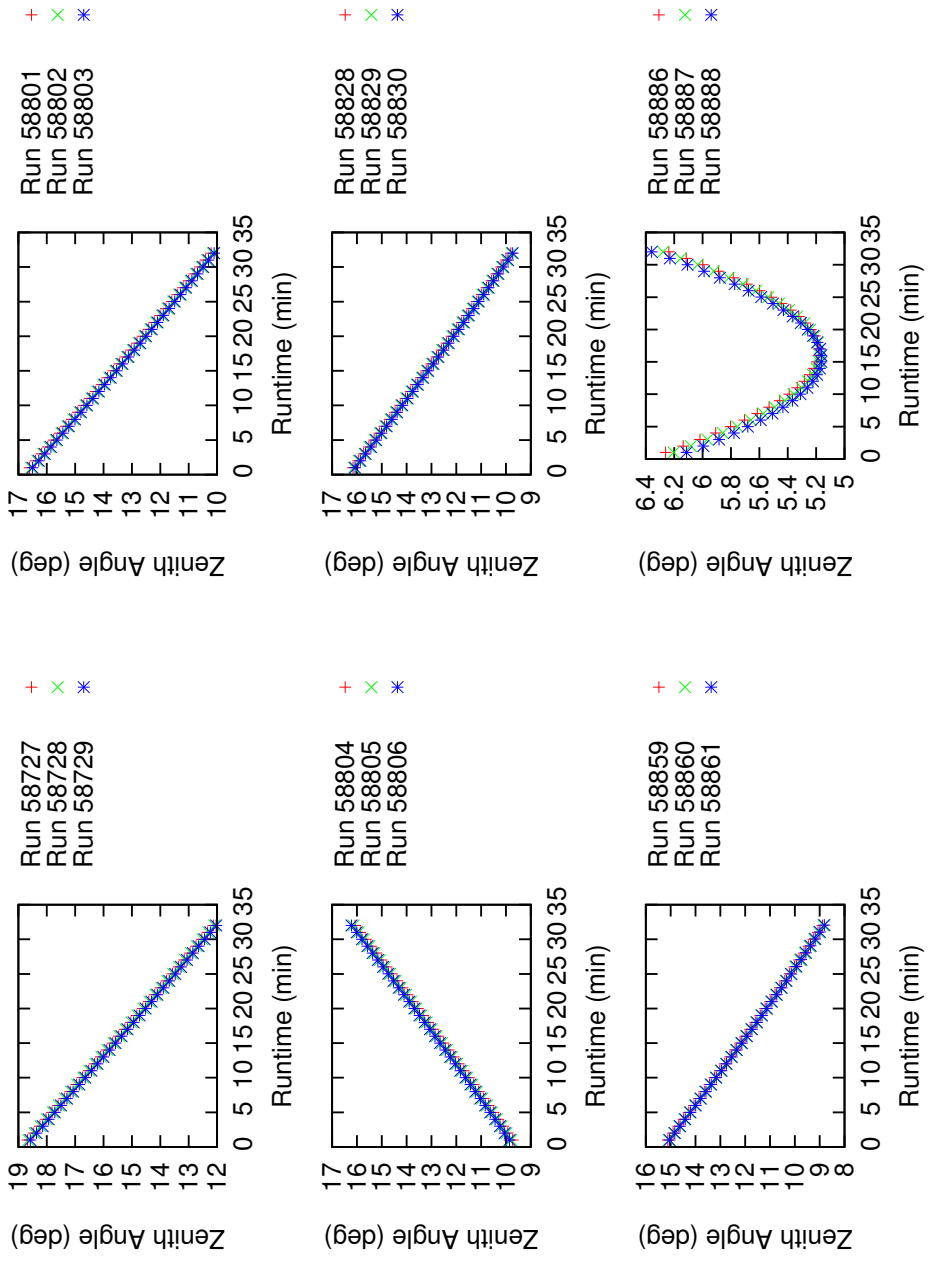

Figure 4: Array pointing zenith angle as a function of runtime for all considered On/Off runs. Each box compares three runs (labeled by the H.E.S.S. internal run number) taken consecutively as a OFF/ON/OFF run triple.

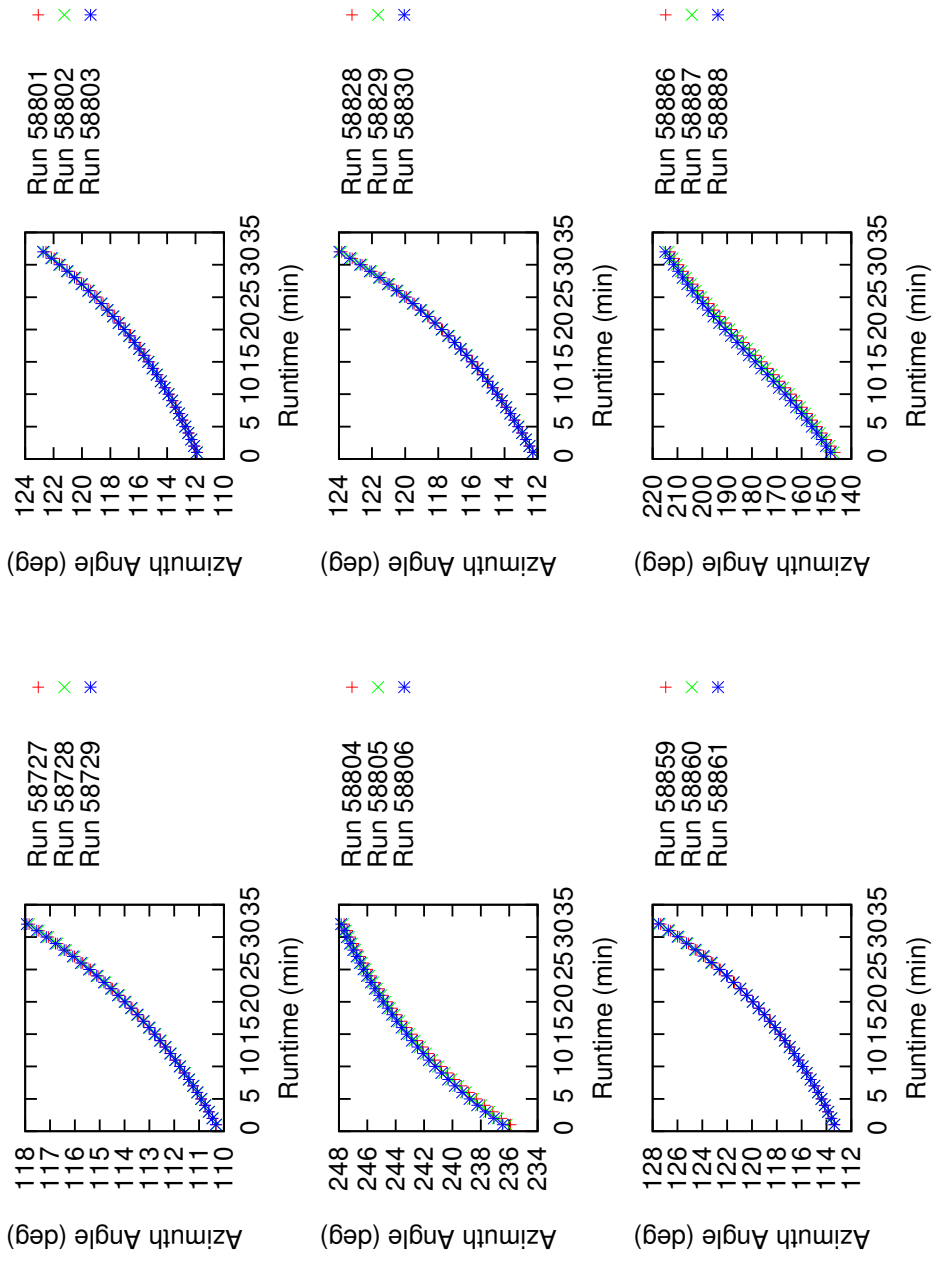

Figure 5: Array pointing azimuth angle as a function of runtime for all considered On/Off runs. Each box compares three runs (labeled by the H.E.S.S. internal run number) taken consecutively as a OFF/ON/OFF run triple.

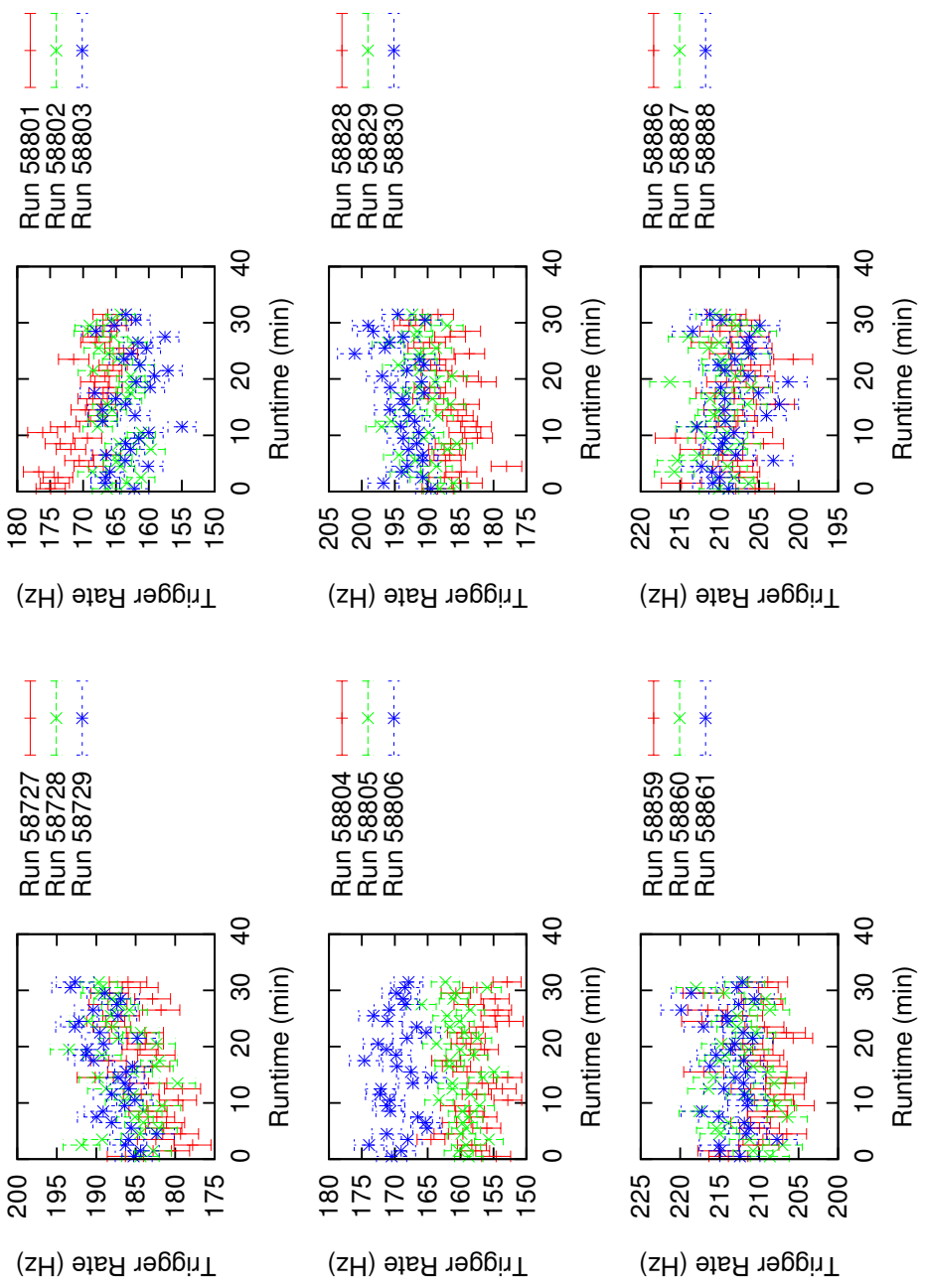

Figure 6: H.E.S.S. array trigger rate as a function of runtime for all considered On/Off runs. Each box compares three runs (labeled by the H.E.S.S. internal run number) taken consecutively as a OFF/ON/OFF run triple.

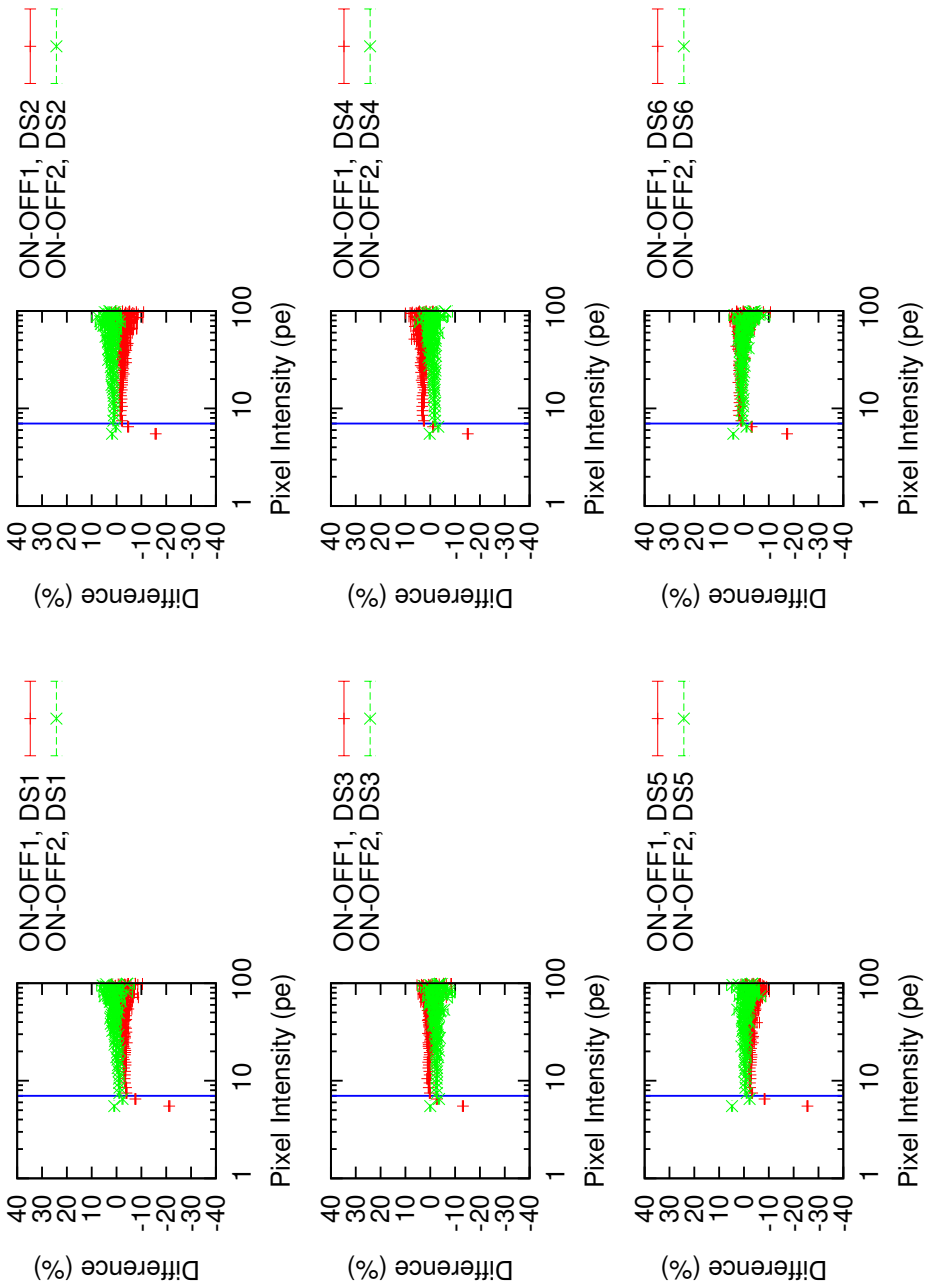

Figure 7: Relative pixel intensity difference, i.e. relative difference in the number of times a given intensity is measured in one of the pixels, for each of the six investigated On/Off run triples. Shown in green is the relative pixel intensity difference for ON-OFF1 and in red ON-OFF2 for each dataset respectively. The blue line indicates 7 pe. The data passed event preselection and standard '0510' image cleaning. Large differences in the number of pixels with intensity below 7 pe are visible. Above intensities of ~ 7 pe, non-zero intensity differences that are, however, nearly independent of the considered pixel intensity are observed. Those constant shifts can be explained by the constant (preselected) rate shifts between the On and the Off data runs.

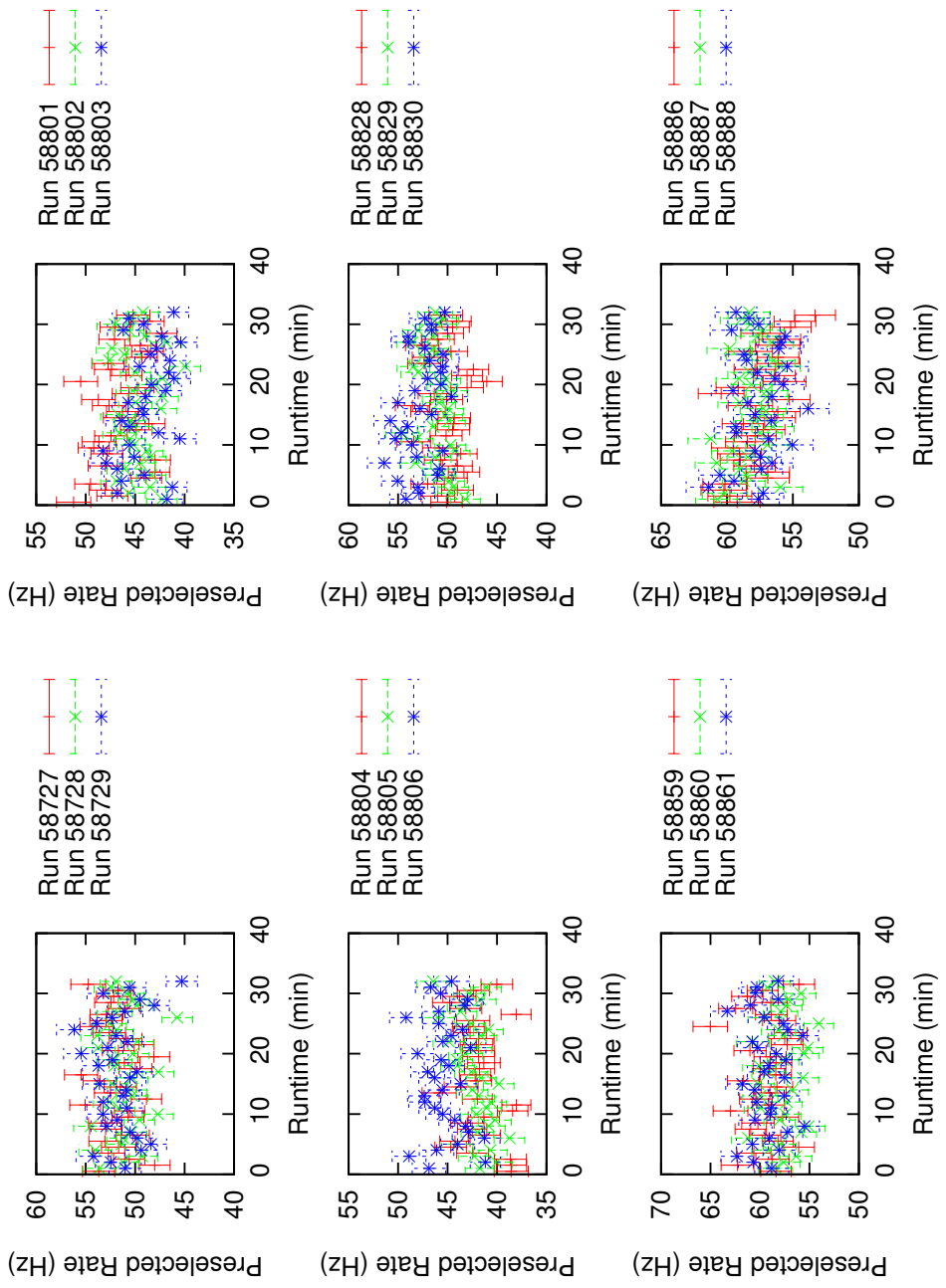

Figure 8: Preselected event rate as a function of observation time. Only events where the number of triggered telescopes is equal to the number of read out telescopes are considered. The data is '0710' image cleaned. Each box compares three runs (labeled by the H.E.S.S. internal run number) taken consecutively as a OFF/ON/OFF run triple.

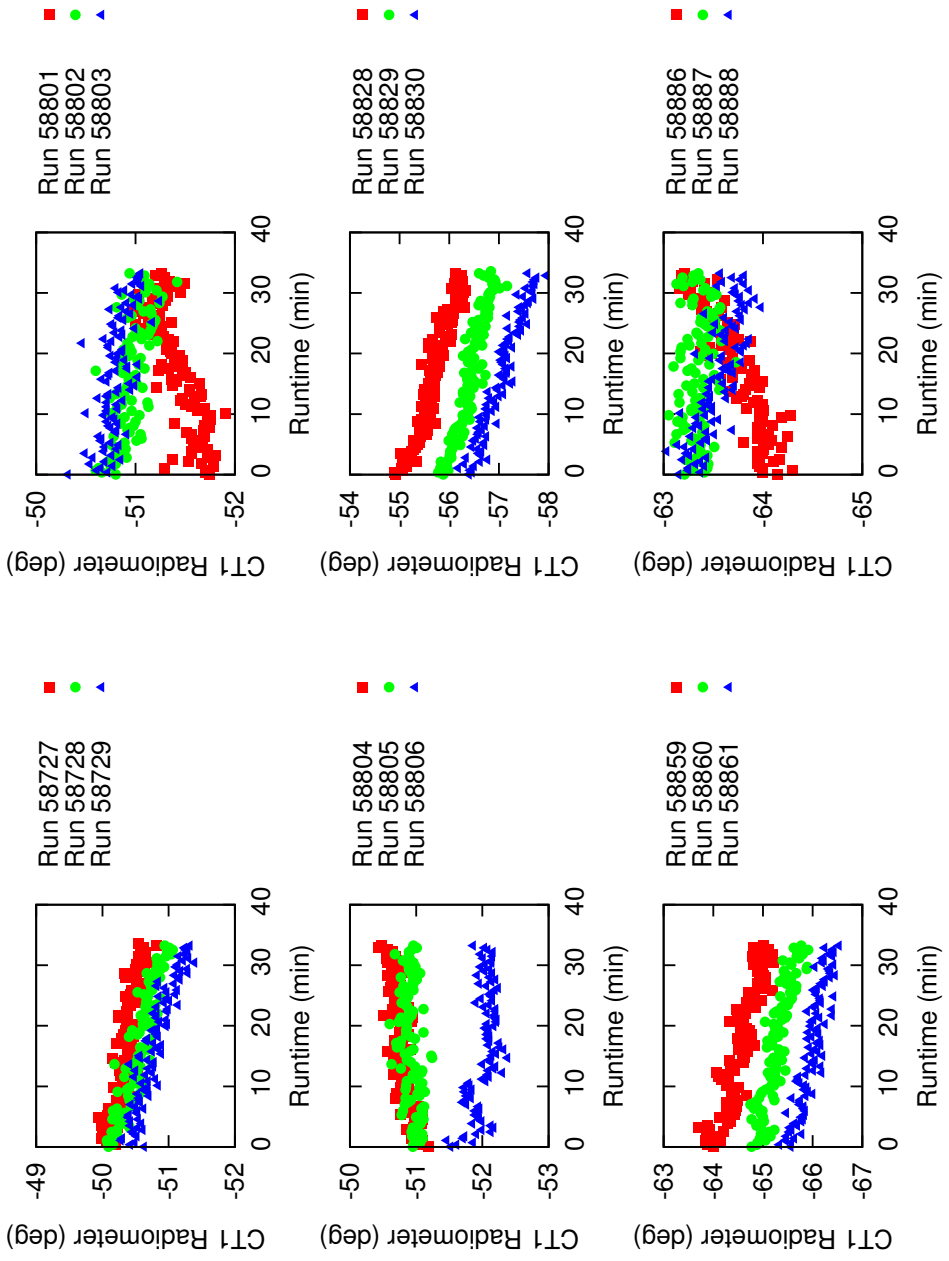

Figure 9: CT1 radiometer temperature as a function of observation time. Each box compares three runs (labeled by the H.E.S.S. internal run number) taken consecutively as a OFF/ON/OFF run triple.

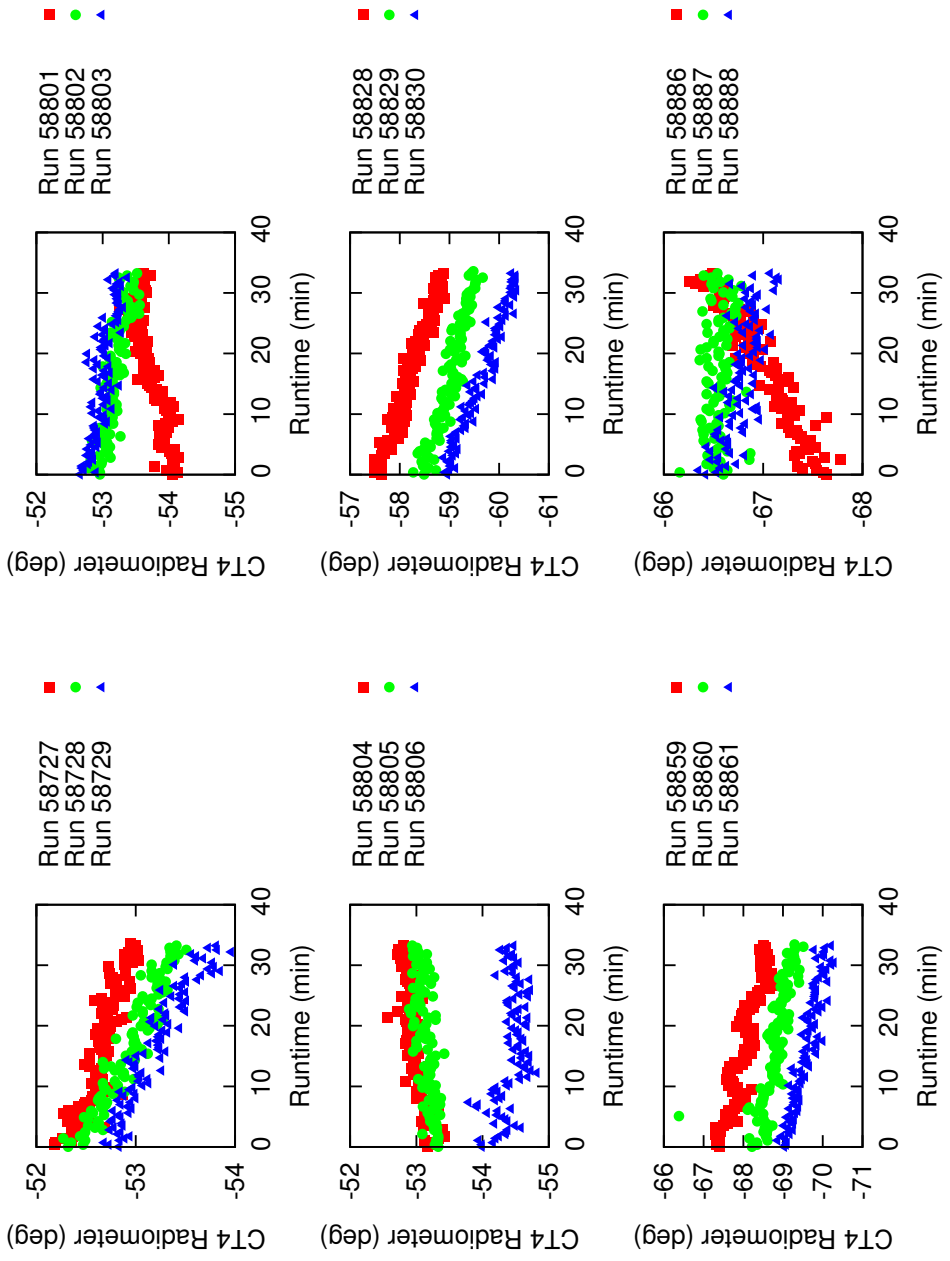

Figure 10: CT4 radiometer temperature as a function of observation time. Each box compares three runs (labeled by the H.E.S.S. internal run number) taken consecutively as a OFF/ON/OFF run triple.

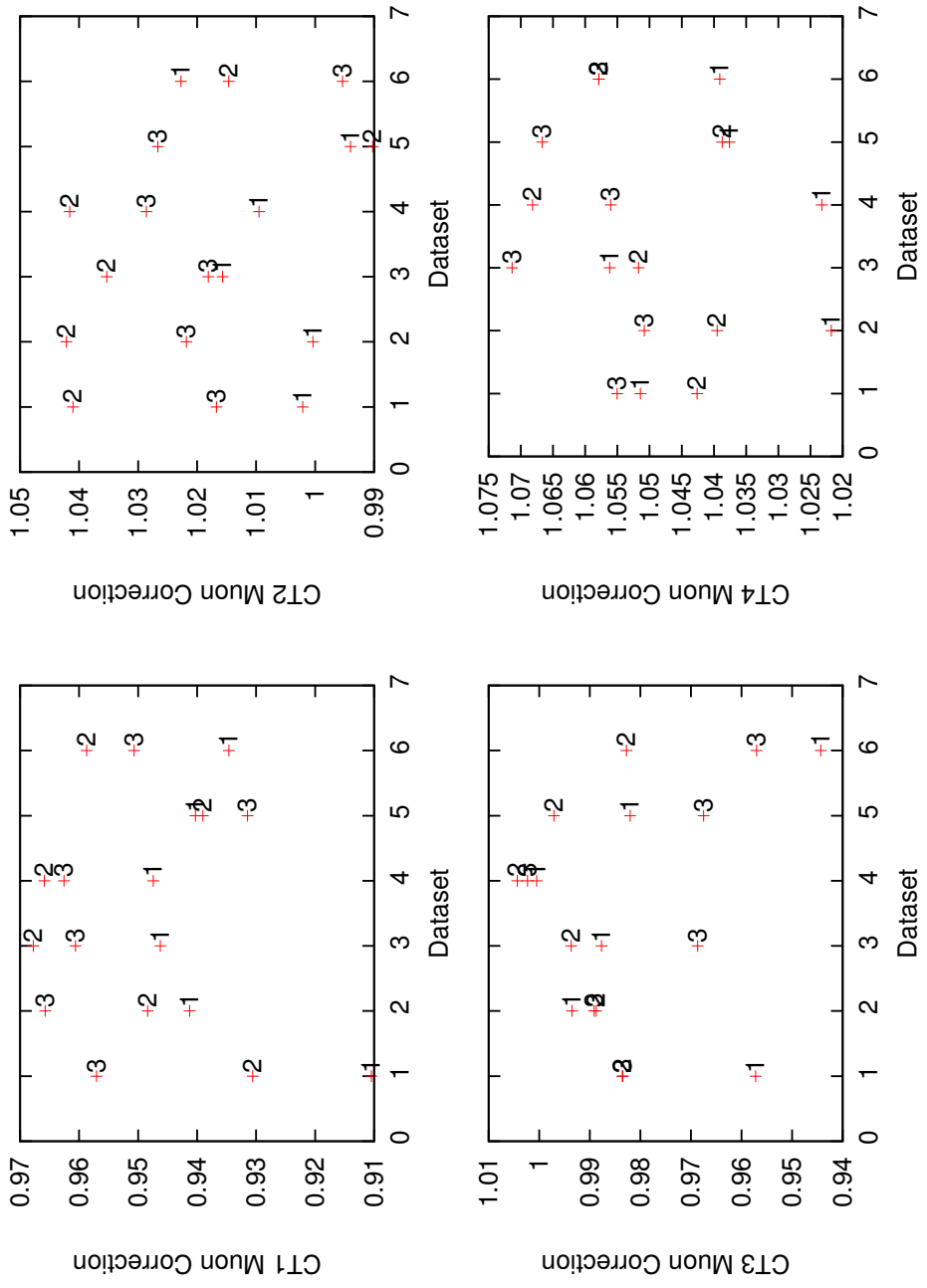

Figure 11: Muon correction coefficients for each of the six considered OFF/ON/OFF datasets. The numbers right to the datapoints label whether the datapoints belongs to an OFF1 (1), an ON (2) or an OFF2 (3) run.

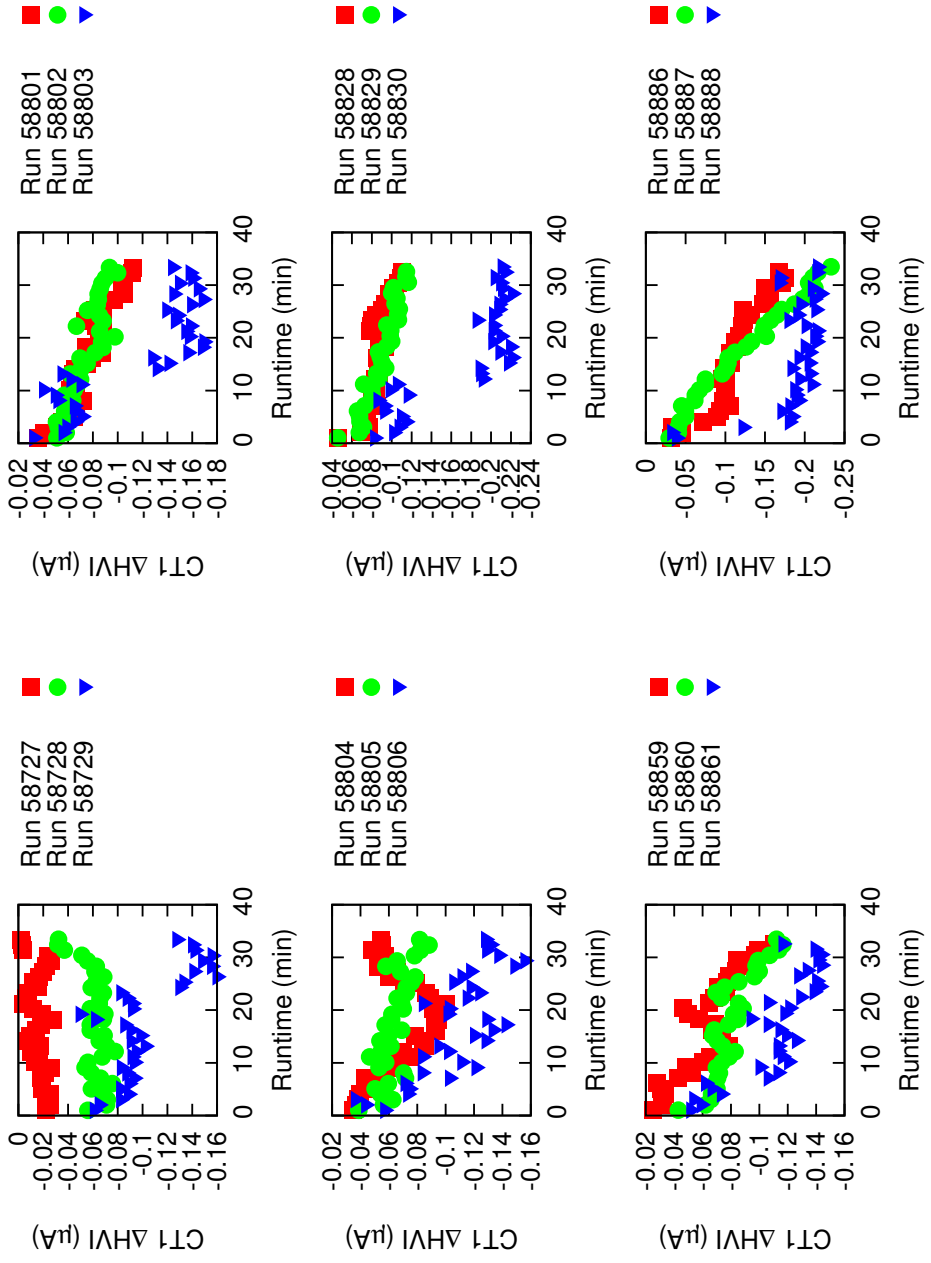

Figure 12: Average PMT current in CT1 relative to the start of the run. Each box compares three runs (labeled by the H.E.S.S. internal run number) taken consecutively as a OFF/ON/OFF run triple.

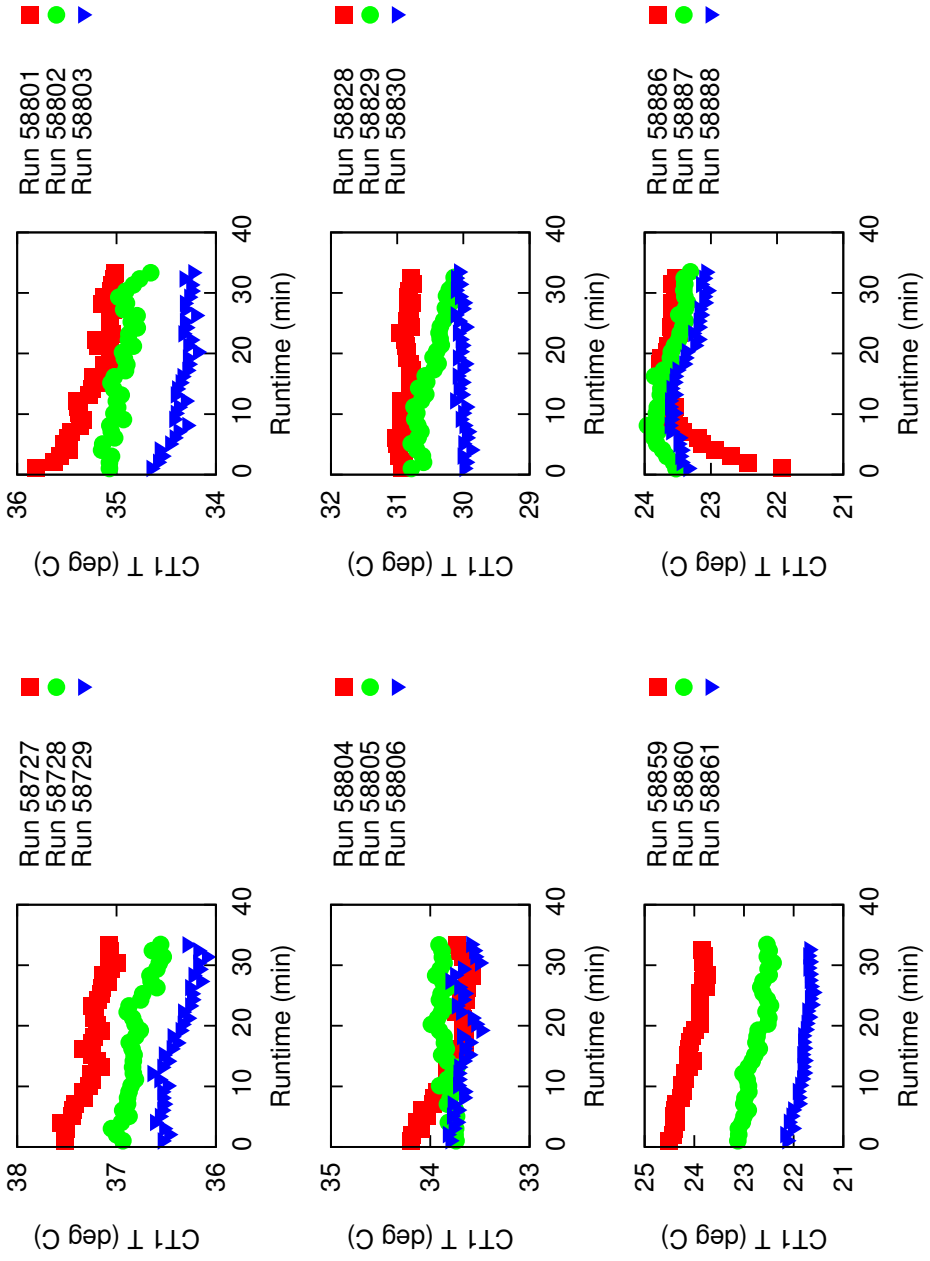

Figure 13: Average CT1 camera temperature. Each box compares three runs (labeled by the H.E.S.S. internal run number) taken consecutively as a OFF/ON/OFF run triple.

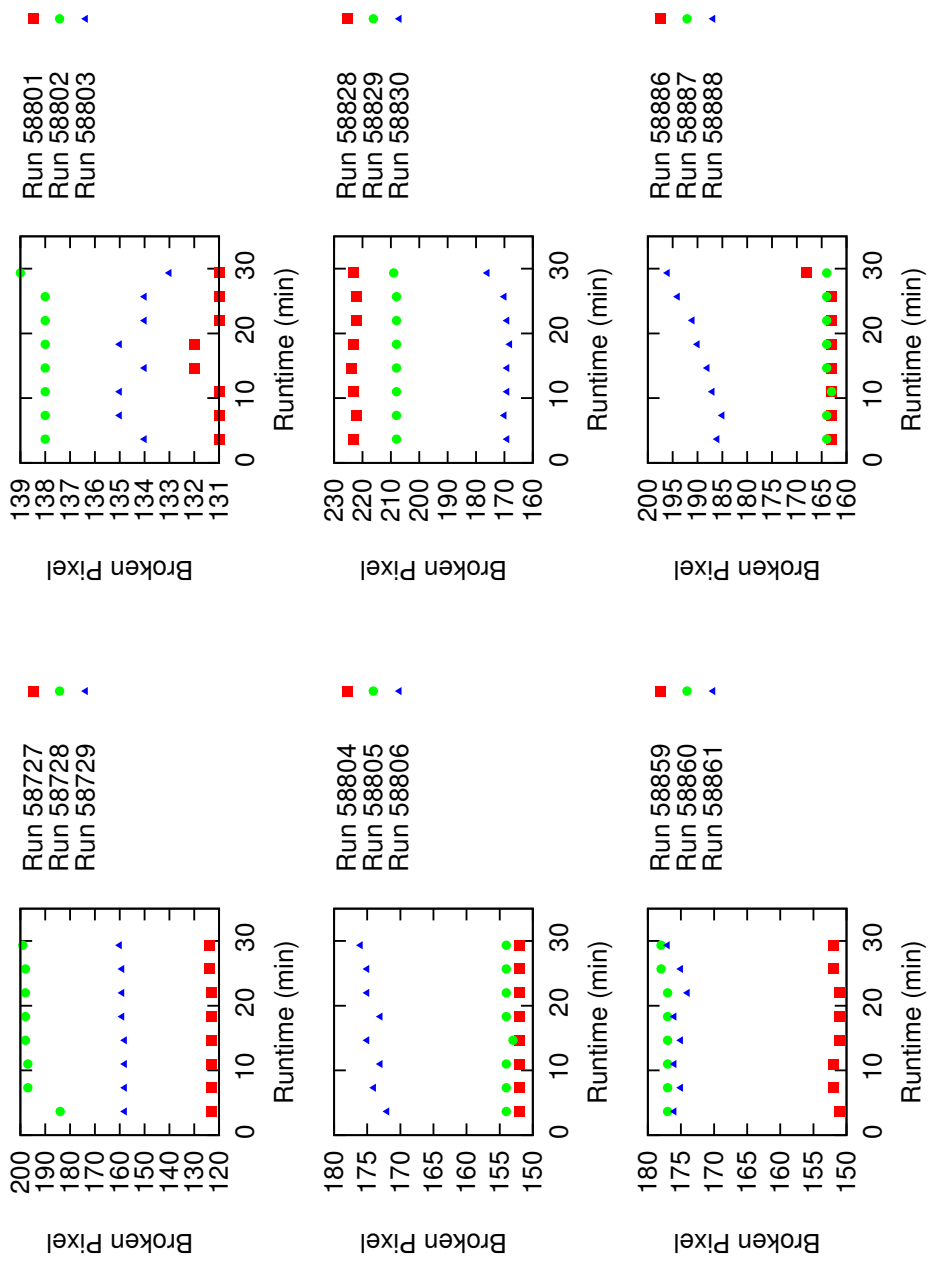

Figure 14: Number of broken pixels (pixels which never measure a non vanishing signal in the corresponding time interval) as a function of observation time. Each box compares three runs (labeled by the H.E.S.S. internal run number) taken consecutively as a OFF/ON/OFF run triple.

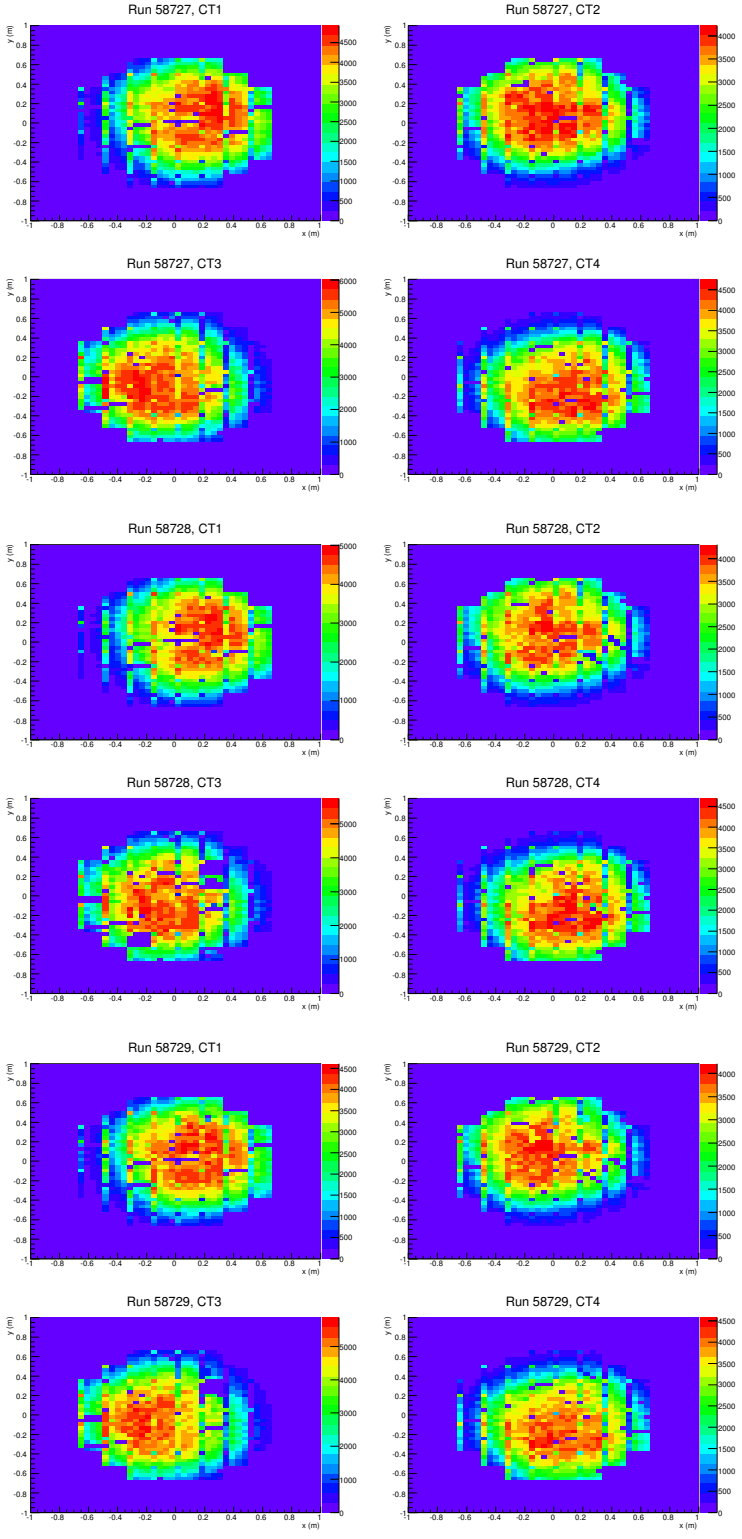

Figure 15: Number of times (color scale) a pixel in the camera triggers with a non vanishing signal during the runtime. The upper 2x2 panels show CT1-CT4 for run 58727 which is an OFF1 run. The next 2x2 panels below show CT1-CT4 for run58728 which is the corresponding ON run. The lower 2x2 panels show CT1-CT4 for run 58729 which is the corresponding OFF2 run.

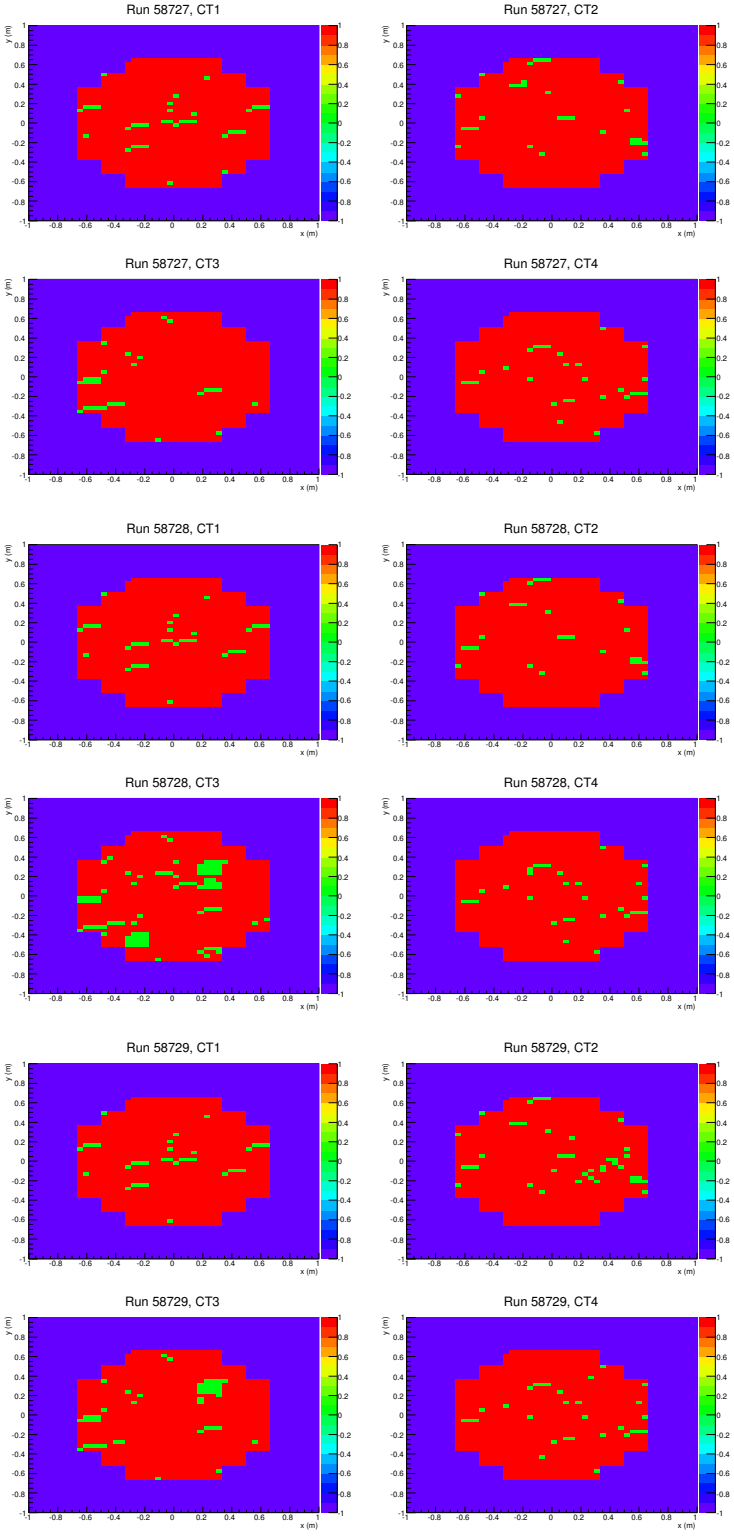

Figure 16: Spatial distribution of the broken pixels in one OFF1/ON/OFF2 dataset. Broken pixels are indicated by green points. Working pixels are indicated by red points. The upper 2x2 panels show the results for the OFF1 run 58727, the next 2x2 panels for the ON run 58728 and the lower 2x2 panels for the OFF2 run 58729. Note the broken drawer (4X4 PMTs) in CT3 in the ON and OFF2 run that is not broken in the OFF1 run.

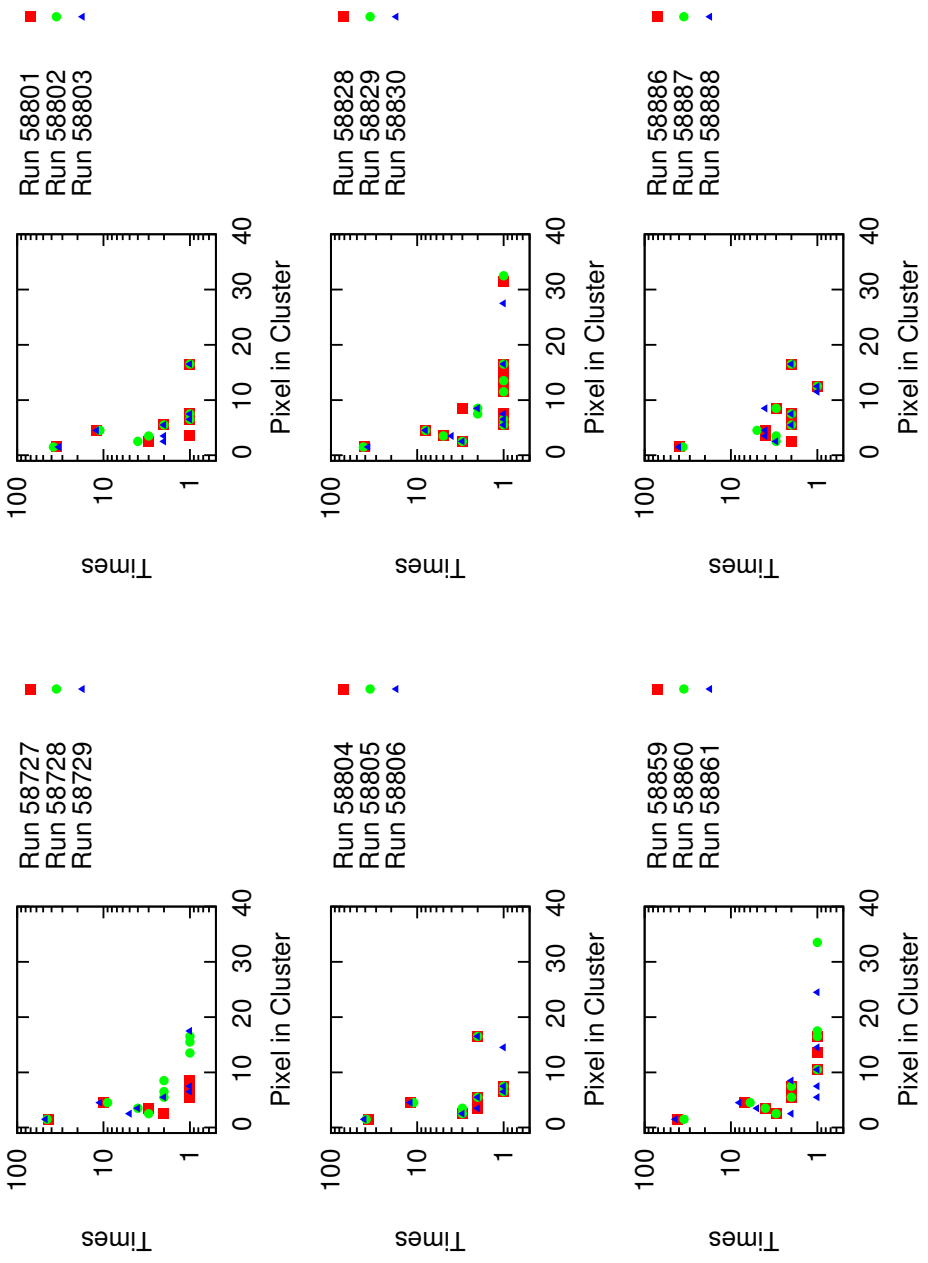

Figure 17: Number of broken pixel clusters as a function of the cluster size. A cluster of broken pixels is a formation of broken pixels where each broken pixel has at least one neighboring broken pixel. The cluster size is the number of pixels in the cluster. Each box compares three runs (labeled by the H.E.S.S. internal run number) taken consecutively as a OFF/ON/OFF run triple.

Appendix C: Driftscan Data Quality Plots

This appendix is a collection of detailed data quality plots for the driftscan dataset that is considered in this thesis.

- Figures 18 and 19 show the event rate and the radiometer temperature as a function of time for eleven driftscan observation runs. In case of two runs (run 75763 and run 76011), the radiometer temperature is varying by much more than 1° during the run and the runs are discarded in the following analysis.

- Figure 20 shows for the remaining nine observation runs the number of broken pixels as a function of observation time individually for all four telescopes. For three runs (runs 75783, 76042 and 58753), almost one complete telescope was not operational. Those observation runs are also discarded from the driftscan analysis.

- Figure 21 shows the total number of broken pixel in all four telescopes as a function of time. In three of the observation runs that have not already been discarded before, the total number of broken pixel is very large ($\sim$ 400 - 700). The runs (75707, 75815 and 76072) are discarded from the further driftscan analysis.

- Figure 22 shows the event rate (red) and the night sky background difference relative to the start of the run (green) as a function of observation time. The night sky background difference is calculated with H.E.S.S. Col. [2004] via

$$\Delta\text{NSB/MHz} = (32.35 \pm 0.06)\Delta I/\mu\text{A} \; .$$

  where ΔI is the average PMT current difference relative to the start of the run. Figure 12 for the On/Off dataset shows that the average PMT current difference relative to the start of the run is also drifting by $\sim (0.2 - 0.4)\,\mu$A/h corresponding to $\sim$ (6 $-$ 12)MHz/h if no NSB difference is present at all. The plot is thus to be taken with care although it hints towards a correlation between the NSB level and the trigger rate. The 'effect' has been investigated in detail but no strong conclusion could eventually be drawn due to possible systematic effects.

- Figure 23 shows the preselected and '0710' image cleaned event rate (red) and the radiometer temperature (green) as a function of runtime.

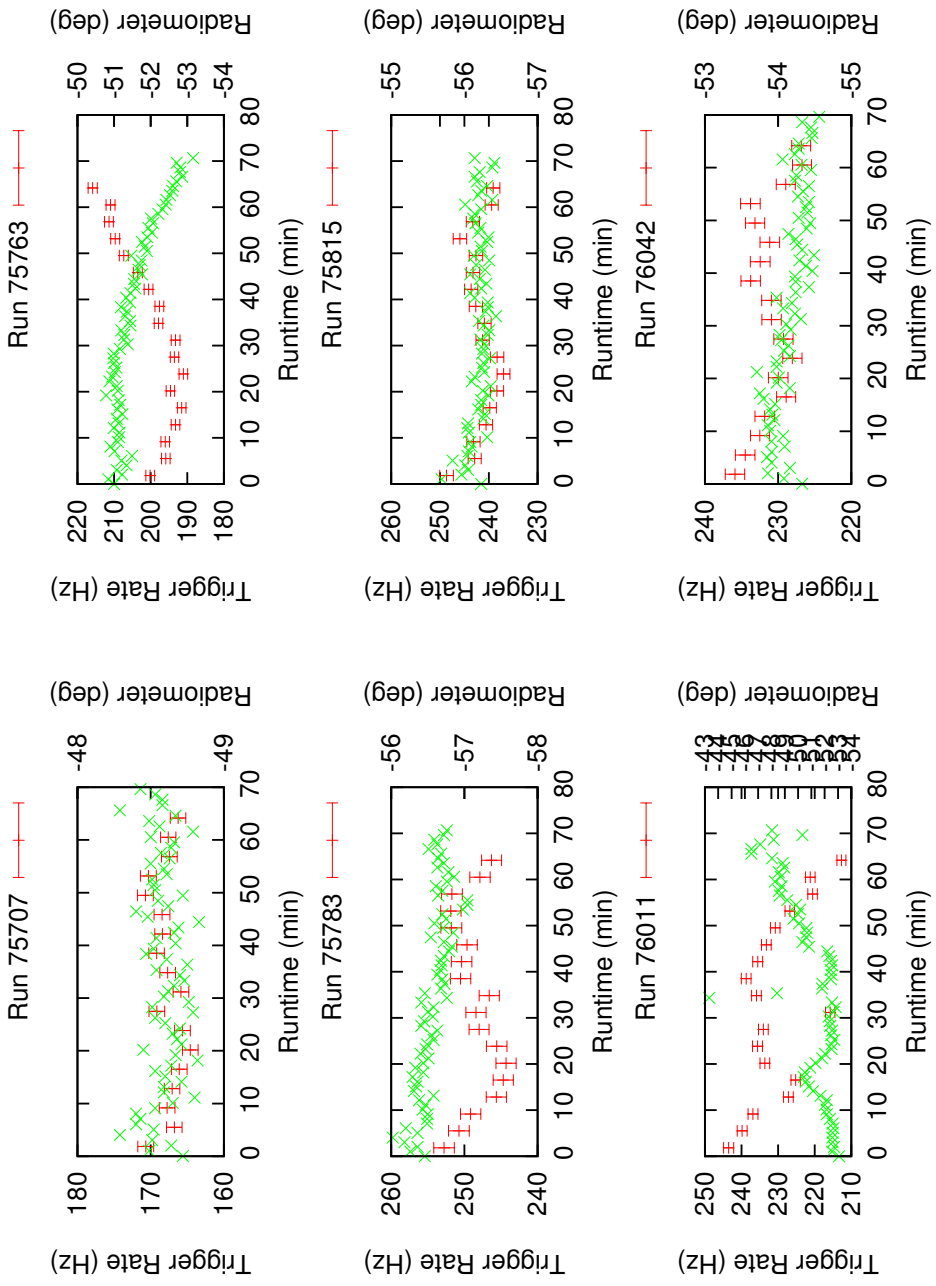

Figure 18: Array trigger rate (red) and one telescope radiometer temperature (green) as a function of observation time. The runs 75763 and 76011 are discarded due to large radiometer temperature variations.

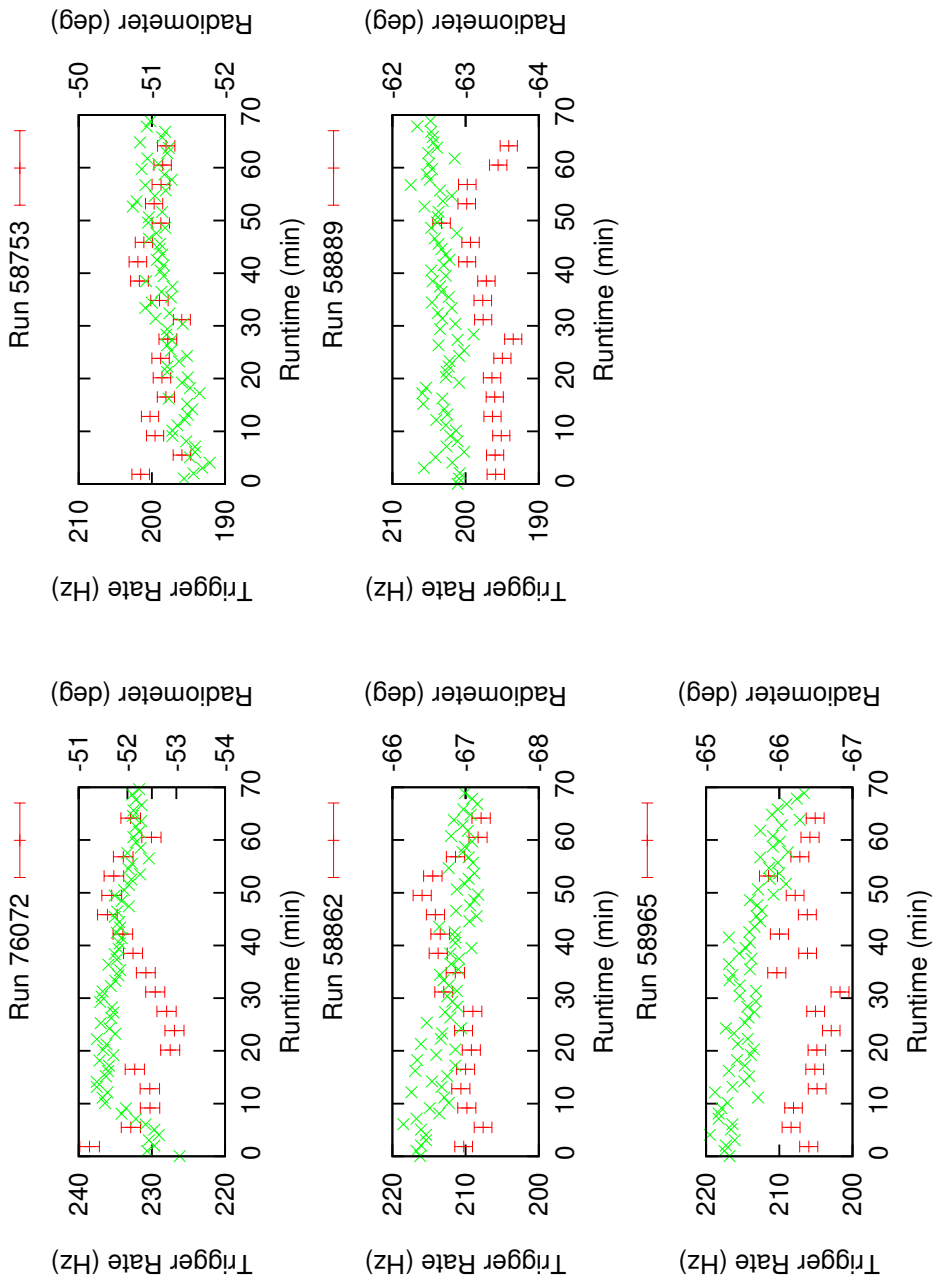

Figure 19: Array trigger rate (red) and one telescope radiometer temperature (green) as a function of observation time.

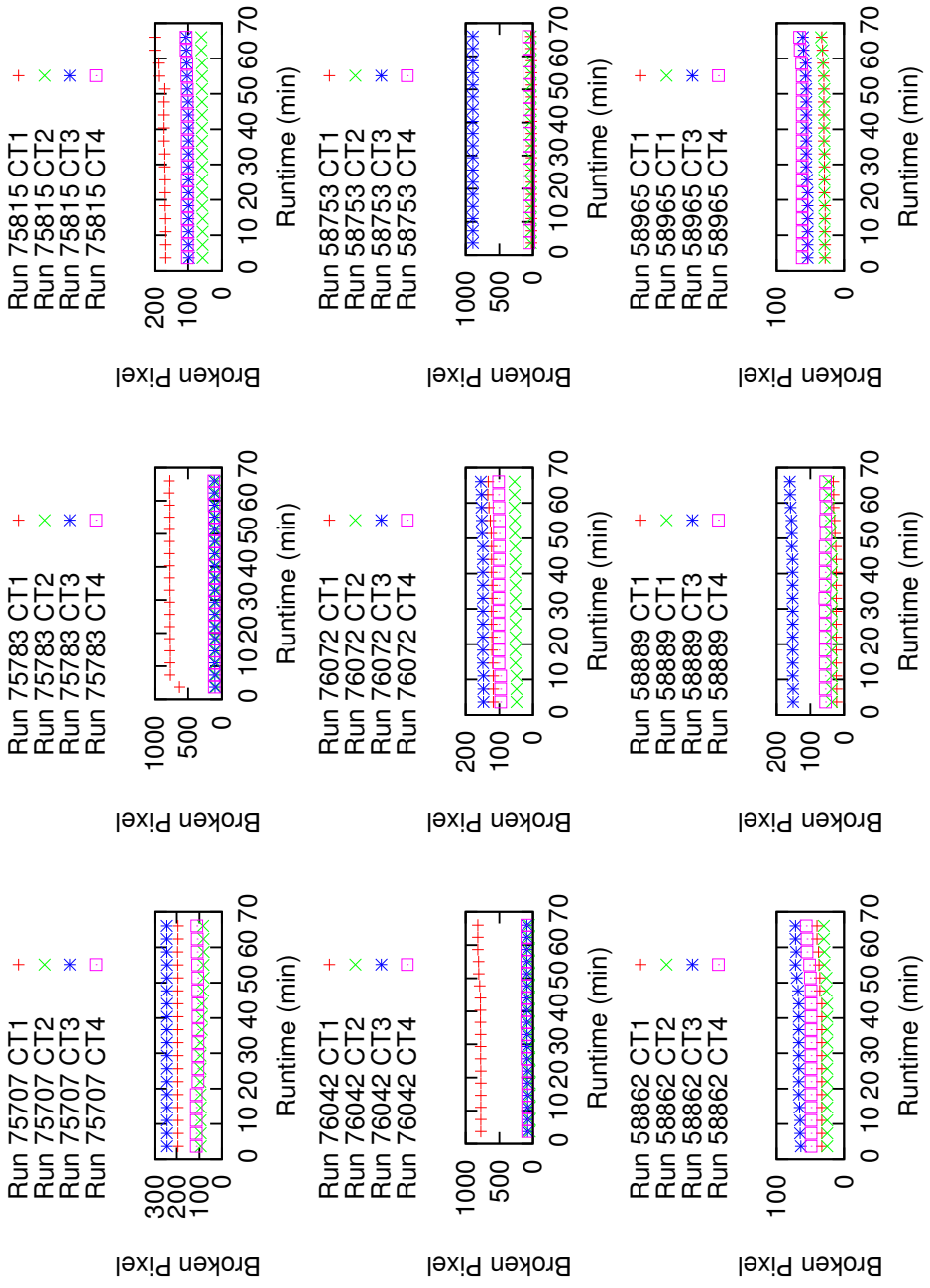

Figure 20: Number of pixels without data for each telescope as a function of observation time. Note that in run 75783, 76042 and 58753 almost one complete telescope (960 pixels) did participate in the event trigger but was not read out.

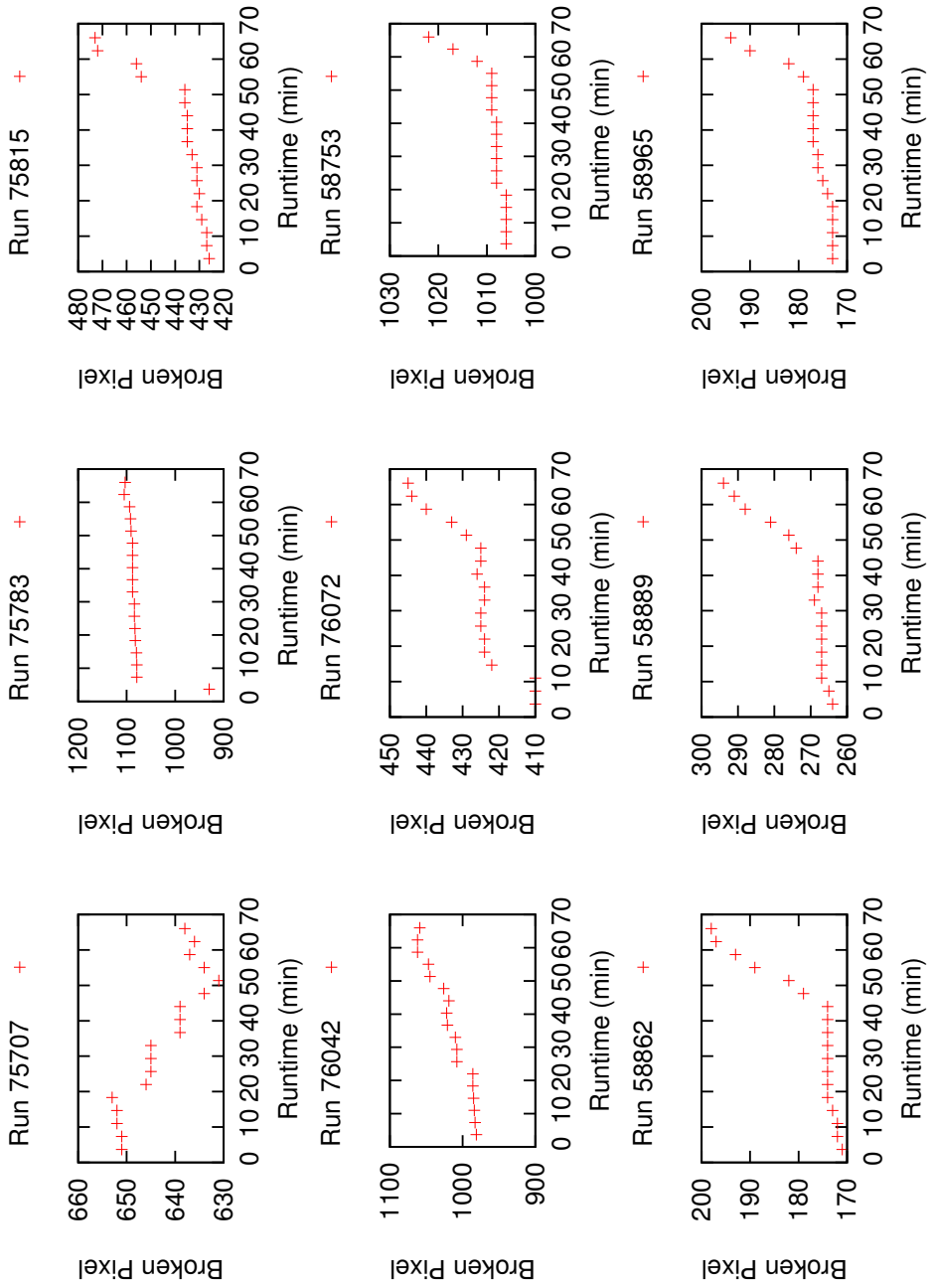

Figure 21: Total number of broken pixels, i.e. the sum of the number of broken pixels over the four telescopes, as a function of observation time. The runs 75707, 75815 and 76072 have an unusually large number (more than ~ 400) of broken pixels and are discarded. After also discarding the runs where almost one complete telescope (960 pixels) did not send data (runs 75783, 76042 and 58753), only three runs remain. For those three runs (runs 58862, 58889 and 58965), the number of broken pixels is significantly increasing after ~ 40 min of observation time.

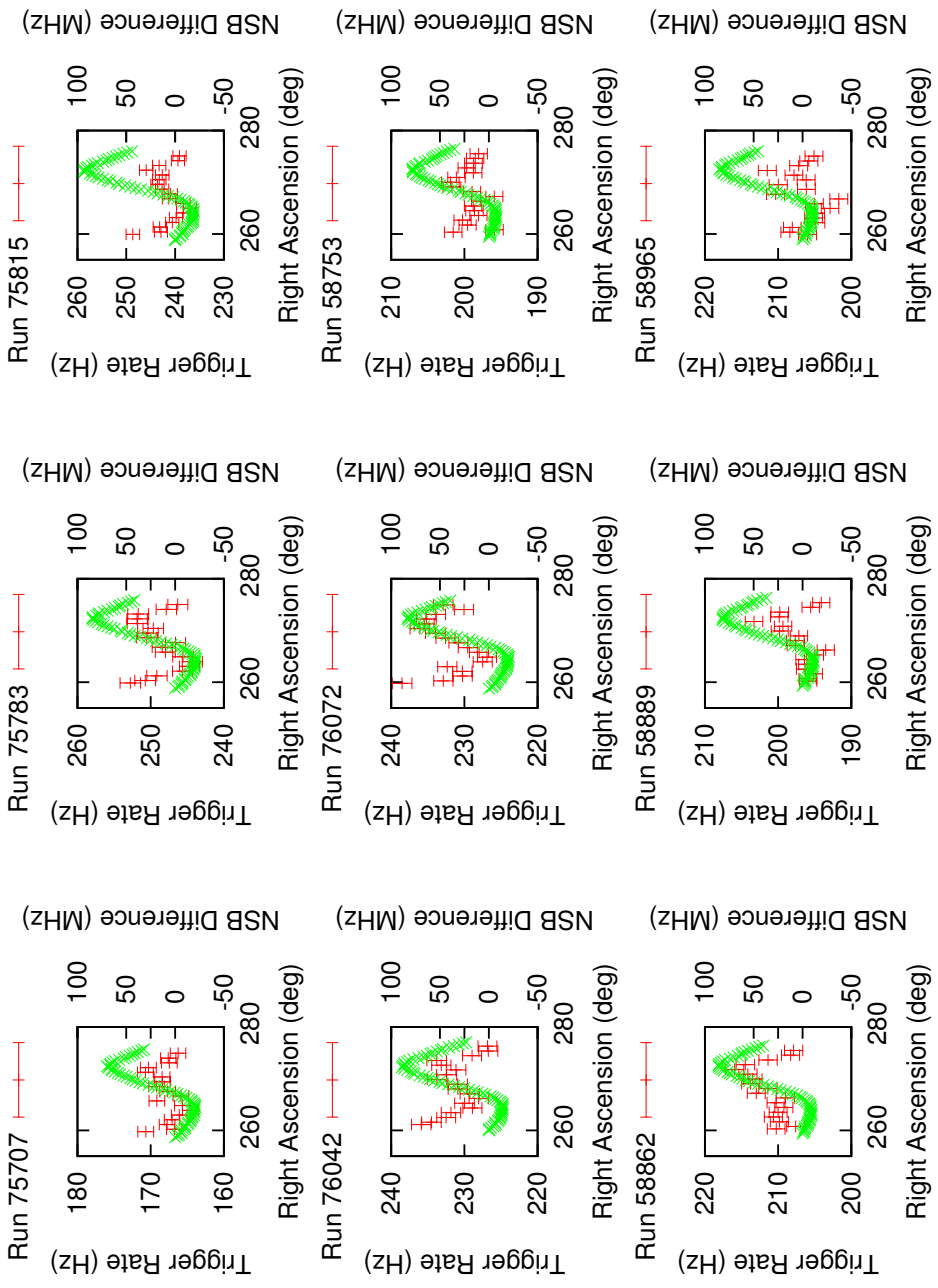

Figure 22: Trigger rate (red) and night sky background (NSB, green) as a function of right ascension pointing position for all driftscan runs that are not discarded due to large radiometer temperature variations. The NSB is measured via the average PMT current relative due to the first pointing position.

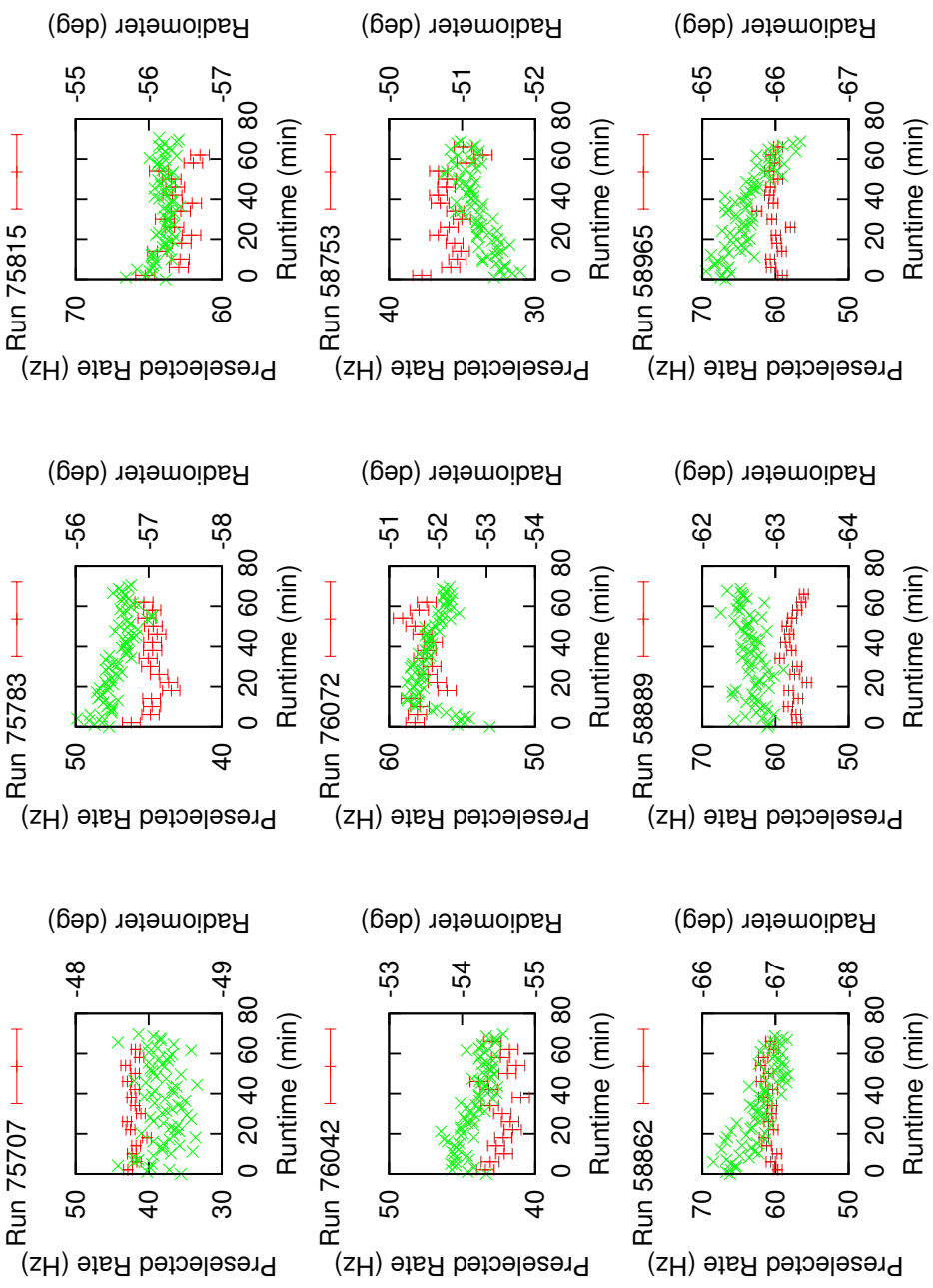

Figure 23: Preselected and '0710' image cleaned event rate (red) and radiometer temperature (green) as a function of observation time for all driftscan runs that have not been discarded due to large radiometer temperature variations.

Appendix D: Gaussian Distributed Exposure Ratio and Excess Significance

In the course of an analysis of γ-ray data recorded with Cherenkov telescopes the number of events in a signal region (N_{ON}) is typically compared to the number of events in a background region (N_{OFF}). Signal and background region are observed with a differing exposure and thus the γ-ray event excess is calculated as $\Delta = N_{\mathrm{ON}} - \alpha N_{\mathrm{OFF}}$ where α is the ratio of the exposures of the signal region to the background region. Traditionally, the statistical significance (S_{LiMa}) of the calculated excess is calculated by using the expression

$$S_{\mathrm{LiMa}} = \mathrm{sign}(\Delta)\sqrt{-2\left(N_{\mathrm{ON}}\ln(\frac{\overline{N_{\mathrm{ON}}}}{N_{\mathrm{ON}}}) + N_{\mathrm{OFF}}\ln(\frac{\overline{N_{\mathrm{OFF}}}}{N_{\mathrm{OFF}}})\right)} \tag{13}$$

where

$$\overline{N_{\mathrm{ON}}} = \frac{N_{\mathrm{ON}} + 1/\alpha\ \alpha N_{\mathrm{OFF}}}{1 + 1/\alpha} = \frac{\alpha}{1+\alpha}\left(N_{\mathrm{ON}} + N_{\mathrm{OFF}}\right) \tag{14}$$

and

$$\overline{N_{\mathrm{OFF}}} = \frac{\alpha\ 1/\alpha N_{\mathrm{ON}} + N_{\mathrm{OFF}}}{1+\alpha} = \frac{1}{1+\alpha}(N_{\mathrm{ON}} + N_{\mathrm{OFF}}) \tag{15}$$

are the weighted means of the number of events in the signal and background region. The quoted expression for the significance of a γ-ray event excess has been first derived in Li and Ma [1983]. The result can also be derived with a profile likelihood method (see Rolke et al. [2005] for general comments on the profile likelihood approach). The starting point is the general likelihood function (L) for the problem given by

$$L = \mathrm{Pois}(N_{\mathrm{ON}}, \alpha b + s)\mathrm{Pois}(N_{\mathrm{OFF}}, b) \tag{16}$$

where s is the unknown number of signal events which is the parameter of interest and b is the unknown number of background events which is a 'nuisance parameter'.
The null hypothesis ($s = 0$) has thus the likelihood function

$$L_0 = \mathrm{Pois}(N_{\mathrm{ON}}, \alpha b)\mathrm{Pois}(N_{\mathrm{OFF}}, b)\ . \tag{17}$$

The nuisance parameter b is 'profiled out' of the likelihood function, i.e. the likelihood function is maximized with respect to the nuisance parameter, with the condition

$$\frac{\partial L_0}{\partial b} = 0 \tag{18}$$

which leads directly to $b = \overline{N_{\mathrm{OFF}}}$ where $\overline{N_{\mathrm{OFF}}}$ is given by eq. 15. The likelihood function of the alternative hypotheses ($s \neq 0$) is maximized by $s = \Delta$ or

$$L_1 = \mathrm{Pois}(N_{\mathrm{ON}}, N_{\mathrm{ON}})\mathrm{Pois}(N_{\mathrm{OFF}}, N_{\mathrm{OFF}}) \,. \tag{19}$$

The two hypotheses are compared with the test statistic

$$-2\ln(L_0/L_1) = -2\left(N_{\mathrm{ON}}\ln(\frac{\overline{N_{\mathrm{ON}}}}{N_{\mathrm{ON}}}) + N_{\mathrm{OFF}}\ln(\frac{\overline{N_{\mathrm{OFF}}}}{N_{\mathrm{OFF}}})\right)$$

which is assumed to be distributed like a χ^2 distribution with one degree of freedom resulting from the one free parameter (s) of the test statistic if the null hypothesis is true. In other words, the quantity $\mathrm{sign}(\Delta)\sqrt{-2\ln(L_0/L_1)} = S_{\mathrm{LiMa}}$ is assumed to be distributed like a standard normal Gaussian random variable if the null hypothesis is true. The assumption results from the general likelihood principle (see f.i. Zech and Bohm [2010]) but needs not necessarily to be fulfilled for the profile likelihood method. In practice, the assumption can be checked in Monte Carlo simulations and is fulfilled for S_{LiMa}.
The method discussed above can easily be modified to allow an exposure ratio α which is not exactly known but distributed like a Gaussian, $\mathrm{Gaus}(\alpha, \overline{\alpha}, \sigma_\alpha)$, with known mean $\overline{\alpha}$ and known standard deviation σ_α. For this, eq. 16 is modified to

$$L = \mathrm{Pois}(N_{\mathrm{ON}}, \alpha b + s)\mathrm{Pois}(N_{\mathrm{OFF}}, b)\mathrm{Gaus}(\alpha, \overline{\alpha}, \sigma_\alpha) \,. \tag{20}$$

The two nuisance parameters, α and b, are profiled out with condition 18 and

$$\frac{\partial L_0}{\partial \alpha} = 0 \,. \tag{21}$$

This equation leads to the cubic expression

$$\alpha^3 - \alpha(\overline{\alpha} - \sigma_\alpha^2 N_{\mathrm{OFF}}) - \alpha^2(\overline{\alpha} - 1) - \sigma_\alpha^2 N_{\mathrm{ON}} = 0 \,. \tag{22}$$

In the case of $\sigma_\alpha = 0$ this condition leads to $\alpha = \overline{\alpha}$ and the method is equivalent to the ansatz above. The condition for α can in general be solved numerically and the solution can be used to build the test statistic S_{Mod} similar to the method explained above. The reliability of the method can be checked in a Monte Carlo simulation where N_{ON} and αN_{OFF} are selected randomly from the same Poisson distribution with known mean b and fixed $\overline{\alpha}$ and σ_α. A reliable method has to result in a standard normal distributed test statistic. Figure 24 shows the resulting test statistic $S_{\mathrm{LiMa}}(N_{\mathrm{ON}}, N_{\mathrm{OFF}}, \overline{\alpha})$ and $S_{\mathrm{Mod}}(N_{\mathrm{ON}}, N_{\mathrm{OFF}}, \overline{\alpha}, \sigma_\alpha)$ for $b = 3000$ and $\alpha = 0.5$ for two different values (2% and 5% of α) for σ_α. It is clearly visible that S_{LiMa} fits the better to a standard normal distribution the smaller the error on $\overline{\alpha}$. On the other hand, S_{Mod} always fits to a standard normal distribution but gives (on average and in absolute value) smaller significances than S_{LiMa} the larger the error on $\overline{\alpha}$. Figure 25 shows the same test statistic for $b = 100$. A comparison of fig. 25 and fig. 24 shows that S_{LiMa} fits the better to a standard

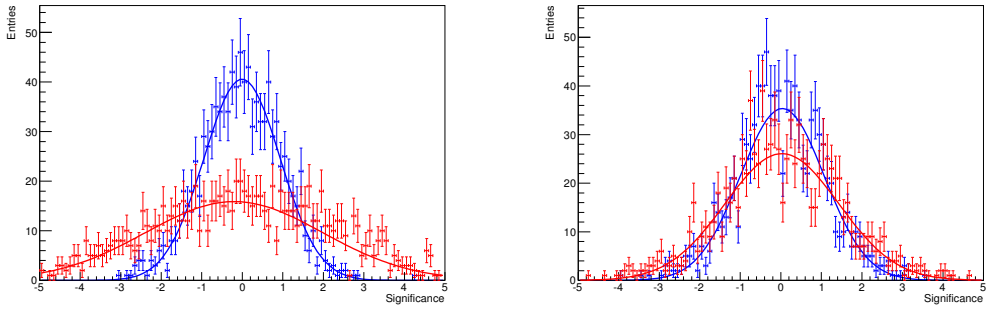

Figure 24: Significance distributions (S_{LiMa} in red and S_{Mod} in blue) for $\overline{\alpha} = 0.5$ and $b = 3000$. The left panel shows the resulting distribution for $\sigma_\alpha = 5\%\,\alpha$ and the right panel for $\sigma_\alpha = 2\%\alpha$. The curves show Gaussian fits to the respective distributions. In the case of 5% error on $\overline{\alpha}$, the width of the Gaussian fits are 1.00 ± 0.02 for S_{Mod} and 2.28 ± 0.08 for S_{LiMa}. In the case of 2% error on $\overline{\alpha}$, the width of the Gaussian fits are 1.05 ± 0.03 for S_{Mod} and 1.43 ± 0.04 for S_{LiMa}. The mean of all fits is compatible with zero.

normal distribution the smaller b and σ_α. It can be concluded that S_{Mod} is a reliable test statistic that is superior to S_{LiMa} if the exposure ratio is Gaussian distributed with a significant width. Whether or not the width of the exposure ratio distribution is relevant depends on the number of expected events and the width itself. A useful criteria that is motivated in chapter 4 is that the application of S_{LiMa} is appropriate if

$$\sqrt{N_{\mathrm{ON}} + \alpha^2 N_{\mathrm{OFF}}} \sim \alpha\sqrt{N_{\mathrm{OFF}}} \gg \sigma_\alpha N_{\mathrm{OFF}}$$

holds.

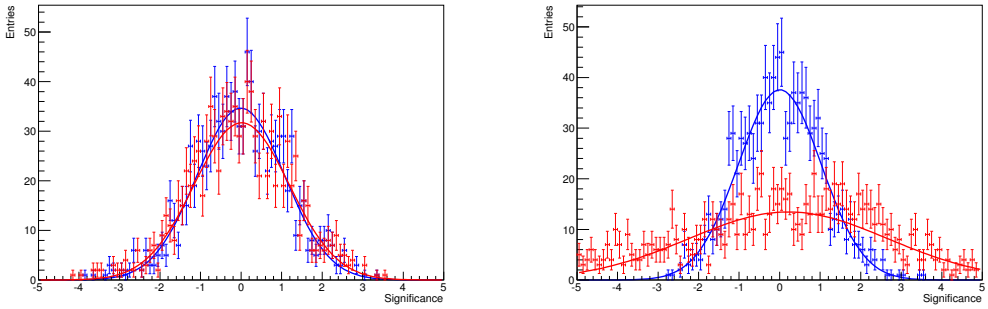

Figure 25: Significance distributions (S_{LiMa} in red and S_{Mod} in blue) for $\overline{\alpha} = 0.5$ and $b = 100$. The left panel shows the resulting distribution for $\sigma_\alpha = 5\%\alpha$ and the right panel for $\sigma_\alpha = 30\%\ \alpha$. The curves show Gaussian fits to the respective distributions. In the case of 5% error on $\overline{\alpha}$, the width of the Gaussian fits are 1.07 ± 0.03 for S_{Mod} and 1.25 ± 0.04 for S_{LiMa}. In the case of 30% error on $\overline{\alpha}$, the width of the Gaussian fits are 1.03 ± 0.03 for S_{Mod} and 2.5 ± 0.1 for S_{LiMa}. The mean of all fits is compatible with zero.

Appendix E: Precise Upper Limit on $\langle \sigma v \rangle$ - A Blueprint

A method to derive statements and especially upper limits on the velocity averaged WIMP annihilation cross section $\langle \sigma v \rangle$ based on Cherenkov telescope data analyzed with background subtraction algorithms was discussed in chapter 4. A more precise method is discussed in this appendix. The method is more complicated than the one discussed in chapter 5 and not yet completely implemented.

Expected Number of γ-ray Events from WIMP Annihilation

The starting point is the expression

$$\frac{d^2\Phi}{d\Omega dE} = \frac{\langle \sigma v \rangle}{2M^2} \frac{dN_\gamma}{dE_\gamma} J \, . \tag{23}$$

for the expected differential diffuse γ-ray flux for a WIMP of mass M. Here,

- the 'particle physics factor' is introduced as

$$\kappa \mathrm{PPF}(M, E) = \frac{\kappa \langle \sigma v \rangle_0}{2M^2} \frac{dN_\gamma}{dE_\gamma} \tag{24}$$

  where the nominal velocity averaged annihilation cross section is chosen to be $\langle \sigma v \rangle_0 = 3 \cdot 10^{-26}$ cm^3/s and expresses the typical order of magnitude of a thermal relic WIMP DM velocity averaged annihilation cross section. The scaling parameter κ is introduced to express the deviation of the velocity averaged annihilation cross section $\langle \sigma v \rangle = \kappa \langle \sigma v \rangle_0$ from the nominal velocity averaged annihilation cross section.

- The 'astrophysical factor' is given by

$$J(l, b) = \frac{1}{4\pi} \int_{\mathrm{LoS}} ds \, \rho^2(r(s[l, b])) \tag{25}$$

  and depends on the galactic longitude (l) and latitude (b) viewing direction.

Equation 23 leads to the following number of expected γ-ray events from WIMP annihilation

$$\kappa N_{\mathrm{ON}}^{\mathrm{DM},i}(M) = \kappa \frac{T^i_{\mathrm{Live}}}{T^i_{\mathrm{Run}}} \int dt \int_{\Omega(t)} d\Omega' \, \mathrm{Exc}_{\mathrm{ON}}(l', b') \, J(l', b') \, P^i(l', b', t, M) \tag{26}$$

in the signal region for one subdataset i (for instance one observation run in a rotated pixel method analysis). Here,

- T^i_{Run} is the observation or runtime and T^i_{Live} is the livetime, i.e. the dead time corrected runtime, of run i. The first integration, $\int dt$, is an integration over infinitesimal runtime intervals.
- The FoV $\Omega(t)$ depends in general on the time t as the equatorial or galactic pointing position can change during the run (f.i. in a driftscan observation).
- The function $\mathrm{Exc}_{\mathrm{ON}}(l', b')$ is zero/one if the solid angle element $d\Omega' = dl'\ db'\ \cos(b')$ is/is not excluded in the signal region (f.i. due to the presence of astrophysical γ-ray sources that are not of interest for the analysis).
- The last factor in eq. 26 is

$$P^i(l', b', t, M) = \int_{T^i}^{M} dE\ \mathrm{A}^i_{\mathrm{Eff}}(\phi', \theta', \psi', E)\ \mathrm{PPF}(M, E)\ .$$

  The effective area $\mathrm{A}_{\mathrm{Eff}}$ depends on the azimuth (ϕ') and zenith (θ') angle of the solid angle element $d\Omega'$ as well as the offset ψ' from the array pointing position. The horizon system coordinates ϕ' and θ' as well as ψ' can be obtained from the equatorial coordinates of the solid angle element $d\Omega'$ and the observation time t. Additionally, the effective area depends on the number of operating telescopes and their optical configuration as measured in muon correction factors during the runtime (see H.E.S.S. Col. [2006]). The same as for the effective area holds for the parameters of the energy threshold $T^i = T^i(\phi', \theta', \psi')$ which is defined as the maximum of the trigger and safe energy (see H.E.S.S. Col. [2006]) threshold.

The total expected number of DM annihilation γ-ray events detected in the signal region in a dataset consisting out of multiple subdatasets (i) is then given by $\sum_i N^{\mathrm{DM},i}_{\mathrm{ON}}$. Similarly, the expected number of DM annihilation γ-ray events $N^{\mathrm{DM},i}_{\mathrm{OFF}}$ that are detected in the background region for run i is calculated to be $N^{\mathrm{DM},i}_{\mathrm{ON}}$ and the total number of expected DM annihilation excess γ-ray events after background subtraction is thus $\sum_i (N^{\mathrm{DM},i}_{\mathrm{ON}} - \alpha_i N^{\mathrm{DM},i}_{\mathrm{OFF}})$.

Measurement of $\langle\sigma v\rangle$

The velocity averaged annihilation cross section $\langle\sigma v\rangle$ is measured relative to the defined nominal $\langle\sigma v\rangle_0$ via a measurement of the scaling factor κ. For each run in a dataset consisting of $i = 1..n$ runs the number of events in the signal (N^i_{ON}) and background (N^i_{OFF}) region is measured together with the exposure ratio $\bar{\alpha_i}$. The true exposure ratio α_i is assumed to be a Gaussian distributed random variable with mean $\bar{\alpha_i}$ and standard deviation σ^i_α. A particle DM model with nominal velocity averaged annihilation cross section $\langle\sigma v\rangle_0$ predicts $N^{\mathrm{DM},i}_{\mathrm{ON/OFF}}$ detected DM annihilation γ-ray events in the signal/background region. $N^{\mathrm{DM},i}_{\mathrm{ON/OFF}}$ is assumed to be a Gaussian random variable with

mean $\bar{N}^{\mathrm{DM},i}_{\mathrm{ON/OFF}}$ and standard deviation $\sigma^i_{\mathrm{NON/NOFF}}$ resulting f.i. from uncertainties in the effective detection area. Other probability density models for $N^{\mathrm{DM},i}_{\mathrm{ON/OFF}}$ can easily be implemented below. Given a particle DM model with velocity averaged annihilation cross section $\langle\sigma v\rangle = \kappa\langle\sigma v\rangle_0$ the likelihood function for the detection of $N^i_{\mathrm{ON/OFF}}$ events in the signal/background region is then

$$L(\kappa|\Xi,\theta) = \begin{array}{c} \prod_i \ \mathrm{Pois}(N^i_{\mathrm{ON}}, \alpha_i\bar{b}_i + \kappa N^{\mathrm{DM},i}_{\mathrm{ON}})\ \mathrm{Pois}(N^i_{\mathrm{OFF}}, \bar{b}_i + \kappa N^{\mathrm{DM},i}_{\mathrm{OFF}}) \\ \mathrm{Gaus}(\alpha_i, \bar{\alpha}_i, \sigma^i_\alpha)\ \mathrm{Gaus}(N^{\mathrm{DM},i}_{\mathrm{ON}}, \bar{N}^{\mathrm{DM},i}_{\mathrm{ON}}, \sigma^i_{\mathrm{NON}})\ \mathrm{Gaus}(N^{\mathrm{DM},i}_{\mathrm{OFF}}, \bar{N}^{\mathrm{DM},i}_{\mathrm{OFF}}, \sigma^i_{\mathrm{NOFF}}) \end{array} \tag{27}$$

where $\mathrm{Pois}(k,\bar{k})$ denotes the probability to observe the value k in a Poisson distributed sample with mean $\bar{k}$ and $\mathrm{Gaus}(x,\bar{x},\sigma)$ denotes the probability to observe a value x in a Gaussian distributed sample with mean $\bar{x}$ and standard deviation σ. The nuisance parameters $\theta = \alpha_i, \bar{b}_i, N^{\mathrm{DM},i}_{\mathrm{ON/OFF}}$ are 'profiled out' of the likelihood function using the condition $\partial L/\partial\theta = 0$ leading to the profile likelihood function $L_P(\kappa|\Xi)$ which only depends on the observed or predicted parameters $\Xi = N^i_{\mathrm{ON/OFF}},\ \bar{\alpha}_i,\ \sigma^i_\alpha, \bar{N}^{\mathrm{DM},i}_{\mathrm{ON/OFF}}, \sigma^i_{\mathrm{NON/NOFF}}$ and the scaling parameter κ that is to be measured. In practise, a confidence interval (or an upper limit) for κ can be constructed as the acceptance region of the null hypothesis for the profile log likelihood ratio test using statistical analysis algorithms provided in the RooStat package (see f.i. Moneta et al. [2010]). First tests of this package, which is also commonly applied in analyses of accelerator high energy physics data, indicate that very reliable statistical statements based on flexible likelihood functions can be obtained with reasonable computational efforts.

The method described here to infer statements on $\langle\sigma v\rangle$ introduces less approximations than the method described in chapter 5. Additionally, the direct measurement of $\langle\sigma v\rangle$ via the scaling parameter κ has, compared to the measurement of the number of excess events described in chapter 5 or the measurement of the excess γ-ray flux described in H.E.S.S. Col. [2011a] the advantage that uncertainties, f.i. in the effective area, can directly be propagated to uncertainties in $\langle\sigma v\rangle$ via the algorithms implemented in RooStat.

Bibliography

K. N. Abazajian and J. P. Harding. Constraints on WIMP and Sommerfeld-enhanced dark matter annihilation from HESS observations of the galactic center . *Journal of Cosmology and Astroparticle Physics*, 2012.

Abdo et al. A measurement of the spatial distribution of diffuse tev gamma-ray emission from the galactic plane with milagro. *The Astrophysical Journal*, 688, 2008.

Acero et al. Constraints on the galactic population of tev pulsar wind nebulae using fermi large area telescope observations. *The Astrophysical Journal*, 773, 2013.

Ackermann et al. Fermi LAT search for dark matter in gamma-ray lines and the inclusive photon spectrum. *Phys. Rev. D*, 86, 2012a.

Ackermann et al. Fermi-lat observations of the diffuse γ-ray emission: Implications for cosmic rays and the interstellar medium. *The Astrophysical Journal*, 750, 2012b.

Ackermann et al. Detection of the Characteristic Pion-decay Signature in Supernova Remnants. *arXiv:1302.3307*, 2013.

Actis et al. Design concepts for the cherenkov telescope array cta: an advanced facility for ground-based high-energy gamma-ray astronomy. *Experimental Astronomy*, 32, 2011.

Adriani et al. PAMELA Results on the Cosmic-Ray Antiproton Flux from 60 MeV to 180 GeV in Kinetic Energy. *Phys. Rev. Lett.*, 105, 2010.

Aharonian et al. The hess survey of the inner galaxy in very high energy gamma rays. *The Astrophysical Journal*, 636, 2006.

Aharonian et al. Hess observations of the supernova remnant rx j0852: Shell-type morphology and spectrum of a widely extended very high energy gamma-ray source. *The Astrophysical Journal*, 661, 2007.

Aharonian et al. High energy astrophysics with ground-based gamma ray detectors. *Reports on Progress in Physics*, 71, 2008a.

Aharonian et al. Discovery of very-high-energy gamma-ray emission from the vicinity of psr j1913+ 1011 with hess. *Astronomy and Astrophysics*, 484, 2008b.

Aharonian et al. Hess very-high-energy gamma-ray sources without identified counterparts. *Astronomy and Astrophysics*, 477, 2008c.

Aharonian et al. Detection of very high energy radiation from hess j1908+ 063 confirms the milagro unidentified source mgro j1908+ 06. *arXiv:0904.3409*, 2009.

Albert et al. Observation of vhe gamma radiation from hess j1834-087/w41 with the magic telescope. *The Astrophysical Journal Letters*, 643, 2006.

Alcock et al. The macho project: Microlensing results from 5.7 years of large magellanic cloud observations. *Astrophysical Journal*, 542, 2000.

AMS-II Col. First Results from the Alpha Magnetic Spectrometer on the International Space Station: Precision Measurement of the Positron Fraction in Primary Cosmic Rays of 0.5-350 GeV. *Phys. Rev. Lett.*, 110, 2013.

C. D. Anderson. The Apparent Existence of Easily Deflectable Positives. *Science*, 76, 1932.

ANTARES Col. Performance of the front-end electronics of the ANTARES neutrino telescope. *Nuclear Instruments and Methods in Physics Research A*, 622, 2010.

Aprile et al. Dark matter results from 100 live days of xenon100 data. *Phys. Rev. Lett.*, 107, 2011.

Arbey et al. Supersymmetry confronts Bs to mu+mu-: Present and future status. *Phys. Rev. D*, 87, 2013.

R. Argurio. Introduction to supersymmetry. *Lecture notes PHYS-F-417, University of Bruxelles*, 2011.

ATLAS Col. Search for dark matter and large extra dimensions in events with a jet and missing transverse momentum with the ATLAS detector. *arXiv:1210.4491*, 2012a.

ATLAS Col. Observation of a new particle in the search for the Standard Model Higgs boson with the ATLAS detector at the LHC. *Physics Letters B*, 716, 2012b.

Atwood et al. The large area telescope on the fermi gamma-ray space telescope mission. *The Astrophysical Journal*, 697, 2009.

Auger et al. Extensive cosmic-ray showers. *Rev. Mod. Phys.*, 11, 1939.

Aye et al. Atmospheric Monitoring for the H.E.S.S. Project. *arXiv:0307452*, 2003.

H. W. Babcock. The rotation of the Andromeda Nebula. *Lick Observatory Bulletin*, 19, 1939.

A. Balzer. Systematic studies of the h.e.s.s. camera calibration. *Diploma Thesis, ECAP Erlangen*, 2010.

A. N. Baushev. Principal properties of the velocity distribution of dark matter particles on the outskirts of the solar system. *Monthly Notices of the Royal Astronomical Society: Letters*, 417, 2011.

Becherini et al. Advanced analysis and event reconstruction for the cta observatory. *arXiv:1211.5997*, 2012.

Begeman et al. Extended rotation curves of spiral galaxies - dark haloes and modified dynamics. *Monthly Notices to the Royal Astronomical Society*, 249, 1991.

Bell et al. W/Z Bremsstrahlung as the Dominant Annihilation Channel for Dark Matter. *Phys. Rev. D*, 2011.

Berge et al. Background modelling in very-high-energy γ-ray astronomy. *Astronomy and Astrophysics*, 466, 2007.

Bergstrom et al. Observability of gamma rays from dark matter neutralino annihilations in the Milky Way halo. *Astroparticle Physics*, 9, 1998.

Bergstrom et al. Gamma Rays from Kaluza-Klein Dark Matter. *PRL*, 94, 2005.

Bergstrom et al. Investigating gamma-ray lines from dark matter with future observatories . *Journal of Cosm. and Astropart. Phys.*, 2012.

Bernabei et al. On the investigation of possible systematics in WIMP annual modulation search. *European Physics Journal C*, 18, 2000.

Bernabei et al. Dark Matter Particles in the Galactic Halo. *International Journal of Modern Physics D*, 13, 2004.

Bernabei et al. New results from DAMA/LIBRA. *European Physics Journal C*, 67, 2010.

K. Bernloehr. Geomagnetic effects on showers relevant fo the h.e.s.s. experiment. *H.E.S.S. internal note*, 2005.

Bernloehr et al. Monte carlo design studies for the cherenkov telescope array. *arXiv:1210.3503*, 2013.

K. Bernlohr. Impact of atmospheric parameters on the atmospheric Cherenkov technique. *Astroparticle Physics*, 12, 2000.

K. Bernlöhr. Simulation of imaging atmospheric Cherenkov telescopes with CORSIKA and sim_telarray. *Astroparticle Physics*, 30, 2008.

Bernlöhr et al. The optical system of the H.E.S.S. imaging atmospheric Cherenkov telescopes. Part I: layout and components of the system. *Astroparticle Physics*, 20, 2003.

Bertone et al. Particle Dark Matter: Evidence, Candidates and Constraints. *Physics Reports*, 405, 2005.

H. J. Bhabha and W. Heitler. The Passage of Fast Electrons and the Theory of Cosmic Showers. *Royal Society of London Proceedings Series A*, 159, 1937.

Bidin et al. Kinematical and chemical vertical structure of the galactic thick disc. ii. a lack of dark matter in the solar neighborhood. *Astrophysical Journal*, 751, 2012.

Boer et al. The supersymmetric interpretation of the EGRET excess of diffuse Galactic gamma rays. *Physics Let. B*, 636, 2006.

J. Bovy and S. Tremaine. On the local dark matter density. *Astrophysical Journal*, 756, 2012.

Boyarsky et al. The Role of Sterile Neutrinos in Cosmology and Astrophysics. *Ann. Rev. Nucl. Part. Sci.*, 59, 2009.

Bradač et al. Revealing the Properties of Dark Matter in the Merging Cluster MACS J0025.4-1222. *The Astrophysical Journal*, 687, 2008.

T. Bringmann. *Cosmological Aspects of Universal Extra Dimensions*. Stockholm University, 2005.

Bringmann et al. New Gamma-Ray Contributions to Supersymmetric Dark Matter Annihilation. *JHEP*, 2008.

J. P. Brownstein and J. W. Moffat. The bullet cluster 1e0657-558 evidence shows modified gravity in the absence of dark matter. *Monthly Notices to the Royal Astronomical Society*, 382, 2007.

Buckley et al. The status and future of ground-based tev gamma-ray astronomy. *arXiv:0810.0144*, 2008.

J. F. Carlson and J. R. Oppenheimer. On multiplicative showers. *Phys. Rev.*, 51, 1937.

Carrigan et al. Charting the tev milky way: Hess galactic plane survey maps, catalog and source populations. *arXiv:1307.4868*, 2013.

Casanova et al. Molecular clouds as cosmic-ray barometers. *arXiv:0904.2887*, 2009.

R. Catena and P. Ullio. A novel determination of the local dark matter density. *Journal of Cosmology and Astroparticle Physics*, 2010, 2010.

CDMS Col. Dark Matter Search Results Using the Silicon Detectors of CDMS II. *arXiv:1304.4279*, 2013.

Cembranos et al. Photon spectra from WIMP annihilation. *Phys. Rev. D*, 83, 2011.

Chadwick et al. Sensing atmospheric conditions using MIR radiometers. In *American Institute of Physics Conference Series*, volume 515 of *American Institute of Physics Conference Series*, 2000.

Chang et al. An excess of cosmic ray electrons at energies of 300-800 GeV. *Nature*, 456, 2008.

R.C.G. Chaves. Extending the H.E.S.S. Galactic Plane Survey. *arXiv:0907.0768*, 2009.

Chaves et al. Hess j1848-018: Discovery of vhe gamma-ray emission from the direction of w 43. *Proceedings to the 25th Texas Symposium*, 2008.

V. Chepel and H. Araujo. Liquid noble gas detectors for low energy particle physics. *arXiv:1207.2292*, 2012.

Churchwell et al. The spitzer/glimpse surveys: a new view of the milky way. *Publications of the Astronomical Society of the Pacific*, 121, 2009.

O. Chwolson. Über eine mögliche Form fiktiver Doppelsterne. *Astronomische Nachrichten*, 221, 1924.

T. Cirelli and S. Giesen. Antiprotons from Dark Matter: Current constraints and future sensitivities. *arXiv:1301.7079*, 2013.

Clowe et al. A Direct Empirical Proof of the Existence of Dark Matter. *The Astrophysical Journal*, 648, 2006.

CMS Col. Search for Dark Matter and Large Extra Dimensions in pp Collisions Yielding a Photon and Missing Transverse Energy. *Phys. Rev. Lett.*, 108, 2012a.

CMS Col. Observation of a new boson at a mass of 125 GeV with the CMS experiment at the LHC. *Physics Letters B*, 716, 2012b.

F. Combes. Distribution of co in the milky way. *Annual Review of Astronomy and Astrophysics*, 29, 1991.

Cornils et al. The optical system of the H.E.S.S. imaging atmospheric Cherenkov telescopes. Part II: mirror alignment and point spread function. *Astroparticle Physics*, 20, 2003.

R.M. Crocker. Non-thermal insights on mass and energy flows through the galactic centre and into the fermi bubbles. *Monthly Notices of the Royal Astronomical Society*, 423, 2012.

R.M. Crocker and F. Aharonian. Fermi bubbles: giant, multibillion-year-old reservoirs of galactic center cosmic rays. *Physical Review Letters*, 106, 2011.

J.M. Davis and E.S. Cotton. Design of the quartermaster solar furnace . *Solar Energy*, 1, 1957.

Deyoung et al. The HAWC Observatory. In *38th COSPAR Scientific Assembly*, volume 38 of *COSPAR Meeting*, 2010.

P. A. M. Dirac. The Quantum Theory of the Electron. *Royal Society of London Proceedings Series A*, 117, 1928.

Djannati-Atai et al. New companions for the lonely crab? vhe emission from young pulsar wind nebulae revealed by hess. *arXiv:0710.2247*, 2007.

G. Dobler. A last look at the microwave haze/bubbles with wmap. *The Astrophysical Journal*, 750, 2012.

Dobler et al. The fermi haze: a gamma-ray counterpart to the microwave haze. *The Astrophysical Journal*, 717, 2010.

A. D. Dolgov. Neutrinos in Cosmology. *Physics Reports*, 370, 2002.

Doro et al. Dark matter and fundamental physics with the cherenkov telescope array. *Astroparticle Physics*, 2012.

Egberts et al. Diffuse tev gamma-ray emission in the hess galactic plane survey. *arXiv:1308.0161*, 2013.

Ehret et al. Production and Detection of Axion-Like Particles in a HERA Dipole Magnet - Letter of Intent for the ALPS experiment. *arXiv:hep-ex/0702023*, 2007.

Eidelman et al. Particle Data Booklet. *Physics Letters B*, 592, 2004.

D. Eidenmueller. Hadron suppression using a cluster finder algorithm for the h.e.s.s. telescope system. *Diploma Thesis, HU Berlin*, 2002.

Einasto et al. Dynamic evidence on massive coronas of galaxies. *Nature*, 250, 1974.

A. Einstein. Lens-Like Action of a Star by the Deviation of Light in the Gravitational Field. *Science*, 84, 1936.

Engel et al. Extensive air showers and hadronic interactions at high energy. *Annual Review of Astronomy and Astrophyscs*, 61, 2011.

Evoli et al. Antiprotons from dark matter annihilation in the Galaxy: astrophysical uncertainties. *Phys. Rev. D*, 85, 2012.

Fatuzzo et al. High energy cosmic-ray diffusion in moleculr clouds: A numerical approach. *Astrophysical Journal*, 725, 2010.

D. J. Fegan. Gamma/hadron separation at tev energies. *Journal of Physics G: Nuclear and Particle Physics*, 23, 1997.

G. J. Feldman and R. D. Cousins. Unified approach to the classical statistical analysis of small signals. *Phys. Rev. D*, 57, 1998.

E. Fermi. On the Origin of the Cosmic Radiation. *Physical Review*, 75, 1949.

Fermi Col. Observations of Milky Way dwarf spheroidal galaxies with the fermi large area telescope detector and constraints on dark matter models. *Astrophys. Journ.*, 712, 2010.

Fermi Col. Measurement of Separate Cosmic-Ray Electron and Positron Spectra with the Fermi Large Area Telescope. *Physical Review Letters*, 108, 2012.

Fermi-LAT Col. Search for gamma-ray spectral lines with the fermi large area telescope and dark matter implications. *arXiv:1305.5597*, 2013.

Fiasson et al. Optimization of multivariate analysis for iact stereoscopic systems. *Astroparticle Physics*, 34, 2010.

D. P. Finkbeiner and M. Su. Strong evidence for gamma-ray line emission from the inner galaxy. *arXiv:1206.1616*, 2012.

Fox et al. Missing energy signatures of dark matter at the LHC. *Phys. Rev. D*, 85, 2012.

A. Franckowiak and D. Malyshev. Spectrum and Morphology of the Fermi Bubbles. In *International Cosmic Ray Conference*, 2013.

S. Funk and J. Hinton. Comparison of Fermi-LAT and CTA in the region between 10-100 GeV. *ArXiv e-prints*, 2012.

Funk et al. The trigger system of the H.E.S.S. telescope array. *Astroparticle Physics*, 22, 2004.

W. Galbraith and J. V. Jelley. Light Pulses from the Night Sky associated with Cosmic Rays. *Nature*, 171, 1953.

Gentile et al. The cored distribution of dark matter in spiral galaxies. *Monthly Notices of the Royal Astronomical Society*, 351, 2004.

A. Geringer-Sameth and S.M. Koushiappas. Exclusion of Canonical Weakly Interacting Massive Particles by Joint Analysis of Milky Way Dwarf Galaxies with Data from the Fermi Gamma-Ray Space Telescope. *Phys. Rev. D*, 107, 2011.

S. Gillessen. Arcsecond level pointing of the hess telescopes. *Proceedings to the International Cosmic Ray Conference*, 2003.

V.L. Ginzburg. Radiation by uniformly moving sources. *Physics-Uspekhi*, 39, 1996.

Gnedin et al. The mass profile of the galaxy up to 80 kpc . *The Astrophysical Journal Letters*, 720, 2010.

P. Gondolo. Non-Baryonic Dark Matter. *Lectures delivered at the NATO Advanced Study Institute "Frontiers of the Universe", astro-ph/0403064*, 2003.

Goodman et al. Constraints on dark matter from colliders. *Phys. Rev. D*, 82, 2010.

Gorski et al. Healpix: a framework for high-resolution discretization and fast analysis of data distributed on the sphere. *The Astrophysical Journal*, 2005.

Governato et al. Cuspy no more: how outflows affect the central dark matter and baryon distribution in cold dark matter galaxies. *Monthly Notices of the Royal Astronomical Society*, 422, 2012.

Grasso et al. On possible interpretations of the high energy electron-positron spectrum measured by the Fermi Large Area Telescope. *Astroparticle Physics*, 32, 2009.

A. Gupta and S. Mathur. A huge reservoir of ionized gas around the milky way: Accounting for the missing mass? *Astrophysical Journal*, 756, 2012.

S. Hassani. *Mathematical Physics*. Springer, 3rd edition, 2002.

Heck et al. CORSIKA: A Monte Carlo Code to Simulate Extensive Air Showers. *Forschungszentrum Karlsruhe, Wissenschaftliche Berichte*, FZKA 6019, 1998.

HEGRA Col. Performance of the stereoscopic system of the HEGRA imaging air Cherenkov telescopes: Monte Carlo simulations and observations. *Astroparticle Physics*, 10, 1999.

W. Heisenberg. *Kosmische Strahlung*. Springer, 1st edition, 1943.

W. Heitler. *The Quantum Theory of Radiation*. Oxford University Press, 3st edition, 1954.

V. Hess. Ueber Beobachtungen der durchdringenden Strahlung bei sieben Freiballonfahrten. *Zeitschrift f. Physik*, 1912.

H.E.S.S. Col. Calibration of cameras of the H.E.S.S. detector. *Astroparticle Physics*, 22, 2004.

H.E.S.S. Col. Very high energy gamma rays from the composite SNR G 0.9+0.1. *Astronomy and Astrophysics*, 432, 2005a.

H.E.S.S. Col. Discovery of very-high-energy gamma-rays from the galactic centre ridge. *Nature*, 439, 2005b.

H.E.S.S. Col. Observations of the Crab nebula with HESS. *Astronomy and Astrophysics*, 457, 2006.

H.E.S.S. Col. Energy spectrum of cosmic-ray electrons at tev energies. *Phys. Rev. Lett.*, 101, 2008.

H.E.S.S. Col. Exploring a SNR/Molecular Cloud Association Within HESS J1745-303. *Astronomy and Astrophysics*, 483, 2008.

H.E.S.S. Col. Probing the ATIC peak in the cosmic-ray electron spectrum with H.E.S.S. *Astronomy and Astrophysics*, 508, 2009.

H.E.S.S. Col. Spectrum and variability of the Galactic center VHE gamma-ray source HESS J1745-290. *Astronomy and Astrophysics*, 503, 2009.

H.E.S.S. Col. Search for a Dark Matter annihilation signal from the Galactic Center halo with H.E.S.S. *Phys. Rev. Lett.*, 106, 2011a.

H.E.S.S. Col. Very-high-energy gamma-ray emission from the direction of the Galactic globular cluster Terzan 5. *Astronomy and Astrophysics*, 531, 2011b.

H.E.S.S. Col. Search for Lorentz Invariance breaking with a likelihood fit of the PKS 2155-304 flare data taken on MJD 53944. *Astroparticle Physics*, 34, 2011.

H.E.S.S. Col. Discovery of gamma-ray emission from the extragalactic pulsar wind nebula N157B with H.E.S.S. *Astronomy and Astrophysics*, 545, 2012.

H.E.S.S. Col. Search for photon line-like signatures from Dark Matter annihilations with H.E.S.S . *Phys. Rev. Lett.*, 110, 2013.

Hessels et al. Psr j1856+ 0245: Arecibo discovery of a young, energetic pulsar coincident with the tev γ-ray source hess j1857+ 026. *The Astrophysical Journal Letters*, 682, 2008.

C. T. Hill. Monopolium. *Nucl. Phys. B*, 224, 1983.

A. M. Hillas. Cerenkov light images of EAS produced by primary gamma. In F. C. Jones, editor, *International Cosmic Ray Conference*, volume 3 of *International Cosmic Ray Conference*, 1985.

A. M. Hillas. Topical review: Can diffusive shock acceleration in supernova remnants account for high-energy galactic cosmic rays? *Journal of Physics G Nuclear Physics*, 31, 2005.

A.M. Hillas. Differences between gamma-ray and hadronic showers. *Space Science Reviews*, 75, 1996.

Hinshaw et al. Nine-Year Wilkinson Microwave Anisotropy Probe (WMAP) Observations: Cosmological Parameter Results. *arXiv:1212.5226*, 2013.

J. A. Hinton and W. Hofmann. Teraelectronvolt Astronomy. *Annual Review of Astronomy and Astrophysics*, 47, 2009.

Hirayama et al. The EGS5 Code System. *SLAC Report*, SLAC-R-730, 2005.

E. Hivon. The healpix primer. *astro-ph/9905275*, 1999.

D. Hooper and S. Profumo. Dark matter and collider phenomenology of universal extra dimensions. *Physics Reports*, 453, 2007.

S. Hoppe. The H.E.S.S. survey of the inner Galactic plane. *International Cosmic Ray Conference*, 2008.

Hou et al. The spiral structure of our milky way galaxy. *arXiv:0903.0721*, 2009.

W. Hu and S. Dodelson. Cosmic microwave background anisotropies. *Ann. Rev. Astron. and Astrophys.*, 40, 2002.

E. Hubble. *The Realm of the Nebulae.* Yale Univ. Press, 1982 reprint edition, 1936.

IceCube Col. Measurement of the Anisotropy of Cosmic-ray Arrival Directions with IceCube. *Astrphysical Journal Letters*, 718, 2010.

IceCube Col. Search for dark matter from the Galactic halo with the IceCube Neutrino Telescope. *Phys. Rev. D*, 84, 2011.

IceCube Col. Search for dark matter annihilations in the Sun with the 79-string IceCube detector. *arXiv:1212.4097*, 2013a.

IceCube Col. Search for Neutrinos from Annihilating Dark Matter in the Direction of the Galactic Center with the 40-String IceCube Neutrino Observatory. *arXiv:1210.3557*, 2013b.

J. D. Jackson. *Classical Electrodynamics.* John-Wiley and Sons, 3rd edition, 1998.

F. Jegerlehner and A. Nyffler. The muon g-2. *Phys. Rep.*, 477, 2009.

Jungmann et al. Supersymmetric Dark Matter. *Physics Reports*, 267, 1996.

P.M.W. Kalberla and J. Kerp. The hi distribution of the milky way. *Annual Review of Astronomy and Astrophyscs*, 47, 2009.

T. Kaluza. Zum Unitaetsproblem der Physik. *Sitzungsberichte der Preussischen Akademie der Wissenschaften*, 96, 1921.

Kanbach et al. The project egret (energetic gamma-ray experiment telescope) on nasa's gamma-ray observatory gro. *Space Science Reviews*, 49, 1989.

O. Klein. Quantentheorie und fuenfdimensionale Relativitaetstheorie. *Zeitschrift fuer Physik A*, 37, 1926.

Knapp et al. Extensive air shower simulations at the highest energies. *Astroparticle Physics*, 19, 2003.

Kuhlen et al. Dark matter direct detection with non-maxwellian velocity structure. *Journal of Cosmology and Astroparticle Physics*, 2010, 2010.

Kuhlen et al. An off-center density peak in the milky way's dark matter halo? *arXiv:1208.4844*, 2013.

V. Kulilovskiy. A search for Neutrino Emission from the Fermi Bubbles with the ANTARES telescope. In *International Cosmic Ray Conference*, 2013.

Laffon et al. Evidence for vhe emission from snr g22. 7-0.2 region with hess. *arXiv:1110.6890*, 2011.

Laffon et al. Discovery of the mysterious gamma-ray source hessj1832-093 in the vicinity of snr g22. 7-0.2. *Proceedings to the 33nd ICRC*, 18, 2013.

LHCb Col. First evidence for the decay Bs to mu+mu-. *Phys. Rev. Lett.*, 110, 2013.

T.-P. Li and Y.-Q. Ma. Analysis methods for results in gamma-ray astronomy. *Astrophysical Journal*, 272, 1983.

T. Linden and S. Profumo. Probing the Pulsar Origin of the Anomalous Positron Fraction with AMS-02 and Atmospheric Cherenkov Telescopes. *arXiv:1304.1791*, 1996.

M. Longair. *Galaxy Formation*. Springer, 1st edition, 1998.

M. Longair. *The Cosmic Century*. Cambridge University Press, 1st edition, 2007.

M. Longair. *High Energy Astrophysics*. Cambridge University Press, 3rd edition, 2011.

C. Lunardini and S. Razzaque. High energy neutrinos from the fermi bubbles. *Physical Review Letters*, 108, 2012.

K. J. Mack. Axions, Inflation and the Antrophic Principle. *Journal of Cosmology and Astroparticle Physics*, 2011, 2011.

G. Maier and J. Knapp. Cosmic-ray events as background in imaging atmospheric Cherenkov telescopes. *Astroparticle Physics*, 28, 2007.

S.P. Martin. A Supersymmetry Primer. *arXiv:hep-ph/9709356*, 2013.

A. Mellinger. A Color All-Sky Panorama Image of the Milky Way. *Astronomical Society of the Pacific*, 121, 2009.

P. Mertsch and S. Sarkar. Fermi gamma-ray bubbles from stochastic acceleration of electrons. *Physical Review Letters*, 107, 2011.

M. Milgrom. A modification of the newtonian dynamics as a possible alternative to the hidden mass hypothesis. *Astrophysical Journal*, 270, 1983a.

M. Milgrom. A modification of the newtonian dynamics - implications for galaxies. *Astrophysical Journal*, 270, 1983b.

R. A. Millikan. High Frequency Rays of Cosmic Origin. *Science*, 1925.

Moneta et al. The RooStats Project. *arXiv:1009.1003*, 2010.

J. W. Mueller. Dead-time problems. *Nuclear Instruments and Methods*, 112, 1973.

T. Murach. A mono reconstruction software for phase ii of the h.e.s.s. experiment. *Master Thesis, HU Berlin*, 2012.

S. H. Neddermeyer and C. D. Anderson. Note on the Nature of Cosmic-Ray Particles. *Physical Review*, 51, 1937.

Nolan et al. Detailed studies of atmospheric calibration in imaging Cherenkov astronomy. *Astroparticle Physics*, 34, 2010.

J.H. Oort. The force exerted by the stellar system in the direction perpendicular to the galactic plane and some related problems. *Bulletin of the Astronomical Institutes of the Netherlands*, 6, 1932.

Ostriker et al. The size and mass of galaxies, and the mass of the universe. *The Astrophysical Journal*, 193, 1974.

A. Pais. *Inward Bound*. Oxford Univ. Press, 1994 reprint edition, 1986.

PAMELA Col. An anomalous positron abundance in cosmic rays with energies 1.5-100GeV. *Letters to Nature*, 458, 2009.

PAMELA Col. PAMELA Measurements of Cosmic-Ray Proton and Helium Spectra. *Science*, 332, 2011.

Parsons et al. Systematic uncertainties in air shower measurements from high-energy hadronic interaction models. *Astroparticle Physics*, 34, 2011.

Pascoli et al. On the neutrino mass spectrum and neutrinoless double-beta decay. *Physics Letters B*, 558, 2003.

M. Paz Arribas. First monte carlo studies for the array level trigger system in cta. *Master Thesis, HU Berlin*, 2008.

R. D. Peccei. QCD, Strong CP and Axions. *arXiv:hep-ph/9606475v1*, 1996.

R. Penrose. *The Road to Reality*. Vintage Books, 10th edition, 2005.

A. A. Penzias and R. W. Wilson. A Measurement of Excess Antenna Temperature at 4080 Mc/s. *Astrophysical Journal*, 142, 1965.

M. E. Peskin and D. V. Schroeder. *An Introduction to Quantum Field Theory*. Westview Press, 1st edition, 1995.

A. H. G. Peter. Wimp astronomy and particle physics with liquid-noble and cryogenic direct-detection experiments. *Phys. Rev. D*, 83, 2011.

Pieri et al. Implications of high-resolution simulations on indirect dark matter searches. *Phys. Rev. D*, 83, 2011.

Piron et al. Temporal and spectral gamma-ray properties of mkn 421 above 250 gev from cat observations between 1996 and 2000. *Astronomy and Astrophysics*, 374, 2001.

Planck Col. Detection of the Galactic Haze with Planck. *arXiv:1208.5483v1*, 2012.

Planck Col. Planck 2013 results. XVI. Cosmological parameters. *Submitted to Astronomy and Astrophysics*, 2013.

M. Pohl and D. Eichler. Fermi constrains dark-matter origin of high-energy positron anomaly. *Astrophys. Journ. Lett.*, 712, 2010.

Preu et al. Study of the photon flux from the night sky at La Palma and Namibia, in the wavelength region relevant for imaging atmospheric Cherenkov telescopes. *Nuclear Instruments and Methods in Physics Research A*, 481, 2002.

S. Profumo and T. Linden. Gamma-ray lines in the fermi data: is it a bubble? *Journal of Cosmology and Astroparticle Physics*, 2012.

Rajaraman et al. LHC Bounds on Interactions of Dark Matter. *Phys. Rev. D*, 84, 2011.

Rolke et al. Limits and confidence intervals in the presence of nuisance parameters. *Nuclear Instruments and Methods in Physics Research Section A*, 551, 2005.

G.P. Rowell. A new template background estimate for source searching in TeV gamma-ray astronomy. *Astronomy and Astrophysics*, 410, 2003.

Rubin et al. Extended rotation curves of high-luminosity spiral galaxies. IV - Systematic dynamical properties, SA through SC. *Astrophysical Journal*, 225, 1978.

Sanchez-Conde et al. The search for axion-like-particles with Fermi and Cherenkov telescopes. *arXiv:1001.1892*, 2010.

D.S. Seljebotn. Wavemoth-fast spherical harmonic transforms by butterfly matrix compression. *The Astrophysical Journal Supplement Series*, 199, 2012.

G. Servant and T. M. P. Tait. Elastic scattering and direct detection of Kaluza-Klein dark matter. *New Journal of Physics*, 4, 2002.

G. Servant and T. M. P. Tait. Is the lightest Kaluza-Klein particle a viable dark matter candidate? *Nuclear Physics B*, 650, 2003.

Sheidaei et al. Discovery of very-high-energy gamma-ray emission from the vicinity of psr j1831-952 with hess. *arXiv:1110.6837*, 2011.

Sloan et al. Infrared Emission Spectrum of the Atmosphere. *Journ. of the Optical Soc. of America*, 45, 1955.

D. Smith and N. Weiner. Inelastic Dark Matter. *Phys. Rev. D*, 64, 2001.

S. Smith. The Mass of the Virgo Cluster. *Astrophysical Journal*, 83, 1936.

D. Sobczyńska. The background from single electromagnetic subcascades for a stereo system of air Cherenkov telescopes. *Journal of Physics G Nuclear Physics*, 36, 2009.

G. Spengler. Signatures of ultrarelativistic magnetic monopoles in imaging atmospheric cherenkov telescopes. *Diploma Thesis, HU Berlin*, 2009.

Sternheimer et al. Density effect for the ionization loss of charged particles in various substances. *Phys. Rev. B*, 26, 1982.

L.E. Strigari. Galactic searches for dark matter. *arXiv:1211.7090*, 2012.

Strong et al. The galprop cosmic-ray propagation code. *arXiv:0907.0559*, 2009.

Su et al. Giant gamma-ray bubbles from fermi-lat: active galactic nucleus activity or bipolar galactic wind? *The Astrophysical Journal*, 724, 2010.

A. Tasitsiomi and A. V. Olinto. Detectability of neutralino clumps via atmospheric Cherenkov telescopes. *Phys. Rev. D*, 66, 2002.

Terrier et al. Discovery of a pulsar wind nebula associated with igr j18490-0000. In *Aip Conference Proceedings*, volume 1085, 2008.

Tibolla et al. A new source discovered close to the Galactic Center: HESSJ1741-302. *AIP Conf. Proc.*, 1085, 2008.

M. S. Vallarta and R. P. Feynman. The Scattering of Cosmic Rays by the Stars of a Galaxy. *Physical Review*, 55, 1939.

VERITAS Col. Detection of Pulsed Gamma Rays Above 100 GeV from the Crab Pulsar. *Science*, 334, 2011.

M. G. Walker and J. Penarrubia. A method for measuring (slopes of) the mass profiles of dwarf spheroidal galaxies. *Astrophysical Journal*, 742, 2011.

Walsh et al. 0957 + 561 A, B - Twin quasistellar objects or gravitational lens. *Nature*, 279, 1979.

M. Weber and W. de Boer. Determination of the local dark matter density in our galaxy. *Astronomy and Astrophysics*, 509, 2010.

Weekes et al. Observation of TeV gamma rays from the Crab nebula using the atmospheric Cerenkov imaging technique. *Astrophysical Journal*, 342, 1989.

C. Weniger. A tentative gamma-ray line from Dark Matter annihilation at the Fermi Large Area Telescope . *Journal of Cosm. and Astropart. Phys.*, 2012.

B. H. Wiik and K. H. Mess. Recent results in electron - positron and lepton -hadron interactions. *DESY Report 82-011*, 1982.

Wommer et al. Diffuse tev emission at the galactic centre. *Monthly Notice of the Royal Astronomical Society*, 387, 2008.

G. Zech and G. Bohm. *Introduction to Statistics and Data Analysis for Physicists*. Verlag Deutsches Elektronen-Synchrotron, 2010.

F. Zwicky. Die Rotverschiebung von extragalaktischen Nebeln. *Helvetica Physica Acta*, 6, 1933.

F. Zwicky. On the Masses of Nebulae and of Clusters of Nebulae. *Astrophysical Journal*, 86, 1937.

List of Figures

List of Tables

Selbständigkeitserklärung

Ich erkläre, dass ich die vorliegende Arbeit selbständig und nur unter Verwendung der angegebenen Literatur und Hilfsmittel angefertigt habe.

Berlin, den Gerrit Christian Spengler